Dissertation submitted in partial satisfaction of the requirements for the degree of Doctor of Philosophy in Physics

Visualization of quasiparticles in quantum materials at high magnetic fields

Francisco Martín Vega

October 2021

Thesis supervisors
Isabel Guillamón and Hermann Suderow
Universidad Autónoma de Madrid

Agradecimientos

Nunca he tenido claro qué quería ser de mayor. Ni si quiera ahora lo sé. Lo que sí creo es que el niño que algún día fui me miraría con admiración. Y no por todos los conocimientos científicos que haya podido adquirir durante estos años. Eso es lo de menos. Lo más importante es que este largo y no siempre amable camino que se culmina con esta tesis me ha servido para evolucionar como persona. Desde aquel chaval que llegó al laboratorio lleno de dudas sin casi atreverse a hablar con nadie hasta el chaval algo más crecidito que escribe estas líneas. Lleno de dudas, por supuesto, pero mucho más cerca de ser la persona que quiere ser. Y eso es, sin ningún lugar a duda, gracias a todos los que me habéis acompañado durante estos años. Porque el mundo es un lugar bastante hostil que ciertas personas consiguen que acabes amando.

Tengo que empezar dando las gracias a Hermann e Isabel. Siempre dispuestos a ayudar. Con lo que sea, como sea y cuando sea. Sois el contrapunto necesario para mi pesimismo. Me habéis enseñado que aunque no sepas hacia dónde vas, casi siempre acabas llegando a algún sitio. Sois unos científicos excelentes, pero por encima de eso sois buenas personas. Siempre me sentiré muy afortunado de haber caminado a vuestro lado. No querría olvidarme de todos los buenos profesores con los que me he cruzado tanto en la carrera como en el máster, con un agradecimiento especial a José Gabriel por introducirme al mundo de la materia condensada y abrirme las puertas del laboratorio.

Como no podía ser de otra forma, gracias a mis compañeros en el laboratorio, porque saber que hay gente que entiende de primera mano lo que sientes te ata a la cordura. A Pepe, mi hermano mayor de tesis. Hermanos de fracaso, claro. Paraguas y comodín. Una mano amiga en un terreno desconocido. Aunque igual no seas consciente de ello, has hecho mucho bien por mí. Gracias por ser como eres y por aguantar todos mis lloros. Otra que se ha hartado de escucharme día a día quejándome de la vida es Raquel, mi hermana pequeña de tesis. Porque no nos olvidemos, Raquel, eres muy pequeña, aunque puedas sifonar de Yeti sin ayuda. Te admiro y siempre serás un referente. Ojalá algún día una economía la mitad de planificada que tus clivajes. Eso sí, algo más exitosa, porque si no, estamos apañados. Siguiendo esta línea, Víctor, tú serías mi hermano mellizo, pero casi que prefiero no imaginarme algo así. Gracias por tu buen rollo y por estar siempre a la contra en cualquier debate, por absurdo que sea. Le das vidilla a la vida. Gracias por supuesto a Edwin, un trabajador de la ciencia. Sigues ostentando el puesto de canoso de laboratorio pese a mis arduos esfuerzos por destronarte. Gracias por alimentarme con bollitos inesperados y por ser el único que me entendía cuando ponía el Tour en el laboratorio. Gracias también a Antón. Fuiste indispensable para que no entrara en pánico al enfrentarme por primera vez a una dilución. Siempre traté de tomar buena nota de tus consejos. Gracias a Marta, la última incorporación. Estoy convencido de que tus habilidades de escalada te vendrán muy bien para el

armatoste de 22 T. Mucho ánimo, porque te irá bien seguro. Gracias a Beilun, posiblemente el mejor fichaje de la historia del laboratorio. Eres una máquina. Lástima que seas del Arsenal, no se puede tener todo. Gracias también a David por los ratos que compartimos.

Gracias, cómo no, a Rafa, Chema y Sara, que corréis el mundo para desfacer agravios y enderezar entuertos. Siempre ocupados, pero siempre disponibles. No hay problema que no podáis resolver. Y, lo importante, la vida en el laboratorio es infinitamente más agradable con vosotros, aunque a Chema le divierta demasiado asustarme. Por suerte siempre está Sara cerca para echarse las manos a la cabeza. Rafa, tú y yo sabemos que eres el principal culpable de que mi equipo funcione. Así que gracias. Supongo. Aunque te aseguro que he disfrutado mucho más con el aceite de tu pueblo que con el criostato. Gracias también a Andrés por su ayuda en mis inicios en el laboratorio. Gracias a Javier y a Juan Antonio por su ayuda con la electrónica, y a Nacho por su ayuda con los programas. Gracias a Luisa, Ana Isabel, e Irene por facilitarnos los papeleos, y gracias también al personal de limpieza, en especial a Reyes, que nos debe odiar por los *¡No! ¡No pases ahí!*

Gracias a Mariano, entre otras muchas cosas, por todos los trabajos que hicimos juntos en la carrera y en el máster (en realidad eran todos el mismo). Gracias a Laura por todos esos momentos extracientíficos tan agradables, a Isidoro por tirar de nosotros para ir a comer a psicología, y a todos los que hacían del rato de la comida el más agradable del día.

Evidentemente me tengo que acordar de mis amigos, los pesados de siempre, porque por mucho que diga que no tengo, alguno que otro hay. Nico, Dani, María, Nelson, Lore, Celia. Sinceramente, no entiendo por qué seguimos siendo amigos, pero si algo he aprendido en estos años es que querer entenderlo todo casi nunca es el camino más corto hacia la felicidad. Gracias por las barbacoas, las copas Davis, los polvorones en agosto, los Trivials (aunque por motivos que aún ignoro no os parezca un buen plan para Nochevieja). No me gustaría recurrir al tópico de *no podría tener mejores amigos*, y por supuesto que no lo voy a hacer. Está feo mentir en público y más aún cuando queda por escrito. Pero sobre todo gracias por no mandarme a la mierda por mucho que me meta con vosotros. No tengo ninguna intención de dejar de hacerlo, por cierto.

No sería lo que soy sin mi familia. Gracias a mi hermano, la versión mejorada de mí. Tan iguales y tan distintos. Mi streamer favorito y mi compañero de juegos. Llevamos, literalmente, toda la vida juntos, y aún no me he cansado de ganarte. Posiblemente porque casi siempre pierdo, claro. Por supuesto, muchísimas gracias a mis padres. Siempre alimentasteis esa curiosidad que acabó por convertirme en científico. Todo el bien que hay en mí os lo debo a vosotros. Gracias, gracias, gracias.

Siempre he sido de dejar lo mejor para el final. Gracias a Bea. Mi compañera de vida. Mi compañera de todo. Ya está. Y si está es gracias a ti. Siempre estás para hacer lo bueno mejor y lo malo menos malo. Gracias por ser la Cina.

Contents

Abstract

The electronic band structure of solids contains relevant information about their behavior, particularly in metals and superconductors. There is a recent thrust that allows achieving detailed understanding of the band structure in an energy range just a few meV close to the Fermi level. This is supported by experiments that provide detailed measurements of the electronic band structure and in some cases by calculations. Scanning Tunneling Microscopy (STM) stands out because of the superior resolution in energy, the spatial imaging capabilities and because it provides empty as well as filled electronic states.

Here, I will address the problem of understanding better superconductivity, for which I have chosen a few model systems. Superconductivity often emerges close to vanishing magnetism. However, the emergence of superconductivity often obscures the processes that destroy magnetism. To understand such processes, I have first studied the band structure of $Ce(Ru_{0.92}Rh_{0.08})_2Si_2$, with a magnetic ground state that can be easily modified by an applied magnetic field. My results show that the Zeeman splitting by the magnetic field eliminates magnetism, without radically modifying the low energy band structure, which is dominated by Kondo hybridization between Ce $4f$-electrons and conduction electrons.

I have then addressed the band structure of WTe_2, finding a band structure close to the Fermi level that compares very well to density functional calculations. I have shown that in this case the band structure does not change when applying a magnetic field. I have furthermore addressed the surface band structure, finding relevant features that point to the presence of surface bands close to the topologically nontrivial type II Weyl points of the bulk band structure.

I have then analyzed a superconducting system, Au_2Pb, where superconductivity arises in a phase where a structural distortion has opened a gap in a Dirac cone of the band structure. I will show that the superconducting density of states is finite at the Fermi level and explore the possibility that this feature is connected to the closing of the Dirac cone at the surface. I will discuss possible superconducting states that might arise in this situation.

Finally, I have studied the superconductor FeSe. I have measured the temperature and magnetic field dependence of the superconducting gap and the vortex lattice in a hitherto unexplored field range (up to 15 T). My results show that the bottom of an electron band lies completely within the superconducting gap. This peculiar situation produces a hitherto unobserved electron-hole asymmetry in the superconducting density of states. Furthermore, I find a new charge density wave at high magnetic fields, whose wavevector varies with field together with the wavevector of the vortex lattice. This unique effect might be related to the peculiar low energy band structure of this system.

Resumen

La estructura de bandas de los sólidos contiene información relevante acerca de su comportamiento electrónico, particularmente en metales y superconductores. Últimamente, se han concentrado muchos esfuerzos en la comprensión detallada de la estructura de bandas en un rango de energía de sólo unos pocos meV alrededor del nivel de Fermi. Estos esfuerzos se han apoyado en experimentos que proporcionan medidas detalladas de la estructura de bandas electrónica y, en algunos casos, en cálculos. La microscopía de efecto túnel (STM) destaca en este aspecto gracias a su resolución en energía, superior a otras técnicas, su capacidad para obtener imágenes con resolución espacial y gracias a que es capaz de resolver tanto estados electrónicos vacíos como ocupados.

En esta tesis, abordaré el problema la superconductividad, tratando de comprender mejor algunos aspectos relevantes. Para ello, he elegido varios sistemas modelo. La superconductividad aparece a menudo cerca de fases magnéticas. Sin embargo, la aparición de la superconductividad suele eclipsar los procesos que destruyen el magnetismo. Para entender estos procesos, en primer lugar he estudiado la estructura de bandas en $Ce(Ru_{0.92}Rh_{0.08})_2Si_2$, cuyo estado fundamental magnético puede ser modificado fácilmente aplicando un campo magnético. Mis resultados muestran que el desdoblamiento Zeeman inducido por el campo magnético elimina el magnetismo sin modificar radicalmente la estructura de bandas a bajas energías, dominada por la hibridación Kondo entre los electrones $4f$ del Ce y los electrones de conducción.

Posteriormente, he abordado la estructura de bandas en WTe_2, determinando una estructura de bandas cerca del nivel de Fermi consistente con cálculos teóricos. Se ha demostrado que en este caso la estructura de bandas no cambia al aplicar campo magnético. También he explorado la estructura de bandas en la superficie, encontrando características que apuntan a la presencia de bandas de superficie cerca de los puntos de Weyl de tipo II topológicamente no triviales de la estructura de bandas del volumen.

Asimismo, he analizado un sistema superconductor, Au_2Pb, en el que la superconductividad aparece en una fase en la que una distorsión estructural ha abierto un gap en un cono de Dirac de la estructura de bandas. Mostraré que la densidad de estados superconductora es finita al nivel de Fermi y exploraré la posibilidad de que este fenómeno esté conectado con el cierre del cono de Dirac en la superficie, discutiendo posibles estados superconductores que puedan surgir en esta situación.

Por último, he estudiado el superconductor FeSe. He medido la dependencia del gap superconductor con la temperatura y el campo magnético, así como la red de vórtices en un rango de campo magnético no explorado hasta ahora (hasta 15 T). Mis resultados muestran cómo el fondo de una banda de electrones se encuentra

completamente dentro del gap superconductor. Esta situación tan particular da lugar a una asimetría electrón-hueco en la densidad de estados superconductora que no ha sido observada hasta ahora. Adicionalmente, he encontrado una nueva onda de densidad de carga a altos campos magnéticos cuyo vector de onda varía con el campo junto con el vector de onda de la red de vórtices. Este efecto tan peculiar puede estar relacionado con la estructura de bandas tan singular de este sistema a bajas energías.

1 Introduction

Unveiling the electronic properties of quantum materials is essential to walk towards new applications. In this sense, condensed matter systems provide a unique framework to explore some collective phenomena which cannot be accessed in any other way. A great example of these collective phenomena is superconductivity, where quantum coupling of electrons results in a macroscopic state which displays zero electric resistance. The dream of room temperature superconductivity that would turn the industry of applications upside down is still far, but the discovery of high critical temperature superconductivity in copper based, and more recently, in iron based compounds, has provided new scenes to explore the microscopic origin of unconventional superconductivity and eventually find out the recipe for room temperature superconductors.

In this first chapter, I will present some remarks on conventional and unconventional superconductivity, as well as a brief introduction to different techniques used to measure the electronic band structure of different materials that will be useful to understand the context of the experimental results that will be discussed throughout this thesis.

1.1 Introduction to superconductivity

In 1908, Heike Kamerlingh Onnes managed to liquefy He at the Leiden Laboratory having access for the first time to temperatures below 4.2 K, the boiling temperature of liquid He. This allowed him to explore the behavior of electrical resistivity in different metallic materials in a temperature range out of the influence of thermal excitations. In 1911, when probing the electrical resistivity of mercury, one of the purest compounds that could be obtained at that time, he observed a drop in the resistivity of several orders of magnitude in a temperature range of a few mK around 4.15 K [1] (see fig. 1.1). The result was so striking that he originally thought that there was a problem with his experimental instruments, but all of them were working properly. He had just discovered superconductivity.

Soon after, it was realized that the superconducting state was destroyed above some critical values of temperature, T_c, magnetic field, H_c, and electrical current density, J_c, which are different for each superconductor. The evolution of the critical

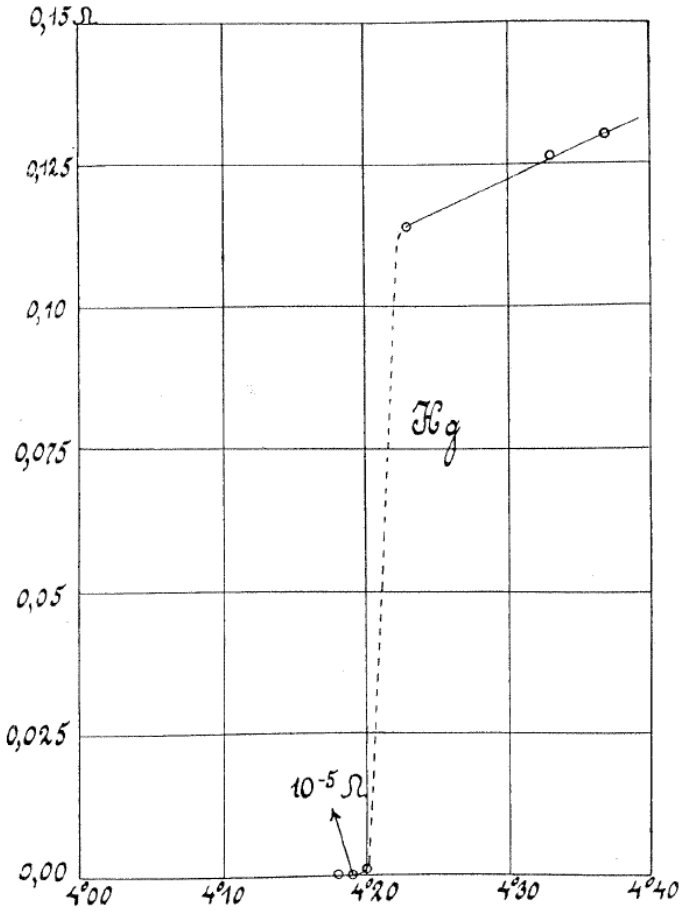

Figure 1.1: Adapted from [1]. Measured resistivity (vertical axis) versus temperature (horizontal axis) in mercury by H.K. Onnes in 1911 showing the superconducting transition at 4.2 K.

field with temperature was experimentally determined and it follows a parabolic shape:

$$H_c(T) = H_c(0)\left[1 - (T/T_c)^2\right] \tag{1.1}$$

The difference between the free energies of the normal (G_n) and superconducting states (G_s), which stands for the energy required to destroy superconductivity by unit of volume, can be written as a function of the critical field:

$$G_n - G_s = \mu_0 \frac{H_c^2(T)}{2}, \tag{1.2}$$

where μ_0 is the vacuum magnetic permeability.

For two decades after the discovery of superconductors, it was believed that they were just characterized by the zero resistance state. It was in 1933 when W. Meissner and R. Ochsenfeld noticed that magnetic properties of materials were completely altered in the superconducting state. They observed that when applying

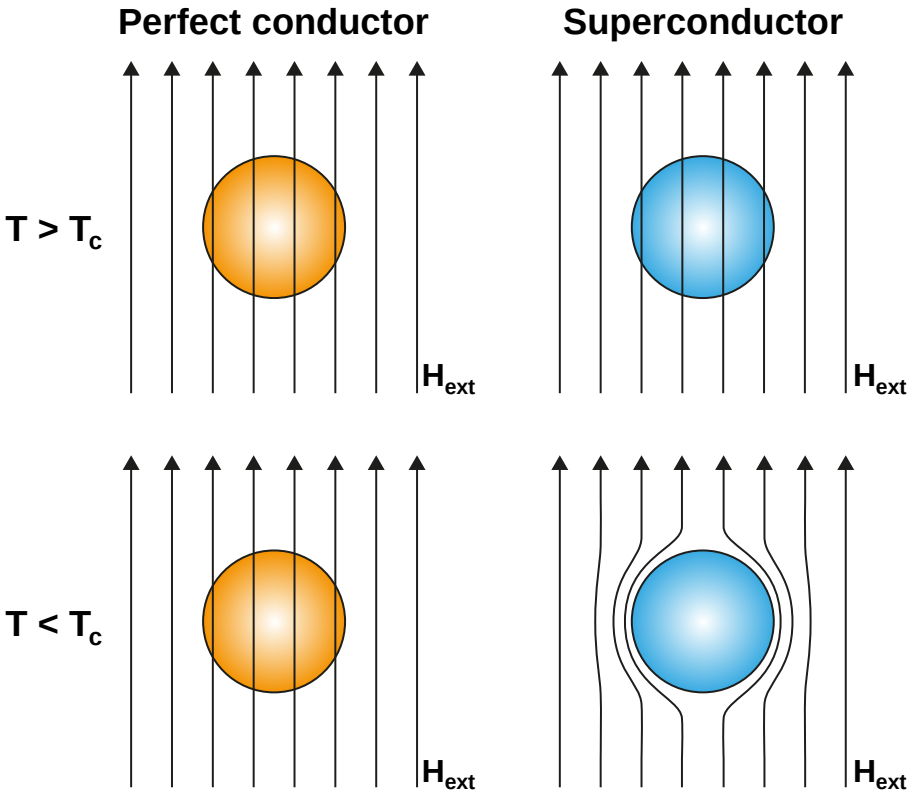

Figure 1.2: Schematic representation of the behavior of a perfect conductor (left) and a superconductor (right) under an externally applied magnetic field. Below the superconducting critical temperature, magnetic field is expelled from the superconductor, which acts as a perfect diamagnet. Field lines are represented as black arrows.

a magnetic field, as long as it was not higher than H_c, it was expelled from the inside of the superconducting material [2] (see fig. 1.2). This perfect diamagnetism in superconductors is known as the Meissner effect, and it is observed regardless of whether magnetic field is applied before or after the superconducting transition.

The first phenomenological theory to explain the electrodynamic properties of superconductors and the Meissner effect was proposed in 1935 by the brothers Fritz and Heinz London [3]. In this picture, the expulsion of magnetic field is produced by supercurrents flowing in the surface of the superconductor, which screen the external field. Supercurrents flow in a small region of the surface where magnetic field is not perfectly expelled, but decays exponentially with the distance inside the superconductor. The characteristic length of this exponential decay is called London penetration depth, λ_L.

This flux expulsion occurs just in type I superconductors. Type II superconductors, far more numerous, allow the magnetic field to enter the sample in form of flux quanta. To make this classification of superconductors in two types and analyze their properties, we need to go beyond London theory and describe Ginzburg-Landau theory. Most of the known superconducting compounds are type II and show magnetic behaviors that are essentially different from that of type I superconductors. The classification of superconducting materials in

these two types came thanks to the Ginzburg-Landau theory, which provided a phenomenological explanation for many experimentally observed macroscopic properties of the superconducting state.

1.1.1 Ginzburg-Landau theory

In 1950, L.D. Landau and V.L. Ginzburg published a phenomenological quantum theory describing the thermodynamic properties of the superconducting transition. This theory is based on the theory of second order phase transitions previously developed by Landau, which states that a second order phase transition occurs when there is a gradual change in the state of the system but its symmetry changes abruptly at the transition temperature. The reduced symmetry most ordered phase is the low temperature one. To describe the transition, there is an order parameter in the free energy whose value is zero in the least ordered symmetric phase and gradually increases with decreasing temperature. In the superconducting transition, the order parameter introduced by the Ginzburg-Landau theory is a complex wave function, $\Psi = |\Psi| e^{i\phi}$, describing the macroscopic properties of the superconducting condensate. The squared modulus of this wavefunction, $|\Psi|^2$, provides the density of superconducting electrons. Ginzburg and Landau built a free energy functional in terms of the order parameter Ψ to describe the superconducting state:

$$G = \int d\vec{r} \left[\frac{1}{2m^*} |(i\hbar\nabla + e^*\vec{A})\Psi|^2 + \alpha|\Psi|^2 + \beta|\Psi|^4 + \frac{1}{2\mu_0}(\nabla \times \vec{A})^2 - (\nabla \times \vec{A})\vec{H} \right], \quad (1.3)$$

where α and β are phenomenological parameters specific for each material, $\vec{A}$ is the vector potential, $\vec{H}$ is the external magnetic field, and m^* and e^* are the mass and the charge of the superconducting electrons, respectively. As I will discuss below, BCS theory shows that m^* and e^* are, respectively, two times the mass and two times the charge of the electron. Ginzburg-Landau differential equations can be obtained by minimizing the free energy functional with respect to Ψ and $\vec{A}$:

$$\frac{1}{2m^*}(i\hbar\nabla + e^*\vec{A})^2\Psi + \beta|\Psi|^2\Psi = -\alpha\Psi \quad (1.4)$$

$$-\vec{j} = \frac{\nabla^2\vec{A}}{\mu_0} = \frac{ie^*\hbar}{2m^*}(\Psi^*\nabla\Psi - \Psi\nabla\Psi^*) + \frac{e^{*2}}{m^*}|\Psi|^2\vec{A} \quad (1.5)$$

These two equations describe the evolution of the magnetic field and the order parameter in a superconductor. In this case, as the whole magnetization of the system is considered, one can access the inner structure of the superconducting state finding that there are alternative solutions for the magnetic response of a superconductor apart from the perfect Meissner effect. In certain situations, magnetic field can penetrate in a non-uniform way giving rise to an inhomogeneous distribution of normal and superconducting regions. The Ginzburg-Landau theory

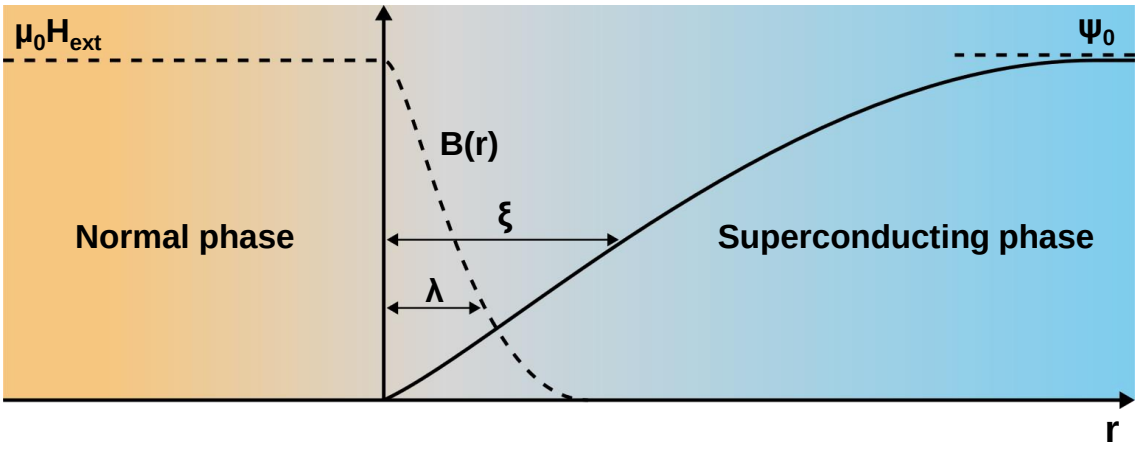

Figure 1.3: Evolution of the magnetic field and the superconducting order parameter in an interface between a normal metal and a superconductor showing the two characteristic lengthscales of Ginzburg-Landau theory, λ and ξ, for a type I superconductor.

describes the spatial variations of the superconducting properties in terms of two characteristic lengthscales: the penetration depth, λ, which is related to the London penetration depth and represents the distance over which magnetic field penetrates in the superconductor, and the coherence length, ξ, which accounts for the distance over which the order parameter decays with respect to its equilibrium value (see fig. 1.3). Both length scales present a similar temperature dependence around the critical temperature, T_c:

$$\lambda, \xi \propto \frac{1}{(T_c - T)^{1/2}} \tag{1.6}$$

Therefore, the ratio of these two lengths is temperature independent and it is defined as the Ginzburg-Landau parameter:

$$\kappa = \lambda/\xi \tag{1.7}$$

The relation between λ and ξ, and thus, the value of κ, determines the response of a superconductor to an external magnetic field. A few years after the publication of the Ginzburg-Landau theory, A.A. Abrikosov predicted a new type of superconducting system based on the value of the Ginzburg-Landau parameter, which establishes if the penetration of magnetic field and the consequent creation of interfaces between normal and superconducting regions is energetically favorable or not [4]. For $\xi \gtrsim \lambda$ ($\kappa \lesssim 1/\sqrt{2}$) the field penetration is not energetically favorable, but for $\lambda \gtrsim \xi$ ($\kappa \gtrsim 1/\sqrt{2}$), magnetic field penetration through normal state domains lowers the total energy of the system. Superconducting materials with perfect Meissner effect are called type I superconductors, while superconductors in which magnetic field can penetrate are called type II superconductors.

As I will discuss below, in type II superconductors, the magnetic field penetrates the superconductor through flux tubes or vortices [4]. The magnetic flux going

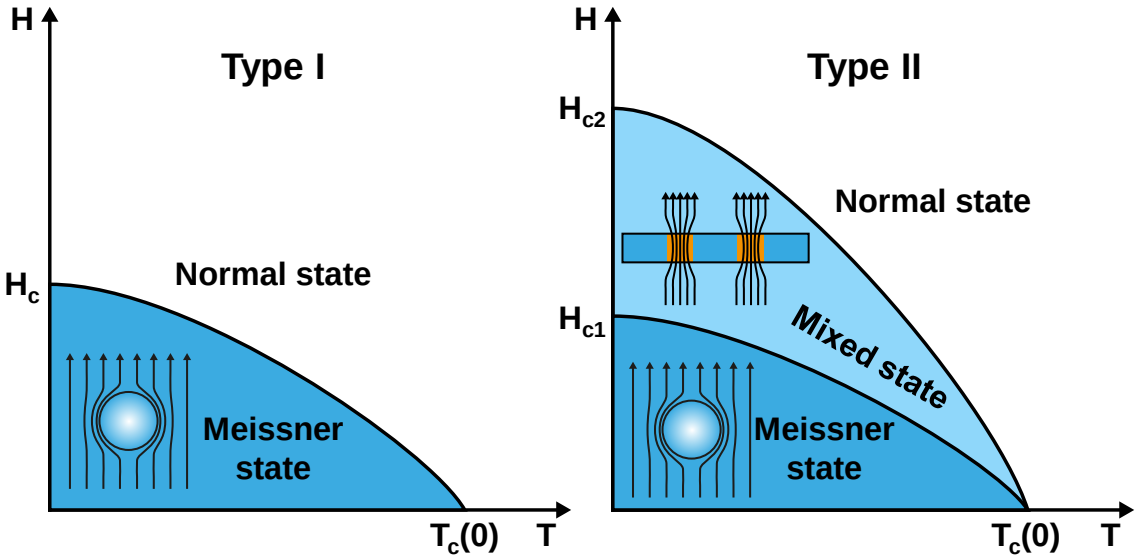

Figure 1.4: Schematic magnetic field versus temperature phase diagram of type I (left) and type II (right) superconductors.

through a normal phase inside a type II superconductor is an integer number of times the quantum flux, Φ_0:

$$\Phi_0 = \frac{h}{2e} = 2.068 \times 10^{-15} \text{ Wb}, \tag{1.8}$$

where h is the Planck constant and e is the electron charge. It is important to note that there is a term $2e$ in the denominator due to the formation of Cooper pairs in the superconducting phase as explained by BCS theory (see section 1.2).

Type I superconductors are perfect diamagnets below the critical field, which is given by

$$H_c = \frac{\Phi_0}{4\sqrt{2}\pi\lambda\xi} \tag{1.9}$$

In type II superconductors there are two critical fields, H_{c1} and H_{c2}. Below H_{c1} there is Meissner effect. Above H_{c1} magnetic field starts penetrating until superconductivity is fully destroyed above H_{c2}. The region between H_{c1} and H_{c2} in which there is coexistence between the superconducting state and magnetic field is known as the mixed state or Shubnikov phase [5]. Ginzburg-Landau theory provides the following expressions for H_{c1} and H_{c2}:

$$H_{c1} = \frac{\Phi_0}{4\pi\mu_0\lambda^2} \ln\kappa \tag{1.10}$$

$$H_{c2} = \frac{\Phi_0}{2\pi\mu_0\xi^2} \propto 1 - \frac{T}{T_c} \tag{1.11}$$

Figure 1.4 shows the temperature dependence of the critical fields for type I and type II superconductors. Although eq. (1.11) predicts a linear increase of H_{c2} as temperature approaches 0 K, experimental determinations of $H_{c2}(T)$ are below the extrapolated linear dependence. Refined calculations show that $H_{c2}(0)$ is 0.69 times the value obtained from the Ginzburg-Landau theory [6].

1.1.2 Superconducting vortices

As stated by Abrikosov in 1957, in the mixed state of type II superconductors, magnetic field penetrates in the form of quantized field lines known as superconducting vortices. Each vortex consists of a normal state central core in which the order parameter goes to zero, and circular supercurrents surrounding this core flowing in the direction that would generate a field that coincides with the applied magnetic field. Figure 1.5a sketches the evolution of the order parameter, the magnetic field and the supercurrent density inside a superconducting vortex. The superconducting density of states goes to zero in the vortex core and recovers the equilibrium values in a typical distance of the order of ξ. On the other hand, the magnetic field is maximum in the vortex core and gradually decays in a typical distance of the order of λ as we move away from the core. Each vortex carries a quantum of flux and its energy by unit of length is given by

$$\epsilon = \frac{\Phi_0^2}{4\pi\mu_0\lambda^2}\ln\left(\frac{\lambda}{\xi}\right) \tag{1.12}$$

Since field lines of all the vortices are parallel, the magnetic interaction between them is repulsive. Abrikosov showed that this interaction results in the arrangement of the vortices in a triangular lattice with hexagonal symmetry (see fig. 1.5b). This vortex lattice receive the name of Abrikosov lattice and is the most common arrangement of vortices in the mixed state of type II superconductors. However, vortices arranged in a square lattice have also been experimentally observed in some superconducting compounds [7]. The intervortex distance in a triangular and a square lattice decreases with applied magnetic field (B) according to the following expressions:

$$d_\triangle = \left(\frac{4}{3}\right)^{1/4}\left(\frac{\Phi_0}{B}\right)^{1/2} \tag{1.13}$$

$$d_\square = \left(\frac{\Phi_0}{B}\right)^{1/2} \tag{1.14}$$

These equations show that the intervortex distance only depends on the applied magnetic field. In this picture, the upper critical field H_{c2} can also be understood as the value of the magnetic field at which the distance between two consecutive vortices becomes smaller than the coherence length, ξ.

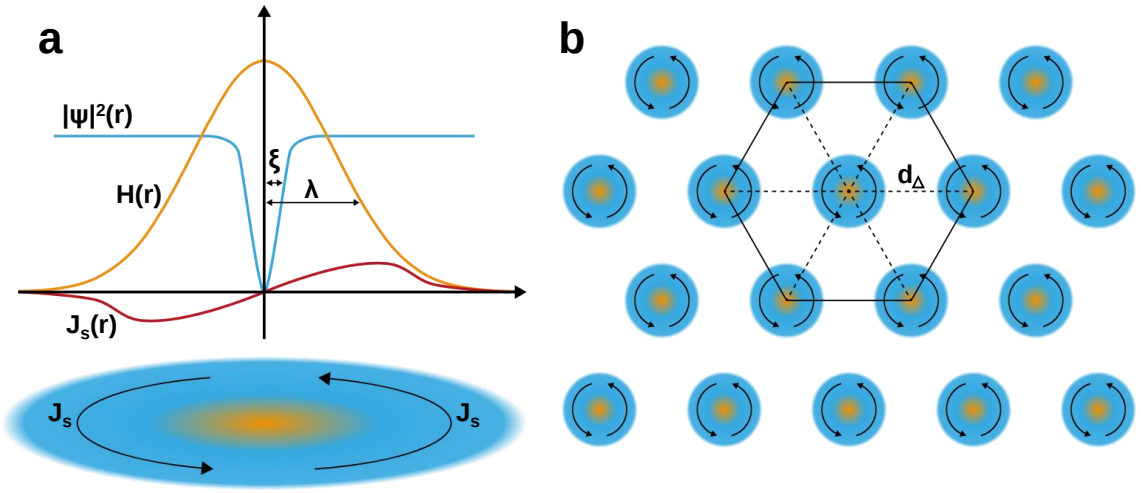

Figure 1.5: (a) Schematic representation of a superconducting vortex showing the behavior of the order parameter (blue), the magnetic field (orange) and the supercurrent density (red) inside the vortex core. (b) Top view of a triangular Abrikosov vortex lattice.

There are different vortex imaging techniques that have been developed during the last decades. Magnetic decoration [8], SQUID-on-tip [9] and magnetic force microscopy (MFM) [10] are some examples of magnetic field sensitive experiments that can resolve single vortices over large areas. However, they are only useful at relatively low magnetic fields, when the distance between vortices is of the order or below λ. The overlap between vortices at higher magnetic fields results in a loss of contrast in the images obtained by magnetic field sensitive techniques that eventually leads to the loss of single vortex resolution. This problem can be solved by directly measuring the spatial variations of the density of states using scanning tunneling microscopy (STM) [11, 12]. STM allows for direct observation of vortices at any field below H_{c2} given the fact that the superconducting density of states varies on a lengthscale of the order of ξ, which only becomes of the order of the intervortex distance at H_{c2}. Therefore, STM arises as a very versatile technique with which one can obtain detailed information of the electronic properties of single vortex cores while having access to the structural and dynamic properties of the lattice. Nonetheless, at very low magnetic fields, the intervortex distance becomes comparable to the rather small STM field of view (~1 μm^2, see section 2.3.2), what eventually hinders the STM observation of very large vortices.

1.2 BCS theory

Although the phenomenological theories introduced above achieved to accurately describe many properties of superconductors, it was not until 1957 that J. Bardeen, L.N. Cooper and J.R. Schrieffer came up with a consistent microscopic explanation for the superconducting state. This microscopic theory is known as the BCS theory [13, 14].

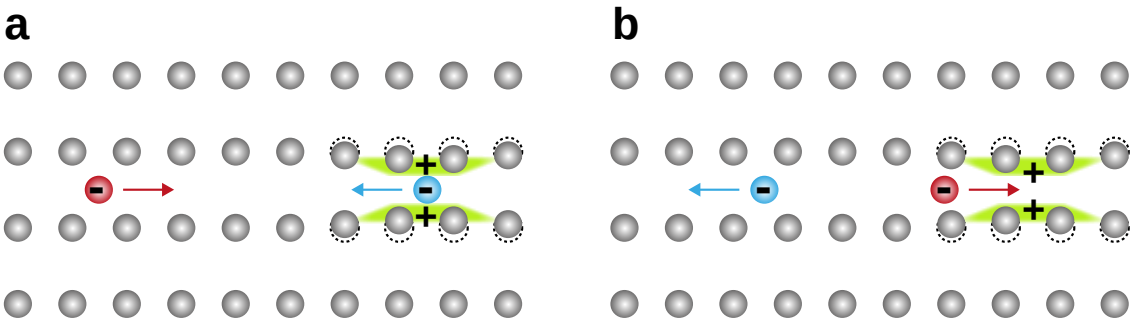

Figure 1.6: Schematic representation of the phonon mediated electron-electron pairing. (a) An electron (blue) moving to the left attracts the ions of the lattice (grey) creating an accumulation of positive charge (green shadow). (b) A second electron (red) moving to the right feels the positive charge imbalance and is attracted to it.

Several experimental observations pointed to a very unusual behavior of electrons in the superconducting phase. For instance, it was observed that the electronic contribution to the specific heat vanished below the superconducting transition. An entropy reduction in the superconducting phase was also reported. This suggested that, since the symmetry of the crystal remains unchanged in the superconducting transition, there should be a higher electronic order in the superconducting state. But probably the most determinant hint came from the discovery of the isotope effect in 1950 [15, 16], which exposed the relevance of the crystal lattice in superconductors. The isotope effect leads to a difference on the superconducting critical temperature of the same metal using different isotopes. Thus, even if the lattice symmetry is not altered by the superconducting transition, it was clear that it should somehow affect the conduction electrons in the superconducting phase.

It was H. Fröhlich in a previous work also in 1950 who explained the contribution of the crystal lattice to the superconducting state proposing that the electron-phonon interaction results in a weak attractive electron-electron interaction [17]. This process is schematically represented in fig. 1.6. In this picture, a negatively charged electron moving through the crystal would attract the possitive ions of the lattice by simple Coulomb interaction, what would create a local accumulation of possitive charge. A second electron moving by the same region would thus be attracted to the possitive charge cloud, absorbing the phonon associated to the lattice vibration.

Six years after Fröhlich's proposal, L.N. Cooper rigorously proved the existence of bound states close the the Fermi level. These states are formed by pairs of electrons of opposite momenta and spin when the attractive interaction between electrons overcomes Coulomb repulsion [18]. The bound electrons are called Cooper pairs. As the movement of the ions in the lattice is much slower than the almost instant Coulomb repulsion, the attractive interaction between electrons is retarded. Therefore, the typical distance between coupled electrons that form a Cooper pair is of the order of 100 nm as estimated from the Fermi velocity of electrons, $v_F \sim 10^8$ cm/s, and the frequency of the vibrations of the lattice, $\omega_D \sim 10^{13}$ s^{-1}, where ω_D is the Debye frequency. This distance in which the Cooper

pair wavefunction is coherent is known as the intrinsic coherence length, ξ_0, and represents the size of the Cooper pair.

Bardeen, Cooper and Schrieffer extended Cooper's approach to the case of many electrons. BCS theory states that if the effective interaction between electrons is attractive, the system becomes unstable and the total energy is reduced by the formation of Cooper pairs. The superconducting ground state is then described by a single macroscopic wave function that is coherent within a distance of ξ_0. Since ξ_0 is much larger than the typical electron-electron distance in a metal, which is of the order of 1 Å, there is some overlap between Cooper pairs that gives rise to a quantum coherent state. When Cooper pairs are exposed to an external electric field, they move through the lattice as a particle with an electric charge of $2e$. As all Cooper pairs form a coherent state, the movement of each of them is determined by the dynamics of all the other pairs. This way, the zero resistance state is explained by the fact that the movement of Cooper pairs, as a coherent state, is not affected by the presence of imperfections or impurities in the lattice, which are responsible for the finite electric resistance in normal metals.

BCS theory managed to describe the equilibrium superconducting properties already explained by the phenomenological theories and introduced the concept of the superconducting gap, Δ. This gap represents an energy region around the Fermi level in which electronic excitations are not allowed. The BCS spectrum for the available excited states in a superconductor is given by

$$E_k = \sqrt{\Delta^2 + \epsilon_k^2}, \tag{1.15}$$

where $\epsilon_k = (\hbar^2 k^2/2m) - E_F$ is the kinetic energy and Δ, the superconducting gap. As ϵ_k can be arbitrarily small, eq. (1.15) manifests that the minimum energy required to create an excited state is equal to Δ (see fig. 1.7a). Therefore, Δ represents a gap in the quasiparticle energy spectrum. However, since electrons in the superconducting ground state are forming Cooper pairs close to the Fermi level, the total minimum energy needed to break a Cooper pair and create excited states is 2Δ. From eq. (1.15), in the limit $\epsilon_k \gg \Delta$, the normal metal free electron gas picture is recovered.

The total amount of electronic states is conserved in the superconducting transition:

$$N_n(\epsilon_k)d\epsilon_k = N_s(\epsilon_k)dE_k, \tag{1.16}$$

where N_n and N_s are the density of states in the normal and superconducting states, respectively. Combining eq. (1.15) and eq. (1.16) and assuming that $N_n(\epsilon)$ can be considered constant and equal to $N_n(0)$, one can obtain the following analytic expression for the normalized superconducting density of states:

$$\frac{N_s(E)}{N_n(0)} = \begin{cases} 0 & E < \Delta \\ \dfrac{E}{\sqrt{E^2 + \Delta^2}} & E > \Delta \end{cases} \tag{1.17}$$

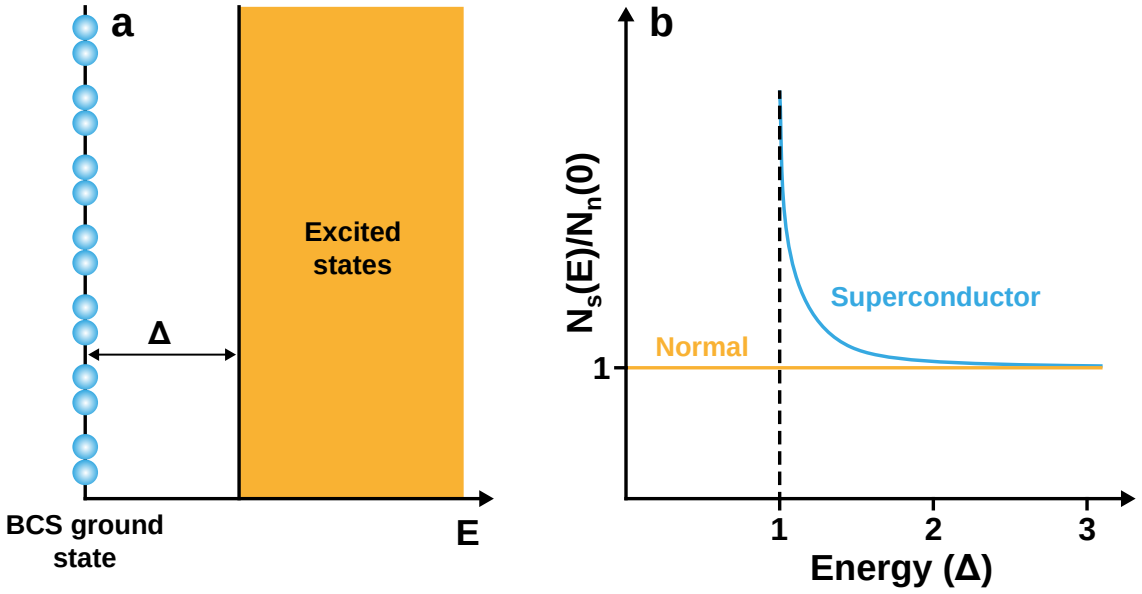

Figure 1.7: (a) Schematic representation of the ground state and the first excited states in a superconductor showing the energy gap, Δ. (b) BCS density of states (blue) normalized to the normal state density of states (orange).

Figure 1.7b plots the superconducting density of states showing the absence of states inside the superconducting gap and a divergence at $E = \Delta$ known as the quasiparticle peak. Besides, BCS theory also unveils a relation between the value of the superconducting gap at zero temperature and the superconducting critical temperature for the case of weak electron-phonon interaction:

$$\Delta = 1.76 k_B T_c \tag{1.18}$$

Figure 1.8a shows the BCS numerical solution for the evolution of the superconducting gap size with temperature, $\Delta(T)$. The value of Δ is nearly constant up to $T_c/2$. Above that temperature, the presence of thermally excited quasiparticles gradually diminishes the gap size until it eventually becomes zero at T_c. Figure 1.8b depicts the temperature evolution of the superconducting density of states showing the gradual effect of temperature smearing until the curve is completely flat at $T = T_c$.

The equivalence between phenomenological Ginzburg-Landau theory and microscopic BCS theory was established in 1959 by L. Gor'kov [19]. Ginzburg-Landau equations can be derived from BCS theory in a temperature range close to the second order transition at T_c identifying the order parameter Ψ with the macoscopic BCS wavefunction, which is directly related to Δ. Although these equations would only be strictly valid close to T_c, the results obtained using Ginzburg-Landau equations are in practice reliable enough in a temperature range well below T_c. In his work, Gor'kov redefined the two characteristc lengths of the superconducting state in terms of microscopic parameters:

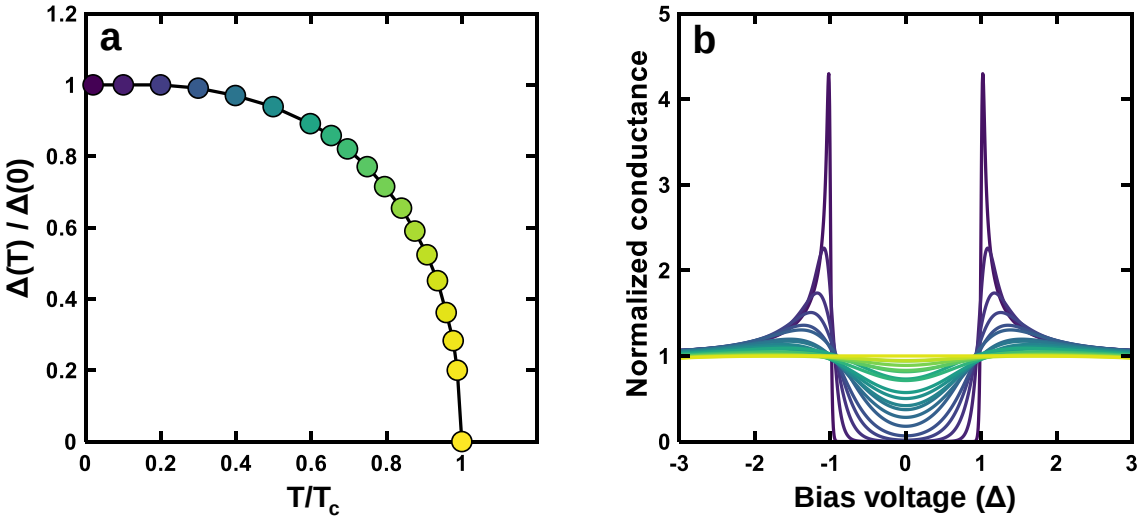

Figure 1.8: (a) Superconducting gap size versus temperature obtained numerically from BCS theory. (b) Normalized tunneling conductance versus bias voltage for different temperatures featuring the BCS superconducting density of states convoluted with the derivative of the Fermi function for different temperatures (see section 2.1.3 for more details). The temperature of each curve is that of the same color point in (a).

$$\xi(T) = 0.74\xi_0\sqrt{\frac{T_c}{T_c - T}} \tag{1.19}$$

$$\lambda(T) = \frac{1}{\sqrt{2}}\lambda_L(0)\sqrt{\frac{T_c}{T_c - T}} \tag{1.20}$$

$$\kappa = 0.96\frac{\lambda_L(0)}{\xi_0} \tag{1.21}$$

with $\lambda_L(0) = \sqrt{3c^2/(8\pi e^2 v_F^2 N(E_F))}$.

Multiband superconductivity

The Fermi surface of a particular compound can consist of several different bands. Multiband superconductivity was first proposed by H. Suhl, B.T. Matthias and L.R. Walker in 1959, who considered a two bands model [20]. Cooper pairs might form through electron-phonon interaction within the same band (intra-band) or among different bands (inter-band). If the electron-phonon interaction strength is very different in different portions of the Fermi surface, one can obtain a situation where the superconducting gap strongly changes over the Fermi surface. For example, there might be one Fermi surface sheet with particularly large intra-band electron-phonon interaction and a gap much larger than in other sheets of the Fermi surface. This is called multigap superconductivity and eventually leads to several superconducting gaps, all closing at a single critical temperature (fig. 1.9). Often, it is sufficient to consider a distribution of the superconducting gaps

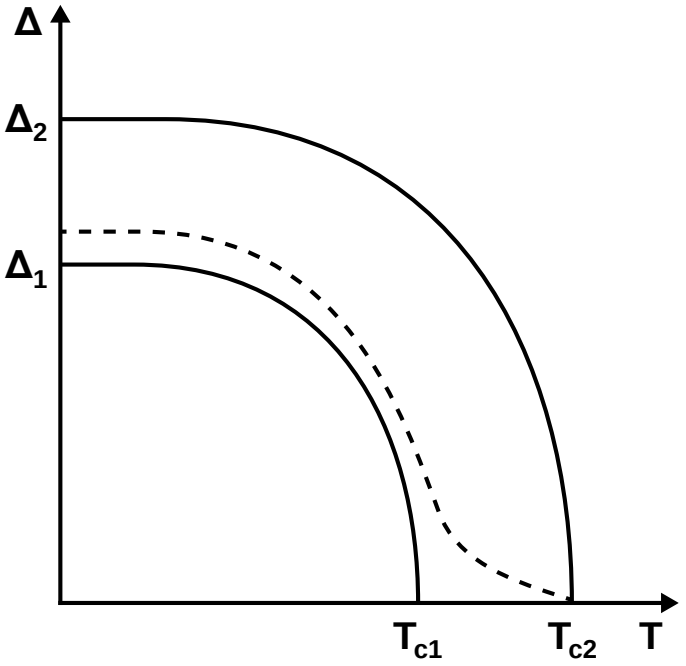

Figure 1.9: Temperature dependence of the superconducting gaps, Δ_1 and Δ_2, in a two band superconductor. As interband scattering is nonzero, the band showing a larger gap induces superconductivity in that with a smaller gap leading to a temperature dependence of the smaller gap that deviates from BCS behavior following the dashed line.

centered around two gap values. Interactions due to impurity scattering generally wash out the differences in the superconducting gap over the Fermi surface. The critical temperature is then generally reduced, up to the level corresponding to an homogeneous superconducting gap over the Fermi surface.

Therefore, the simple model of a two band superconductor is of great use. In this model, assuming that the inter-band scattering is completely negligible, one could in principle consider the superconducting properties of each band separately and define two superconducting gaps and two critical temperatures. However, electronic bands in real materials are never completely independent, and even if there might be two superconducting gap values, above the expected critical temperature of the smallest gap, the non-zero inter-band scattering makes the Fermi surface shell showing a bigger gap to induce superconductivity in that with a smaller gap. This deviates the temperature evolution of the smaller gap from the BCS prediction and T_c ends up being the same for both bands (see fig. 1.9).

1.3 Unconventional superconducting pairing

In 1986, the discovery of high critical temperature superconductivity in cuprates by J.G. Bednorz and K. A. Muller [21] completely shocked the condensed matter community. The electron pairing mechanism in these materials was different from the phonon-mediated one in conventional superconductors described by

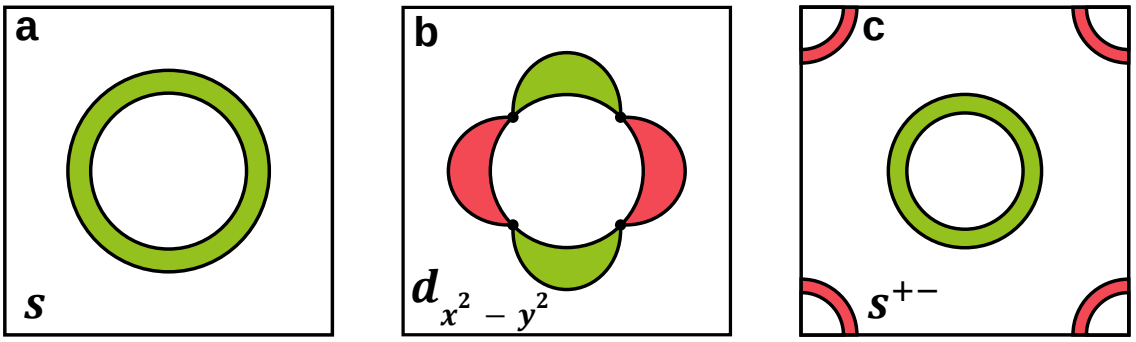

Figure 1.10: Comparison of different symmetries of the superconducting gap function in the k_x-k_y plane. (a) BCS isotropic gap. (b) Gap function with $d_{x^2-y^2}$ symmetry as in cuprates showing four nodes, marked as black dots. (c) Gap function with s^{+-} nodeless symmetry as in multiband iron based superconductors, where the sign change occurs between different pockets of the Fermi surface. Green and red colors represent opposite signs of the gap function.

BCS theory. Some compounds from the cuprates family were reported to display superconducting critical temperatures well above 100 K [22, 23], what brought a lot of excitement regarding possible applications. High-T_c superconductivity was also reported in iron based systems in 2008 [24]. The discovery of high critical temperature superconductivity in cuprates and iron based superconductors was fascinating not just because of the much higher values of T_c with respect to conventional superconductors, but also because in these materials, the formation of Cooper pairs occurs through repulsive Coulomb interaction. Compounds where electronic pairing is not described by BCS theory are known as unconventional superconductors, and a rigorous understanding of their pairing mechanism is still lacking nowadays.

The s-wave order parameter in BCS theory is completely isotropic for a spherical, single band Fermi surface. However, conventional s-wave pairing symmetry is not present in all superconducting materials. Some pairing mechanisms different from BCS electron-phonon interaction are possible. At the beginning of the 1960's, the possibility of pure repulsive electron-electron interaction resulting in a condensate state was studied in the context of ^{3}He superfluidity [25, 26, 27], where the orbital angular momentum of electrons, L, is different from zero. In this framework, there is a decoupling of the BCS gap equation into independent pairing channels for each value of the angular momentum ($L = 0, 1, 2, 3...$). Even if the net electron-electron interaction is repulsive, some channels may show attractive interactions. Unconventional superconductivity arises when at least one of these channels undergoes a superconducting transition at a finite T_c. Angular components of the electron-electron interaction were shown to be attractive at large L by W. Kohn and J. Luttinger in 1965 [28].

To minimize the repulsive Coulomb interaction, the gap function presents sign changes, which typically involve pair wavefunctions with $L \neq 0$ [29]. Unlike retarded electron-phonon interactions, the time scale of electronic fluctuations is much smaller and comparable to that of the motion of electrons. Thus, paired electrons use space

Representation	Parity	Base functions
A_{1g}	$S = 0$	1
A_{1u}	$S = 1$	$\hat{z}k_z; k_x^n + k_y^n;\ n = 1, 3$
A_{2g}	$S = 0$	$k_x k_y (k_x^2 - k_y^2)$
A_{2u}	$S = 1$	$\hat{y}k_x - \hat{x}k_y; k_x k_y (\hat{x}k_x - \hat{y}k_y); k_x k_y k_z (k_x^2 - k_y^2)$
B_{1g}	$S = 0$	$k_x^2 - k_y^2$
B_{1u}	$S = 1$	$\hat{z}(k_x^2 - k_y^2)k_z; \hat{x}k_x^n - \hat{y}k_y^n;\ n = 1, 3$
B_{2g}	$S = 0$	$k_x k_y$
B_{2u}	$S = 1$	$\hat{y}k_x + \hat{x}k_y; k_x k_y (\hat{y}k_x + \hat{x}k_y); k_x k_y k_z \hat{z}$
E_g	$S = 0$	$k_z k_x; k_z k_x^3$ $k_z k_y; k_z k_y^3$
E_u	$S = 1$	$\begin{matrix} \hat{z}k_x^{n+1} \\ \hat{z}k_y^{n+1} \end{matrix}$; $\begin{matrix} \hat{x}k_z k_x^n \\ \hat{y}k_z k_y^n \end{matrix}$ $k_x k_z k_y$ $\begin{matrix} \hat{y}k_x^n \\ \hat{x}k_y^n \end{matrix}$; $n = 0, 2$

Table 1.1: Irreducible representations of the tetragonal point group D_{4h}.

rather than time to avoid Coulomb repulsion, what results in highly anisotropic gap functions in momentum space, $\Delta(\vec{k})$, that can even feature gap nodes in which the sign of the gap function changes. For instance, the $L = 2$ d-wave gap function in cuprates has nodes for $k_x = \pm k_y$ and they show what is called $d_{x^2-y^2}$ superconductivity [30, 31] (see fig. 1.10b).

Actually, cuprates, as well as any superconducting system, have a crystal lattice. Contrary to ^{3}He, where atomic wavefunctions are described by spherical harmonics, electrons in a solid are described by Bloch functions. Bloch functions that build the electronic state at the Fermi surface of a usual metal have the full symmetry of the crystal lattice. In a superconductor with $L \neq 0$, the Cooper pair wavefunction does however not have the full symmetry of the crystal lattice. Instead, its symmetry follows one or several of the irreducible representations of the point group. For instance, in cuprates, the $d_{x^2-y^2}$ superconducting state with $L = 2$ in a crystal with tetragonal symmetry corresponds to the B_{1g} state of the D_{4h} point group [32] (see table 1.1). Other states, singlet and triplet, can be discussed in terms of the corresponding irreducible representation of the point group.

The situation is a bit more complex in multiband systems like iron based superconductors. There, instead of pair wavefunction with finite angular momenta, it is assumed that the pair wavefunction changes sign on different sheets of the Fermi surface. For example, in the two band model shown in fig. 1.10c, the inner Fermi surface sheet (usually a hole pocket) and the outer sheets (usually four electron pockets at the corners of the Brillouin zone), carry each isotropic superconducting pair wavefunctions. However, the relative sign among these changes. This picture is compatible with magnetically mediated interactions that form Cooper pairs by coupling electrons in different sheets. In such a superconducting gap function there are no nodes. This state is called s^{+-} and it is related to the $d_{x^2-y^2}$ state in the sense that there are sign changes of the Cooper pair wave function. However, contrary to the $d_{x^2-y^2}$ state, there are no nodes

because the gap changes sign in different sheets of the Fermi surface. Figure 1.10 compares the gap functions of isotropic s-wave BCS superconductors, $d_{x^2-y^2}$ state in copper based superconductors, and s^{+-} state in iron based superconductors.

Although some other symmetries involving nodes in the gap function have been proposed for the superconducting state of iron based superconductors , s^{+-} symmetry is the most accepted scenario for the majority of iron based compounds, as evidenced, for instance, by the observation of a resonance peak in neutron scattering experiments which has been associated with the sign difference between the electron and hole pockets [33]. Superconductivity with s^{+-} symmetry requires electronic interaction to be stronger between different pockets than within them. Spin fluctuations have been consensually established as the main mechanism behind the inter-pocket interaction as the $\vec{q}$ vector of the spin density wave ground state coincides with the distance between electron and hole pockets in reciprocal space.

Up to this point, all the superconducting paired states I have described are spin singlet ($S = 0$), but there is yet another situation that involves spin triplet ($S = 1$) superconducting pairing [34]. Pauli principle forces the Cooper pair wavefunction to be antisymmetric under momentum and spin exchange. The pair wavefunction can be split into an orbital and a spin part. To fulfill the anticommuting properties of fermions, if the paired electrons are in a spin singlet state (antisymmetric), the orbital part of the wave function must be symmetric with angular momentum $L = 0$ (s-wave), 2 (d-wave), *etc.* Contrarily, spin triplet states (symmetric) are accompanied by an antysimmetric orbital wavefunction with $L = 1$ (p-wave), 3 (f-wave), *etc.* One example of spin triplet superconductivity can be found in UTe_2, which has been recently reported as an unconventional superconductor where ferromagnetic fluctuations drive the superconducting transition [35, 36]. The irreducible representations of the tetragonal D_{4h} point group for the case of a triplet state ($S = 1$) are shown in table 1.1.

1.3.1 Correlations close to quantum criticality

Superconductivity in cuprates, iron based and heavy fermion compounds appears close to an antiferromagnetic phase upon doping or pressure. Figure 1.11 shows two typical temperature versus doping or pressure phase diagrams for unconventional superconductors where a superconducting dome arises neighboring and even coexisting with antiferromagnetism. Cuprates and iron based superconductors display very rich phase diagrams, including a pseudogap and a spin glass phase in cuprates or a nematic phase coupled to a structural transition in iron based superconductors.

In fig. 1.11 we observe quantum phase transitions in which antiferromagnetism disappears at zero temperature. To understand the phase diagrams that lead to the appearance of superconductivity, it is necessary to understand what happens with the electronic correlations when magnetism disappears. Thus, we decided to address a system where antiferromagnetism disappears by a control parameter, without having superconducting correlations that obscure the low energy properties

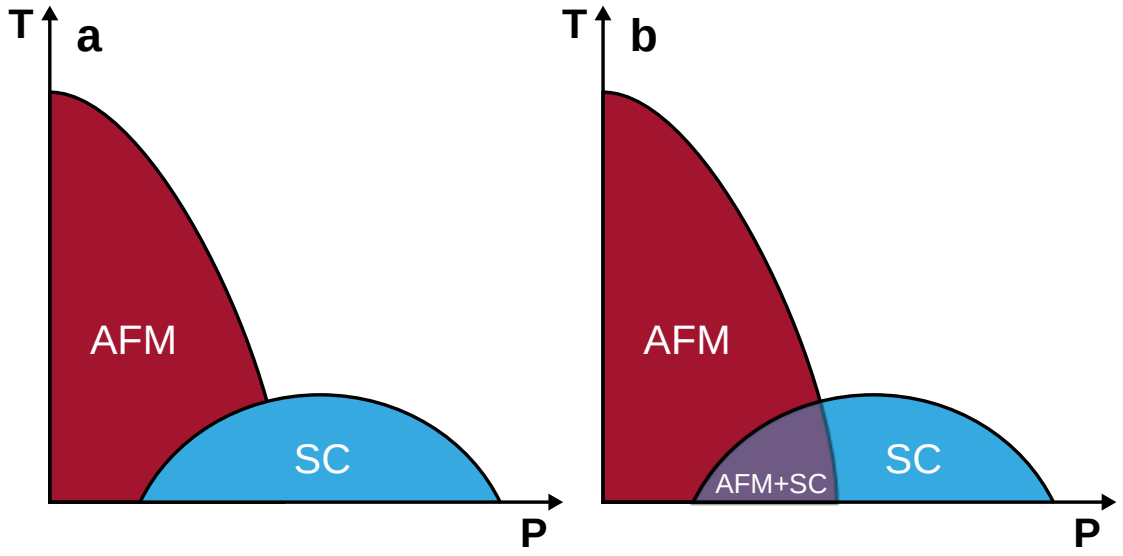

Figure 1.11: Schematic temperature versus pressure or doping generic phase diagrams for unconventional superconductors showing (a) competition between antiferromagnetism (red) and superconductivity (blue) and (b) coexistence between antiferromagnetic and superconducting phases.

of the band structure. It is very difficult to find such systems, because magnetism is generally a robust phenomenon and it is not easy to find an accesible control parameter to make such an experiment. For this purpose, the best materials are probably heavy fermion metals. There, f-electrons hybridize with conduction electrons, transferring their magnetic entropy to the free electron bath at very low temperatures. When these order magnetically, the energy range required to modify or eliminate magnetism is drastically reduced with respect to the range required in other magnetic systems. Thus, quantum critical points are particularly easy to access. With this in mind, we have studied the phase diagram of a prototypical antiferromagnetic heavy fermion, where antiferromagnetism disappears into a paramagnetic phase by applying a magnetic field of several Tesla (see chapter 3).

1.4 Experimental determination of band structures

In condensed matter systems, the band structure represents the available electronic states as a function of the energy and the momentum. The shape of the band structure in different materials is key to understand its electronic behavior. However, the experimental determination of electronic band structures presents some challenges, particularly under high magnetic fields or in situations where the band structure changes with magnetic field.

Angle-resolved photoemission spectroscopy (ARPES) is probably the most popular technique to measure the surface band structure of crystalline compounds. It uses the photoelectric effect and record the energy and angle dependence of the

electrons extracted from the probed material by a beam of photons. Although ARPES has been proved to be a reliable technique to map the band structure for occupied states below the Fermi energy, it cannot access unoccupied states above the Fermi level. Besides, this technique can only be used at zero magnetic field.

The study of quantum oscillations can also be used to measure the band structure of different materials. When magnetic field is strong enough and the mean free path of the electrons in the sample is large enough for them to complete full cyclotron orbits without being scattered, the band structure becomes quantized into discrete Landau levels. When ramping the magnetic field, this quantization produces oscillations in macroscopic parameters that depend on the density of states, such as the electronic resistivity (Shubnikov-de Haas effect) or the magnetic susceptibility (de Haas-van Alphen effect) [37]. When plotted against one over the magnetic field, the frequencies of these oscillations are proportional to the size of the maximal areas of the Fermi surface in momentum space in the plane perpendicular to the direction of the applied magnetic field. Thus, varying the orientation of the magnetic field with respect to the sample, the three-dimensional structure of the Fermi surface can be measured. The main drawback of this technique arises when working with systems whose band structure presents changes with magnetic field. In this situation, the changes in the size of the Fermi surface pockets with magnetic field will complicate the determination of single frequencies and this technique might fail. Furthermore, the states above and below the Fermi level are not accessible.

STM measures the band structure of different compounds through quasiparticle interference scattering (QPI). This technique is based on the analysis of the oscillating patterns on the surface of the sample coming from the scattering of electrons around impurities or defects. In contrast to ARPES, that can only probe occupied states, studying the evolution of these QPI patterns as a function of the energy we can reconstruct the band structure above and below the Fermi energy. QPI is perfectly compatible with high magnetic fields and it allows to map the changes in the band structure with magnetic field. Besides, the energy resolution of QPI measurements is determined by the energy resolution of the STM. In our case, this energy resolution is of the order of 9 μeV (see section 2.3.3), which is much higher than that typical ARPES systems. QPI technique is discussed more in detail in section 2.1.4.

In this thesis, I have used quasiparticle interference to measure the band structure of three different materials. In chapter 3, I will present QPI measurements in the different magnetic phases of the antiferromagnetic heavy fermion $Ce(Ru_{0.92}Rh_{0.08})_2Si_2$. In chapter 4, I will show the bulk band structure measured in the semimetal WTe_2 and discuss its consistence with first principles calculations, and, in chapter 6, I used this technique to measure the electron and hole pockets of the iron based superconductor FeSe in a very small energy range around the Fermi level.

1.5 Scope

In the following chapters I will present a review of all the technical, experimental and analytical work I have accomplished during my PhD thesis. The purpose of this thesis was to build and operate a new experimental setup that enabled scanning tunneling microscopic measurements at the highest standards of low temperature and high magnetic field, and take advantage of it to investigate novel electronic properties and how they are affected by very high magnetic fields in some interesting materials. In chapter 2, I will present the experimental methods I developed and used in my PhD. Among these, a STM capable of working at 100 mK and magnetic fields as high as 17 T. I set up, improved and characterized this system. The system is now fully operational and contains several original solutions to the technological challenges involved in cooling and applying high magnetic field to scanning microscopes [38]. I will also describe the software I developed to be able to carry out the representations and analysis discussed in the other chapters of this thesis [39].

In chapter 3, I will present a model antiferromagnetic system, $Ce(Ru_{0.92}Rh_{0.08})_2Si_2$, in which antiferromagnetism disappears with the application of a magnetic field. I will show in detail how the magnetic field modifies the band structure (obtained through tunneling conductance and quasiparticle interference experiments) and discuss the consequences for the magnetic transitions.

In chapter 4, I will present results obtained in a model topological semimetal, WTe_2, where I have characterized the band structure using quasiparticle interference. I will show detailed aspects of electronic scattering and discuss their relation to the bulk band structure.

In chapter 5, I will present results obtained in the supposedly simple superconductor Au_2Pb. I will provide measurements of the superconducting gap and its temperature and magnetic field evolution. The large amount of states we find at zero bias is very puzzling and show, together with band structure calculations, the possible unconventional nature of superconductivity in Au_2Pb, related to the topological properties of its band structure.

Finally, in chapter 6, I will discuss the iron based superconductor FeSe. I will determine its band structure and vortex lattice, reproducing previous results showing that this material is a two-gap superconductor with a very small Fermi energy and a strong one-dimensional electronic character. I will study, for the first time, the properties of the vortex lattice at high magnetic fields, unveiling Zeeman splitting in the superconducting band structure and the influence of the periodic vortex lattice in the electronic properties of a novel high field superconducting phase.

2

Experimental methods

As obvious as it sounds, the experiment is the biggest deal for any experimental scientist. Reliable research requires deep knowledge about the specifics of the experimental setup and its limitations as well as the different measuring techniques used. Besides, when the researcher him or herself is directly involved in the setting up process, overcoming any eventual complication becomes far easier.

Scanning tunneling microscopy (STM) is a very powerful well-established technique in condensed matter physics to investigate the electronic properties of different materials. However, only a few groups around the world count with low temperature and high magnetic field STM setups [40]. In this thesis, I modified previous designs of standard STMs used in the lab to build up and characterize a small-sized ceramic STM capable to operate at very low temperatures (below 100 mK) and very high magnetic fields (up to 17 T). Such low temperatures are achieved using a dilution refrigerator, while high magnetic fields are provided by superconducting magnets. In this chapter, I will review the basic principles behind dilution cryogenics and scanning tunneling microscopy, going through the different STM measuring techniques. Furthermore, I will discuss all the efforts to reduce mechanical and electrical noise in the experiment.

STM control frameworks were also upgraded throughout this thesis implementing a new USB based digital unit to handle all the electronic signals going to and coming from the STM. This new device significantly reduced the data acquisition time, but it forced us to come up with new software to manage the different signals of the experiment and to process the huge amount of collected data. The fundamentals of the data acquisition and data analysis software I developed during this thesis will be also presented in this chapter.

2.1 Scanning tunneling microscopy

The first scanning tunneling microscope (STM) was conceived and developed by G. Binnig and H. Rohrer at IBM laboratories in Zurich in 1981 [41]. The invention of the STM was a revolution for the study of materials at the nanoscale, and only five years after, in 1986, they were awarded the Nobel Prize in Physics. The functioning of this device relies in the combination of two well-known physical principles: the quantum tunneling effect between an atomically sharp tip and a flat conducting

sample through a vacuum barrier, and the piezoelectric effect that provides precise subnanometric positioning of the tip over the sample. STM allows us to study the electronic properties down to atomic scale and is highly sensitive to the surface topography and the shape of electronic wavefunctions.

2.1.1 Principle of operation

In 1961, J. Bardeen came up with a tunneling Hamiltonian to understand planar junctions experiments applying time dependent perturbation theory [42]. He stated that the overlap of the wavefunctions of the two electrodes was responsible for electrons tunneling from one electrode to the other. Soon after the STM was invented, J. Tersoff and D.R. Hamann applied Bardeen's theory to STM [43, 44] using the typical distances found in experiments. Assuming a weak interaction between the tip and the sample, they treated Bardeen's Hamiltonian in first order perturbation theory. In this formalism, considering an elastic tunneling regime where the energy is conserved, the expressions for the current flowing between the two electrodes are the following:

$$\begin{aligned} I_{sample\to tip} &= \frac{4\pi e}{\hbar}\int_{-\infty}^{\infty} |M|^2 N_s(E_s)N_t(E_t)[f(E_s)(1-f(E_t))]dE \\ I_{tip\to sample} &= \frac{4\pi e}{\hbar}\int_{-\infty}^{\infty} |M|^2 N_s(E_s)N_t(E_t)[f(E_t)(1-f(E_s))]dE, \end{aligned} \tag{2.1}$$

where e is the electron charge, $\hbar$ the Plank constant, N_s and N_t the densities of states of sample and tip, respectively, and $f(E,T)$ the Fermi distribution function[1] for an energy, E, and a temperature, T. $|M|^2$ stands for the tunneling matrix element or transmission probability. From eq. (2.1), the current is given by

$$\begin{aligned} I &= I_{sample\to tip} - I_{tip\to sample} = \\ &= \frac{4\pi e}{\hbar}\int_{-\infty}^{\infty} |M|^2 N_s(E_s)N_t(E_t)[f(E_s)(1-f(E_t)) - f(E_t)(1-f(E_s))]dE, \end{aligned} \tag{2.2}$$

where E_s and E_t are the energies of the states at the sample and tip, respectively. When applying a voltage, V, between the two electrodes, the Fermi levels of tip and sample are shifted by eV (see fig. 2.1). Thus, $E_s = E - eV$ and $E_t = E$, and eq. (2.2) can be written as

$$I = \frac{4\pi e}{\hbar}\int_{-\infty}^{\infty} |M|^2 N_s(E-eV)N_t(E)[f(E-eV) - f(E)]dE \tag{2.3}$$

For simplicity, the Fermi function can be approached by a Heaviside step function, $f(E) \approx \Theta(-E)$. This approximation is valid for temperatures at which k_BT is well

[1] Fermi distribution function: $f(E,T) = (1 + exp(\frac{E-E_F}{k_BT}))^{-1}$, where E_F is the Fermi energy and k_B is the Boltzmann constant.

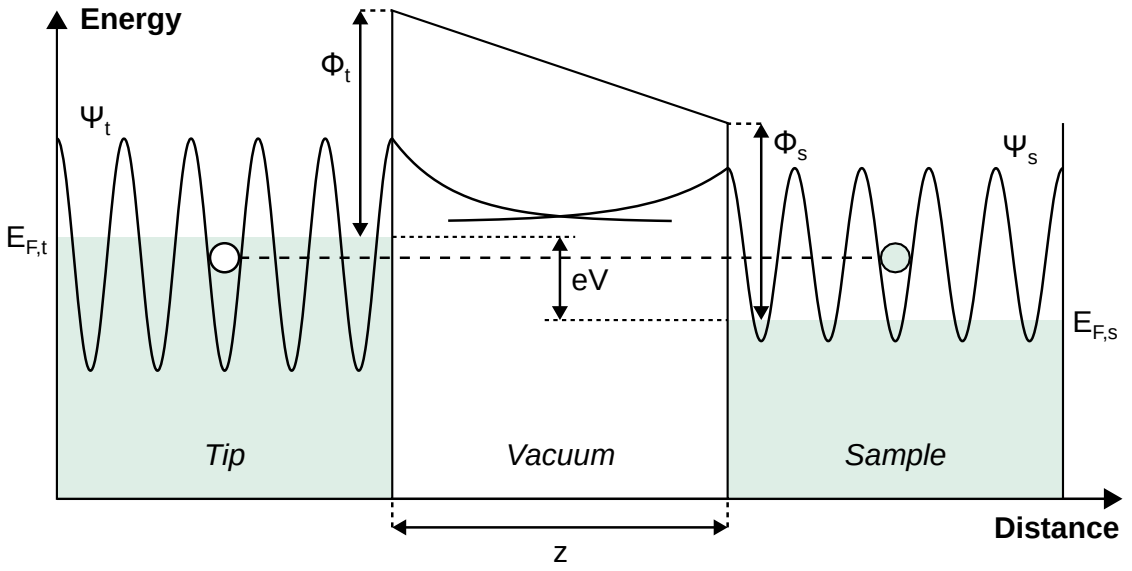

Figure 2.1: Schematic diagram of the tunneling process between the tip and the sample thorough a vacuum barrier of width z. When a positive voltage, V, is applied to the sample, electrons tunnel from occupied states in the tip (Ψ_t) to empty states in the sample (Ψ_s). ϕ_t and ϕ_s stand for the work function of the tip and sample, respectively.

below the energies where we observe changes in the densities of states. For instance, in a usual metal, the density of states is flat at energies below some meV, so at 4.2 K ($k_BT \simeq 0.36$ meV) we can apply the Heaviside step function substitution in the different expressions. However, in a heavy fermion metal or in a semimetal, the density of states presents lots of variations inside an energy range of a few meV around the Fermi level. Thus, one has to cool down to 100 mK to be able to use the Heaviside function approximation. Making this assumption, the limits in the integral in eq. (2.3) are truncated:

$$I = \frac{4\pi e}{\hbar} \int_0^{eV} |M|^2 N_s(E - eV) N_t(E) dE \tag{2.4}$$

We can model a one-dimensional energy barrier of width z and height ϕ, being ϕ the average workfunction of tip and sample (see fig. 2.1). In the limit $eV \ll \phi$ we can assume that the matrix element $|M|^2$ does not depend on energy. Hence, we can write

$$|M|^2 \propto exp(-e\frac{\sqrt{2m\phi}}{\hbar}z), \tag{2.5}$$

where z would be the tip-sample distance and m is the mass of the tunneling electron. Using this expression for the matrix element, eq. (2.4) turns into:

$$I = c\, e^{-\frac{z}{z_\phi}} \int_0^{eV} N_s(E - eV) N_t(E) dE, \tag{2.6}$$

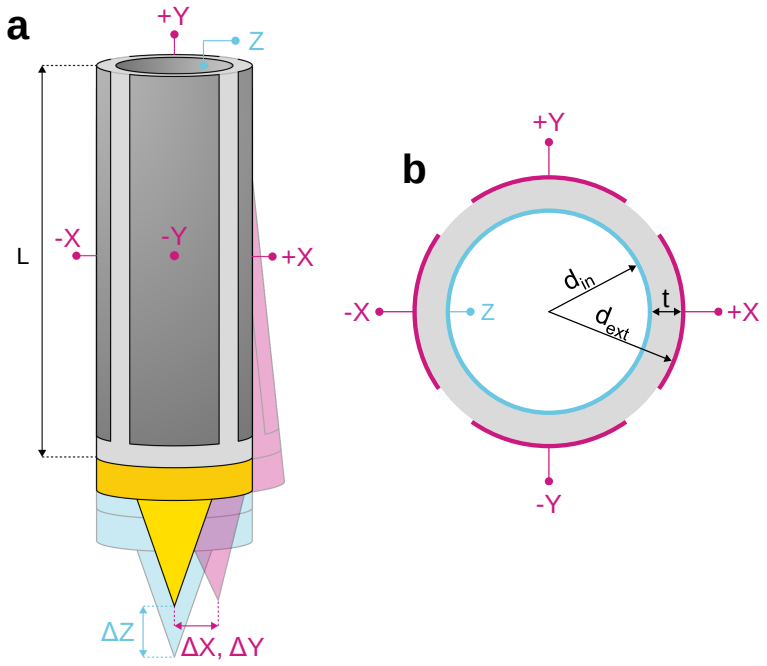

Figure 2.2: (a) Sketch of the piezotube where the STM tip is mounted. Electrodes +X, −X, +Y and −Y for the in-plane movement, and Z for the vertical movement are depicted in dark grey over the ceramic material (light grey). Vertical and lateral movements of the tip are illustrated in blue and magenta, respectively. (b) Cross-section view of the piezotube showing the electrodes configuration.

where c is a proportionality constant that absorbs all prior constants, and we define $z_\phi \equiv \frac{\hbar/\sqrt{8m}}{\sqrt{\phi}}$ as a parameter dependent on the average workfunction, ϕ. The tunneling current decays exponentially with the distance, and thus, it is highly sensitive to small variations in the separation between tip and sample, which is key in the huge resolution of the STM in the vertical direction. Introducing typical values for the workfunction in metals of around 5 eV in eq. (2.6), we obtain that the tunneling current increases by one order of magnitude when the tip-sample distance is reduced in 1 Å.

The piezoelectric effect allows to move the tip over the sample with subnanometric precision. This effect is based on the ability of piezoelectric materials to deform when a voltage difference is applied to them. Typical piezoelectric deformations in STM are of the order of some nm/V. The configuration we use is a piezoceramic tube. The tip is attached to one of the edges of the piezotube while the other edge is fixed to the STM body. The outer electrode of the piezotube is divided into four sections that are responsible for the lateral movement of the tip over the sample. The inner electrode accounts for the vertical displacement (see fig. 2.2). This way, applying voltage differences to the different electrodes we can reproducibly position the tip over the sample in the subnanometric scale.

Combining the tunneling effect and the piezoelectric effect, topographic images of the sample mapping the electronic density over the surface can be taken. These topography records can be obtained using two different modes of operation: the

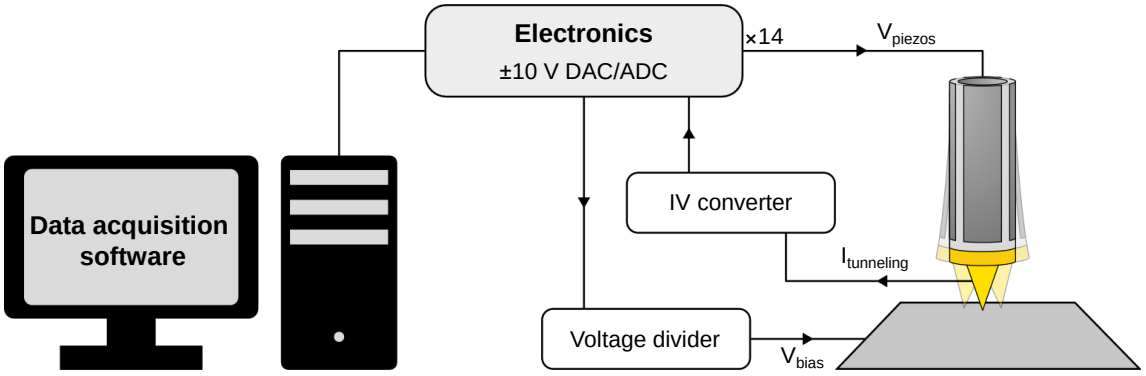

Figure 2.3: Schematic representation of the STM control unit. DAC modules of the electronics send the bias voltage signal to the sample as well as amplified signals to the piezos. The tunneling current is read by an ADC module. All operations are governed by the data acquisition software.

constant height and the constant current modes. For the first one, a constant voltage is applied to the Z electrode of the piezotube as it scans along x and y directions. The value of the tunneling current as a function of the position, $I(x, y)$, will change following the spatial variations in the density of states of the sample, N_s, which occur at atomic scale, and provide, in a first approximation, the atomically resolved corrugation or topography of the surface. However, this mode of operation is restricted to very flat areas where the size of the surface corrugation should be far below the tip-sample distance at the beginning of the experiment. On the other hand, the constant current mode sets a constant setpoint value for the tunneling current and uses a PID feedback loop to adjust the voltage sent to the Z electrode to keep the current constant at the setpoint value during the scan. In this case, from the voltage signal sent to piezo[2] Z as a function of the position, $V_Z(x, y)$, one can reconstruct the topography of the surface. All topographic images presented in this thesis were acquired using the constant current mode.

To manage all the signals needed for the STM to operate, we use a digital electronics unit developed at the university support services (Segainvex [45]) that includes DAC (digital to analog) and ADC (analog to digital) modules to send and read signals from the experiment, respectively. DACs provide DC voltage signals between −10 V and +10 V that are amplified by a factor 14 before sending them to the piezos. Bias voltage signal is normally attenuated using a voltage divider to increase the energy resolution of the measurements. The tunneling current is read by an ADC after going through a current to voltage converter with a gain that can be adjusted from 10^5 to 10^9 V/A. The electronics unit is controlled using homemade software that implements a digital PID loop. A diagram of the STM control unit is shown in fig. 2.3. All the data acquisition software will be discussed more in detail in section 2.4.1.

[2]For simplicity, we use the word *piezo* when referring to the different electrodes of the piezotube.

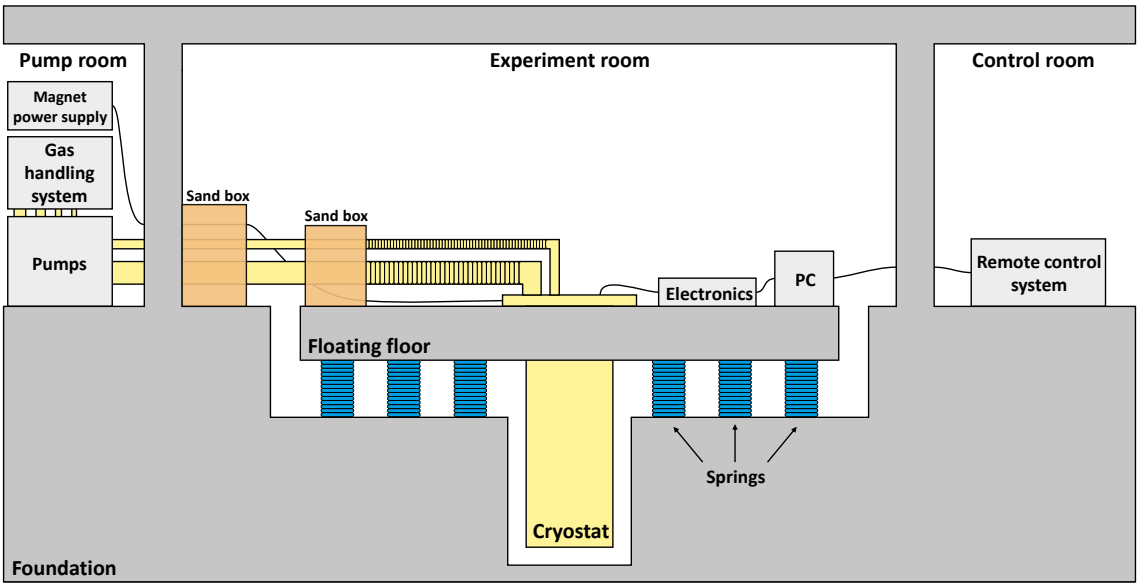

Figure 2.4: Schematic diagram of the experimental setup. The cryostat is fixed to a floating floor that isolates the experiment from the vibrations of the pumps of the system and from the rest of the vibrations of the building. The tubes coming from the pump room pass through two sand boxes to reduce the mechanical noise before touching the floating floor. The experiment is remotely controlled from the outside.

2.1.2 Vibration isolation

The exponential dependence of the tunneling current on the tip-sample distance makes STM measurements extremely sensitive to mechanical vibrations. In the tunneling regime, tip and sample are separated just by a few Å, and, as we discussed above, a change of 1 Å in the distance typically produces a change in the tunneling current of one order of magnitude. Vibrations should produce variations in the position of the tip and the sample that, ideally, leave the tunneling current unaffected. In practice, this means that these variations are smaller than the noise level of the voltage sent to the piezo. Typical values of the tunneling current noise levels produce changes in the tip-sample distance of the order of the pm. Thus, reducing mechanical vibrations is key in every STM setup.

Noise attenuation becomes challenging when working at very low temperatures inside a dilution refrigerator. In this configuration we have to deal with all the vibrations coming from the pumps needed for the gas handling operations regarding the dilution unit. First important aspect in this matter is to fix the dilution insert to the ^{4}He cryostat in such a way that it takes advantage of the large spring supported mass and does not vibrate independently from it. We used glass fiber to cover some parts of the insert so that the fitting inside the cryostat was as tight as possible. The free space in the upper part of the dilution unit was filled with EVA foam to minimize the ^{4}He evaporation rate. EVA foam forces the passage of He vapor close to the inner walls of the Dewar, which improves their cooling and increases the He holding time.

As a general rule, the resonant frequency of the STM head should be as large as possible, while keeping that of the supporting assembly as low as possible. This way, low frequency perturbations, that are unavoidable in practice, will move the tip and sample in phase holding their relative position stable [11]. In section 2.3 we describe the homemade STM we built during this thesis and we discuss the material choices for noise reduction purposes.

The standard method used in our laboratory to mechanically isolate the whole cryostat from the vibrations of the building was to suspend it from the ceiling on some ropes that absorbed all the mechanical vibrations. During this thesis we moved the experimental setup we assembled to a new laboratory taking the mechanical isolation system to the next level as the experiment was installed inside an anti-vibration room with a floating floor (see fig. 2.4). The cryostat is fixed to a 15.7 ton concrete block holding on 18 springs with elastic constant $k = 3 \times 10^4$ N/m that separate it from the building foundation. The resonant frequency of this system is around 1 Hz, so all mechanical vibrations with frequencies higher than that will be significantly damped by the floating floor.

The pumps of the gas handling system from the dilution unit are placed in a separated room with double wall and glass fiber in between, and all the tubes coming from the pump room go through a sand box that partially absorbs the vibrations before they reach the floating floor. The power supply of the 17 T magnet is also inside the pump room. In this configuration, the whole experiment can be remotely controlled from the outside with no need to go inside the experiment room and step on the floating floor while the experiment is running. Therefore, the eventual mechanical and acoustic vibrations caused by usual system management situations are reduced to minimum.

To characterize the damping system we used two SM-24 geophones from SENSOR Nederland b.v. [46]. Geophones consist of a magnetic mass suspended by a spring inside a coil. The motion of the mass produces an induced voltage in the coil, which we amplify using a EGG 5113 preamplifier by a factor of 500. We then read the resulting voltage using the USB acquisition we will describe later on in section 2.4.1. We record curves with 12000 points in 60 seconds and Fourier transform the obtained signal. The resolution in time is 5 ms. We can thus measure vibrations up to 200 Hz. As the device is a simple damped harmonic oscillator, its resonance modifies the measurement. The natural frequency of the device is 10 Hz with a tolerance of ±2.5 %. We correct the frequency response by multiplying the result with the sensitivity curve provided by the supplier. When we compare the level of vibrations obtained in the floor of the new location with that of the previous location, we observe a decrease by nearly an order of magnitude (fig. 2.5a). To test the mechanical response of the floating floor damping system we turned the pumps on removing their dampers so that they were directly hammering the floor in the pump room. This introduces a large noise level over the entire measured spectrum. Inside the experiment room, we placed a geophone on top of the floating floor and another one on top of the unfloated floor at the edges of the room. Figure 2.5b plots the simultaneously acquired vibrational noise signals by both devices. We see that the additional noise level is reduced by the suspended floor system to a level which is

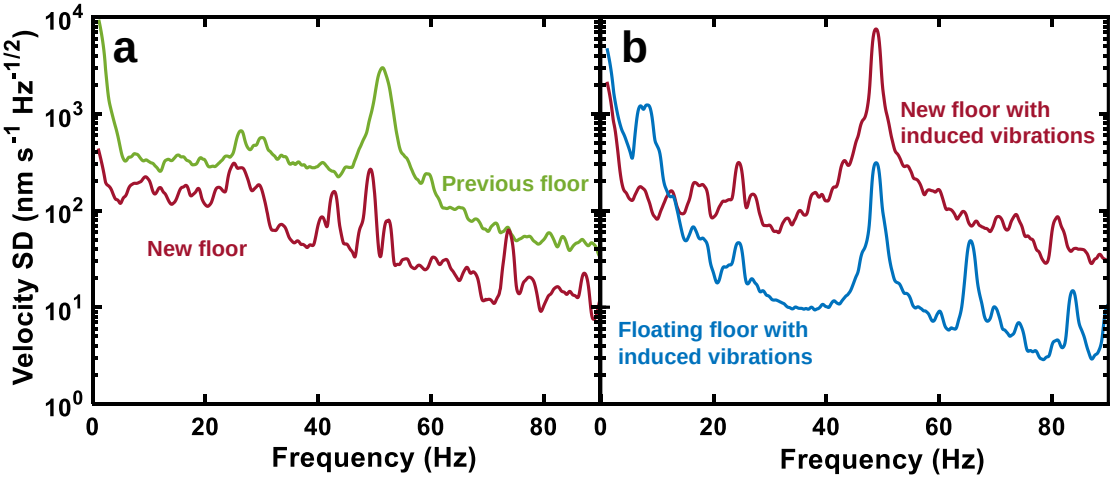

Figure 2.5: Plots of the standard deviation of the velocity of a mass suspended on a damped spring with a resonant frequency of 10 Hz as a function of the frequency. The velocity is measured using an inductive technique (SM-24 Geophone Element). The damping below the resonance is corrected using a sensitivity function provided by the supplier. (a) Results on the floor of the previous location of the cryostat (green) and on the floor of the new location (red). (b) Results in the new location when we were operating a pump without rubber damping support. The pump creates large vibrations seen in the red curve. The floating floor (blue line) shows a significant damping of the vibrations.

comparable or better than the floor. Thus, the suspension system allows to isolate the experiment from the environment effectively.

Nevertheless, for frequencies below about 10 Hz, it is very challenging to measure if the floating floor is really efficient or not. To add an additional damping in that range of frequencies, we have tested S-2000A active air damping model from Newport [47] and Gimbal Piston air vibration isolation system from TMC [48]. We observe that the Newport system does not bring any improvement to our setup. Possibly, the system we use to support the cryostat, which is far more complex than the optical tables often used in conjunction with Newport vibration isolators, makes it very difficult to balance all the dampers and may alter their response. It turns out to be very difficult to adjust the Newport devices in such a way that there is no touch between the floating and rigid parts, which introduces a direct connection and removes damping. On the other hand, with TMC dampers, there is considerable room to adjust the position of the cryostat so that suspended and rigid parts are not in direct contact with each other. This results in an efficient damping below approximately 10 Hz.

2.1.3 Spectroscopy with STM

STM can also be used as a powerful tool to probe the spectroscopic properties of the sample with high energy resolution around the Fermi energy. The energy range of all the studies presented in this thesis fulfill the condition $eV \ll \phi$, where ϕ is the average work function of tip and sample. In this limit, the transmission probability

of the tunneling barrier can be assumed to be constant and eq. (2.3) can be written as

$$I(V) \propto \int_{-\infty}^{\infty} N_s(E-eV)N_t(E)[f(E-eV)-f(E)]dE \tag{2.7}$$

For simplicity, in the following discussion I will assume that we are using a normal non-superconducting tip. However, superconducting tips are widely used in scanning tunneling microscopy [49]. In fact, some of the results I will present in the iron based superconductor FeSe (chapter 6) were obtained using a superconducting Pb tip. Tunneling conductance curves measured with superconducting tips accentuate every small feature in the density of states of the sample [50]. When probing a superconducting sample, the resulting conductance curve will present sharper quasiparticle peaks whose voltage position will be at the sum of the superconducting gap sizes of tip and sample, $\Delta_t + \Delta_s$ (see section 2.3.3). Besides, superconducting tips open the door for Josephson spectroscopy.

Coming back to the case of a normal metallic tip, the density of states, N_t, can be approached to a constant value in this small energy range we are considering. Therefore, eq. (2.7) can be simplified to

$$I(V) \propto \int_{-\infty}^{\infty} N_s(E-eV)[f(E-eV)-f(E)]dE \tag{2.8}$$

Differentiating the tunneling current with respect to the applied voltage we obtain the following expression for the tunneling conductance, $\sigma(V)$

$$\sigma(V) = \frac{dI(V)}{dV} \propto \int_{-\infty}^{\infty} N_s(E)\frac{\partial f(E-eV)}{\partial V}dE \tag{2.9}$$

Tunneling conductance is proportional to the convolution of the density of states of the sample and the derivative of the Fermi function. Hence, from STM tunneling

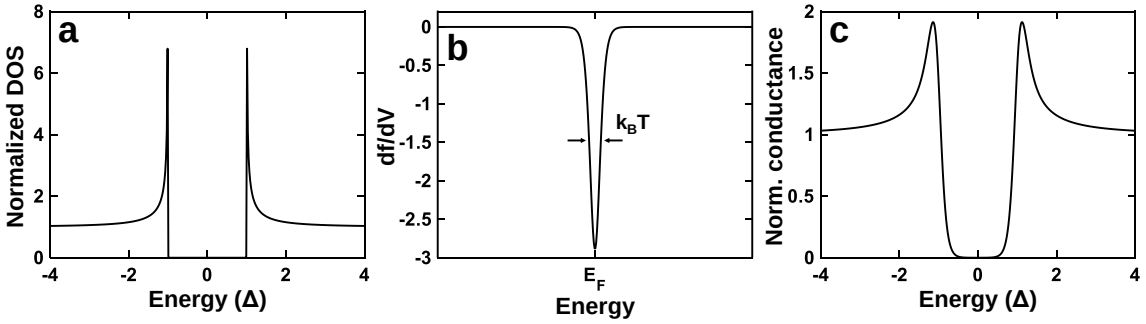

Figure 2.6: (a) Density of states for a BCS superconductor as a function of the energy in units of the superconducting gap, Δ. (b) Derivative of the Fermi distribution at a temperature T. The width at half maximum is k_BT. (c) Measured tunneling conductance curve for a sample displaying the density of states in (a) at the same temperature, T. The shape of the curve is the result of the convolution of the density of states (a) and the derivative of the Fermi distribution (b) following eq. (2.9).

conductance versus bias voltage curves one can extract information about the density of states of the sample. The derivative of the Fermi function displays a bell shape with a width given by k_BT (see fig. 2.6b). At very low temperatures, the width of this bell becomes very narrow and it tends to a Dirac delta function, $\delta(E - eV)$, as the temperature, T, goes to zero. In this extremely low temperatures limit, the tunneling conductance is directly proportional to the density of states of the sample:

$$\sigma(V) = \frac{dI(V)}{dV} \propto N_s(E = eV) \tag{2.10}$$

Thus, we can use STM tunneling conductance measurements to directly determine the density of states of the sample as a function of the energy. However, this is not always true due to the so-called setpoint effect.

Setpoint effect

STM allows to spatially map the spectroscopic properties of the sample as we will discuss in the following section. To obtain 2D maps, feedback loops are widely used for tip positioning before every spectroscopic curve is taken. The setpoint value of the feedback loop can affect the results of the measurements if there is a dependence on the position, $\vec{r} = (x, y)$, in the density of states [51, 52].

In the low temperature limit, assuming a normal metallic tip, from eq. (2.6), the tunneling current can be written as

$$I(\vec{r}, V) = C \int_0^{eV} N_s(\vec{r}, E)dE, \tag{2.11}$$

where we define $C \equiv c\, d^{-\frac{z}{z_\phi}} N_t(0)$ for simplicity. The setpoint current will be thus given by:

$$I_0 = I(\vec{r}, V_0) = C \int_0^{eV_0} N_s(\vec{r}, E)dE, \tag{2.12}$$

where V_0 is the setpoint voltage. Differentiating eq. (2.11) we obtain the following expression:

$$\frac{dI(\vec{r}, V)}{dV} = CN_s(\vec{r}, eV) \tag{2.13}$$

Comparing eqs. (2.12) and (2.13) we obtain a conductance that depends on the setpoint current, I_0, and voltage, V_0 as

$$\sigma(\vec{r}, V) = \frac{dI(\vec{r}, V)}{dV} = \frac{I_0 N_s(\vec{r}, eV)}{\int_0^{eV_0} N_s(\vec{r}, E)dE} \tag{2.14}$$

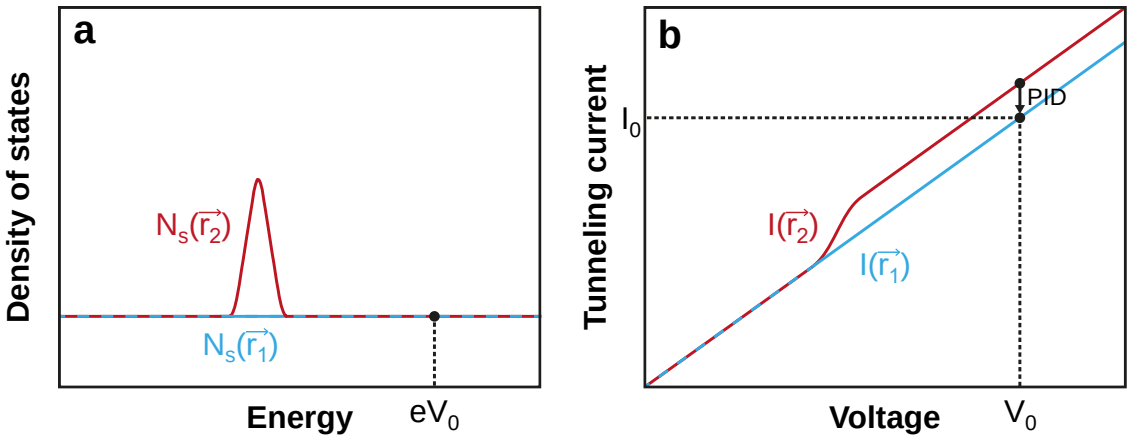

Figure 2.7: Illustrative example of the setpoint effect. (a) Schematic density of states as a function of the energy on two different positions on the surface of the sample, $\vec{r}_1$ (blue) and $\vec{r}_2$ (red). (b) Tunneling current obtained from eq. (2.11) at these two positions. If the PID loop is acting at the position V_0, it will result in a correction of the current curve such that $I(\vec{r}_1, V_0) = I(\vec{r}_2, V_0)$. Thus, the prefactor C in eq. (2.11) will be different in $\vec{r}_1$ than in $\vec{r}_2$.

From this relation we can conclude that, although the tunneling conductance is proportional to the density of states of the sample, the proportionality constant can vary with the position if the integrated density of states up to the setpoint voltage presents spatial inhomogeneities. Figure 2.7 illustrates the setpoint effect for a case in which the density of states as a function of the energy on site 1 ($\vec{r}_1$) is slightly different to that on site 2 ($\vec{r}_2$). Both curves coincide in most of the energy range, but on site 2 there is a peak in the density of states at a certain energy below eV_0. As the tunneling current is defined as the integral of the density of states multiplied by a constant C (eq. (2.11)), we see from the example in fig. 2.7 that the feedback loop can introduce a modification in C as a function of the position, $C(\vec{r})$, leading to a spatial variation in the $\frac{dI}{dV}(\vec{r}, V)$ images that makes it impossible to obtain the density of states, $N(\vec{r}, E)$, directly from $\frac{dI}{dV}(\vec{r}, V)$. To correct for this issue, we can divide each conductance curve, $\frac{dI}{dV}(\vec{r}_i, V)$, by the value of the conductance in that site $\vec{r}_i$ at a voltage close to and below V_0:

$$\frac{\sigma(\vec{r}_i, V)}{\sigma_0(\vec{r}_i, V_0)} = \frac{N_s(\vec{r}_i, eV)}{N_s(\vec{r}_i, eV_0)} \tag{2.15}$$

This simple correction eliminates the spatially varying prefactor $C(\vec{r})$ and provides normalized tunneling conductance curves that are indeed proportional to the density of states of the sample.

2.1.4 Scanning spectroscopy with STM

Scanning tunneling spectroscopy (STS) allows to study local differences in the electronic properties of a sample taking advantage of the high spatial resolution

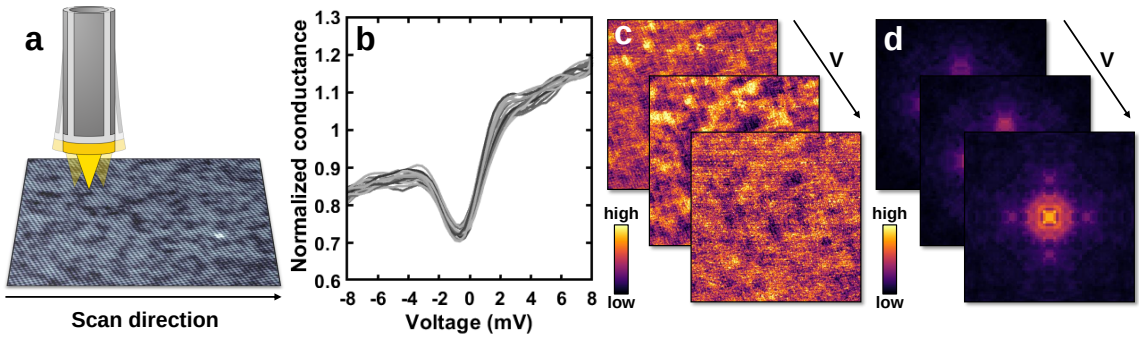

Figure 2.8: Schematic representation of the simultaneous topographic and spectroscopic data acquisition process. The data shown in this example belong to some QPI measurements in $Ce(Ru_{0.92}Rh_{0.08})_2Si_2$. As the tip scans over the sample (a), at every pixel of the image the feedback loop is disconnected and a spectroscopic IV curve is taken. Tunneling conductance curves (b) are obtained by differentiating these IV curves. Conductance curves can be rearranged into conductance maps for different bias voltages (c). Fourier transforming these conductance maps (d) the spectroscopic properties can be studied in reciprocal space.

of STM. Following the spatial spectroscopic differences is key, for instance, to map superconducting vortex lattices or to study the quasiparticle interference scattering (QPI) in the surface of the sample.

Spectroscopic maps are normally acquired simultaneously to a topographic image. The tip scans over the sample with the feedback loop on to keep the current constant as in the usual acquisition process of a topographic image, but in this case, the tip stops at every pixel of the image and the feedback loop is disconnected to take a spectroscopic current versus bias voltage curve (IV curve). Then, the feedback loop is reconnected and the tip moves to the next point of the scan keeping the current constant. After the whole scan is finished, every pixel of the topography has an associated IV curve. Numerically differentiating these IV curves we obtain tunneling conductance versus bias voltage curves that can be used to build up spectroscopic images mapping the value of the tunneling conductance as a function of the position and the bias voltage (see fig. 2.8).

Forth and back scans of the tip over the surface result in two separated images for each measurement. Besides, two voltage ramps (from positive to negative, and backwards) are taken at each point of each image. Typical image dimensions range from 64×64 to 512×512 pixels. Thus, a spectroscopic measurement holds a huge amount of IV curves, each of them containing from 64 to 512 points. To choose the size of the images and the IV curves we have to reach a compromise between the space and energy resolution desirable to study a particular phenomenon and the available time for the measurements. In our case, the latter is usually limited by the remaining time until the next helium transfer to keep the experiment cold. Thanks to the improvement and work made during this thesis, the time between helium transfers in the setup that I mounted is around 6-7 days when operating at base temperature (0.1 K), what provides more than enough time to perform large spectroscopic measurements. Besides, the new data acquisition system implemented

along this thesis using digital USB based electronics (see section 2.4.1) has noticeably reduced the time of the measurements. With previous analog electronics, it could take around 60 hours to measure a 512×512 pixels image with 64 points in the IV curves. Our new standards allow us to perform even larger images of 512×512 pixels with up to 256 points in the spectroscopic curves in less than 24 hours without increasing the noise level. However, this major improvement in the acquisition process brings the necessity to deal with very heavy files (of the order of several gigabyte) when coming to data analysis. In section 2.4.2, I discuss how we addressed this new situation developing new data treatment software.

QPI analysis

Studying the quasiparticle interference scattering (QPI) in STS measurements one can get information about the band structure of the sample. The relation between the measured local density of states (LDOS) and the momentum eigenstates $\Psi(\vec{r_k})$ is given by

$$\mathrm{LDOS}(E, \vec{r}) \propto \sum_{\vec{k}} |\Psi(\vec{r_k})|^2 \, \delta(E - \epsilon(\vec{k})), \tag{2.16}$$

where $\vec{k}$ is the wavevector and $\epsilon(\vec{k})$ is the dispersion relation of the material. When the periodicity of the crystal is broken by the presence of impurities or defects on the surface, electrons are scattered around producing oscillations in the LDOS. These scattering processes are typically elastic. In this picture, scattering between states with $\vec{k_i}$ and $\vec{k_f}$ will give rise to a modulation with $\vec{q} = \vec{k_f} - \vec{k_i}$ in the LDOS that can be observed in the tunneling conductance with the STM. The scattering between an initial state, i, and a final state, f, is described by the Fermi golden rule:

$$w(i \to f) \propto \frac{2\pi}{\hbar} |V(\vec{q})|^2 \, N_i(E_i, \vec{k_i}) N_f(E_f, \vec{k_f}), \tag{2.17}$$

where $E_i = E_f$ for elastic scattering, $\vec{q} = \vec{k_f} - \vec{k_i}$ is the scattering vector, N_i and N_f the initial and final densities of states, and $V(\vec{q})$ the scattering potential. This scattering potential can be different for different types of impurities or defects, and it can also be anisotropic [54]. We can define the joint density of states (JDOS) from the momentum-resolved density of states of the sample:

$$\mathrm{JDOS}(\vec{q}, E) = \int N(\vec{k}, E) N(\vec{k} + \vec{q}, E) d^2\vec{k} \tag{2.18}$$

From eq. (2.17) and eq. (2.18) we can deduce that, in first approximation, the scattering $\vec{q}$ vectors connecting states with higher JDOS will produce a higher QPI signal.

The intensity of the scattering signal depends on the strength of the scattering potential at $\vec{q} = \vec{k_f} - \vec{k_i}$, $V(\vec{q})$, and the JDOS. The scattering potential can be anisotropic and can enhance or reduce the scattering intensity at a given $\vec{q}$. The

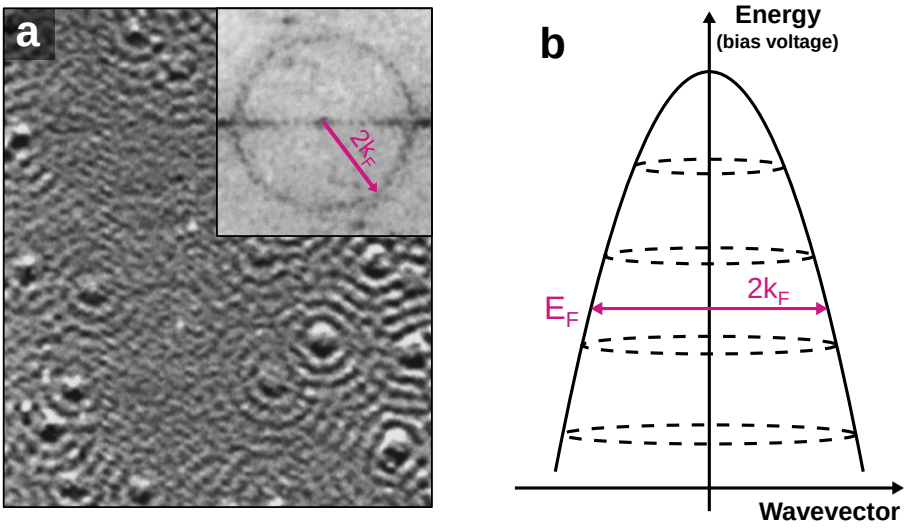

Figure 2.9: (a) Adapted from [53]. Constant current STM topographic image taken at 150 mK in Cu(111) with a bias voltage of −5 mV. In the presence of point like defects, electrons are scattered producing oscillating patterns on the surface. Fourier transform of the image indicating the main scattering vector is shown in the inset. (b) Schematic diagram illustrating how the parabolic dispersion relation in Cu(111) could be reconstructed by measuring the main scattering vector for different values of the bias voltage.

JDOS provides the amplitudes of the density of states (DOS) at initial and final scattering states and will be higher at certain locations on the band structure, for example at van Hove anomalies or when scattering occurs between flat parts of the Fermi surface. Thus, by plotting the maxima in the scattering intensity as a function of the bias voltage, we can follow the JDOS for certain $\vec{q}$ as a function of the energy. Using this information, we can reconstruct the electronic dispersion relation (see fig. 2.9). This reconstruction is most easily obtained in those parts of the band structure that interact with defects and impurities and provide largest V. Furthermore, STM can follow the band structure of the material for both occupied and empty states, what is a major advantage if we compare it with techniques like angle-resolved photoemission spectroscopy (ARPES), that can only access states below the Fermi energy.

Noise reduction is essential in QPI measurements when trying to identify the different $\vec{q}$ vectors. As can easily be understood, JDOS($\vec{q}$) contains all the symmetry operations of the crystal at its surface. However, $V(\vec{q})$ includes additional components depending on the internal shape of the defects and the way these interact with the electrons of the compound. Being mostly interested in JDOS ($\vec{q}$), we can use the symmetry properties of the crystal to enhance the signal to noise ratio [55]. For instance, in a square lattice with four-fold symmetry, all the scattering information in reciprocal space can be collapsed into just one quadrant. Therefore, if we take the average value of the four quadrants of our 2D fast Fourier transform (FFT) maps after applying the proper rotation and mirroring operations, the QPI signal is enhanced over the background noise, that

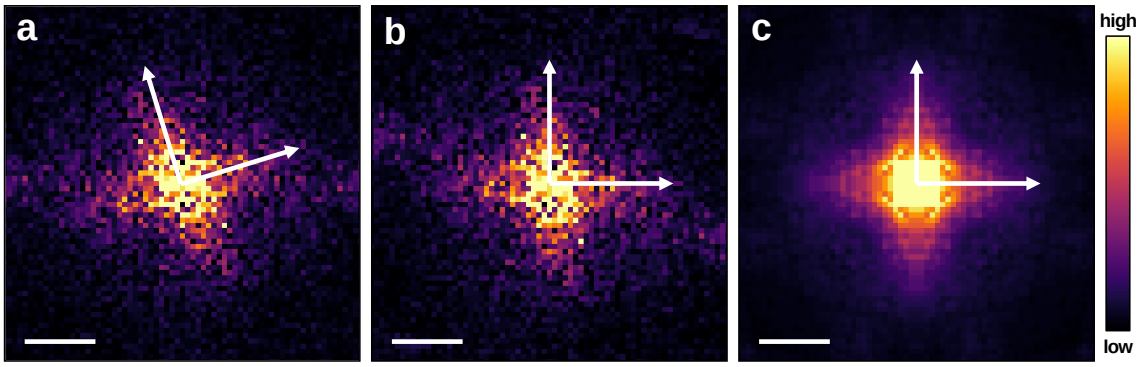

Figure 2.10: (a) 2D FFT of a conductance map measured at 1 mV in $Ce(Ru_{0.92}Rh_{0.08})_2Si_2$ with STM. White arrows mark the direction of the crystallographic axes. (b) 16.5° rotation of the image to align the crystallographic axes with the vertical and horizontal directions. (c) Four-fold symmetrization of the image to enhance the signal to noise ratio. The size of the scale bar is 0.4 π/a, where a is the lattice constant.

is ideally averaged out to zero. Figure 2.10 illustrates the symmetrization process for a case of a 4-fold symmetry crystal. After rotating the 2D-FFT maps to align the crystallographic axes with the vertical and horizontal directions, we apply the symmetry averaging operations and crop the images to the first Brillouin zone limits. As one would expect, the averaging processes applied will be different for crystals showing different symmetries.

Once the data is symmetrized we can follow the different $\vec{q}$ vectors with the energy to reconstruct the band structure of the material. In section 2.4.2, I will describe the data analysis software I developed to simplify this procedure.

It is worth mentioning that when Fourier transforming the conductance maps, the central point of the 2D-FFT corresponds to the sum of the values of all the individual pixels in the conductance map and is useless for the scattering analysis. Large wavelength oscillations or modifications of the density of states generally produce a large signal for the few pixels around the central pixel. These are usually difficult to interpret, and often have only a weak dependence on energy. However, if there is an energy dependence, these pixels close to the center of the Fourier transform might be also indicative of long wavelength scattering processes. In case these large wavelength modulations are not crucial, we can apply a Gaussian core subtraction to the center of the maps in order to reduce the intensity at the smallest wavevectors and increase the contrast of the images.

2.2 Cryogenics

Since the beginning of the 20th century, the development of cryogenic technologies has opened the door to very interesting novel physical phenomena like superconductivity. STM has been evidenced as a very powerful tool to explore the electronic properties of materials at very low temperatures.

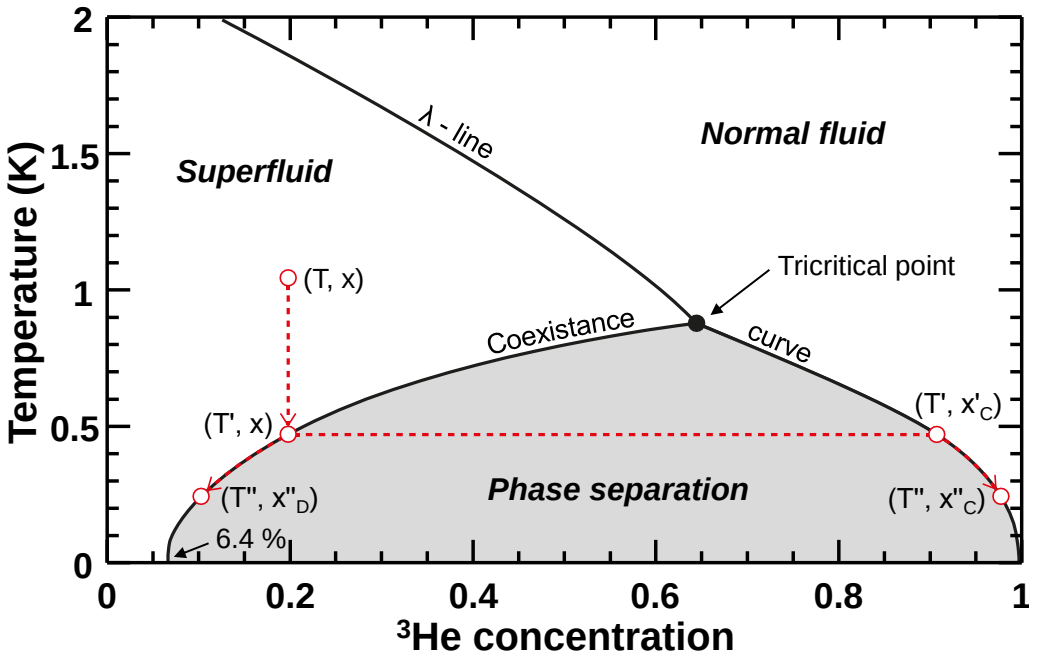

Figure 2.11: Temperature (T) versus ^{3}He concentration (x) phase diagram for a ^{3}He/^{4}He mixture. For $x = 0$ there is no ^{3}He, and for $x = 1$ there is only ^{3}He in the mixture.

Among all the cryogenic techniques, ^{3}He/^{4}He dilution refrigeration stands out as a very versatile one when working with STM. First of all, it allows to cool down the STM below 100 mK. At such low temperatures thermal excitations are considerably reduced increasing the energy resolution in the spectroscopic measurements ($k_BT \simeq 8.6$ μeV at 100 mK). Besides, dilution refrigerators are able to ceaselessly maintain the experiment at those very low temperatures. This is specially important for us when trying to perform the long spectroscopic measurements we described in the previous section.

In a dilution cryostat, the cooling power at temperatures below 100 mK is larger than that in other cryogenic methods [56]. Furthermore, unlike techniques like adiabatic demagnetization, the functioning of the dilution system is not affected by the presence of a magnetic field. This turns to be crucial for us as our experimental setup is equipped with a 17 T superconducting magnet to perform high magnetic field STM measurements.

In this section, I will describe the principle of operation of a dilution refrigerator and how we implemented it to cool the STM well below 100 mK.

2.2.1 Dilution refrigerator

The working principle of dilution cryogenics is based on the quantum properties of a mixture of the two stable isotopes of helium, ^{3}He and ^{4}He [57]. Figure 2.11 shows the temperature (T) versus ^{3}He concentration (x) phase diagram for a ^{3}He/^{4}He mixture. Above the coexistence curve, the mixture can be in the superfluid state

at the left side of λ-line or in the normal fluid phase at the right side. Below the coexistence curve there is a phase splitting into a concentrated phase (C) rich in ^{3}He and a dilute phase (D) rich in ^{4}He. As the density of ^{3}He is lower than that of ^{4}He, the concentrated phase will float over the dilute phase.

To illustrate the phase separation process we can take the starting point (T, x) with $x = 0.2$ in fig. 2.11 inside the superfluid region. When the temperature decreases at a constant concentration, the mixture reaches the coexistence curve at $T = T'$ and separates into a dilute phase and a concentrated phase. If the temperature keeps going down until $T = T''$, ^{3}He concentration in the concentrated phase will grow up to x''_C, while that in the dilute phase will go down to x''_D. Thus, ^{3}He concentration in both phases depends on the temperature following the coexistence curve. When the temperature is further reduced, ^{3}He concentration is almost 1 below 0.1 K, and it varies between 0.07 at 0.1 K and 0.064 at 0 K in the dilute phase. The fact that the ^{3}He concentration at zero temperature in the dilute phase is finite is key in the performance of the dilution refrigerator [58].

To understand the lack of separation into pure ^{3}He and ^{4}He even at 0 K we have to recall quantum statistics. ^{4}He is a boson with zero nuclear spin. Below 0.5 K it is in the superfluid state and the amount of excited phonons and rotons is very small. Therefore, it remains inert from a thermodynamic perspective. On the other hand, ^{3}He has nuclear spin 1/2 and it obeys Fermi-Dirac statistics. In the range of temperatures where a dilution refrigerator operates, ^{3}He can be considered as a Fermi liquid with a renormalized effective mass whose value depends on the concentration in the dilute phase. In this model, the balance of the chemical potentials in both phases provides the equilibrium condition:

$$\mu_{3C}(T, x_C) = \mu_{3D}(T, x_D), \tag{2.19}$$

where $\mu_{3C} \equiv g_{3C} \equiv h_{3C} - Ts_{3C}$ and $\mu_{3D} = (\partial G_{3D}/\partial n_3)_{T,P,n_4}$[3]. The latent heat of vaporization of ^{3}He in the concentrated phase at zero temperature is related to the chemical potential through $L_{3C}(0) = -\mu_{3C}(0)$. Therefore, the energy required to extract one atom of ^{3}He from the concentrated phase is $L_{3C}(0)/N_A = -\mu_{3C}(0)/N_A$, where N_A is the Avogadro constant. On the other hand, the binding energy of one atom of ^{3}He in the dilute phase is $-\mu_{3D}(0,0)/N_A$. As $\mu_{3D}(0,0)$ is bigger than $\mu_{3C}(0)$, the binding energy of ^{3}He to ^{4}He atoms is higher than that among ^{3}He atoms and thus, there is a flow of ^{3}He atoms from the concentrated to the dilute phase. However, this process is limited because the binding energy in the dilute phase decreases as x_D increases. Since ^{3}He atoms follow Fermi-Dirac statistics, the Fermi energy ($k_B T_F(x_D)$) increases with the concentration. Then, as $\mu_{3D}(0, x_D)/N_A = -\epsilon_{3D}(0, x_D) + k_B T_F(x_D)$, the binding energy $\epsilon_{3D}(0, x_D)$ varies

[3] Upper and lower case letters represent extensive and molar quantities, respectively. h, s and g stand for the molar enthalpy, entropy and Gibbs free energy, respectively, and n for the number of moles. Subscripts 3 and 4 refer to ^{3}He and ^{4}He.

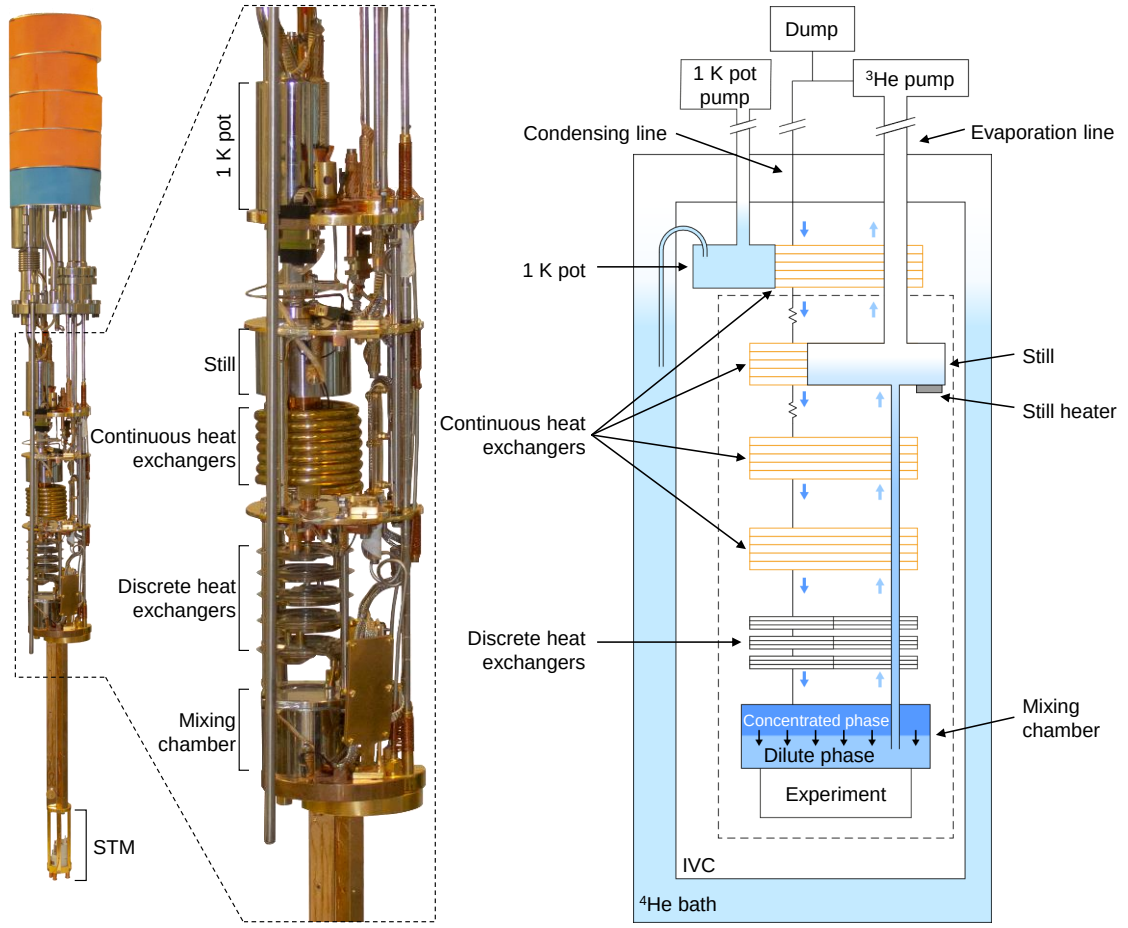

Figure 2.12: Photograph (left) and schematic diagram (right) of our dilution refrigerator.

with the concentration to keep the chemical potential constant. Substituting in eq. (2.19), the equilibrium condition can be rewritten as

$$L_{3C}(0)/N_A = -\epsilon_{3D}(0, x_D) + k_B T_F(x_D) \tag{2.20}$$

Introducing measured values for the Fermi temperature and the binding energy, the concentration below which the transfer of ^{3}He atoms from the concentrated to the dilute phase is no longer energetically favorable is $x_D = 0.064$ [56].

This means that, at equilibrium, there is a non-zero amount of of particles in the dilute phase. Hence, if the concentration of ^{3}He atoms is reduced in the dilute phase, some ^{3}He atoms will cross the interface from the concentrated phase to the dilute phase to fulfill the equilibrium condition. This process is responsible for the cooling in the system since the enthalpy of ^{3}He is larger in the dilute phase than in the concentrated phase.

Figure 2.12 shows a photograph of the dilution system used during this thesis together with a schematic diagram depicting the main parts of a dilution refrigerator. The ^{3}He/^{4}He mixture is injected through the condensing line and it is precooled by the 1 K pot, that is a small vessel filled with liquid ^{4}He from the bath that

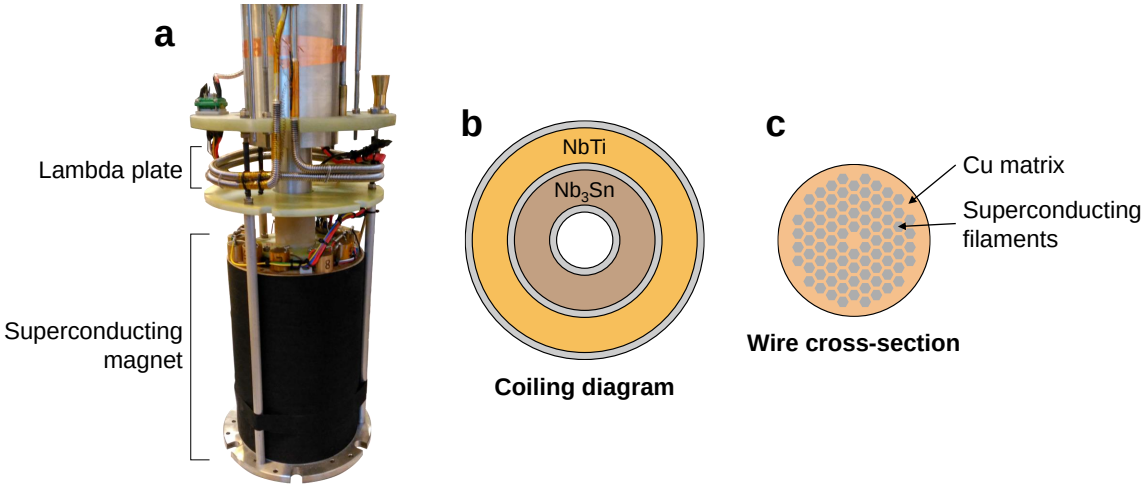

Figure 2.13: (a) Photograph of a 17 T superconducting magnet with its supporting structure. (b) Top view diagram of the coiling of the superconducting magnet. Two different superconducting materials are used: NbTi and Nb_3Sn. (c) Sketch of a cross-section cut of the superconducting wires used to build the magnets. Superconducting filaments are embedded into a copper matrix.

is continuously pumped out to reduce its temperature down to 1.5 K. At this temperature, some impedances keep the value of the pressure above the vapor pressure of ^{3}He limiting the flux and allowing condensation. After leaving the 1 K pot, the mixture goes through several heat exchangers where it is cooled down using the enthalpy of the outgoing mixture coming upwards in the dilute phase.

Phase separation takes place in the mixing chamber, which is the coldest part of the dilution system. There, the concentrated phase is floating over the dilute phase. The mixing chamber is connected to the still or evaporator, that is the place where the liquid-gas interface is located. The dilution of ^{3}He atoms is forced by a pumping system that constantly removes ^{3}He from the dilute phase in the still. This way, ^{3}He concentration is reduced in the still producing an osmotic pressure gradient between the still and the mixing chamber that drives ^{3}He atoms towards the still after crossing the phase boundary in the mixing chamber. The ^{3}He flowing upwards in the dilute phase is used to cool down the mixture coming down to the mixing chamber in the concentrated phase. The difference between the vapor pressures of ^{3}He and ^{4}He at the still temperature ($\sim$ 0.7 K) implies that, when the still is pumped, the main part of the evaporated gas is pure ^{3}He. Sometimes it is necessary to apply some heat to the still in order to keep its temperature at around 0.7 K to improve the efficiency of the process. The evaporated ^{3}He is purified in a liquid nitrogen trap with activated carbon filters before it reenters the cryostat in the concentrated phase. The choice of the initial ^{3}He concentration and volume of the mixture is crucial for the phase separation to occur inside the mixing chamber and for the liquid-gas interface to lie inside the still.

The experiment, in our case, the STM, is thermally attached to the mixing chamber, which is the coldest part of the cryostat. The dilution refrigerator used in our experimental setup is the model MX400 from Oxford Instruments [59] (see

fig. 2.12). For the gas handling system, we used Kelvinox 25 model from the same company. The design, assembly and leak testing operations regarding all the pumping lines were performed during this thesis. As we discussed in the former section, the gas handling system and the pumps are placed outside the experiment room to reduce the mechanical vibrations.

Our cryostat is equipped with a 17 T superconducting magnet also from Oxford Instruments (see fig. 2.13). The magnet consists of two concentric coils that use two different superconducting materials. The outer one is made of NbTi wires, with lower values of the critical magnetic field and critical current, and the inner one uses $NbSn_3$ wires, that remain superconducting to higher magnetic field and current. Superconducting wires consist of several filaments of superconducting material embedded inside a copper matrix. In this configuration, copper provides mechanical stability and is a low resistance parallel conduction path for the huge currents that circulate through the superconducting filaments in case the values for the superconducting critical temperature or the critical current are exceeded [60]. In case the magnet quenches, there is a security system with a set of diodes to avoid high voltages at the leads and a set of low impedance parallel resistors to absorb part of the heat generated by the decaying circulating current.

Liquid ^{4}He refrigeration is needed for the superconducting magnet to work. One of the main advantages of superconducting coils is that, once they are charged, they can work in persistent mode with no need of any current supply. This way we reduce the ^{4}He evaporation rate and the helium consumption of the system. Besides, mechanical noise associated to helium boiling off is also decreased. Finally, current fluctuations and noise associated to magnetic field changes are also hindered. To operate in persistent mode, the coil is shunted by a superconducting switch with a heater. Turning on the heater we connect the magnet to the current supply for charging and discharging operations, but when the heater is off the magnet becomes a closed circuit with no losses.

This magnet provides magnetic fields up to 15 T at 4.2 K and up to 17 T at 2 K. On the top part of the magnet there is a copper serpentine with a needle valve (lambda plate). Pumping through the needle valve, the temperature of the bath goes down to 2 K below the lambda plate while it stays at 4.2 K above [61]. This way we are able to transfer helium to the cryostat even if the magnet is delivering the maximum magnetic field (17 T).

2.3 Implementation of the setup

Many of the properties that can be explored with a STM depend strongly on the magnetic field. In fact, if the field is strong enough, it can even modify the materials giving rise to new phases. However, high magnetic field environments can produce heating and mechanical noise issues that have to be addressed when designing a very low temperature STM. In this section, I present the high magnetic field ceramic STM I developed and characterized for this thesis. I will show as well how we made sure

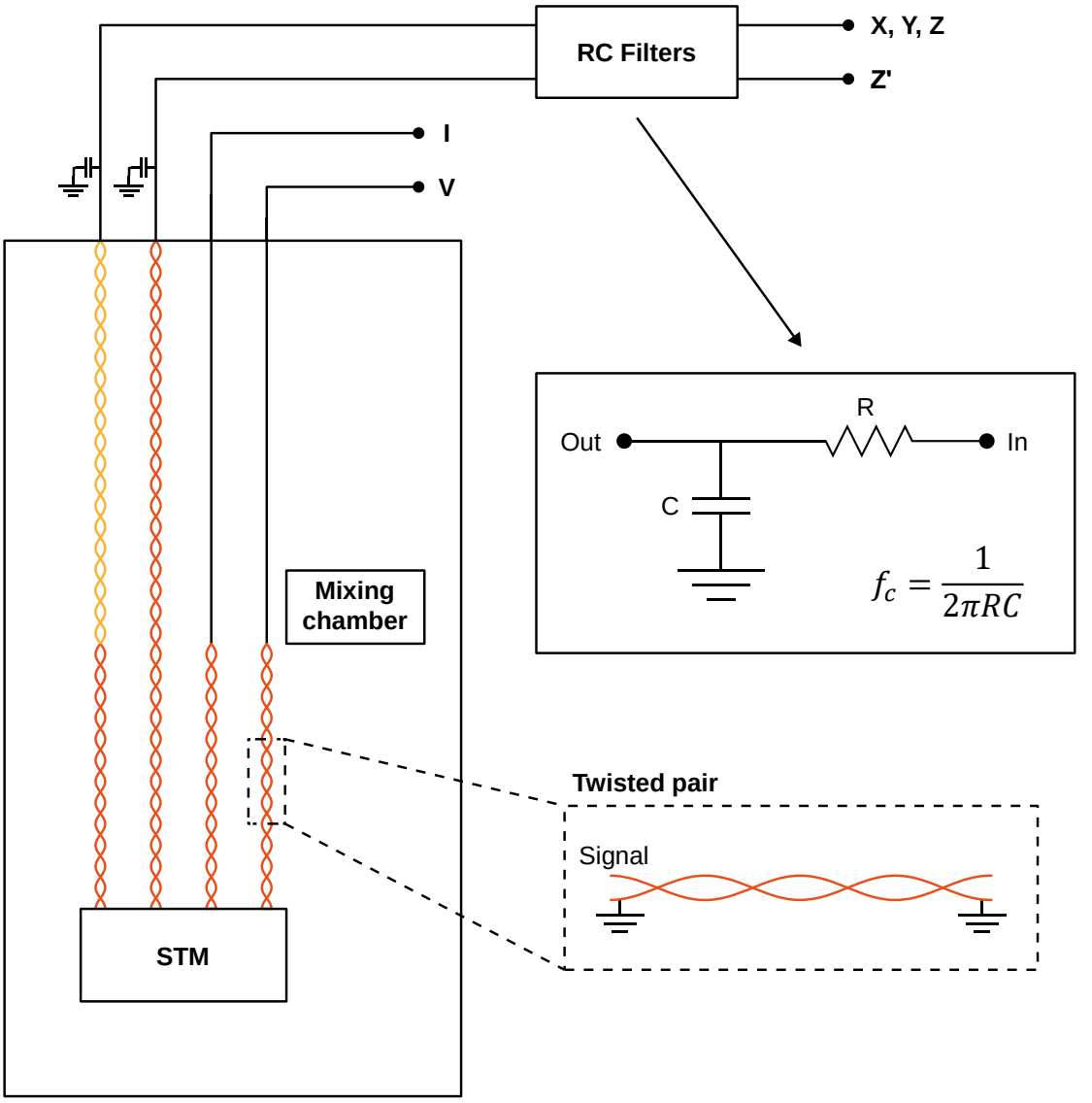

Figure 2.14: Schematic diagram of the wiring of the experiment. RC filters are used outside the cryostat at room temperature to filter high voltage signals for the piezos (X, Y, Z, Z′). The cut-off frequency, f_c, depends on the values used for the resistance, R, and the capacitance, C. Twisted pairs of manganin and copper are depicted in yellow and orange, respectively.

that the resolution in voltage of the tunneling conductance curves, which provides the resolution in energy of the features we can resolve in the density of states, is not larger than the thermal energy. Finally, I will discuss the method we use to prepare the tip and sample for STM measurements in cryogenic conditions.

2.3.1 Wiring and thermalization

When working with a dilution refrigerator STM, the wiring of the setup must be carefully designed to keep all the signals as clean as possible while avoiding heating

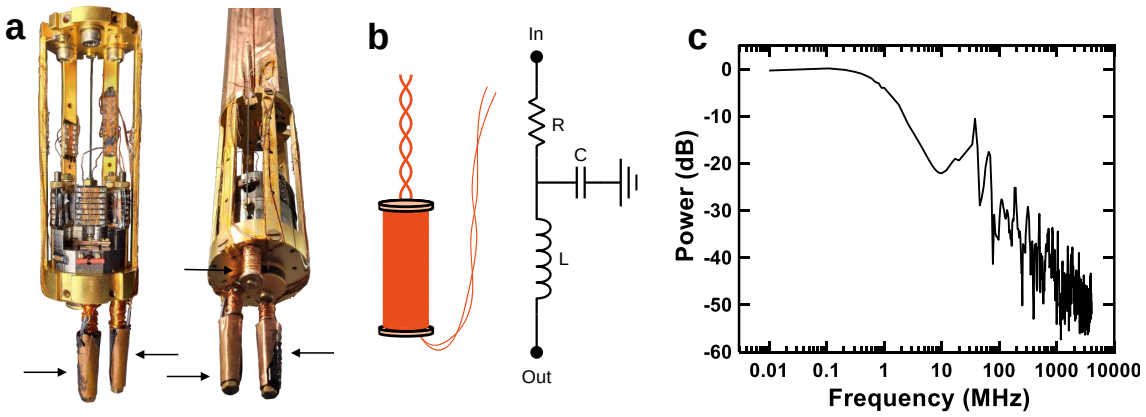

Figure 2.15: (a) Photographs of the supporting structure for the STM showing the small coils (black arrows) used to filter the signals. (b) Cartoon representation of one of the coils together with the diagram of the RCL filter. (c) Measured gain versus frequency for one of the coils.

of the experiment. A proper filtering and screening of the electric signals is needed to obtain a resolution in voltage that allows to perform density of states measurements that are limited by the thermal energy and not by the noise in the voltage.

The wiring of our system was entirely designed and assembled during this thesis. It can be divided in two different stages. The first one goes from the external connectors outside the cryostat at room temperature to some other connectors in mixing chamber (~ 80 mK), and the second one carries the signals from these connectors in the mixing chamber down to the STM.

In the first stage, we used twisted pairs for the signal of the piezos (X, Y, Z, Z′). The twist is made using a cable carrying the signal, which can be a manganin cable (200 Ω), and a copper cable that is grounded. Thanks to the twist, both cables are strongly joined all over the length, what means that we have a large resistance and a distributed capacitance to ground [62, 63]. As the wires display a resistance of ~ 200 Ω and a capacitance to ground of ~ 1 nF, they act as a continuous RC filter for high frequency signals (see fig. 2.14). In this first stage, we use manganin for the signals X, Y, and Z. It presents significantly lower thermal conductivity than copper and it reduces the thermal contact between the outside of the cryostat and the mixing chamber. Besides, manganin wires display higher resistance than copper wires, improving the filtering of the signals. However, for the signal going to the piezostacks for the coarse vertical movement (Z′) we use copper wires. This way the resistance of the circuit is decreased allowing for the fast voltage ramps needed for the inertial motion (see section 2.3.2). The signals for the current (I) and the bias voltage (V) come down to the mixing chamber in a coaxial cable to ensure a perfect screening.

For the connections between the mixing chamber and the STM we use twisted pairs of copper for all the signals to enhance thermalization. High voltage signals of the piezos (X, Y, Z, Z′) and current and voltage signals (I, V) follow separated paths down to the STM to avoid noise induction in the latter. The signals of the piezos

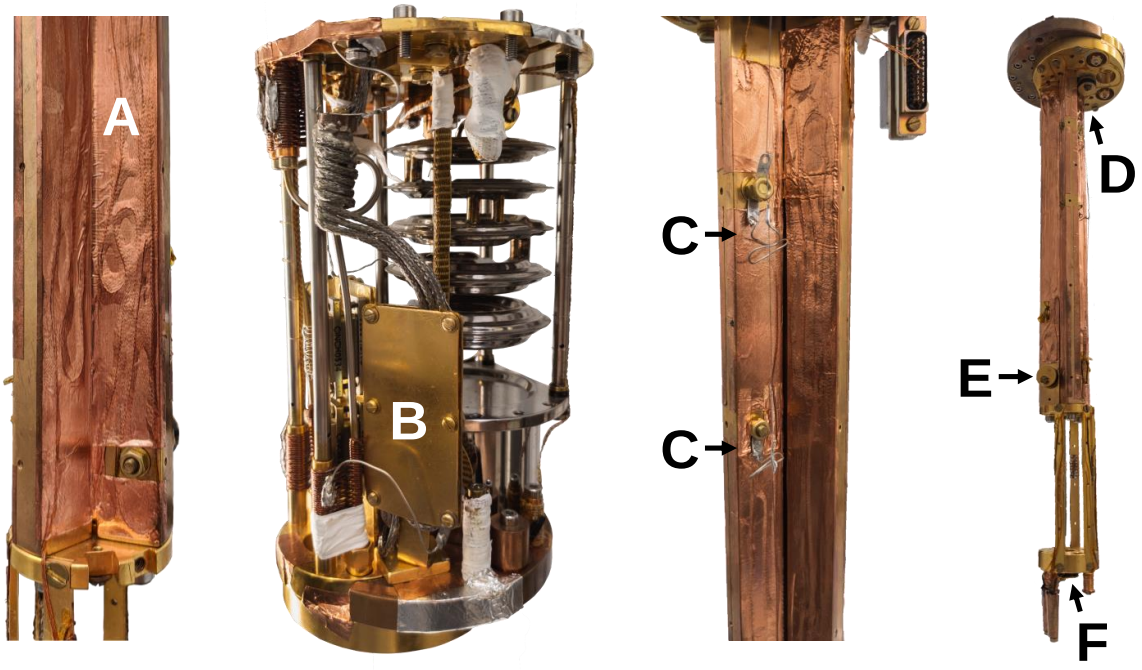

Figure 2.16: Photographs of the insert illustrating the thermalization mechanisms. All the wires come down to the experiment stuck to the copper structure (A). We use copper plates coated with gold (B) to thermalize the wires in several stages. The piano string needed for the movement of the sample holder is also thermalized in different points (C). Germanium (D), RuO_2 (E) and Cernox (F) thermometers are installed at different locations of the copper structure that supports the STM.

are filtered outside the cryostat using low-pass RC filters with cut-off frequencies of 10 kHz for X, Y and Z, and 50 kHz for Z$'$.

To improve high frequency filtering of the signals, the wires coming down from the mixing chamber are wound around three different small copper cylinders before they are soldered to the STM body. These small coils are fixed to the bottom part of the STM supporting structure as shown in fig. 2.15a. The purpose of this winding is twofold. First, to improve the thermalization of the wires as detailed below, and second, to induce a high impedance for the high frequency signals that pass through the RC circuit (see fig. 2.15b). The main conduction at high frequencies occurs through the skin effect, which increases the impedance at high frequencies. Using powder surrounding the signal-carrying wire, we increase the surface ratio of the wire, improving the damping by the skin effect. Furthermore, the particles are magnetic, what helps eliminate spurious resonances that might appear depending on winding conditions [64].

The whole cabling system is tested by introducing a signal through one cable and collecting it on another cable, both being joined at low temperatures. We can see that the attenuation at high frequencies of the whole system is considerable (see fig. 2.15c). Thus, the use of a set of different filters is very efficient to clean up the electronic signal and achieve high bias voltage resolution.

The thermal contact between the mixing chamber and the STM should be as good as possible to reach temperatures below 100 mK. The STM is placed in a copper structure that is fixed to the mixing chamber. This copper structure is coated with gold to increase its thermal conductivity. All the wires coming down from the mixing chamber are stuck to this structure using varnish and copper tape (fig. 2.16(A)) to help thermalization and provide a last capacitance. The wires go up and down several times over the structure to increase the contact surface. The wires coming from outside the cryostat at room temperature are thermalized at the different stages of the dilution refrigerator (1 K pot, still and mixing chamber). At every stage, they are sandwiched between two gold-coated copper plates that are screwed to the insert (fig. 2.16(B)) [65]. We use high thermal conductivity vacuum grease to enhance thermal exchange between the cold plates and the wires. The steel cable used to mechanically control the position of the sample holder from the outside is also thermalized at several points using thick copper wires coated with tin (fig. 2.16(C)). The functioning of this positioning system will be described below.

We installed three Lake Shore [66] resistance thermometers to monitor the temperature of the coldest part of the experiment (see fig. 2.16(D,E,F)). The first one is a germanium based thermometer (D) that lies next to the mixing chamber and operates in a range from 50 mK to 100 K. It provides submillikelvin sensibility with an excellent reproducibility of ± 0.5 mK at 4.2 K. However, it is not recommended at very high magnetic fields due to its strong magnetoresistance. The second one is a RuO_2 based thermometer (E). It works down to 50 mK with low magnetic field-induced errors below 1 K and it is placed in the top part of the STM cage. Finally, a Cernox thin film sensor (F) is installed right below the STM. It ranges from 100 mK to 300 K and it presents the best performance under magnetic field.

Four terminal resistance measurements are performed using a Lake Shore Model 372. Thanks to all the thermalization methods described above, when the mixing chamber is at 80 mK, the temperature read of the closest thermometer to the STM is of around 85 mK.

2.3.2 Realization of the STM

As a general rule, magnets that supply the more intense magnetic fields leave the smaller room for the experiment inside the coiling. For instance, the inner diameter of the most powerful hybrid magnets in high magnetic field facilities is of around 20 mm. The cross-section diameter of previous standard STM designs in our group was no smaller than 40 mm [67]. Nonetheless, this already compact STMs still did not fit in the very narrow space inside the most powerful superconducting magnets we work with in the lab (17 T and 22 T). Hence, the size our STM designs had to be further reduced and a 30 mm diameter STM was built [68].

As I introduced in section 2.1.2, to minimize sensitivity to mechanical vibrations, the resonance frequency of the head of the STM should be as high as possible. Materials with the larger ratio between the Young modulus and the density present

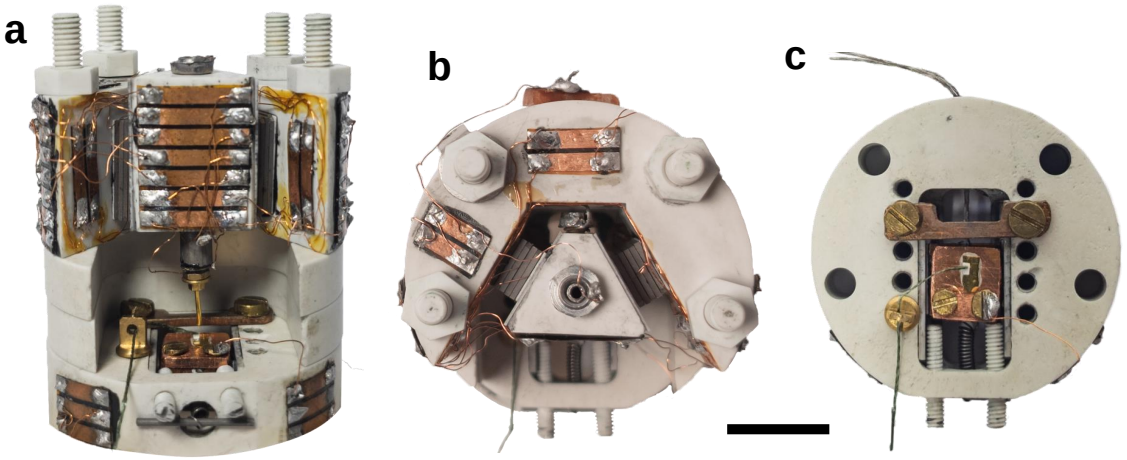

Figure 2.17: Photographs of the shapal-made STM built in this thesis. (a) Front view. (b) Top view. (c) Top view of the base part. Horizontal scale bar is 10 mm long.

the highest resonance frequencies (see table 2.1). All the microscopes in our lab were made of a non-magnetic titanium alloy (Ti-Grade 5) that provided the good thermal conductivity at low temperatures expected for a metal. However, metallic components can be a problem at very low temperatures due to the Joule heating produced by Foucault currents when ramping the magnetic field. To avoid this issue, for the STM we constructed in this thesis we modified the 30 mm design using shapal instead of titanium. Shapal is a non-magnetic, non-metallic, light and rigid ceramic material with a Young modulus to density ratio even larger than in Ti-Grade 5. Besides, its thermal conductivity is quite good at low temperatures. The main drawback of shapal lies in its brittleness. Although it turns to be very challenging to machine, even the smallest pieces were successfully obtained in the workshop of the university (Segainvex [45]). Mechanical properties and thermal conductivity of sapphire position it as an interesting option to consider for low temperature STM purposes. Nevertheless, it is more expensive and even more fragile than shapal.

Figure 2.17 shows some pictures of the shapal STM we assembled. The base part (fig. 2.17c) includes a rail coated with alumina for the movement of the sample holder described in section 2.3.4. The sliding piece is made of shapal while we use copper for the sample holder. Two non-magnetic copper-beryllium springs, one in the bottom and another one in the front, are tied to the sliding piece to keep the

Material	Density (kg m^{-3})	Young modulus (GPa)	Ratio × 100
TiGrade 5 (Ti6Al4V)	4420	110	2.4
Al 7075	2700	70	2.5
Macor	2520	66	2.6
Shapal	2900	190	6.6
Sapphire (α-Al_2O_3)	3980	340	8.5
WC	15500	550	3.5

Table 2.1: Properties of typical materials used in STM designs [11].

sample holder over the sliding track and to help it recover the rest position when the tension in the piano string is released. The guillotine for the cleaving process can be fixed at different positions using the available threaded holes, and the rest position of the sample holder can be adjusted by moving the two screws in the front. We usually glue two samples in the sample holder: a sample of the material of interest for the experiment and a sample of the same material of the tip (typically gold). This way we can clean and sharpen the tip using the indentation method that will be described in section 2.3.4. A copper wire for the bias voltage contact is soldered to one of the corners of the sample holder.

The tip filament is glued to a small tip-holder screw that is fixed to one of the edges of the piezotube. In our STM design, we place the tip on the piezotube while the sample is glued on top of the sample holder. The piezotube deformation depends on its geometry and on the voltage difference applied to the different electrodes ($V_{x,y}$, V_z) [69]:

$$\begin{aligned} \Delta X = \Delta Y &= \frac{0.9 d_{31} l^2 V_{x,y}}{d_m t} \\ \Delta Z &= \frac{d_{31} l V_z}{t}, \end{aligned} \tag{2.21}$$

where l is the length of the piezotube, t, its thickness, and d_m the average between the inner an outer diameters. The so-called piezoelectric coefficient (d_{31}) takes a value of 0.31 Å/V at 4.2 K in the piezoelectric materials we used. In our particular case, l = 11 mm, d_m = 2.667 mm and t = 254 μm. Therefore, since we apply voltage differences of ±140 V, our maximum scanning area is 1.4 × 1.4 μm^2 and the maximum vertical displacement is 370 nm.

The piezotube is screwed to a mobile shapal prism that has some tracks to collect all the contacts for the piezos (X, Y, Z) and the current (I). Using a spring, this mobile piece is attached to two stacks of piezoelectric plates that are responsible for the macroscopic movement of the tip in the vertical direction (Z′). Each of the piezostacks consists of five 10 mm × 5 mm × 0.5 mm piezoelectric plates that present a shear deformation when a voltage difference is applied between its faces. The direction of the shear deformation depends on the sign of the applied voltage. Each plate counts with a corner cut that marks its polarity. To synchronize the deformation of all of the plates inside a stack we glued them as shown in fig. 2.18a using Stycast 2850FT. To apply the voltage signals needed for the deformation, copper wires are glued between consecutive plates with conductive silver epoxy. Applying a sawtooth voltage signal to the piezostacks (fig. 2.18b), they behave as an inertial motor with a working principle based on the stick-slip effect [38]. During the slow part of the voltage ramp (several ms), the piezostacks deform upwards or downwards dragging the mobile prism by means of friction. The fast part of the sawtooth signal (∼ 5 μs) forces the piezostacks to recover the non-deformed situation very rapidly sliding over the mobile piece without moving it. This way, repeating the cycles of the sawtooth signal sent to the piezostacks we achieve a continuous

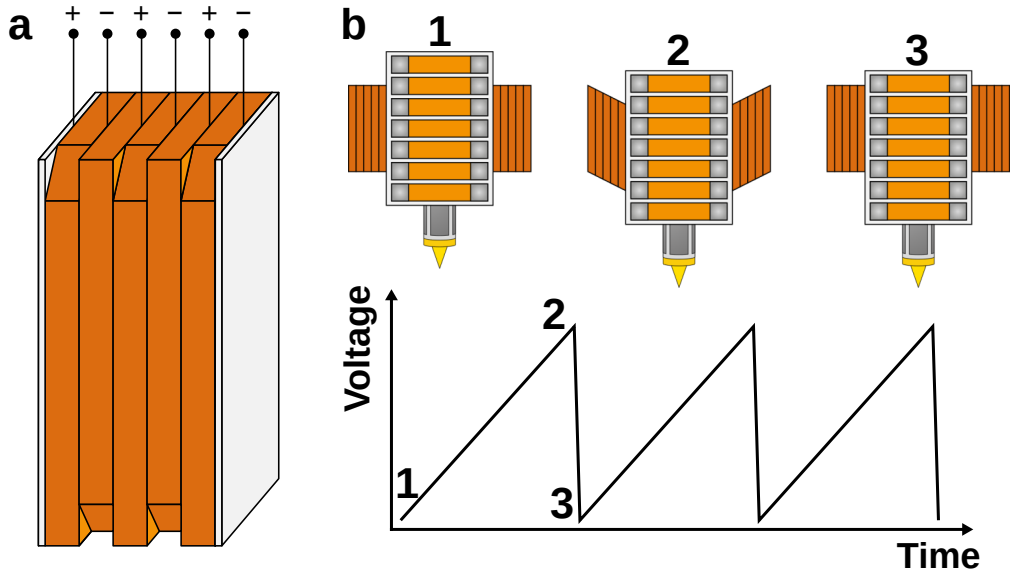

Figure 2.18: (a) Schematic representation of a piezostack consisting of 5 piezoelectric sheets sandwiched by two pieces of alumina. The polarity of two consecutive sheets is opposite. (b) Schematic representation of the coarse vertical inertial movement of the tip produced by the piezostacks when a sawtooth voltage signal is applied. The mobile head of the STM is dragged by the deformation of the piezostacks during the slow voltage ramp (1 - 2). Then, the piezostacks go rapidly back to their initial position sliding over the STM head.

motion of the tip in the vertical direction. Inverting the sign of the sawtooth signal we change the direction of the movement. This process is described in more detail in Ref. [38].

The principles behind this effect are far from trivial. The functioning is based on the interplay between a force that joins the two parts together and allows motion when they are moved slowly, and a force that leads to detachment of both parts when they are moved rapidly. This interplay is particularly tricky when the motor is operated in a vertical position, as in our case. In this situation, the only force that keeps the mobile prism together to the STM body is the force applied through the spring in the back part of the STM. There are several designs of piezoelectric motors [70, 71, 72, 73]. Improvements are mostly based on systems that hold some piezos still and move others fast in such a way that they are operated in a step-by-step manner [74]. However, this increases the size of the microscope and is not really efficient as the motion principle still requires a balance between attachment and sliding. In our microscope, we provide this balance by searching for the position of the mobile part which produces largest motion. Besides, for both contact surfaces we use alumina coated with graphite, which is stiff enough so that both parts remain toghether when they move (stick), but breaks on fast shear action allowing motion when it is required to slip [38].

The implementation of digital electronics has considerably simplified the STM control unit. All the signal reading, processing, sending and amplifying procedures

are managed by one single device (LHA-Digimod from Segainvex) connected to a measuring computer. This electronics device is not bigger than a shoe box and the data acquisition software to control it can even run in a non specially powerful laptop, what makes the whole experimental system very portable and opens the door to use it in high magnetic field facilities.

2.3.3 Characterization of the setup

Our STM was designed to work at very low temperatures and very high magnetic fields. It is attached to the cold part of a dilution refrigerator inside a cryostat that counts with a 17 T superconducting magnet. We tested and characterized some STM operations under these extreme conditions to ensure a correct functioning of the system. The choice of non-metallic ceramic shapal for the STM eliminates variations in temperature due to Joule heating when ramping up and down the magnetic field. With previous titanium designs, magnetic field ramps of several Tesla produce a temperature rise of several hundred of millikelvin and the system needed a few minutes to recover the base temperature.

Figure 2.19a shows an atomic resolution topographic image taken at 14 T in a WTe_2 sample (see chapter 4). Low mechanical and electrical noise levels in our system allow to resolve the atomic structure on clean surfaces of the sample even at very high magnetic fields. The digital electronics unit includes voltage attenuation devices that can be applied to the signals sent to piezos X and Y to make use of the entire 16 bit depth of the voltage ramp in a smaller range and increase the spatial resolution of the images.

We used an aluminum tip and an aluminum sample to test the indentation process at 17 T. Applying small voltage ramps to piezo Z we can crash and separate the tip from the sample in a controlled way [75]. In this process, atomic contacts are formed between the sample and the tip apex and we observe step jumps in the tunneling conductance versus distance curves every time every time the contact is widened in one atom and a new conductance channel appears (see fig. 2.19b). The height of the first steps is the value of the conductance quantum, σ_0. Figure 2.19c displays a histogram of the normalized conductance values obtained repeating the indentation process thousands of times. In this histogram we observe a peak near every multiple of the conductance quantum. The particular shape of p-orbitals in aluminum makes the steps in the conductance versus distance staircase-like plot a little tilted [76, 77]. The same indentation process using gold tip and sample produces pretty straight steps and the peaks in the histogram lie right at the conductance quantum and its multiples, but the tilting in the steps when using aluminum drives the peaks in our histogram to slightly lower values.

To characterize the energy resolution of the system we studied the superconducting-superconducting (S-S) tunneling junction using again aluminum for both tip and sample. Aluminum is a well known BCS superconductor below a critical temperature of 1.2 K. When taking spectroscopic IV curves in S-S junctions at very low temperatures, the tunneling current equals zero for voltages

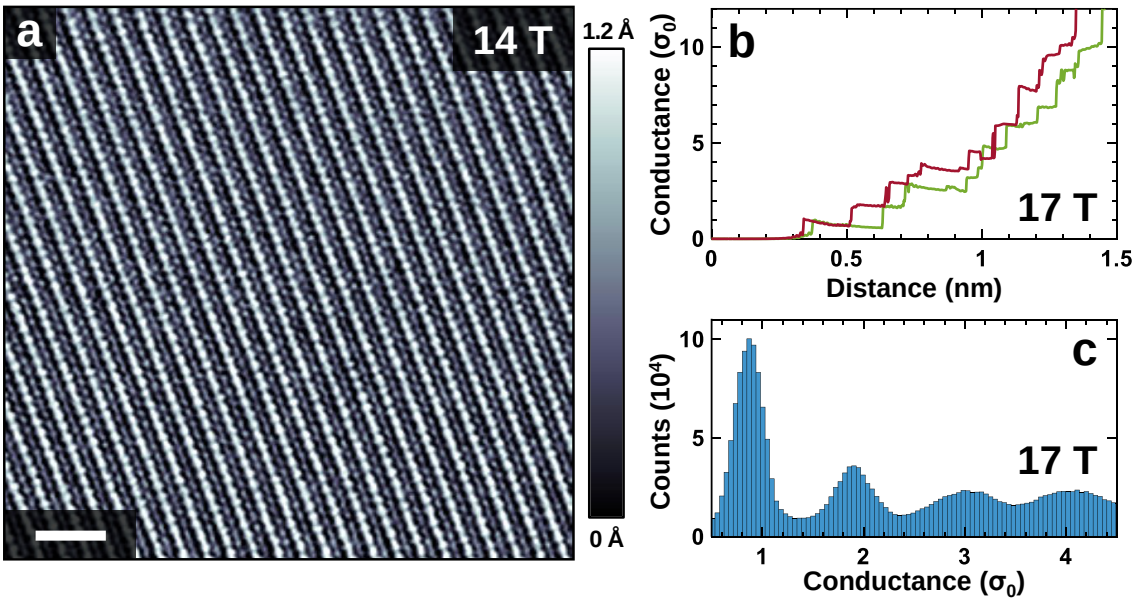

Figure 2.19: (a) Atomic resolution topographic image measured at 14 T in WTe_2. Scale bar: 2 nm. (b) Conductance versus distance curves acquired at 17 T as the aluminum STM tip approaches (green) and separates (red) from the aluminum sample. Conductance values are normalized to the conductance quantum, σ_0. (c) Histogram of the normalized conductance values collected after thousands of indentation cycles at 17 T.

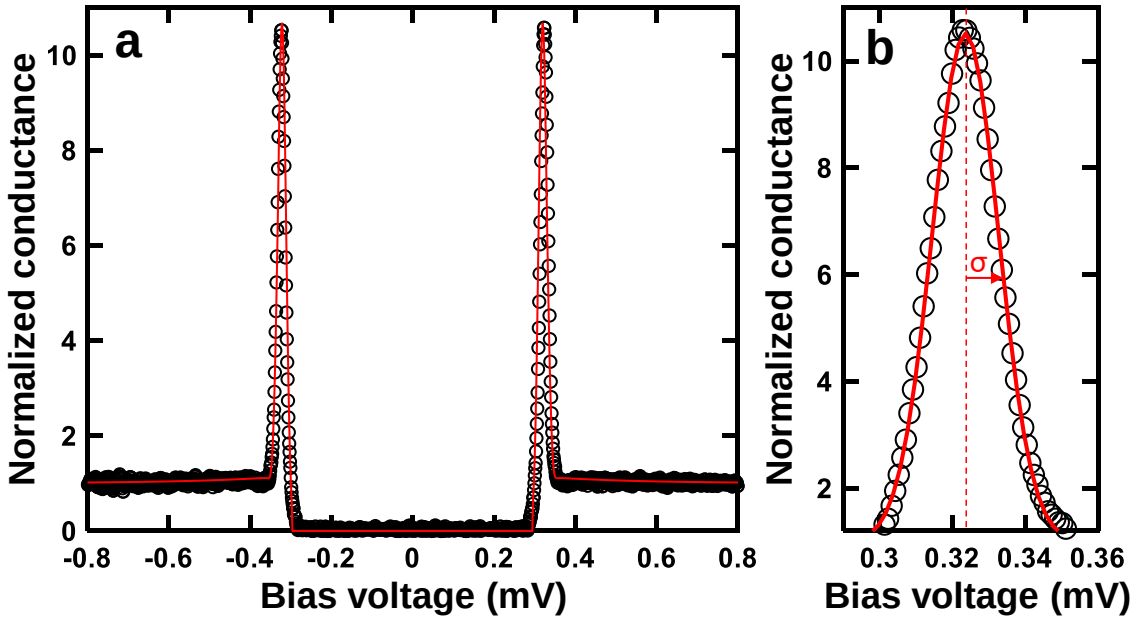

Figure 2.20: (a) Normalized tunneling conductance curve measured in an aluminum sample using an aluminum tip. BCS fit using $\Delta = 161$ μV and T = 100 mK is plotted in red over the experimental points. (b) Zoom into one of the peaks together wit a gaussian fit of the data (red line). From the width at half maximum of the peak, we obtain a value of 9 μV for the energy resolution of the system.

smaller than twice the superconducting gap value, and it presents a jump at $|V| = 2\Delta$ that leads to a divergence in the conductance curves. In the case of aluminum, as the peak broadening effects caused by anisotropy or strong coupling can be neglected [78], the width of the peaks in the conductance curves gives us the energy resolution of the system. Figure 2.20a shows a measured tunneling conductance curve at 100 mK using an aluminum tip and an aluminum sample together with the corresponding BCS fit using $\Delta = 0.161$ meV as the gap value and T = 100 mK. To adjust the finite width of the peak in the conductance curve caused by the voltage noise, we used a gaussian distribution [49]. This way, the energy resolution is given by the σ width of the distribution (fig. 2.20b). We measured a 9 μV energy resolution for the system improving previous standards of the laboratory ($\sim$ 15 μV) and obtaining values better or comparable to literature [40, 67, 79, 80, 81, 82, 83, 84, 85, 86]. We achieve this energy resolution using a single filter that includes all the different cables (see fig. 2.15). Other systems use individual filters for each cable [79] but they do not obtain better values than ours.

2.3.4 Cryogenic sample and tip preparation

Our STM is designed in such a way that we can prepare the sample and the tip in a cryogenic vacuum environment. It has a macroscopic positioning system that allows for a controlled lateral displacement of the sample with respect to the tip. This system is described in [67]. The sample holder is mounted on top of a mobile piece that can slide over a track covered with alumina to reduce friction (see fig. 2.21). Using a Kevlar thread, this sliding piece is connected to a steel cable (piano string) that is soldered to a micrometric screw in the upper part of the cryostat. The movement of the sample holder is mechanically controlled by the tension applied to the piano string when moving the micrometric screw from the outside. The sliding piece is attached to the STM base using two copper-beryllium springs: one in the bottom part that keeps it over the rail, and a second one in the front to help the sample holder recover the rest position when the tension in the piano string is released. We use Kevlar threads to tie the STM to the copper supporting structure. This helps thermalization and keeps the microscope still when we move the micrometric screw. The whole installation and calibration of this system was performed during this thesis.

This positioning system brings several advantages for low temperature STM. First of all, unlike other macroscopic positioning methods that use piezoelectric materials, with this technique we can modify the position of the sample holder without heating the experiment. The micrometric screw allows to move the sample holder up to $\sim$ 5 mm in steps of several hundreds of nanometers. With this design we can access more than one sample in the same sample holder with no need to heat up the experiment and break the vacuum every time we wanted to change the sample. Besides, as the surfaces of a sample are not always perfect, we can explore different regions until we find the suitable one for our measurements.

But what is probably the most interesting feature of this particular design is that this mechanism we use to move the sample holder can also be used to cleave the

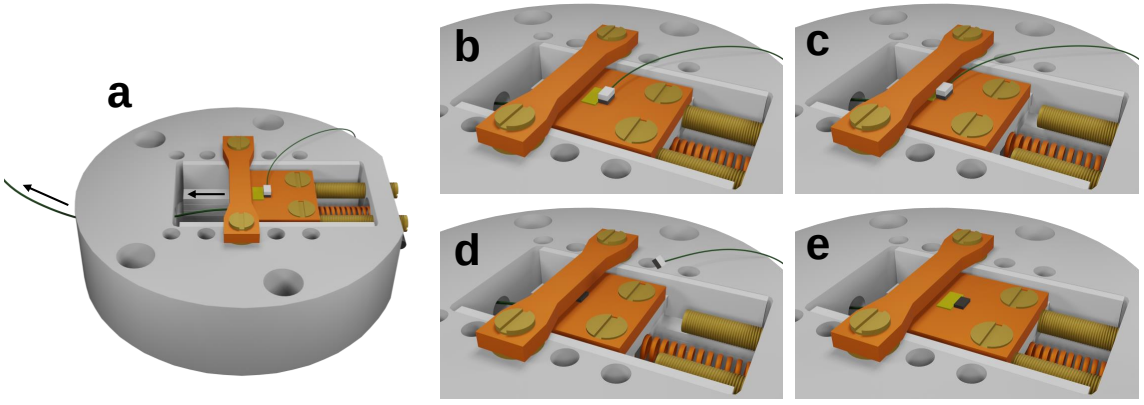

Figure 2.21: 3D illustration of the sample cleaving process. (a) Base part of the STM. The sample holder is mounted on a sliding piece that can be moved from the outside in the direction indicated by the arrows. A gold sample (yellow) and a layered sample (dark grey) are glued on top of the copper sample holder. A piece of alumina (white) is glued on top of the layered sample that is going to be exfoliated. The alumina is connected to a counterweight by a Kevlar thread. (b) The process begins with the sample holder at rest position. (c) The sample holder starts to slide and the alumina hits a copper bar that is placed across the sample holder track. (d) The sample breaks and the counterweight pulls the alumina out of the measuring zone. (e) The sample holder gets back to the initial position with a clean surface to measure.

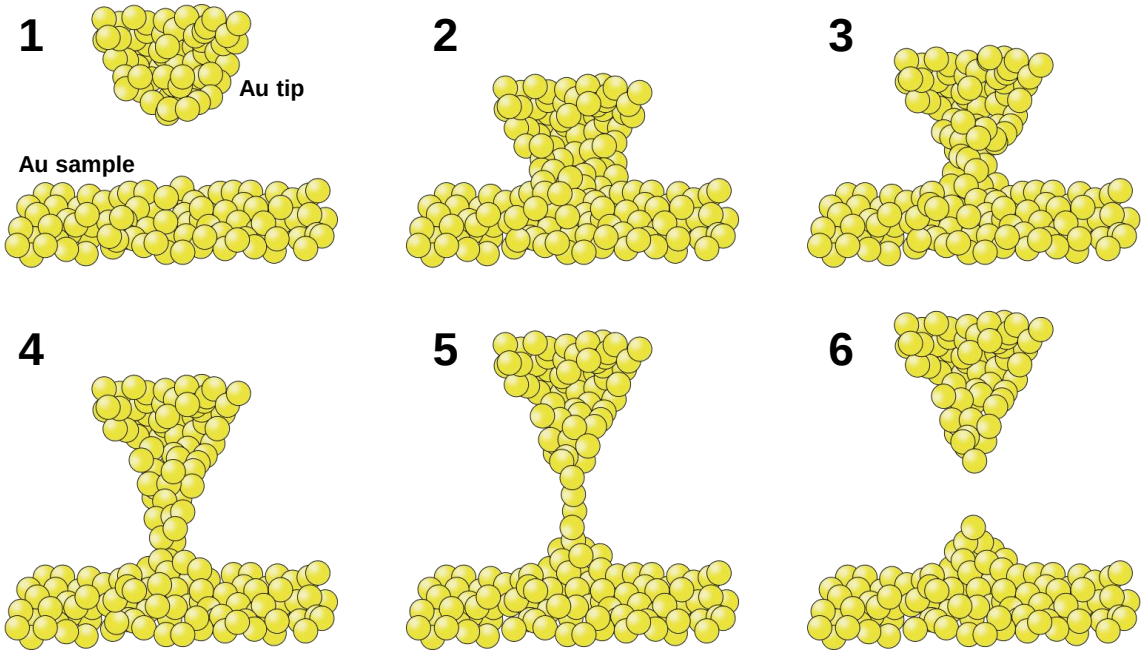

Figure 2.22: Schematic representation of the tip sharpening process. Each ball represents one Au atom. Starting from a separated configuration, the tip moves downwards until it crashes the sample. Then it goes back up and at some point the atomic contact is broken. The tip gets sharper with every iteration of the indentation loop 1-6 until it ends up being one atom wide.

samples *in situ* in cryogenic conditions. The cleaving process can be slightly different depending on the properties of the crystal to be cleaved. For layered samples we use an exfoliation method (see fig. 2.21). We mount the sample in the sample holder with a piece of alumina glued on top. We screw a copper bar across the sliding track that acts as a guillotine. It is important to adjust the height of the guillotine to make sure that everything but the alumina piece can pass below the bar. When the experiment is cold, we move the sample holder with the micrometric screw and the alumina crashes the guillotine. As the interlayer bonding of the sample is weaker than that between the alumina and the sample, provided by the glue, the sample gets exfoliated leaving a clean surface to explore. To avoid eventual blocks in the track on the way back of the sample holder, we glue a counterweight to the alumina to get rid of the exfoliated part of the sample. This exfoliation method was used to cleave the WTe_2 and FeSe samples we measured in this thesis (see chapter 4 and chapter 6, respectively). For harder crystals we can replace the guillotine with a ceramic blade to directly cut the sample in cryogenic conditions as we did in the cleaving process of Rh-doped $CeRu_2Si_2$ or in Au_2Pb (see chapter 3 and chapter 5, respectively).

The tip can also be refined at low temperatures at any stage of the experiment. We use a 0.5 mm diameter metallic filament as a tip. In all the measurements presented in this thesis we use either Au or Pb for the tip, as they present the proper mechanical properties to obtain sharpen apexes after the low temperatures tip fabrication process. The metallic filament is glued to a M1 screw using conducting silver epoxy. This screw fits into a nut that is fixed to the free edge of the piezotube. Before cooling down, we pre-sharpen the tip making a diagonal cut with some scissors.

The procedure we follow to sharpen the tip at low temperatures and cryogenic vacuum using the STM control unit is described in Ref. [75]. For this method to work, apart from the sample of the material of interest, we need to mount a sample of the same material of the tip. Once the experiment is at low temperatures, we use the positioning system described above top place the tip over the sample of its same material. In this configuration, the control feedback loop is disconnected and we send a voltage to the electrode Z of the piezotube to approach the tip towards the sample. When they reach contact, we send small voltage ramps to piezo Z to repeatedly crash and separate the tip from the sample. This process removes any eventual oxide layer from the tip apex, and after several nanoindentation cycles, we achieve single atom point contacts as sketched in fig. 2.22.

2.4 Software

STM control electronics is governed by a computer software that manages all the signals going to and coming from the experiment. This software is used to program the specific measurements and collect and save the measured data. During this thesis, I implemented a new digital USB based electronics system different from the previous analog one used in our lab. These new standards required us to develop

new data acquisition software capable to handle all the digital signals through an USB port [39]. On the other hand, data processing software is needed to treat all the collected raw data and generate the different images and maps to analyze the spectroscopic measurements. The new electronics we set up brought the opportunity to perform larger spectroscopic surveys (more number of points in both topography and spectroscopic curves) in less amount of time. However, the generated files were too heavy (several gigabyte) and the already existing analysis programs became obsolete. Hence, I led the development of a new data treatment software to deal with these big files in a more efficient way [39]. This program also includes some useful tools to analyze the generated images in both real and Fourier space. In the following lines, I will describe the basics of the data acquisition and data processing software we developed during this thesis.

2.4.1 Data acquisition

The digital electronics unit we used is the LHA-Digimod model from Segainvex [45]. Digital to analog (DAC) modules provide voltage signals from −10 V to +10 V with 16 bit resolution (2^{16} points), what results in a resolution in voltage of 0.3 mV. The electronics is connected to the measuring computer through an USB port and it has high voltage amplifiers we use for the signals of the piezos. The data acquisition software that controls the electronics was developed in a Pascal programming environment called Delphi [87]. As sketched in the block diagram of fig. 2.23, the program provides all the tools required to scan over the sample to acquire topographic images. It also manages all the procedures to take single spectroscopic curves. Thus, combining these two features, this software allows us to perform scanning tunneling spectroscopic (STS) studies with full control of all the different parameters.

The scanner module includes an interactive window that controls the position of the tip over the sample and shows the size of the scan, that can be modified before the scanning starts (see screenshots in fig. 2.24). When double-clicking at any point of the window, the program will send the voltage signals to the piezos X and Y to position the tip at that specific location. The speed of the tip when changing its position can be adjusted by the user. The program includes a digital PID algorithm that adjust the voltage value sent to piezo Z to keep the current constant along the scan to acquire topographic images in constant current mode. Proportional (P), integral (I), and differential (D) parameters as well as the setpoint current can be tuned by the user, and the PID feedback loop can be connected or disconnected at any time. The program also offers the possibility to change between x and y for the fast scan direction. While the scan is running, the topographic profile is displayed in real time. There is also a live preview of forth and back topographic images as they are being acquired. After the scan finishes, the topography can be saved in WSxM format [88] and pasted over the scanning window of the scanner module.

To do spectroscopic curves, the program disconnects the PID loop and stores the value of tunneling current as it ramps the bias voltage from $+V_{bias}$ to $-V_{bias}$ and back to $+V_{bias}$. The number of points and the speed of the ramps can be modified using

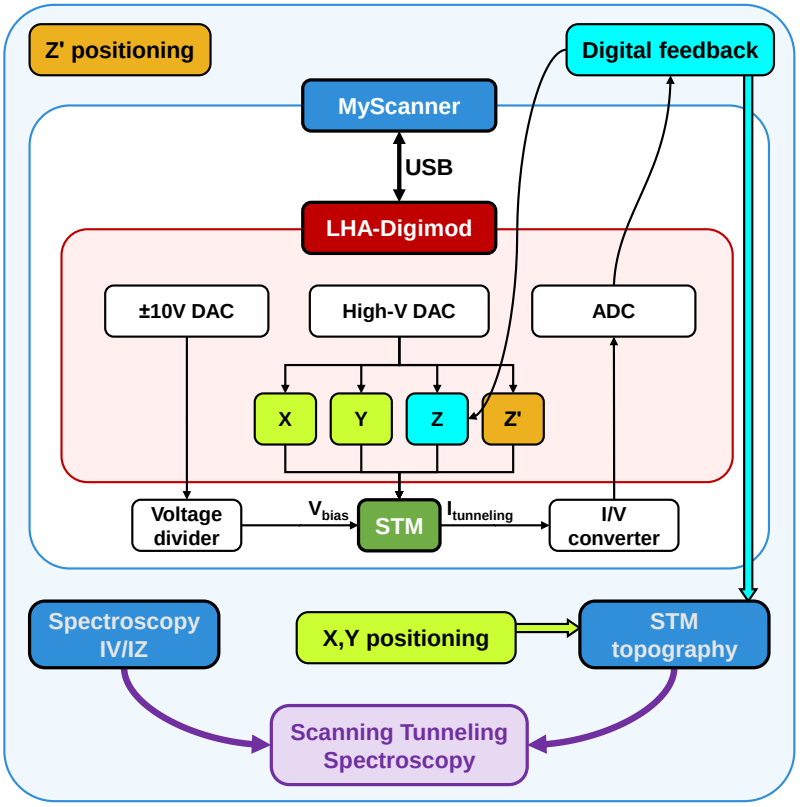

Figure 2.23: Block diagram of the different operations of the data acquisition software and its communication with the digital electronics. There is a coarse positioning module ($Z^{'}$ positioning), a spectroscopic module to take current versus voltage, or current versus distance curves (Spectroscopy IV/IZ) and an image module (STM topography). The program controls the electronics (red box) through a USB controlled interface called LHA-Digimod. The STM setup, with the piezotube, approach system, tip and sample, is indicated by the dark green box. Some additional equipment as the voltage divider and the current to voltage converter are indicated in white boxes. The digital feedback module, schematically shown in light blue, runs to maintain a constant current during operation, fed by the current measurement and acting on the piezo Z. The signal sent to the piezo Z is used to trace the STM topography.

different sliders. This process results in two separated IV curves (forth and back) that can be saved into a binary file. This software offers the possibility of averaging the current measurements from several voltage ramps to build the current versus voltage curve. To keep the same starting conditions for all the averaged curves, the feedback loop is connected and disconnected again between two consecutive ramps. The user can also change the time the feedback is controlling between the ramps. After measuring an IV curve, the program can calculate in real time and plot the derivative of the current versus the voltage. This feature turns to be very useful and it optimizes the experimental time as no external software is needed for a preview of the tunneling conductance. Instead of ramping the bias voltage, similar voltage ramps can be sent to piezo Z recording the value of the current as the height of the tip over the sample varies (IZ curves). This way the program can control, for instance, the indentation process we described in the previous section for tip

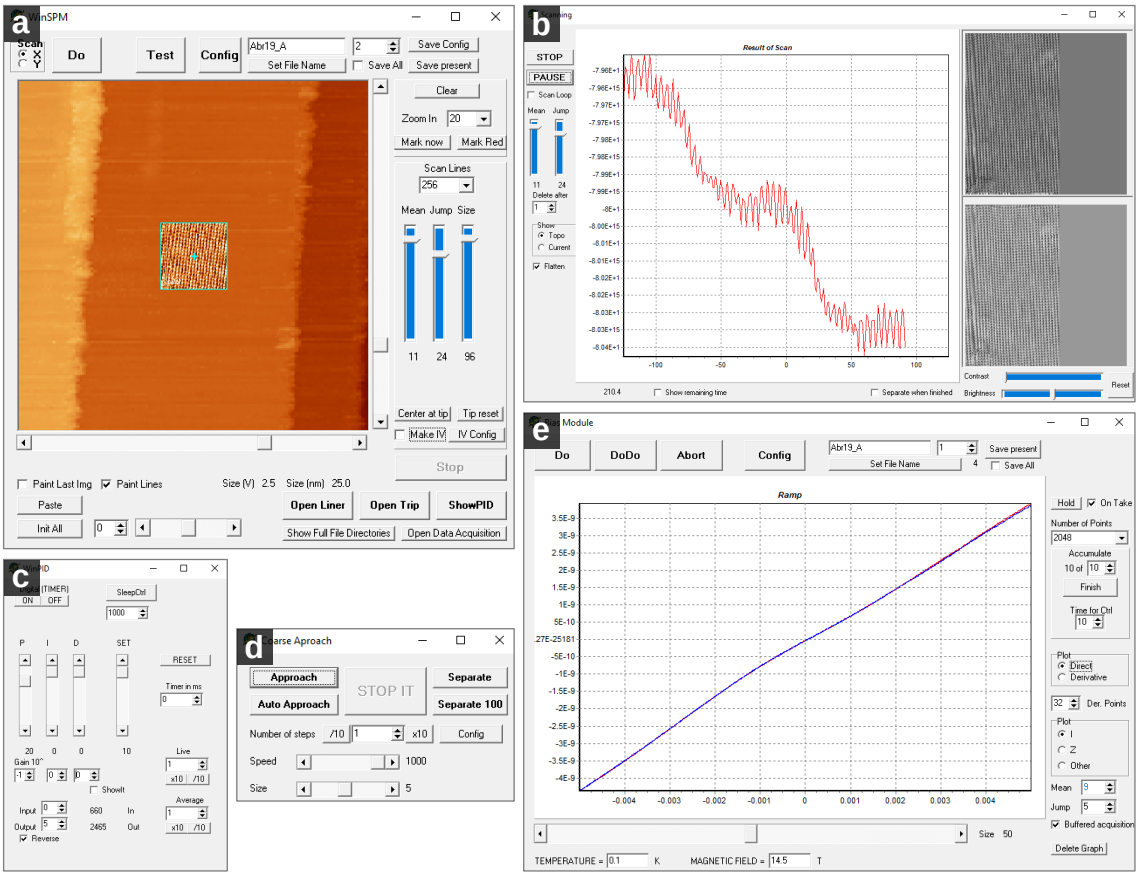

Figure 2.24: Screenshots from the data acquisition software. (a) Scanner interface. Blue cross and blue square mark the position of the tip and the scanning size, respectively. Acquired images depicting terraces and an atomically resolved area are pasted in the background. Data were obtained on FeSe at 100 mK and at a magnetic field of 14.5 T with a bias voltage of 5 mV and a tunneling current of 4 nA. (b) Interface for the live preview of the scan. The central panel shows the live tip height profile and the progress of topographic images made by scanning on the $\pm y$ directions is shown in the right panels. (c) Digital PID feedback interface window. (d) Coarse vertical movement (Z′) control window. (e) Curve acquisition interface showing the current versus voltage as blue and red lines.

sharpening purposes. This method can also be used to measure the quantum of conductance as I discussed in section 2.3.3.

One of the main advantages of using a USB data acquisition system is that it becomes much easier to keep low electronic noise levels. Besides, as it is the most extended protocol regarding digital data transfer, there are plenty of accessible devices and solutions in the market. However, when implementing USB communication routines we had to deal with the associated latency issues. Adapting the USB latency to that of the operating system of the measuring computer is specially important in our case, as the data acquisition software we developed is constantly sending and receiving data through the USB port to maintain the feedback loop operative. To face this intrinsic problem, we exploited the power of USB data buffers when coding our program. USB protocol allows us

to send several orders in packages with no need to wait until the receipt of the answer to each order before sending the next one. Thus, making use of this data buffering, we manage not only to avoid eventual latency issues, but we can also significantly speed up the spectroscopy acquisition process. In fact, we can reduce the acquisition time by more than a factor 10, what becomes specially important when performing large spectroscopic studies. Nevertheless, the use of the USB buffers can be disabled in the program to recover the point by point method.

Combining scanning and spectroscopic tools, the software is capable to perform STS measurements. For that, the tip stops at every pixel of the topography as it scans over the sample, the PID loop is disconnected, and an spectroscopic IV curve is taken before reconnecting the feedback loop and moving to the next point of the scan. The result of the STS measurement is a file with a matrix of points containing the topographic information, and a binary file with all the spectroscopic IV curves. Normally, the program takes four spectroscopic curves at each point of the topography (forth and back in the scan and forth and back in the IV curve). However, spectroscopic curves acquisition can be disabled for either forth or back topography scans to reduce even more the time of the measurements.

Finally, the software incorporates another module to control the coarse vertical movement of the tip over the sample sending sawtooth voltage signals to Z' piezostacks (see section 2.3.2). The program controls the size and speed of the ramps as well as the number of steps. It includes an *autoapproach* function that moves the tip towards the sample until the program detects a current value above a certain threshold. This way we can reach tunneling regime in a controlled way from a separated configuration.

2.4.2 Calculation of images and their treatment

Analyzing STS data we have to deal with two separated files: a 2D matrix with the topographic information, and a binary file containing all the spectroscopic curves obtained along the scanning with no spatial information. It is then necessary to reorganize the spectroscopic data assigning a local position to each curve so that for a given energy (bias voltage) and a given location in the topography we can read just one current value. We used MATLAB environment [89] to develop this software taking advantage of some built-in functions as well as the *app designer* tool for the graphic user interface.

The program is capable of reading raw binary files and generating the conductance matrices needed for further analysis. After this reading process, the program uses these matrices to produce real and reciprocal space images providing different tools to treat them and extract the desired information. As shown in the block diagram of fig. 2.25, the STS analysis unit of the program consists of a reading module and an image processing module that can work independently from each other. Thus, one can use this software just to read binary current versus voltage files and convert them into 2D matrices, but one can also input the program some previously generated 2D matrices and directly enter the image processing part.

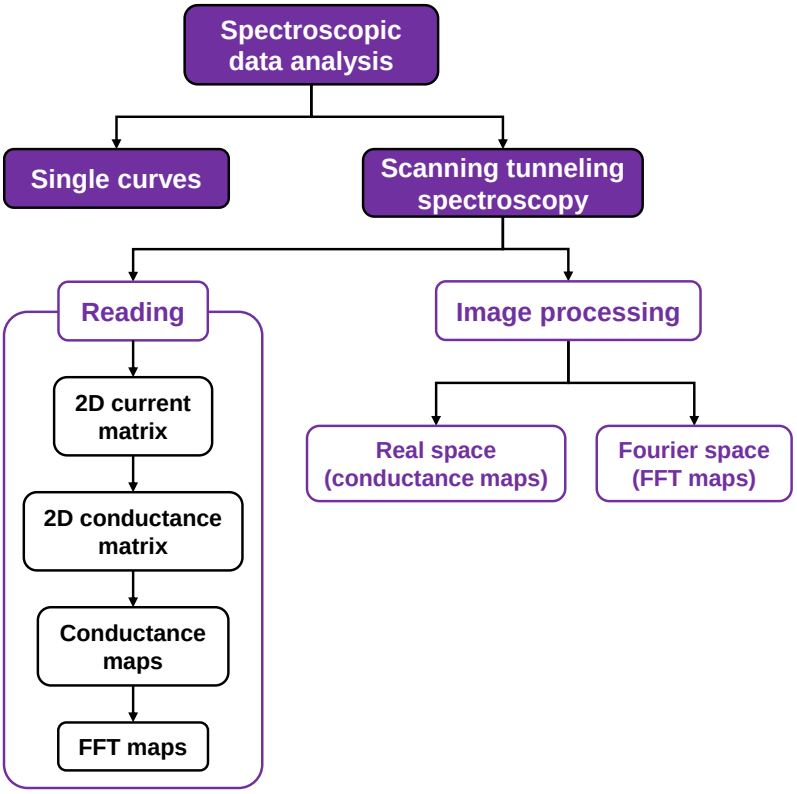

Figure 2.25: Block diagram of the data analysis software. The data are stored in a binary file with the required headers to return image size, position, etc. There is a curve reading module (Single curves) which allows rendering the data and performing basic operations to understand tunneling current curves, such as derivation, temperature deconvolution and plots including many curves. The spectroscopy module (Scanning tunneling spectroscopy) is separated into a reading module (Reading) which creates current and conductance matrices, and from these, conductance and Fourier transform maps at given bias voltage values. The image processing module (Image processing) allows rendering the images in a user friendly manner and making different operations required to understand real and Fourier space images.

Reading module

The reading module needs two main inputs: the N by M dimensions of the topographic image and the corresponding binary file containing the associated spectroscopic curves. As described above, typical spectroscopic techniques take curves in both forth and back directions of the topography scan, and these curves record current data ramping forth and back in bias voltage. Therefore, we will have four different curves for every pixel of the topography, and the total number of curves in the binary file will be $4 \times N \times M$. If there are more than $4 \times N \times M$ curves in the file, the program will use by default the first $4 \times N \times M$ ones, but the user will be able to choose a different starting point. The program gives the option to select which of those four curves will be used to average the tunneling current value at each pixel. The number of rows (N) and columns (M) is read from the size of the topographic image, but the user is also allowed to change those values.

At the beginning of a new analysis, the program asks for the real size of the image and the value of the lattice parameters to generate well defined units in real and reciprocal space.

Although our binary file contains the tunneling current data, the important magnitude for the spectroscopic analysis is the tunneling conductance, that can be obtained by numerically differentiating the current versus voltage curves. The derivatives are made following a least square approach to the finite difference method [90]. The program counts with an interface where the user can modify the number of derivative points used, correct any offset in the voltage and visualize the resulting conductance curves (fig. 2.26b). These curves can also be normalized by the average conductance value inside a certain voltage range to correct for the setpoint effect as we described in section 2.1.3.

Once the conductance curves have been generated, the program organizes them in N by M conductance maps for different energies (bias voltages) so that the value of the pixel (n, m) of a conductance map comes from the spectroscopic curve taken at the pixel (n, m) in the topographic image. The user introduces the range of voltage of the maps, the voltage step between two consecutive maps and a small voltage range, $\delta(V)$, within which conductance values are averaged. As an example, if the user choose to show conductance maps from −10 mV to +10 mV in steps of 2 mV with $\delta(V) = 0.5$ mV, the number of generated maps will be 11, and the conductance value at each pixel inside each map will be computed by averaging ±0.25 mV around the voltage value of each map. The resulting conductance maps are shown in a different interface together with their 2D fast Fourier transform (FFT). If the previewed results are satisfactory, the data can be saved into a structure object that stores all the variables needed for a further image processing analysis.

Image processing module

The image processing module provides a series of useful tools to modify the conductance maps in real space and their corresponding FFT in reciprocal space, but once the different matrices have been generated, they can be freely transformed using any available software. First thing the programs offers is the opportunity to cut the conductance maps introducing starting and final values for the rows and columns to focus the analysis in a specific region. FFTs are automatically recalculated after the cutting process, but the program allows to recalculate them at any point after any modification to the conductance maps.

Real and reciprocal space maps are analyzed separately. The program counts with a live viewer where the user can see in real time the adjustments introduced to the maps (fig. 2.26c,d). Previewed maps can be copied to the clipboard as a raster image or as a vector object using the built-in MATLAB tools. The user can choose among several preset colormaps, and the contrast of the images can be controlled using two sliders. It can be saved individually for each energy. Single spectroscopic curves can be accessed by mouse-clicking in different points of the maps in the viewer, and by click-and-dragging over the maps, the averaged curve inside the selected region

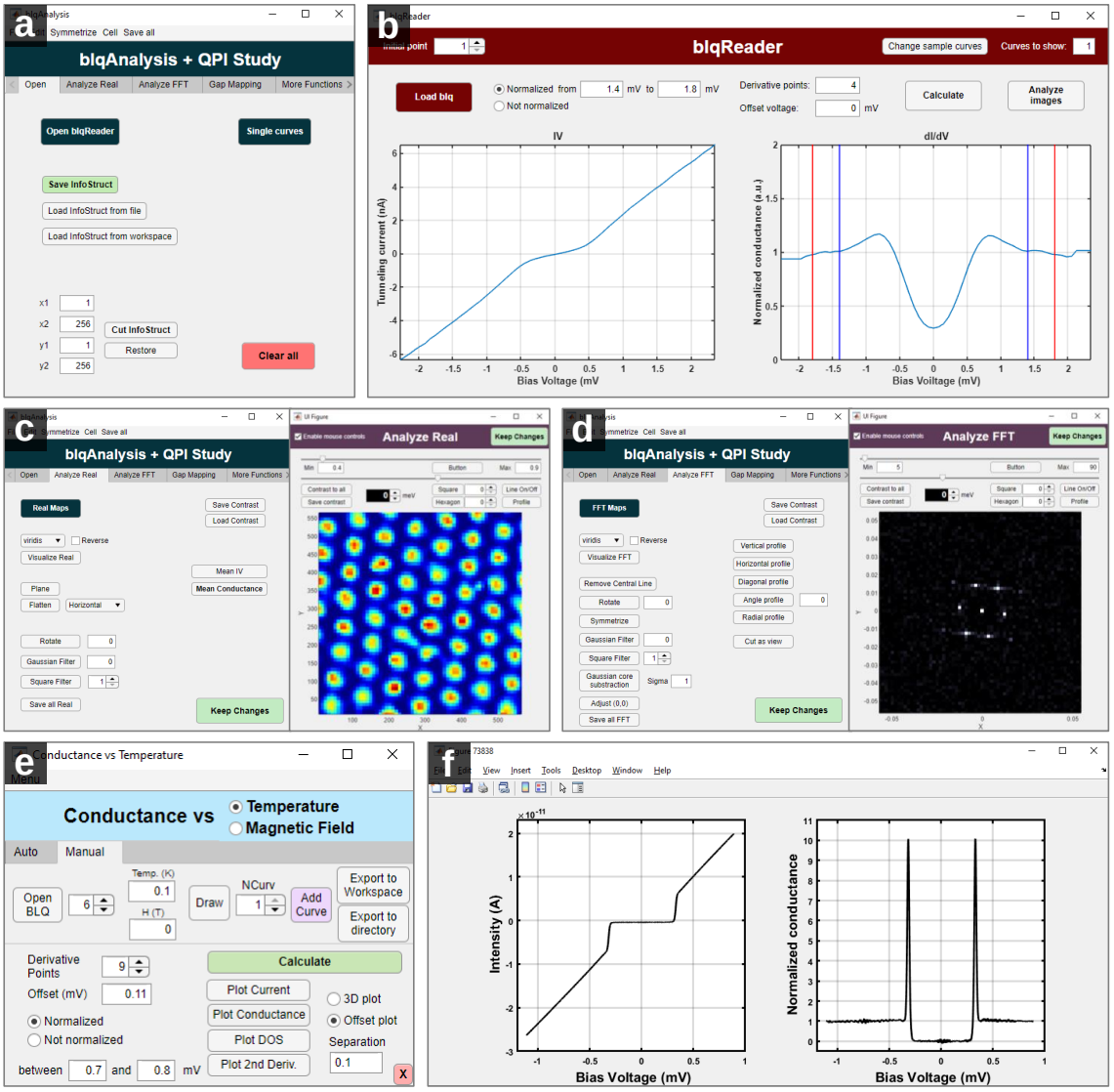

Figure 2.26: Screenshots from the data analysis software. (a) Main window of the program with the different modules separated in menu items. (b) Conductance curves calculation window showing the superconducting gap at a magnetic field of 0.1 T obtained in β-Bi_2Pd as blue lines. (c) Conductance maps visualization window showing an image of the vortex lattice of in β-Bi_2Pd obtained from the zero bias conductance map. (d) Window showing the Fourier transform of the image in (c). A number of operations can be performed on the Fourier transform, like rotating, filtering, symmetrizing, etc. (e) Main window to plot and make calculations on tunneling current and tunneling conductance vs bias voltage curves. (f) Tunneling current (left panel) and tunneling conductance (right panel) obtained using Al tip and sample below 100 mK.

is displayed. The averaged current versus voltage and conductance versus voltage curves in the whole image can be shown by pushing the corresponding buttons in the real space tab of the main window of the program. Real space maps can be rotated a certain angle and gaussian-filters with a certain width σ can also be applied.

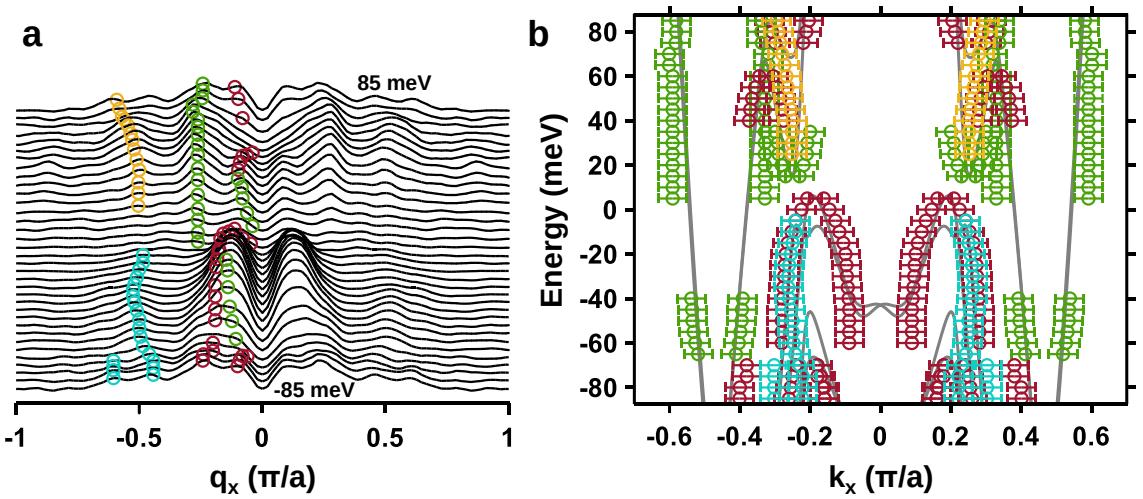

Figure 2.27: Peak tracking example showing one of the QPI measurements we performed in WTe_2 (see chapter 4). (a) $q_y = 0$ profiles of the FFT of the conductance maps along the q_x-direction inside the first Brillouin zone for all the energies of the study (black lines). Colored circles mark the main peaks we observe. (b) Measured $\vec{q}$ vectors in (a) are plotted as colored circles with error bars reconstructing the band structure. Calculated bulk band structure is shown in grey in the background.

Custom profiles can be calculated by positioning a line over the maps in the viewer. The resulting graph will plot the conductance in the z-axis as a function of the energy and the distance along the mentioned line. If the profile is performed in reciprocal space, the FFT amplitude will be plotted as a function of the energy and the k-distance.

Regarding superconducting data, the analysis software counts with some specific tools to calculate and plot the size of the superconducting gap along the image. As for the study of vortices, conductance maps at energies smaller than the gap will provide the contrast needed to observe the vortex lattice. Once the vortex images are generated, we can apply vortex identification and triangulation procedures also developed in our group for a deeper analysis of the vortex lattice [68].

Reciprocal space analysis usually requires more sophisticated operations to extract the needed information from techniques like QPI. FFT tab inside the program offers some specific analysis options for these purposes. First of all, the program allows to remove the unwanted central lines in the vertical and horizontal directions that sometimes appear after Fourier transforming the real space maps. To reduce the noise in FFT maps it is convenient to symmetrize the reciprocal space maps following the symmetry of the crystal lattice. For this matter, as we discussed in section 2.1.4, the user can first rotate the FFT maps to align the crystallographic directions with the vertical and horizontal axes, and then apply the corresponding symmetry transformation. The predefined symmetry operations in the program are a single mirror, a double mirror in two perpendicular directions, and a rigorous 4-fold or 6-fold symmetry, but higher order symmetry operations can be manually applied as well. The FFT tab includes an $n \times n$ pixel averaging filter function to further increase the signal to noise ratio, as well as a Gaussian core subtraction routine

that reduces the intensity at the smallest wavevectors to increase the contrast of the images. Warp correction is also available for minor tweaks if needed. As in the case of real space analysis, FFT images can be gaussian-filtered. Besides, the viewer can instantly alternate between showing the maps just inside the first Brillouin zone (1BZ) and the whole range in k.

Profiles along the main symmetry directions are also accessible in the FFT tab. The user can ask for profiles along the vertical, horizontal and diagonal direction, as well as a radial profile. The result of these operations is a 2D mapping of the FFT amplitude as a function of the energy and the reciprocal space distance along the selected direction. These images provide very useful visual information for QPI analysis. Applying the peak tracking function of the program to these profiles we can follow the position of the main scattering vectors for different energies and plot the reconstructed band structure along the particular direction of the selected profile. Figure 2.27a shows as black lines the $q_y = 0$ profiles extrated from QPI measuremets in WTe_2 (see chapter 4). From the energy evolution of the different peaks we observe (colored circles) we can reconstruct the band structure of the material (fig. 2.27b).

Finally, apart from the STS processing tools, the program includes a single curves analysis unit that differentiates, normalizes and corrects the offset of individual spectroscopic curves (fig. 2.26e,f). This unit counts as well with some algorithms to calculate the density of states versus energy curves by deconvoluting the effects of the temperature of the measurement from the conductance curve of normal-superconducting (N-S) or superconducting-superconducting (S-S) junctions. Single curves can be stored with tagged temperature and magnetic field values, and automated functions inside the program can generate miscellaneous plots including the calculated conductance, density of states or second derivative of the curves at different temperatures or magnetic fields.

3

Magnetic correlations and quantum criticality in Rh-doped $CeRu_2Si_2$

3.1 Magnetism and heavy fermions

Heavy fermion systems are often compounds which include a rare earth and lighter elements of the periodic table. The hybridization between localized $4f$ or $5f$ electrons of the rare earth and the s, p or d conduction electrons of the lighter elements can sometimes lead to metals whose electrons have very large effective masses and small Fermi velocities. Heavy fermion compounds are of great interest in the frame of this thesis because of two relevant aspects. First, they often present magnetic order related to incomplete f-electron shells. Second, their high effective masses result in an anomalously large electronic entropy conserved at very low temperatures which leads to huge Grüneisen parameters. As a consequence, slightly modifying a tuning parameter by doping, magnetic field or pressure, for example, modifies the ground state.

Here, we are particularly interested on the phenomenon of the disappearance of antiferromagnetism, which is often related to the appearance of superconductivity. We studied the changes in the antiferromagnetic properties in a system that has no superconductivity at all. Thus, we can directly access the band structure modifications related to magnetic properties without any superconducting gap opening. The hope is that the achieved understanding will also help better understand situations that lead to the appearance of superconductivity. As we shall see, the result is that we have identified the features in the tunneling conductance which can be directly associated to magnetism and followed their evolution with the magnetic field. All this occurs in an extremely small energy range, of just a few meV, which makes the system very sensitive to the magnetic field through the Zeeman shift of the band structure.

The ground state in a heavy fermion system is typically antiferromagnetic, and upon pressure, the system enters a paramagnetic phase in which electronic properties follow the Fermi liquid picture. These two phases are separated by a

zero temperature phase transition at the so-called quantum critical point (QCP). In some heavy fermion compounds, an unconventional superconducting dome emerges around the QCP. High-T_c superconductivity in cuprates and pnictides appears close to an antiferromagnetic phase as well (see section 1.3.1), and some of the phases in twisted bilayer graphene might also present magnetic properties. Therefore, understanding the origin of these magnetic phases, in particular antiferromagnetism, and how they can be considerably modified by applying a magnetic field, is key to explain such a complex collective phenomenon as unconventional superconductivity.

Antiferromagnetism is intriguing because it can arise in different ways, many of which are related to an exchange interaction between magnetic moments and conduction electrons. For instance, the oscillatory nature of Bloch functions leads to a form of the exchange interaction that changes sign at certain distances, inducing antiferromagnetic order. This occurs in Cr, which is the prototypical antiferromagnet. There, antiferromagnetism arises because there are portions of the Fermi surface which are parallel to each other [91, 92]. This favors antiferromagnetic indirect Ruderman-Kittel-Kasuya-Yosida (RKKY) interactions with a $\vec{q}$ wavevector connecting the two parallel surfaces (see left inset in fig. 3.1). Thus, there is a spin density wave with a wavevector that coincides exactly with the Fermi wavevector connecting the two parallel regions, and a gap opens in the band structure at the nesting wavevector producing a peak in the resistivity [91, 93].

There is yet another situation caused by superexchange, a virtual process by which an electron or hole leaves the ion and is replaced by an electron or hole of opposite spin [94]. When superexchange occurs in a system with highly localized magnetic states, like a few isolated f-electron ions, in coexistence with conduction electrons from a solid of non-f-electron ions, it leads to the Kondo interaction [95]. The Kondo interaction results in kind of a local antiferromgnetism in the sense that it creates a cloud of conduction electrons around the magnetic impurity with opposite spin to that of the localized magnetic moment (see bottom-right inset in fig. 3.1).

Figure 3.1 shows the Doniach diagram summarizing these two aspects and showing how they compete with each other [96]. The temperature of the Kondo interaction depends exponentially on the product of the exchange energy, J, and the density of states, N. On the other hand, the RKKY temperature goes as $J^2 \times N$. We find thus two ground states as a function of J, separated by a zero temperature phase transition at a quantum critical point. One in which the RKKY interaction dominates the Kondo interaction and the system shows RKKY induced antiferromagnetic order, and another one where we find Kondo screened magnetic moments.

The most intriguing features occur in systems which have an f-electron element in each unit cell. In 1977, S. Doniach proposed that heavy electron metals can be understood as Kondo lattices where every single local magnetic moment in the lattice is Kondo screened by the conduction electrons sea [97]. In a situation like this, the behavior is neither that of Cr with the RKKY spin density wave, nor that of isolated magnetic impurities in a simple metal with the Kondo interaction. It

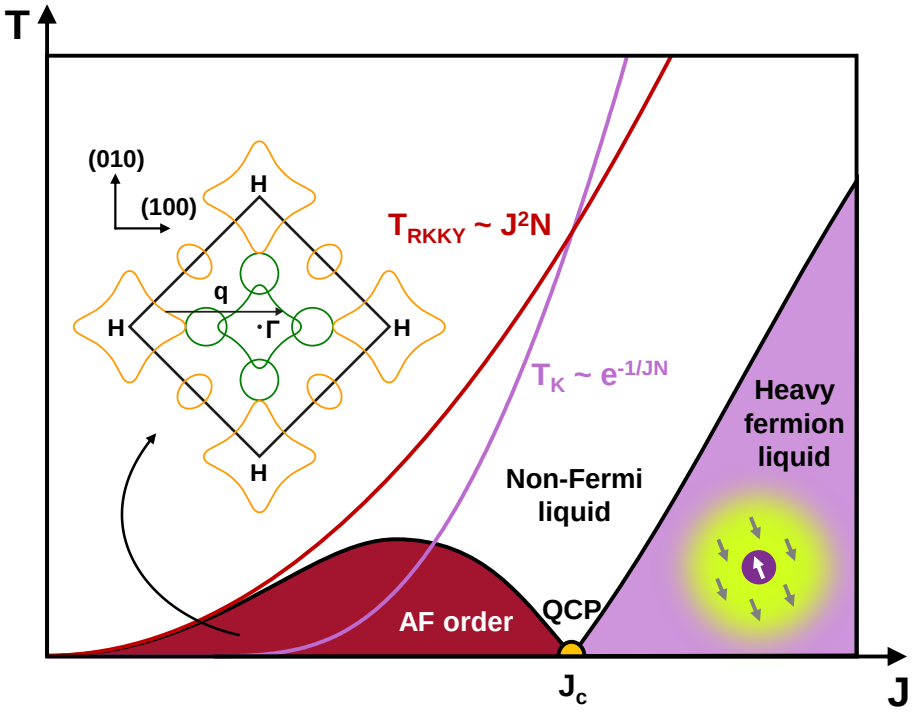

Figure 3.1: Doniach diagram showing the competition between RKKY interaction and Kondo screening in the temperature versus exchange interaction, J, plane. There are two ground states, an antiferromagnetic and a Kondo state, separated by a zero temperature phase transition at the quantum critical point. A non-Fermi liquid phase can arises in the vicinities of the quantum critical point. Left inset: Fermi surface in bulk Cr. Electron and hole pockets are represented by green and orange lines, respectively. Antiferromagnetism originates from the Fermi surface nesting due to the presence of parallel regions connected by the wavevector $\vec{q}$. Bottom-right inset: schematic representation of a local magnetic moment (purple) Kondo screened by the conduction electron (or hole) sea (yellow cloud around the magnetic impurity).

involves each and every electron in the system and one has to think of collective phenomena.

In a simplified picture, we can take an f-electron band and consider its hybridization with a light conduction electron band (see fig. 3.2). The result is a system where there are nearly flat bands in both the antiferromagnetic and the Kondo states. This system is known as a heavy fermion system, and it shows behaviors that are different from the simple spin density wave scenario and RKKY interactions. For instance, there is antiferromagnetism whose wavevector is not connected to any Fermi wavevector and there is no single ion Kondo effect. Instead, heavy fermions are typically good metals with high electron effective masses.

The central question in this debate, which I will address in this chapter, is how does such an antiferromagnet cease to exist, or to say it otherwise, how should we understand such an antiferromagnet: is antiferromagnetism a collective spin density wave phenomenon that disappears at the quantum phase transition, or do electronic correlations disappear with antiferromagnetism?

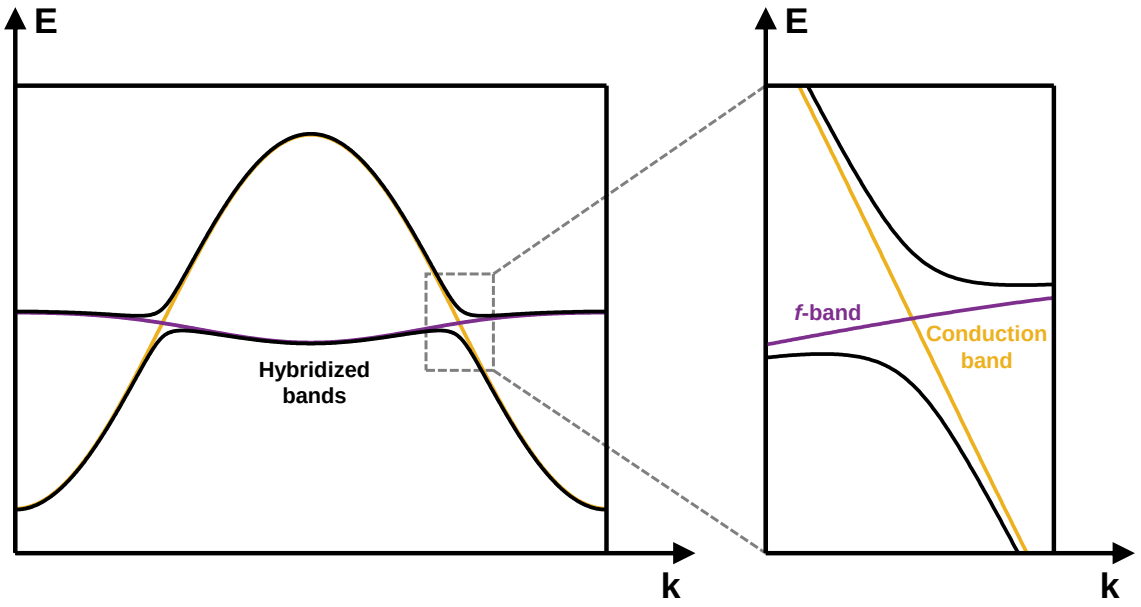

Figure 3.2: Scheme of the hybridization of the band structure in a Kondo lattice at low temperatures. The hybridization between the heavy f-band (purple) and the light conduction band (orange) results in the hybridized bands represented as solid black lines. Right panel shows a zoom into one of the contact points between the heavy and light bands.

To answer this question we need to visualize electronic states around the Fermi level making use of techniques like quasiparticle interference (see section 2.1.4). But before discussing our STM results in the heavy fermion $Ce(Ru_{0.92}Rh_{0.08})_2Si_2$, I will briefly review some singularities which are needed to understand STM experiments in heavy fermion systems.

3.1.1 Kondo tunneling

Tunneling into a single Kondo impurity

Let me start describing the situation of a single Kondo magnetic impurity on the surface of a normal metal. When a magnetic adatom lies on top of a metallic surface, at sufficiently low temperature, the antiferromagnetic exchange interaction between conduction electrons of the metal and the localized magnetic f-state on the Kondo impurity leads to a resonance close to the Fermi level (see fig. 3.3a). If we approach the STM tip to a surface like this, electrons from the tip find three different possibilities to tunnel into the sample. As sketched in fig. 3.3b, they can tunnel into the empty states of the bulk above the Fermi level of the metal with a probability t_1, directly into the Kondo resonance close to the Fermi level with a probability t_2 (this tunneling process is also known as cotunneling [98, 99]), or indirectly into the localized state of the magnetic adatom via spin-flip with a probability t_3. The tunneling current is determined by the quantum interference between the two first

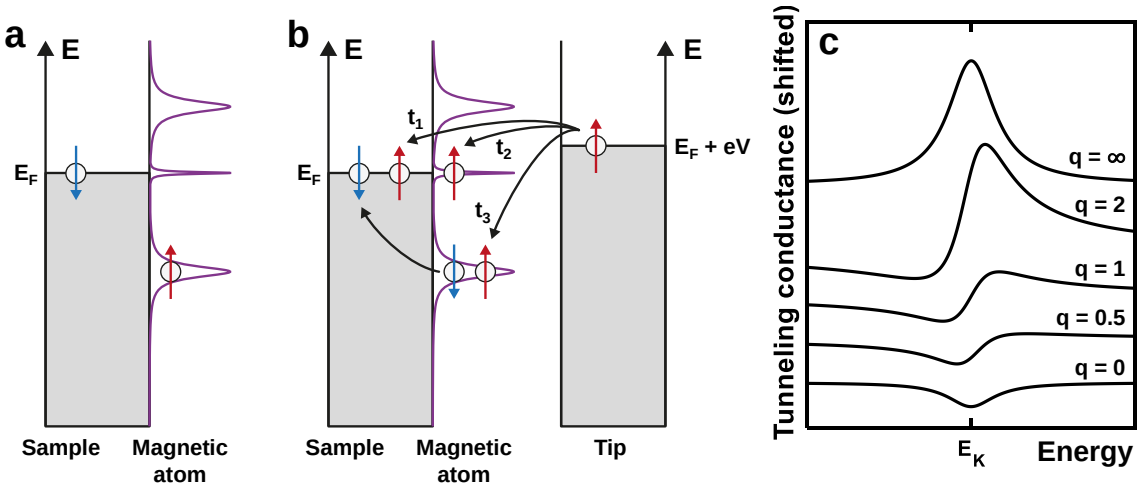

Figure 3.3: (a) Schematic representation of the electronic states in a metallic sample with a Kondo impurity. In addition to the two states of the magnetic atom below and above the Fermi level, a narrow Kondo resonance appears around E_F. (b) Diagram of the three available tunneling channels when approaching the STM tip. Electrons can tunnel to the empty states of the bulk (t_1), to the Kondo resonance (t_2) or to the localized magnetic state via spin-flip (t_3). Spin-up and spin-down states are depicted as red and blue arrows, respectively. (c) Expected shape for the tunneling conductance versus energy curves from eq. (3.1) for different values of the form factor q.

processes, which preserve the spin [100, 101]. The third tunneling channel does not interfere with the other two processes because of the spin flip.

The quantum interference between the two spin-preserving tunneling paths results in an energy spectrum, $\rho(E)$, described by the Fano equation [102]:

$$\rho(E) \propto \rho_0 + \frac{(q+\epsilon)^2}{1+\epsilon^2}, \tag{3.1}$$

where $\epsilon = E - E_0$, with E_0 being the energy position of the Kondo resonance, and the form factor $q \propto t_2/t_1$. Therefore, if we were to measure the tunneling conductance versus bias voltage in a system like this, we would obtain the Fano curves shown in fig. 3.3c with different shapes depending basically on the ratio between the two transmission probabilities, t_2 and t_1.

Tunneling into a Kondo lattice

The situation is a little more complex if instead of a single Kondo impurity we tunnel into a Kondo lattice. Here, the heavy f-band and the conduction band hybridize giving rise to the so-called hybridization energy range [103, 104]. Figure 3.4a illustrates the situation of a Kondo insulator, where the hybridization of the bands results in an absence of states at the Fermi level, and fig. 3.4b pictures the hybridization scheme of a Kondo metal. In both cases, if there is not much disorder, the hybridization energy range provides two sharp peaks located at the

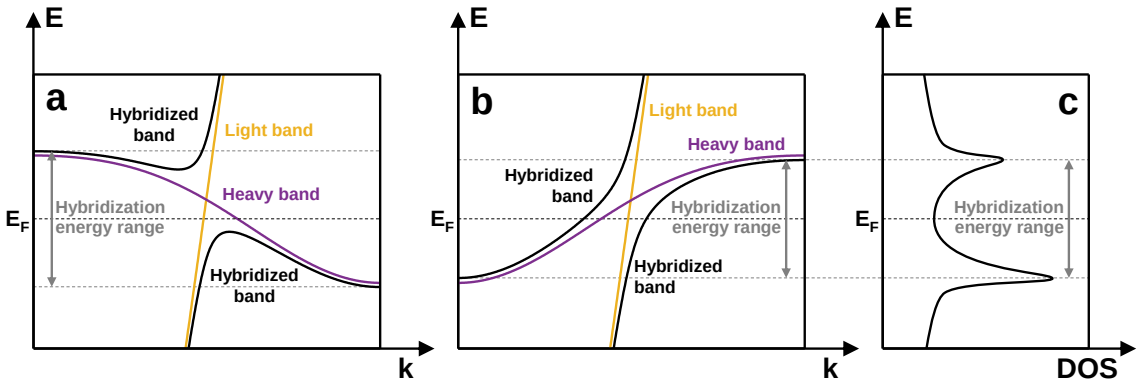

Figure 3.4: Schematic representation of the hybridization of the bands in a Kondo insulator (a) and in a Kondo metal (b). (c) Density of states versus energy expected from the hybridized band structure in (b) featuring two peaks at the energies where the bands are flatter.

energies where the hybridized bands are flatter and the density of states is thus higher (see fig. 3.4c).

This way, STM tunneling conductance versus bias voltage measured in a Kondo lattice feature two peaks inside the hybridization energy range, whose position is directly related to the energy position of the top and bottom of the hybridized bands. The hybridization energy range can be much smaller than that of the Fano resonance as I will discuss below in our STM results.

3.2 $Ce(Ru_{0.92}Rh_{0.08})_2Si_2$: phase diagram and surface characterization

To clarify the question I introduced above regarding antiferromagnetism and how it disappears, we have chosen a system where we have heavy fermions, disorder to produce scattering and study the band structure through QPI, and where we can go from an antiferromagnetic to a paramagnetic phase in a small field range. This system is the 8%-Rh-doped $CeRu_2Si_2$, which shows an antiferromagnetic to paramagnetic phase transition at 2.5 T. There are other compounds such as $YbRh_2Si_2$ which also show vanishing antiferromagnetism with magnetic field [105]. The associated energy scales are however much smaller than those of $Ce(Ru_{0.92}Rh_{0.08})_2Si_2$. For instance, at zero magnetic field, the Néel temperature (T_N) above which the antiferromagnetic phase vanishes in $YbRh_2Si_2$ is lower than 100 mK, what makes it experimentally very challenging to explore the different magnetic phases. In contrast, $Ce(Ru_{0.92}Rh_{0.08})_2Si_2$ shows much higher critical temperatures ($T_N(0\ \mathrm{T}) = 4.2$ K) and the intrinsic doping allows us to directly observe the electronic wavefunctions through QPI. It is important to note that ARPES cannot be used to address a problem like this that requires the application of a magnetic field and very low temperatures, and that other similar compounds

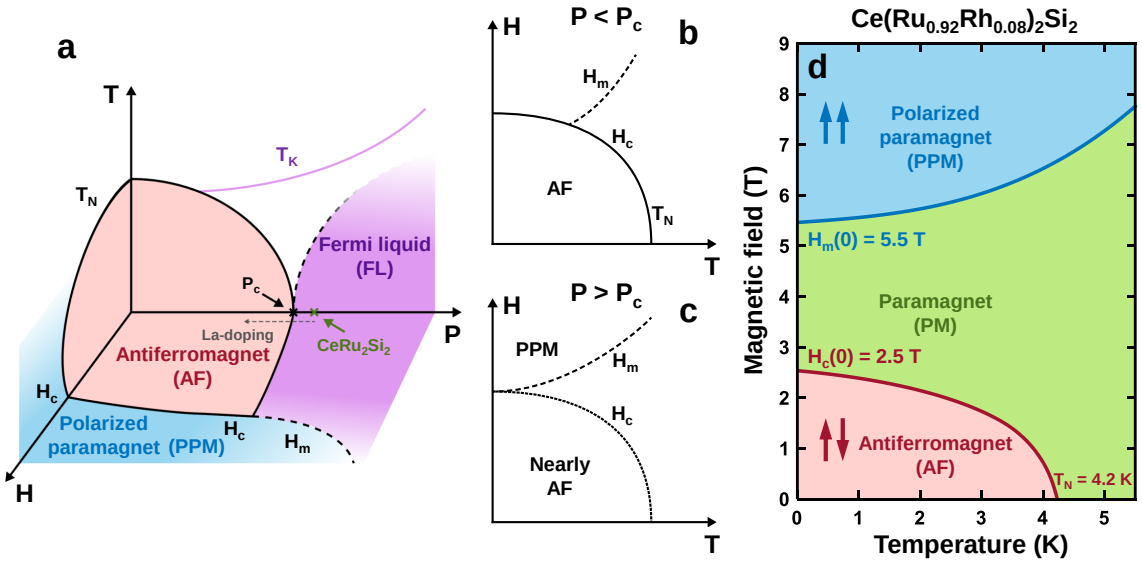

Figure 3.5: (a) Adapted from [106]. Magnetic field-pressure-temperature phase diagram in $CeRu_2Si_2$. (b) Magnetic field versus temperature $CeRu_2Si_2$ phase diagram for pressures below the critical pressure, P_c. The antiferromagnetic to paramagnetic transition at H_c is represented by a solid line. The dashed line marks the pseudo-metamagnetic transition at finite temperatures. (c) Same for pressures above P_c. Low field nearly antiferromagnetic phase and high field polarized paramagnetic phase are separated by a zero temperature transition. (c) Magnetic field versus temperature phase diagram of $Ce(Ru_{0.92}Rh_{0.08})_2Si_2$ showing the two clearly separated magnetic transitions at zero temperature.

require magnetic field or temperature ranges which are out of reach. Hence, working with $Ce(Ru_{0.92}Rh_{0.08})_2Si_2$ sets us in quite a unique and nice situation.

$CeRu_2Si_2$ is a very well known heavy fermion compound that displays different magnetic phases upon pressure and applied magnetic field. The stoichiometric compound displays a paramagnetic ground state that can be driven to an antiferromagnetic phase by applying a slightly negative pressure of a few kbar [107]. This can be achieved by La substitution on the Ce site. Figure 3.5a shows the magnetic field-pressure-temperature phase diagram for $CeRu_2Si_2$. The zero temperature phase transition between antiferromagnetic and paramagnetic states occurs at 7.5 % of La doping. Applying external magnetic field below the critical pressure, P_c, drives the system from an antiferromagnetic to a paramagnetic phase above the critical field $H_c(T)$. The strong interplay between antiferromagnetic and ferromagnetic correlations at H_c can lead to a highly polarized phase at high fields [108, 109].

Close to P_c, the antiferromagnetic and Kondo fluctuations become comparable and the phase transition at H_c is replaced by a so-called pseudo-metamagnetic crossover phenomena, H_m, that is identified by a strong enhancement of the effective mass, a decay in the field induced ferromagnetic fluctuations and a remarkable change in the Fermi surface [107, 108, 111, 112, 113, 114]. For pressures below P_c, the H_m crossover meets the $H_c(T)$ line at a finite temperature. In this situation, at lower temperatures there is an antiferromagnetic to paramagnetic first order metamagnetic transition

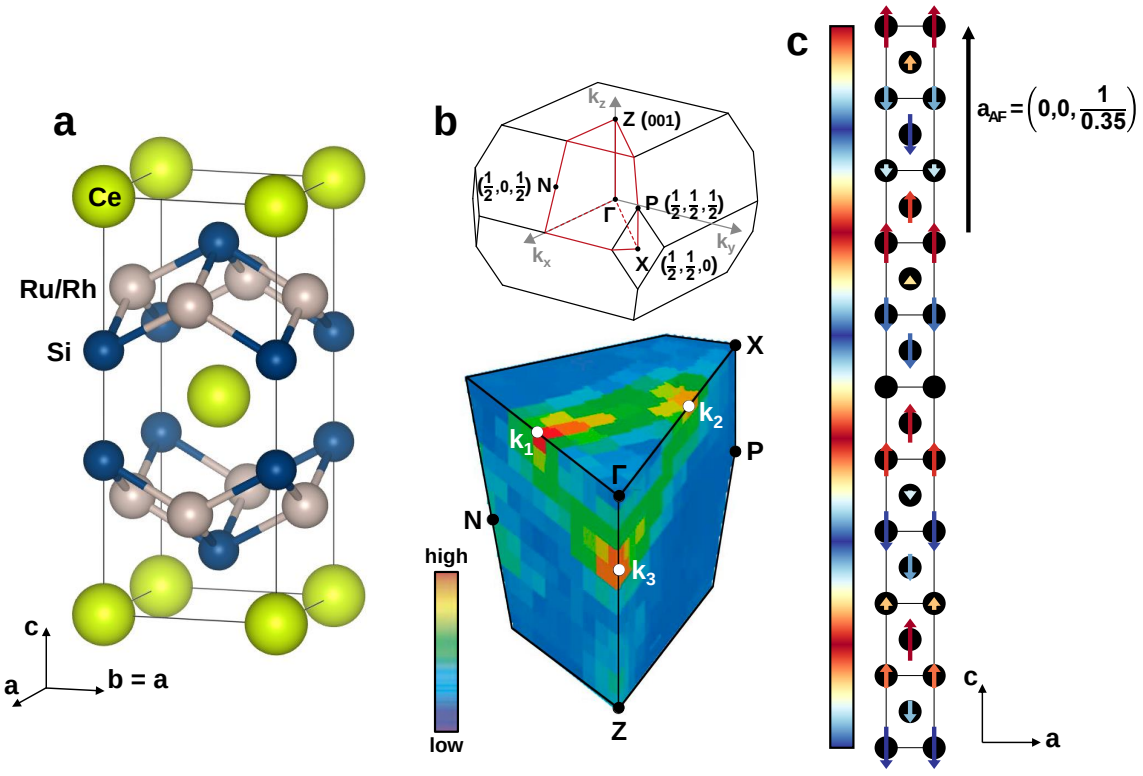

Figure 3.6: (a) Sketch of the tetragonal atomic structure of $CeRu_2Si_2$. Ce, Ru and Si atoms are represented as yellow, grey and blue balls. Rh-doping is introduced by substitution in the Ru sites. (b) Adapted from [110]. Top: Schematic representation of the reciprocal space in $CeRu_2Si_2$. The irreducible first Brilouin zone is delimited by red lines. Bottom: neutron scattering intensity map of constant energy scans acquired with E = 1 meV at 1.5 K showing antiferromagnetic spin correlations at the three wavevectors $\vec{k}_1$, $\vec{k}_2$ and $\vec{k}_3$. (c) Schematic diagram of the spin fluctuation in $Ce(Ru_{0.92}Rh_{0.08})_2Si_2$. We show ten unit cells along c-direction with Ce atoms represented as black circles. Local magnetic moments are aligned to the c-axis and their intensity varies with the antiferromagnetic vector $\vec{k}_3$ following the color scale on the left where deep red and deep blue correspond to spin +1/2 and spin −1/2, respectively.

at $H_c(T)$, and above a certain temperature, a polarized paramagnetic phase arises when crossing the H_m frontier (see fig. 3.5b). For pressures higher than P_c, H_m and H_c concur at T = 0 and we can have a zero temperature transition from a nearly antiferromagnetic phase to a polarized paramagnetic phase (see fig. 3.5c).

Applying positive pressure by substituting Rh on the Ru sites decouples H_m from H_c as shown in the magnetic field versus temperature phase diagram of the 8%-Rh-doped compound in fig. 3.5d. This phase diagram can be obtained from macroscopic specific heat, magnetostriction or thermal expansion measurements, which show clear features at the different phase transitions [111]. The ground state of $Ce(Ru_{1-x}Rh_x)_2Si_2$ is antiferromagnetic for $x > x_c = 0.05$. For x = 0.08, the Néel temperature is 4.2 K and we have two clearly separated zero temperature magnetic transitions. One at 2.5 T above which magnetic order completely vanishes entering a paramagnetic phase, and another one at 5.5 T from the paramagnetic state to a

polarized paramagnetic phase. Therefore, $Ce(Ru_{0.92}Rh_{0.08})_2Si_2$ allows us to explore these magnetic phases in temperature and magnetic field ranges which are easily accessible by the experimental setup developed in this thesis.

$CeRu_2Si_2$ crystallizes in a tetragonal structure belonging to the space group $I4mmm$ with lattice parameters $a = 4.196$ Å and $c = 9.797$ Å [115] (see fig. 3.6a). Neutron inelastic experiments in stoichiometric $CeRu_2Si_2$ show that antiferromagnetic correlations display three peaks at the wavevectors $\vec{k}_1 = (0.31, 0, 0)$, $\vec{k}_2 = (0.31, 0.31, 0)$ and $\vec{k}_3 = (0, 0, 0.35)$, as shown in the intensity map of constant energy scans with $E = 1$ meV inside the first Brillouin zone measured by Kadowaki *et al.* [110] (see fig. 3.6b). This means that there are three main directions along which magnetic fluctuations are expeted to occur in this material. As the fluctuating magnetic moments are oriented along c-axis, the two first in-plane wavevectors, $\vec{k}_1$ and $\vec{k}_1$, are transverse modes, and $\vec{k}_3$ is a longitudinal one.

La-doped $CeRu_2Si_2$ presents transverse antiferromagnetic ordering along $\vec{k}_1$ at zero field. When increasing magnetic field the antiferromagnetic orientation changes from $\vec{k}_1$ to $\vec{k}_2$ before disappearing above H_c. It turns out that doping with Rh favors the antiferromagnetic wavevector $\vec{k}_3$, and thus, as sketched in fig. 3.6c, the ground state of our Rh-doped sample is an antiferromagnet where the spin changes the orientation along c-axis flipping every ~ 3 unit cells.

3.3 STM characterization of the surface

We measured single crystalline samples of $Ce(Ru_{0.92}Rh_{0.08})_2Si_2$ grown by Dai Aoki in Grenoble. We prepared rectangular bars of a few mm long and ~ 0.5 mm wide oriented with the crystallographic c-axis parallel to the long direction. We inserted one of these bars in a small hole in the sample holder and glued it with silver epoxy. Once at 4.2 K, we cleaved the sample with a ceramic blade using the in-situ slider described in section 2.3.4 obtaining very large atomically flat areas. Figure 3.7 shows some scanning electron microscope (SEM) images (a,b,c) as well as an optical microscope image (d) from one of the $Ce(Ru_{0.92}Rh_{0.08})_2Si_2$ samples we measured. In these images we can appreciate how the cleaving process in cryogenic conditions provides atomically flat areas all over the sample. We also spot lines that appear during the breaking process and follow one of the in-plane crystallographic directions. However, there is no evidence of a clear cracking point or modifications of the surface structure by the cracking process like those previously reported in URu_2Si_2 [116]. This shows that $Ce(Ru_{0.92}Rh_{0.08})_2Si_2$ surfaces are free of strain or modifications induced by cracking, probably because the structural bonds are weak along the c-axis.

Figure 3.8a shows one of the STM topographic images we obtained at 100 mK and zero magnetic field inside a 26×26 nm^2 region where we can see the square arrangement of the atoms in the surface. The Fourier transform in the inset features the Bragg peaks of the square lattice together with some scattering signal

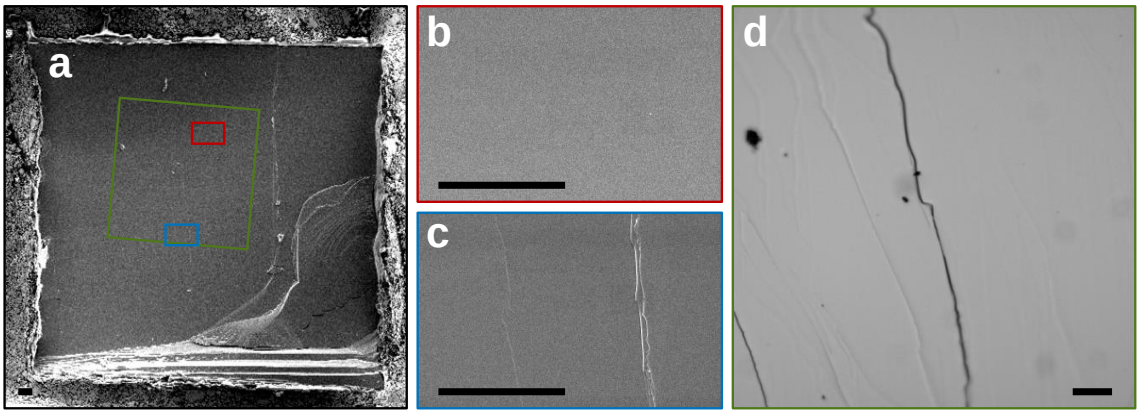

Figure 3.7: (a) Scanning electron microscope (SEM) image taken on one of the measured $Ce(Ru_{0.92}Rh_{0.08})_2Si_2$ samples after the cleaving process at cryogenic conditions. Red and blue boxes mark the positions at which the SEM images in (b) and (c) were taken, respectively. (d) Optical microscope image taken inside the region enclosed by the green box in (a). Black horizontal scale bars are 20 μm long.

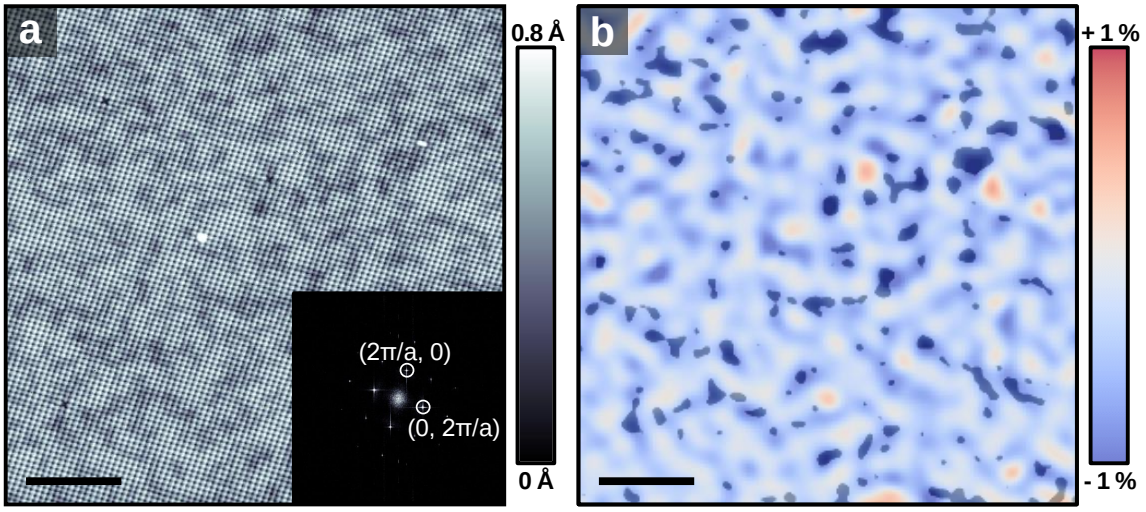

Figure 3.8: (a) STM topograhic image taken at 100 mK and zero magnetic field in $Ce(Ru_{0.92}Rh_{0.08})_2Si_2$ with a bias voltage of 10 mV and a setpoint current of 2.5 nA. Black scale bar is 5 nm long. Fourier transform of the topography is shown in the inset. First order Bragg peaks are marked with white circles. (b) Strain as a function of the position in the same field of view of (a) obtained by comparing the pattern observed in the topography with a perfect undisturbed periodic lattice [52, 117]. Positive (red) and negative (blue) values represent compressed and expanded regions, respectively. The distortion caused by Rh atoms is randomly distributed over the sample, without clustering or any significant internal strain. Strain map is superposed to a binary map of the topography in (a) saturated for height changes below 0.4 Å. Black regions cover an 8.8 % of the sample.

at small wavevectors introduced by the presence of Rh in the sample. Following Refs. [52, 117], we can calculate a strain map from the height displacement observed in the topography. To this end, we compare the pattern observed in fig. 3.8a with that expected for a perfect periodic lattice and assume that height displacements in the topography are due to lateral displacements coming from the Ru/Rh substitution. The resulting strain map is shown in fig. 3.8b, with positive strain (compression) represented in red and negative strain (expansion), in blue. We observe a small (< 1 %) and continuous distribution of strain without any signatures of strain accumulation, what evidences a random distribution of Rh on the Ru sites. The number of Rh atoms in fig. 3.8a can be estimated by saturating the image at a height of about 0.4 Å. The resulting map is plotted in the background of the strain map in fig. 3.8b and shows a distribution of Rh atoms of 8.8 %, which is close to the nominal concentration of 8 %. Besides, we also observe a correlation between the regions of the image with Rh substitution and the regions of the sample showing expansive strain.

3.3.1 Tunneling spectroscopy with magnetic field

We analyzed the tunneling spectrum measuring conductance versus bias voltage curves at 100 mK as a function of magnetic field from 0 T to 7.5 T. Figure 3.9 plots the curves we measured in two different energy scales, ±90 mV and ±8 mV. I used red, green and blue colors to represent the curves taken in the antiferromagnetic, paramagnetic and polarized paramagnetic phase, respectively.

In a bigger energy scale from −90 mV to +90 mV (fig. 3.9a) the spectrum follows the form of the Fano resonance. The general shape of the curves is similar in the different magnetic phases and we do not appreciate any drastic change with magnetic field. This evidences a cotunneling between a resonant state and a continuum. The curves can be fitted to the Fano expression in eq. (3.1) (see black line in fig. 3.9a). We find in particular E_0 = 30 meV, which coincides with the lowest crystal field excitation of $4f$-electrons from Ce in $CeRu_2Si_2$ [118, 119, 120]. Thus, in this energy range, our results evidence cotunneling between resonant $4f$-states and free electrons.

Figure 3.9b shows the tunneling conductance curves measured between −8 mV and +8 mV. Note that in this plot we have removed the linear background from the curves coming from the shape of the Fano resonance. The tunneling conductance curves show a dip close to the Fermi level (fig. 3.9b). The dip remains at all magnetic fields. However, its internal structure is strongly magnetic field dependent. The dip is asymmetric at zero field with a small peak observed at around 2 mV. When increasing the magnetic field, the peak moves inside the dip and the dip widens to approximately twice the zero field value. Black solid lines in fig. 3.9b mark the size evolution of the dip with magnetic field. We identify this gap as the hybridization energy range that hallmarks the Kondo lattice. This hybridization energy range is clearly present in every magnetic phase of the phase diagram, what means that Kondo screening and heavy electrons do not disappear at the quantum phase transition and that they are present in the whole phase diagram.

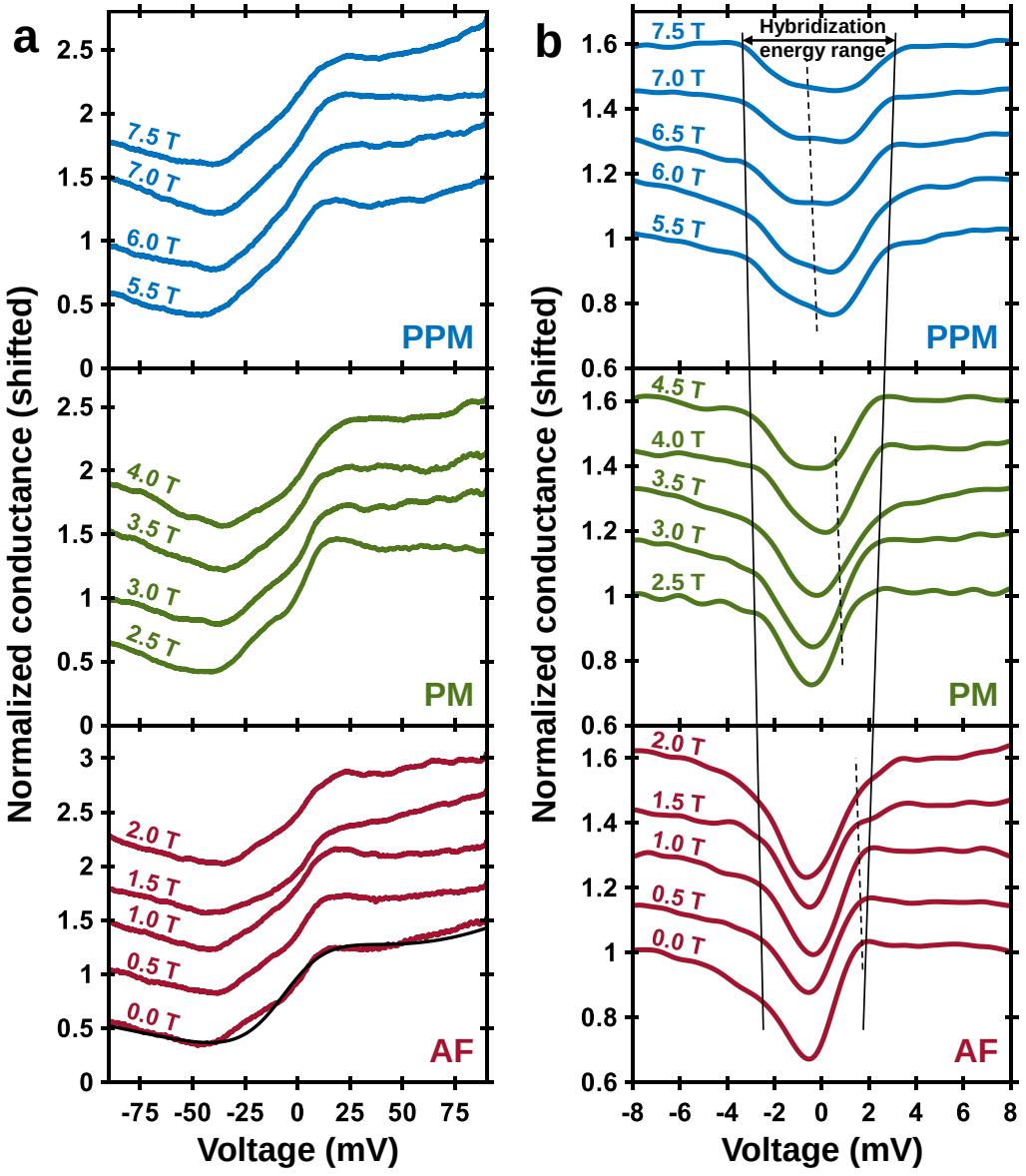

Figure 3.9: (a) Tunneling conductance versus bias voltage curves for different values of the magnetic field for V = ±90 mV. Black line fits the curve at 0 T to the Fano expression using the lowest crystalline field splitting of Ce $4f$-electrons. (b) Tunneling conductance versus bias voltage for V = ±8 mV, where the linear backgrounds coming from the shape of the Fano resonance have been removed. Black continuous lines indicate the hybridization energy range and black dashed lines, the magnetic field evolution of the peak coming from the van Hove anomaly. All data are taken at 100 mK. Data in the antiferromagnetic, paramagnetic and polarized paramagnetic phases are shown in red, green and blue, respectively. Curves are shifted upwards for better visualization.

We can take a closer look at two representative curves at zero magnetic field and at high field. Figure 3.10a shows the hybridization energy range in tunneling conductance versus voltage curves at 0 T and 7 T in the antiferromagnetic and highly polarized phases, respectively. Interestingly, we observe that the sign of the derivative of the conductance curves at zero bias changes through the different

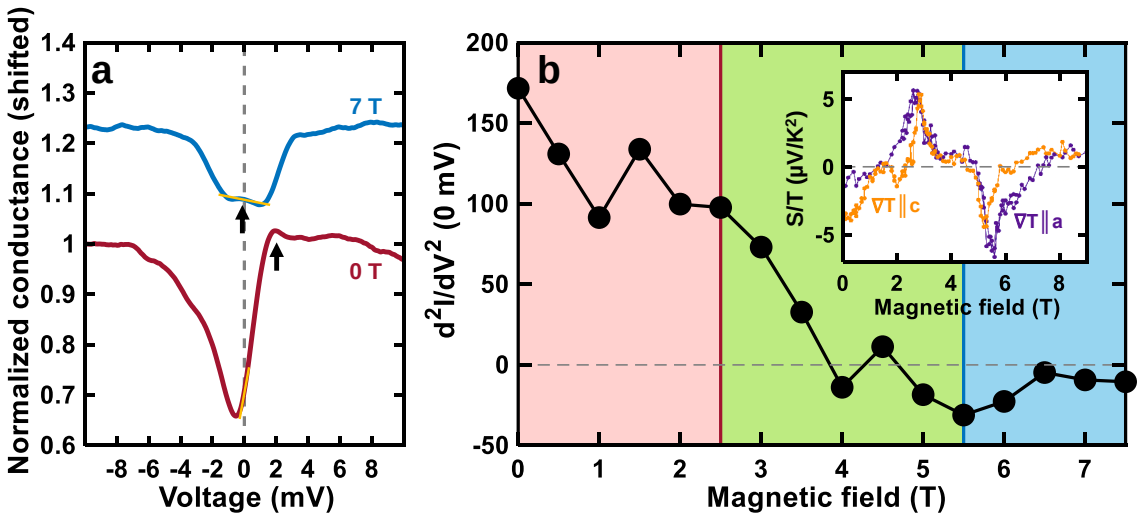

Figure 3.10: (a) Conductance versus bias voltage curves at 0 T (red) and 7 T (blue). Curve at 7 T is shifted upwards for better visualization. Orange lines mark the sign of the derivative of the curves at zero bias. Black arrows mark the peaks coming from a van Hove singularity. (b) Value of the zero bias derivative of the background removed conductance versus voltage curves as a function of the voltage. Antiferromagnetic, paramagnetic and highly polarized regions are shown in red, green and blue, respectively. Inset: adapted from [121]. Measured thermoelectric power parallel to *a*-axis (purple) and to *c*-axis (orange) versus magnetic field.

magnetic phases. It is positive in the antiferromagnetic phase and negative in the high field polarized paramagnetic phase (see slope lines in fig. 3.10a). Figure 3.10b plots the value of the zero bias derivative of the background removed conductance curves we measured as a function of magnetic field. These points display two local possitive peaks at 1.5 T and 4.5 T and a negative peak at 5.5 T coinciding with the paramagnetic to polarized phase transition. Inset in fig. 3.10b shows the macroscopic thermoelectric power measurements of the Seebeck coefficient in this material [121], that mainly depend on the derivative of the density of states at the Fermi level. The tunneling conductance, as well as the thermoelectric power, present a change from a mainly positive sign at low magnetic fields (positive derivative $\mathrm{d}N/\mathrm{d}E$) to a negative sign at high magnetic fields (negative derivative $\mathrm{d}N/\mathrm{d}E$).

To understand the behavior close to the Fermi level we can take a close look on the band structure. The conductance curve at zero field shows a peak at around 2 mV that comes from the increase in the density of states at that energy due to the presence of a van Hove singularity, which arises from the energy overlap between flat regions of the hybridized band structure (see black arrow in fig. 3.10a). As I will further discuss in the following section, as the Zeeman splitting of the hybridized bands becomes stronger with increasing magnetic field, the energy at which the flat parts of the bands overlap varies. Thus, the energy position of the van Hove anomaly evolves with magnetic field. The peak we see in our curve at around 2 mV at 0 T gradually moves to lower energies as magnetic field increases as shown by the black dashed line in fig. 3.9b. This way we end up having the peak right inside the

hybridization energy range at high magnetic fields, what eventually alters the sign of the derivative of the curves at zero bias.

3.4 QPI: band structure evolution through the magnetic transitions

To further explore the shape of the bands through the different magnetic phases of $Ce(Ru_{0.92}Rh_{0.08})_2Si_2$, we performed some quasiparticle interference measurements in each phase. The method we used is described in section 2.1.4. We studied the scattering patterns in three different regions at 0 T, 3 T and 7.85 T in the antiferromagnetic, paramagnetic and polarized paramagnetic phase, respectively. All the measurements were performed at 100 mK.

Figure 3.11a-c show the topographic images of the regions where we performed the QPI analysis at 0 T, 3 T and 7.85 T, respectively. In all of these images we observe the square atomic lattice and some slightly lower areas (darker areas) coming from the Rh defects, which provide the scattering signal needed for the quasiparticle interference measurements. Although we performed the QPI analysis in three different fields of view, we reproducibly found the same kind of surfaces all over the sample. Besides, even if we observe some single impurities on top of the surfaces (white spots in fig. 3.11a-c), the scattering signal is dominated by the presence of Rh defects, that are randomly and homogeneously distributed over the sample. Therefore, all the differences we observe in the scattering patterns measured in the three different cases can be attributed to magnetic field induced modifications in the band structure.

Fourier transforms of the topographic images are shown in the inset of fig. 3.11a-c displaying the Bragg peaks of the square lattice and a huge amount of scattering signal at small wavevectors. We took conductance curves between −10 mV and +10 mV at every pixel of the topographies and built spatially resolved conductance maps for all the energies of the study. Figure 3.11d-f show some of these conductance maps at some representative energies together with their Fourier transforms inside the first Brillouin zone. To enhance the signal to noise ratio in the Fourier transform maps, we symmetrized them following the C4 symmetry of the crystal and applied a 3×3 pixel average filter. We also applied a Gaussian core subtraction centered at $\vec{q} = 0$ to filter out the smallest wavevectors and increase the contrast of the images.

Starting in the antiferromagnetic phase at 0 T, the main part of the scattering signal in the Fourier transform maps displays a circular shape around the center that reaches its maximum intensity between 1 and 2 meV in agreement with the position of the peak from the van Hove anomaly in the tunneling conductance curve I discussed above. At 3 T, the maximum intensity of this circular feature around the center also occurs between 1 and 2 meV, but the intensity of this circle in the adjacent maps at 0 meV and 3 meV is higher than the case at 0 T. For the case of 7.85 T, the maximum intensity of the circular shape is reached between 2 meV and

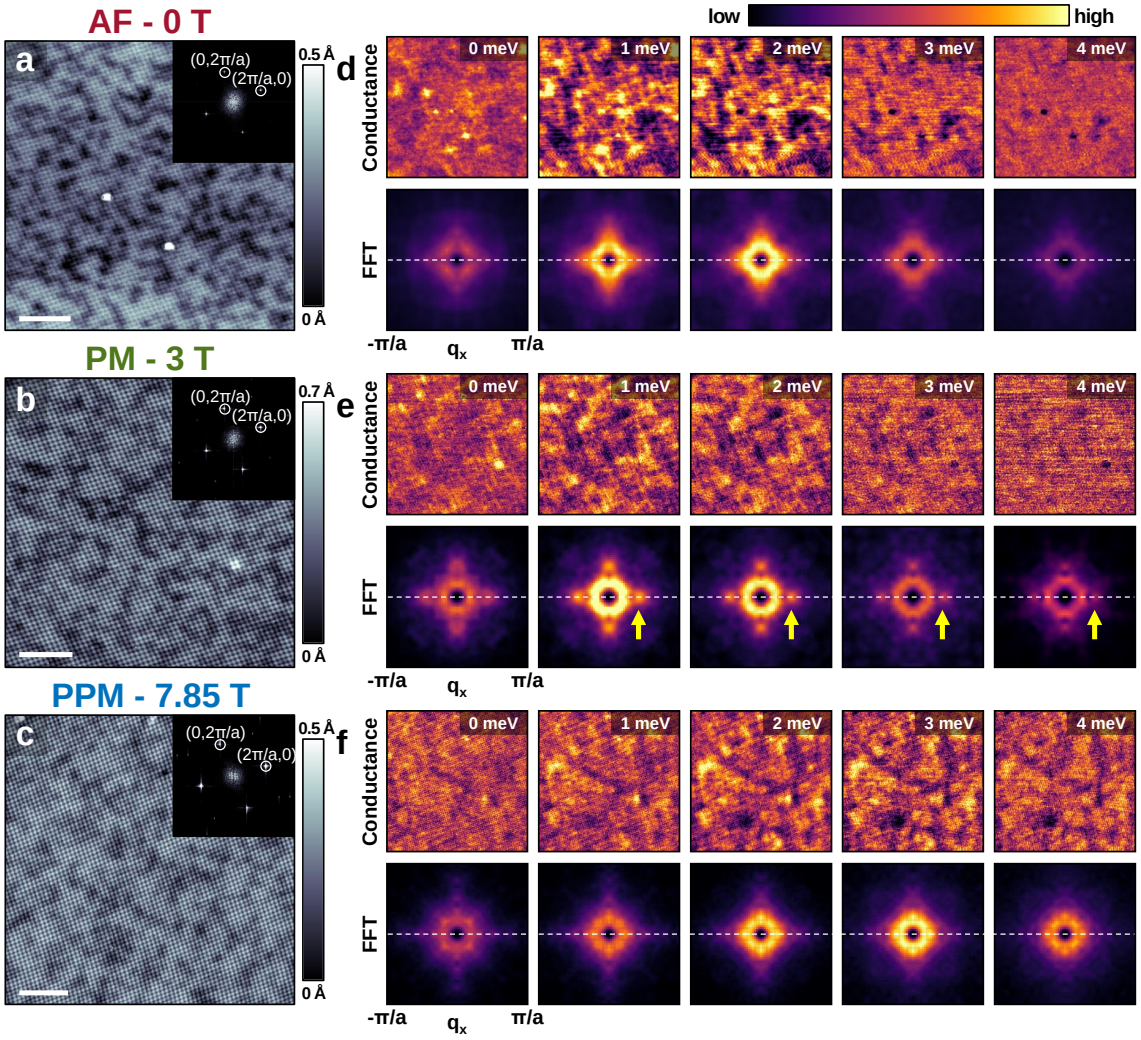

Figure 3.11: (a,b,c) STM topographic images taken at 100 mK and 0 T, 3 T and 7.85 T, respectively, in three different regions where we studied the quasiparticle interference scattering (V_{bias} = 10 mV, $I_{setpoint}$ = 2.5 nA). White horizontal scale bar is 5 nm long. Insets show the Fourier transforms of the images highlighting the first order Bragg peaks. (d) 0 T conductance maps for some representative energies in the same field of view of (a). The symmetrized Fourier transform maps inside the first Brillouin zone are shown below the corresponding conductance map. (e) Same at 3 T in the field of view of (b). (f) Same at 7.85 T in the field of view of (c). Yellow arrows mark the position of a four-fold symmetric scattering point in the paramagnetic phase.

3 meV, but the behavior of this feature is much more homogeneous between 1 meV and 4 meV.

Apart from the circular shape in the center, we also spot some directional features in the maps at 0 T that turn the scattering circle into a star-like shape with the vertices along q_x[1], which is the direction of the square atomic lattice. At 3 T, these features materialize in four scattering points at around 0.45 π/a in q_x that are clearly

[1]As the crystal is four-fold symmetric, q_x and q_y directions are equivalent.

visible in the maps between 1 meV and 4 meV (see yellow arrows in fig. 3.11e). These points are not resolved in the maps at 0 T or at 7.85 T.

To better compare the scattering signal in the three different cases, we took profiles along q_x direction in the Fourier transform maps for all the energies of the study (see white dashed lines in fig. 3.11d-f). Figure 3.12a-c respectively show these profiles at 0 T, 3 T and 7.85 T with q_x in the horizontal axis and energy in the vertical axis. The main part of the scattering lies inside a small energy range slightly above the Fermi level and it extends up to approximately half the Brillouin zone. At 0 T (fig. 3.12a), we see that the main scattering cloud displays an electron-like dispersion at positive energies. At 3 T (fig. 3.12b), we clearly spot an additional scattering vector and the electron-like line features become more obvious. The energy range for enhanced scattering becomes wider with increasing magnetic field. At 7.85 T(fig. 3.12c), the scattering intensity at small $\vec{q}$ is much more spread along the whole energy range.

To understand the profile at 0 T we can discuss a simple hybridization band scheme. To model a band structure that fits our QPI data, we used a sinusoidal approach for the light and heavy bands:

$$E(k_x) = E_0 \cos\left(\frac{\pi}{a}k_x\right) + \epsilon, \tag{3.2}$$

with $E_{0,c} = -110$ meV and $\epsilon_c = 100$ meV for the light conduction band, $E_c(k_x)$, and $E_{0,f} = -0.9$ meV and $\epsilon_f = 1.2$ meV for the heavy f-band, $E_f(k_x)$. Figure 3.12d plots the light conduction band in yellow and the heavy f-band in purple. The hybridization of these two bands is given by:

$$E_h^{\pm}(k_x) = \frac{E_c(k_x) + E_f(k_x)}{2} \pm \sqrt{\left(\frac{E_c(k_x) - E_f(k_x)}{2}\right)^2 + s^2}, \tag{3.3}$$

where we used $s = 2$ meV and $s = 4$ meV for $E_h^+(k_x)$ and $E_h^-(k_x)$, respectively. The hybridized bands are represented by solid black lines in fig. 3.12d. In this simplified picture of a Kondo metal, the top and bottom of the hybridized bands are located right above the Fermi level. In first approximation, to estimate the scattering signal expected from such a band structure, we can calculate the joint density of states (JDOS) and plot it in fig. 3.12g over our QPI profile. The JDOS map will display higher intensity at $\vec{q}$ vectors connecting certain regions of the band structure, for instance flatter parts of the Fermi surface. Arrows in fig. 3.12d,g identify the regions of the band structure responsible for the different lines we observe in the JDOS map. As might be expected, the largest contribution to the scattering comes from the flat portions of the band structure, where van Hove anomalies arise. It is concentrated in a narrow energy range above the Fermi level, enclosed between the bottom and top of the hybridized bands. Among other features, JDOS maps show a vector at positive energies coming from the intra-band scattering in the E_h^+ band that follows an electron-like dispersion. If we compare the calculated JDOS with our QPI profile, we see that it quite well fits our data providing an interpretation for the more intense scattering spots in the QPI data as coming from the scattering

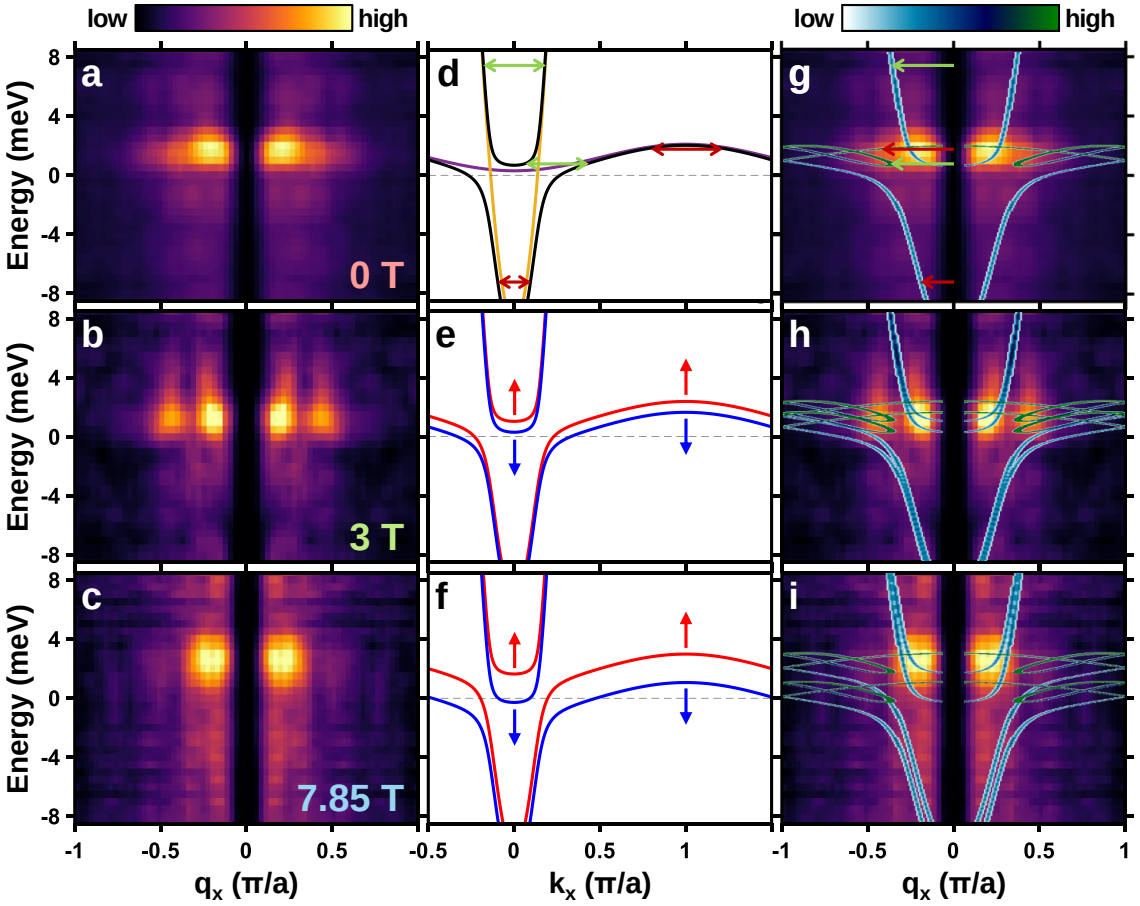

Figure 3.12: (a,b,c) Profiles from the Fourier transform of the conductance maps along q_x inside the first Brillouin zone for all the energies of the study measured at 0 T, 3 T and 7.85 T, respectively. (d) Simplified model for the band structure in $Ce(Ru_{0.92}Rh_{0.08})_2Si_2$ at 0 T. Conduction band is depicted in yellow, heavy f-band, in purple, and hybridized bands, in black. (e,f) Band schemes at 3 T and 7.85 T, respectively, introducing a Zeeman splitting into the hybridized bands. Spin-up and spin-down components are shown in red and blue, respectively. Zeeman splitting of the bands results in a spin imbalance at the Fermi level for the case of 7.85 T as only the spin-down component of the upper band crosses the Fermi level. (g,h,i) JDOS maps calculated from the hybridized band structures in (d,e,f), respectively, plotted over the QPI profiles in (a,b,c). Arrows in (g) identify the position of the scattering $\vec{q}$ vectors marked in (d). Maps in (h,i) are calculated assuming that scattering can only occur between bands with the same spin.

between the flat regions of the hybridized band structure. Intra-band scattering in the E_h^+ band explains the increase of scattering intensity at higher energies. These electron-like dispersive features are better resolved in the QPI profiles at 3 T.

As magnetic field increases, our QPI data show how the enhanced scattering cloud at small $\vec{q}$ in the profiles broadens in energy. To follow this energy broadening using a band structure interpretation similar to what we did with the profiles at zero field, we have to consider Zeeman splitting in the hybridized band scheme. Figure 3.12e,f show the hybridized band scheme at 3 T and 7.85 T, respectively, where we have introduced a Zeeman energy splitting of E_Z/H = 0.12 meV/T to account for the

energy broadening we observe in our QPI data. Up and down spin components of the bands are plotted in red and blue, respectively. JDOS maps in fig. 3.12h,i coming from the split band structure were calculated as in the case of 0 T considering that scattering among bands with different spin directions is forbidden. JDOS maps are in good agreement with the QPI profiles obtained in the paramagnetic phase and in the polarized paramagnetic phase showing how Zeeman splitting can account for the energy broadening of the scattering signal in our QPI data.

In systems where the spin component of the orbital momentum, S is higher than $1/2$, S and L (the orbital component), may not be good quantum numbers and the total angular momentum, $J = S + L$, must be considered. In this situation, the Zeeman energy is given by the following expression [122]:

$$E_Z = \mu_B g_J J H, \tag{3.4}$$

where μ_B is the Bohr magneton, g_J, the Landé g-factor, and H, the applied magnetic field. The Landé g-factor can be obtained as a function of S, L and J [122]:

$$g_J = \frac{3}{2} + \frac{S(S+1) - L(L+1)}{2J(J+1)} \tag{3.5}$$

In Ce systems like this, the multiplet $J = 5/2$ is typically considered, leading to $g_J = 6/7$ [123]. Introducing these values into eq. (3.4), the expected Zeeman energy is $E_Z/H = 0.124$ meV/T. To compare this value with the experiments, let us note that the entry into a polarized paramagnetic phase at 5.5 T implies a magnetic field induced shift in the band structure which is large enough to make one spin polarized band to cross the Fermi level, leaving the other spin polarization unoccupied. The band structure we have calculated following our data (fig. 3.12d) provides such a situation assuming a Zeeman energy of 0.12 meV/T.

Notice that, at 3 T, we observe two spots in our data at around $q_x = \pm 0.45\ \pi/a$ centered at around 1 meV and their dispersive patterns for positive energies. Although there is an increase in the JDOS pattern at finite q_x due to the shifts in the top and bottom of the bands, these features are not fully reproduced by our simple band structure model (see (fig. 3.12h). The presence of this scattering vector suggests the presence of a new band in the paramagnetic phase. The scattering vector slightly reduces as energy increases, pointing to a hole-like character for this band. This band is clearly directional along the crystallographic axes and four-fold symmetric as shown by the QPI maps in (fig. 3.11e). At the highest magnetic field (fig. 3.12i), the Zeeman shift minimizes overlap between portions of the band structure and thus the pattern becomes washed out, as also observed in the experiment.

Measured QPI patterns in fig. 3.12a-c show broadened features rather than lines. This can be explained from an energy broadening of the band structure due to the high electron-electron correlations in this material. To take this into account, we can add a Lorentzian energy broadening, $L(E)$, to the hybridized band structures in fig. 3.12d-f following the model presented by Nagaoka *et al.* [124]:

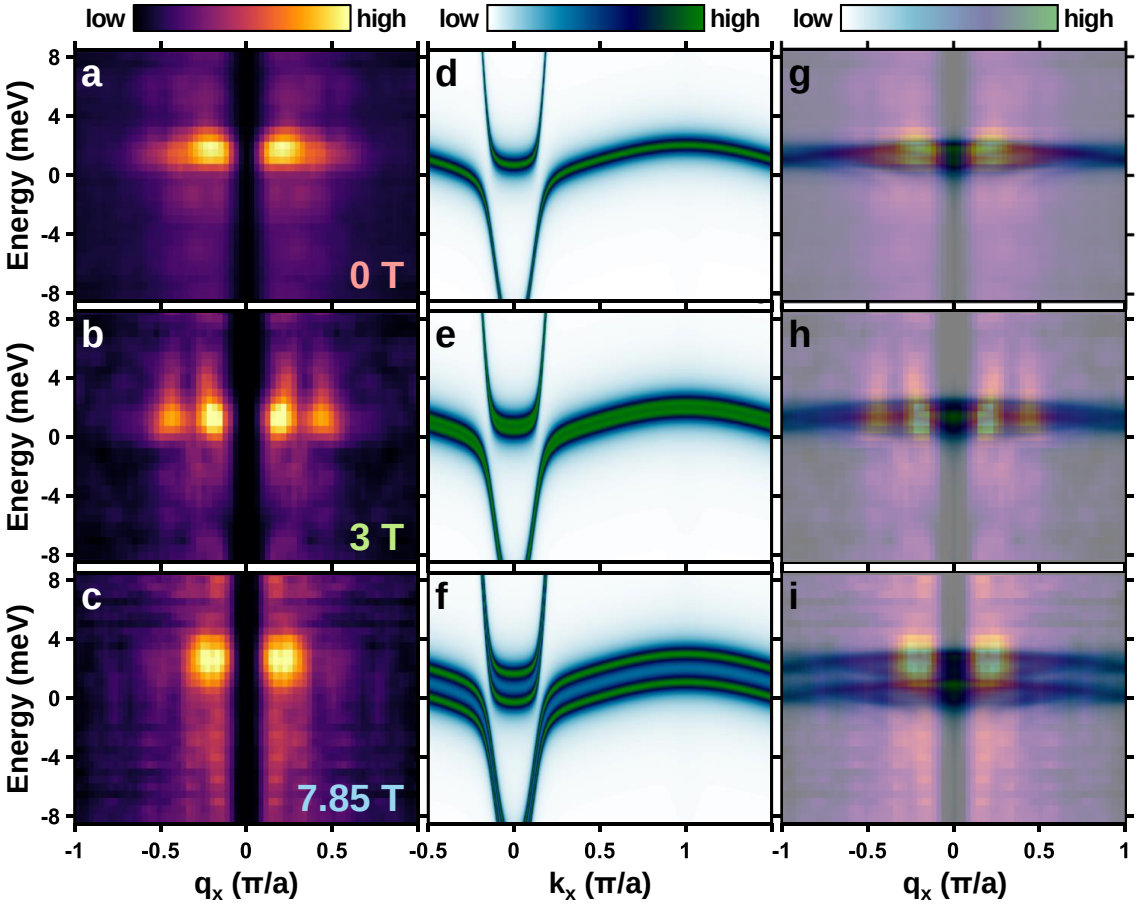

Figure 3.13: (a,b,c) Profiles from the Fourier transform of the conductance maps along q_x inside the first Brillouin zone for all the energies of the study measured at 0 T, 3 T and 7.85 T, respectively. (d,e,f) Hybridized band structure from fig. 3.12d,e,f where we have applied an energy broadening using the Lorentzian function from eq. (3.6) with T = 0.1 K and T_L = 4 K. (g,h,i) JDOS maps calculated from the broadened hybridized band structures in (d,e,f), respectively, plotted over the QPI profiles in (a,b,c). Maps in (h,i) are calculated assuming that scattering can only occur between bands with the same spin.

$$L(E) = \frac{1}{1 + \left(\frac{E}{\sqrt{(\pi k_B T)^2 + 2(k_B T_L)^2}} \right)^2}, \tag{3.6}$$

where k_B is the Boltzmann constant, T, the temperature, and T_L denotes an effective temperature accounting for the electron-electron correlations. Figure 3.13d-f shows the resulting hybridized bands after applying this broadening using T = 0.1 K and T_L = 4 K. Figure 3.13g-i shows the calculated JDOS maps from the broadened bands in fig. 3.13d-f. In this case, we observe blurred structures in the JDOS maps around the energies at which the band structure is flatter instead of the separated line features in fig. 3.12g-i. Thus, we manage to more accurately fit our measured QPI data thanks to the blurring introduced in the scattering predictions by the energy broadening of the bands due to the strong electronic correlations in this compound.

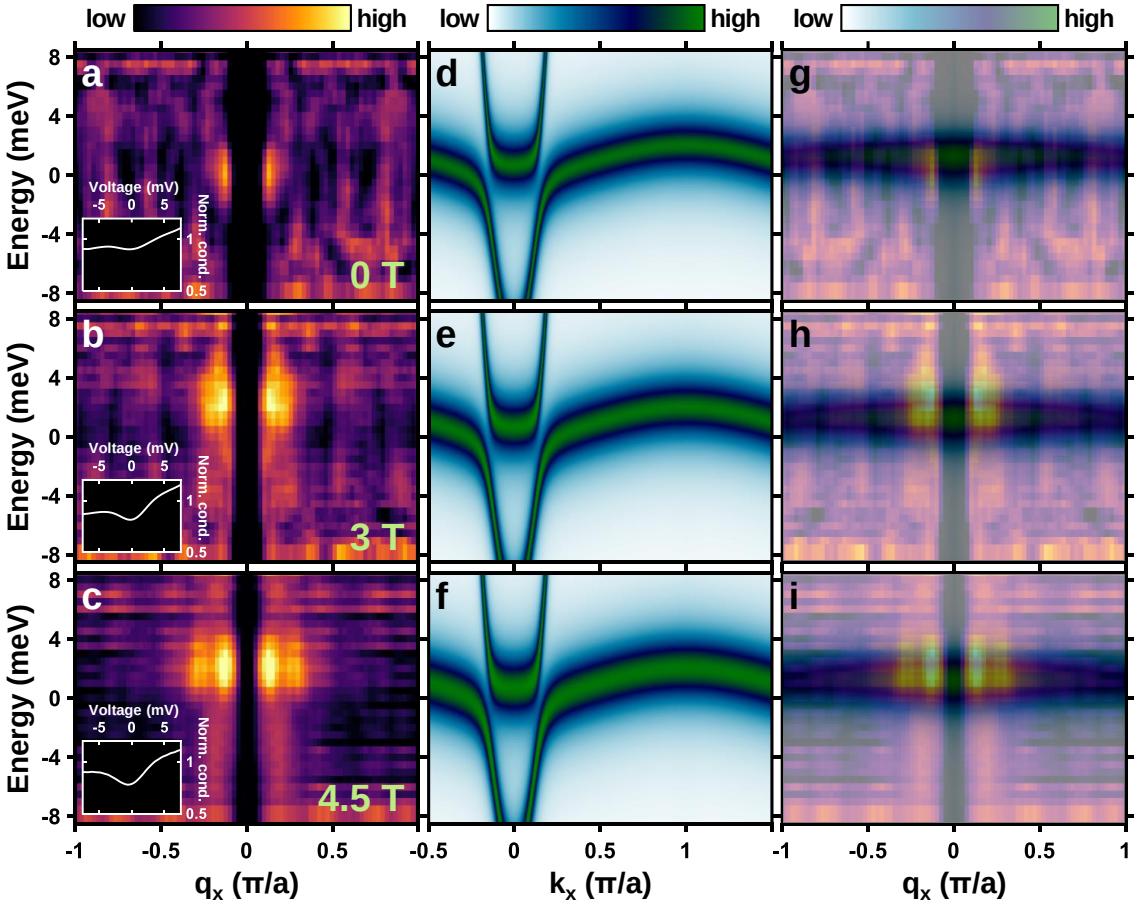

Figure 3.14: (a,b,c) Energy versus q_x profiles from QPI measuments at 5 K and 0 T, 3 T and 4.5 T, respectively in the paramagnetic phase. Insets show the spatially averaged normalized conductance versus voltage curve in each case. (d,e,f) Hybridized band structure taking into account the Zeeman splitting of the bands at each field. We have applied an energy broadening using the Lorentzian function from eq. (3.6) with T = 5 K and T_L = 4 K. (g,h,i) JDOS maps calculated from the broadened hybridized band structures in (d,e,f), respectively, plotted over the QPI profiles in (a,b,c). Maps in (h,i) are calculated assuming that scattering can only occur between bands with the same spin.

The Lorentzian used to broaden the band structure has a width of T_L = 4 K. This observed value of T_L at 100 mK is significantly below the Kondo temperature of 20 K. However, it is of the order of the antiferromagnetic transition temperature. This might further suggest that the formation of antiferromagnetism is connected with flat portions of the band structure. Besides, it is also consistent with the fact that the high field polarized phase is observed mostly as a crossover that is smeared when increasing temperature.

Finally, we studied the QPI patterns at 5 K, above the Néel temperature (4.2 K). Figure 3.14a-c shows the QPI profiles along q_x measured at 5 K and 0 T, 3 T and 4.5 T, respectively, in similar regions to those shown above. The spatially averaged conductance versus voltage curves are plotted in the inset of each panel showing how the hybridization energy range is strongly smeared with no features inside it. The band structure used in the previous cases at low temperature is strongly smeared

at 5 K (fig. 3.14d-f) and the corresponding JDOS contains no clear signatures but a broadened energy range (fig. 3.14g-i). Thus, increasing temperature to 5 K leads to a loss of the sharp effect of moving flat portions of the bands in the Zeeman induced shifts.

3.5 Conclusions

In summary, we have studied the surface of $Ce(Ru_{0.92}Rh_{0.08})_2Si_2$ using the STM observing the square arrangement of the atoms and an ~ 8 % of the surface with slightly reduced density of states due to the Rh doping introduced in the samples. Rh atoms are randomly distributed over the sample and do not induce any significant internal strain.

Tunneling spectroscopic curves show the Fano resonance and the opening of a hybridization energy range that is present through all the different magnetic phases, which means that there is Kondo screening and heavy electrons all over the phase diagram.

Our QPI results are compatible with the hybridization scheme of a heavy f-band and a light conduction band and they show that the hybridized bands undergo a strong Zeeman splitting. This Zeeman splitting drives the different magnetic transitions observed in this material and it is eventually responsible for the nearly ferromagnetic phase at high magnetic fields as only one spin component of the bands crosses the Fermi level. Strong electronic correlations introduce a Lorentzian broadening in the hybridized band structure. The width of this broadening is of the order of the energy associated to the Néel temperature, what suggests that the presence of flat portions of the band structure is key to understand the origin of the antiferromagnetic phase.

4

High magnetic field band structure in the topological semimetal WTe_2

4.1 Transport and topological properties

4.1.1 Huge magnetoresistance

WTe_2 is a semimetal with very low density of states around the Fermi level and a huge mobility. It has recently attracted a lot of attention due to its huge, non-saturating magnetoresistance [125]. Magnetoresistance (MR) is the change in the electrical resistance driven by an external magnetic field. Although it is not predicted to occur just considering a non-interacting free electron model, it is a universal phenomenon in metals and semiconductors. It is defined as

$$\mathrm{MR}(B) = \frac{\rho(B) - \rho(0)}{\rho(0)}, \tag{4.1}$$

where ρ is the electrical resistivity and B is the magnitude of the externally applied magnetic field. It is typically small and positive. The origin of the electrical resistity is the scattering of electrons on a timescale τ, which is the characteristic scattering time. When applying a magnetic field, electrons are forced to describe orbits with an angular velocity equal to the cyclotron frequency, $\omega_c = \frac{eB}{m^*}$, where e is the the electron charge and m^*, its effective mass. Considering a nearly free electron model, a quadratic dependence of the resistivity on the magnetic field, $\rho(B) \propto B^2$, appears as the simplest solution that fulfills Onsager's reciprocity condition $\rho(B) = \rho(-B)$. In the high field limit ($\omega_c\tau \gg 1$) the mean free path is no longer modified by the magnetic field and the magnetoresistance saturates. Quadratic magnetoresistance saturating at high fields is often observed in metals with no or weak electronic correlations [126, 127, 128]. When there is a compensation between the number

of electron and hole carriers, the magnetoresistance continues growing as B^2 up to much higher magnetic fields before reaching saturation. This is the case of the semimetal Bi and some other metals in which there is this compensation between electrons and holes [129, 130, 131]. Eventually, the saturation is never reached if the compensation is perfect [126].

The quadratic behavior of the magnetoresistance can be understood from a semiclassical approach [126]. If we assume that the external magnetic field is applied along z-axis, we can write the resistivity tensor in the transverse plane (x, y) for a free electron gas as

$$\hat{\rho} = \begin{pmatrix} \frac{1}{\sigma_e} & \frac{\eta_e}{\sigma_e} \\ -\frac{\eta_e}{\sigma_e} & \frac{1}{\sigma_e} \end{pmatrix}, \tag{4.2}$$

where $\eta_e = \mu_e B$, μ_e is the electron mobility and σ_e is the zero field conductivity. Note that, in eq. (4.2), ρ_{xx} is equal to ρ_{yy} and non-dependent on magnetic field. Inverting the resistivity tensor we obtain the following expression for the conductivity tensor for a single isotropic electron band:

$$\hat{\sigma}_e = \begin{pmatrix} \frac{\sigma_e}{1+\eta_e^2} & -\frac{\eta_e\sigma_e}{1+\eta_e^2} \\ -\frac{\eta_e\sigma_e}{1+\eta_e^2} & \frac{\sigma_e}{1+\eta_e^2} \end{pmatrix} \tag{4.3}$$

The expression for the resistivity tensor considering hole carriers is similar to eq. (4.3), but there is a change of sign in the off-diagonal terms. When electron and hole carriers are both present and considered as independent conduction channels, one have to include the two contributions in the conductivity tensor:

$$\hat{\sigma} = \hat{\sigma}_e + \hat{\sigma}_h = \begin{pmatrix} \frac{\sigma_e}{1+\eta_e^2} & -\frac{\eta_e\sigma_e}{1+\eta_e^2} \\ -\frac{\eta_e\sigma_e}{1+\eta_e^2} & \frac{\sigma_e}{1+\eta_e^2} \end{pmatrix} + \begin{pmatrix} \frac{\sigma_h}{1+\eta_h^2} & -\frac{\eta_h\sigma_h}{1+\eta_h^2} \\ -\frac{\eta_h\sigma_h}{1+\eta_h^2} & \frac{\sigma_h}{1+\eta_h^2} \end{pmatrix} \tag{4.4}$$

Inverting back $\hat{\sigma}$ unveils the field dependence of the resistivity ρ_{xx}, x being the direction of the current:

$$\rho_{xx} = \frac{n_e\mu_e + n_h\mu_h + \mu_e\mu_h(n_e\mu_h + n_h\mu_e)B^2}{e\left[(n_e\mu_e + n_h\mu_h)^2 + (n_e - n_h)^2\mu_e^2\mu_h^2B^2\right]}, \tag{4.5}$$

where we have used the Drude formula for conductivity, $\sigma = ne\mu$, with n being the carrier density. Note that when electron and hole carrier numbers are equal, the resistivity increases with magnetic field as B^2 without saturation. Figure 4.1 sketches the shape of the resistivity versus magnetic field curves for different values of the electron to hole ratio, n_e/n_h. We can understand the effect of slight deviations of

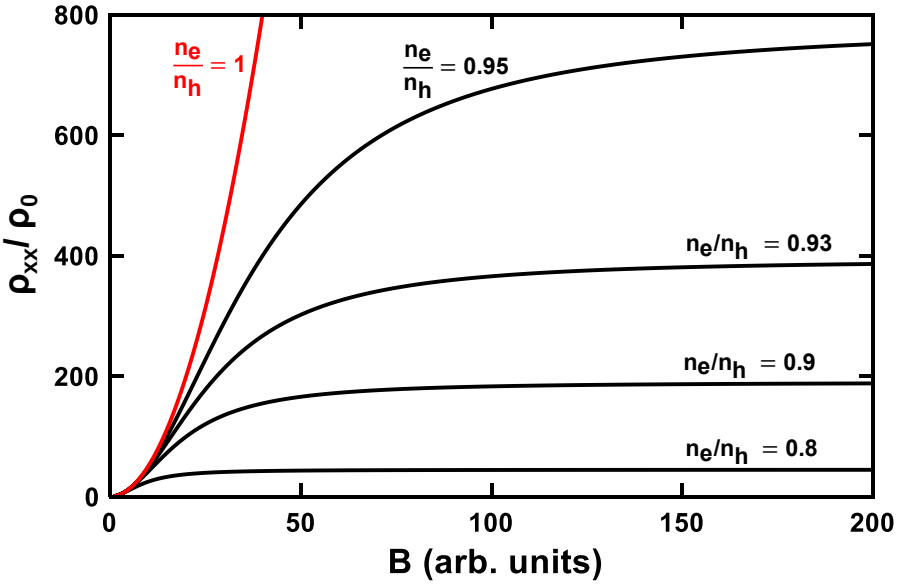

Figure 4.1: Magnetoresistance as a function of magnetic field from eq. (4.5) for different values of the electron to hole ratio, n_e/n_h. Perfect compensation situation is plotted in red.

electron-hole carrier numbers from $n_e/n_h = 1$ by comparing eq. (4.5) for the resistivity with a resonance. Ali *et al.* [125] did so and defined the Q factor of the resonance. As the Q factor of the resonance increases with magnetic field, very small deviations of n_e/n_h from 1 lead to saturation at large B. If B is weaker, the resonance is broader and the B^2 dependence of the magnetoresistance is easily attained. This is the case of high-purity graphite below 0.2 T [132]. Over a few teslas, ρ_{xx} strongly deviates from the square behavior [133]. In high-purity Bi, B^2 magnetoresistance starts falling apart above 1 T and reaches saturation above 10 T [134].

WTe_2 seems to be the first material in which the electron-hole resonance is almost perfect, as it displays a magnetoresistance that increases quadratically up to 10^7 % at 60 T with no signs of saturation [125] (see fig. 4.2). This value for the magnetoresistance is reached when the current flows along a-axis and the magnetic field is applied parallel to c-axis. Some other metallic or semimetallic compounds have been reported to show huge and sometimes non-saturating magnetoresistance [135, 136, 137, 138, 139, 140, 141, 142, 143, 144, 145, 146, 147, 148, 149, 150], but none of them as large and up to such high magnetic fields as WTe_2. The exceptional sensitivity of the resistivity to small changes of the magnetic field at high fields positions WTe_2 as a good candidate to work as a high field temperature sensor in cryogenics. Besides, it is a very easy to exfoliate layered material that can be tuned by chemical doping. Thus, it can be used to build advanced nanostructure devices. Furthermore, high pressure measurements have reported a suppression of the magnetoresistance at around 10.5 GPa accompanied by the emergence of superconductivity with critical temperature up to ~ 6.5 K [151].

The overlap between conduction and valence bands in WTe_2 is extremely small, what typically favors compensation between the two types of carriers. Quantum

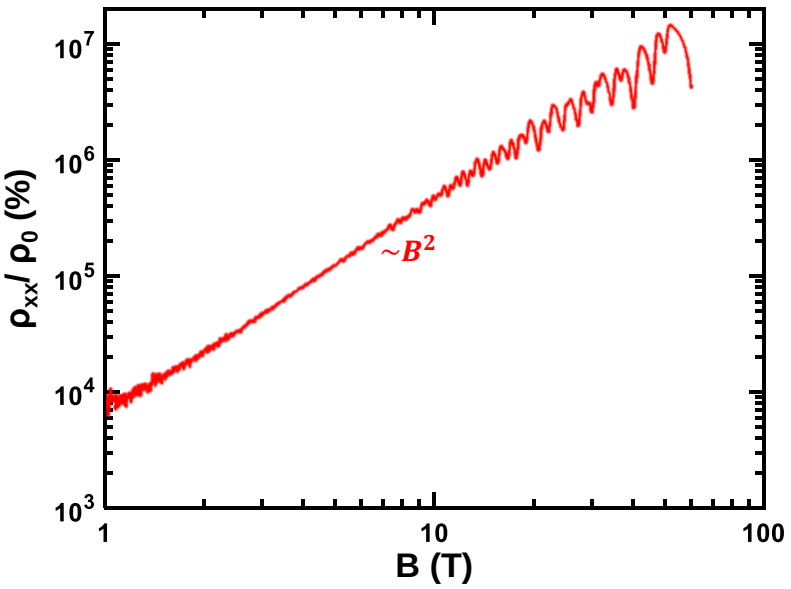

Figure 4.2: Adapted from [125]. Magnetoresistance as a function of magnetic field in WTe_2 showing a quadratic evolution with no signs of saturation up to 60 T.

oscillation measurements confirm that WTe_2 is electron-hole compensated within a precision of 4 % ($n_e = 6.64 \times 10^{19}$ cm^{-3} and $n_h = 6.9 \times 10^{19}$ cm^{-3}) [152]. However, it is still unclear how the magnetic field modifies the band structure in WTe_2 and if it affects in some way the electron-hole compensation. Besides, a rigorous experimental determination of the band structure in WTe_2 for both filled and empty states is still lacking. This is the main issue we tried to address with our QPI measurements, as previous QPI measurements in this material have focused in the topological surface states without discussing the bulk band structure with sufficient detail [153, 154, 155]. While the filled states and the Fermi surface have been measured using ARPES and quantum oscillations, the band structure of empty states has not been addressed in detail.

4.1.2 Weyl semimetal

WTe_2 has been predicted to be a type II Weyl semimetal [156]. In noncentrosymmetric systems like this, band crossings give rise to Weyl points instead of Dirac points. These can host a massless quasiparticle called Weyl fermion [157]. This type of fermion was first predicted in particle physics in 1929 [158]. However, as these quasiparticles break Lorentz invariance, they can only occur in condensed matter systems [156].

Weyl fermions appear as low energy excitations around Weyl points. The massless character of Weyl particles protects Weyl crossings from gapping. There are two possible types of Weyl points with different thermodynamic properties. If the protected band crossing is perpendicular we have the so-called type I Weyl points. Electron and hole bands only overlap at the Weyl points, and thus, type I Weyl semimetals display a closed point-like Fermi surface (fig. 4.3a). On the other hand, a

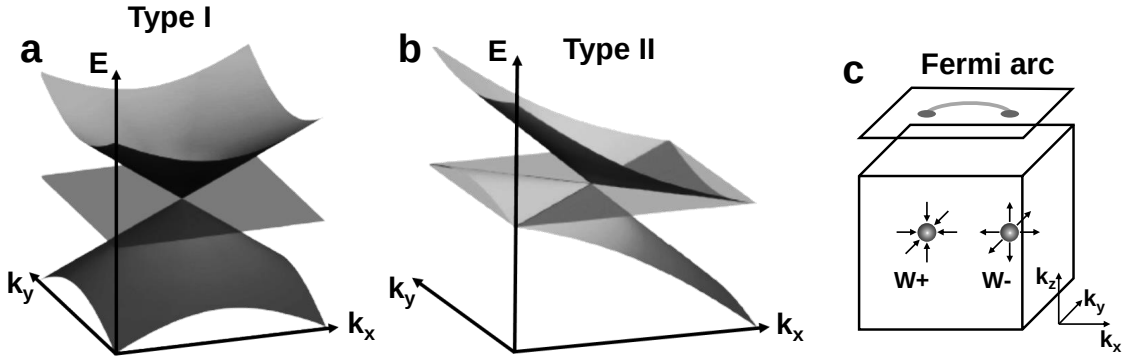

Figure 4.3: (a) Sketch of the perpendicular band crossing giving rise to type I Weyl points with point-like Fermi surface. (b) Type II Weyl points appearing at the contact between electron and hole pockets in a tilted band dispersion. (a) and (b) are adapted from [156]. (c) Schematic representation of a topological Fermi arc connecting the projection of opposite chirality Weyl points into the surface.

type II Weyl point is still a protected crossing, but it emerges at the contact between electron and hole bands in the tilted band dispersion of type II Weyl semimetals (fig. 4.3b). The Fermi surface in this case is open and has a finite density of states [156]. The topological features of type II Weyl points are different than in Weyl points occurring at a single point touch with an untilted band dispersion.

Weyl semimetals set the scene for very unique physical properties, including unconventional magnetotransport behavior [159, 160, 161, 162, 163, 164, 165]. Type I Weyl semimetal state was predicted to exist and experimentally confirmed in the inversion breaking materials of the TaAs family [157, 166, 167, 168, 169, 170, 171].

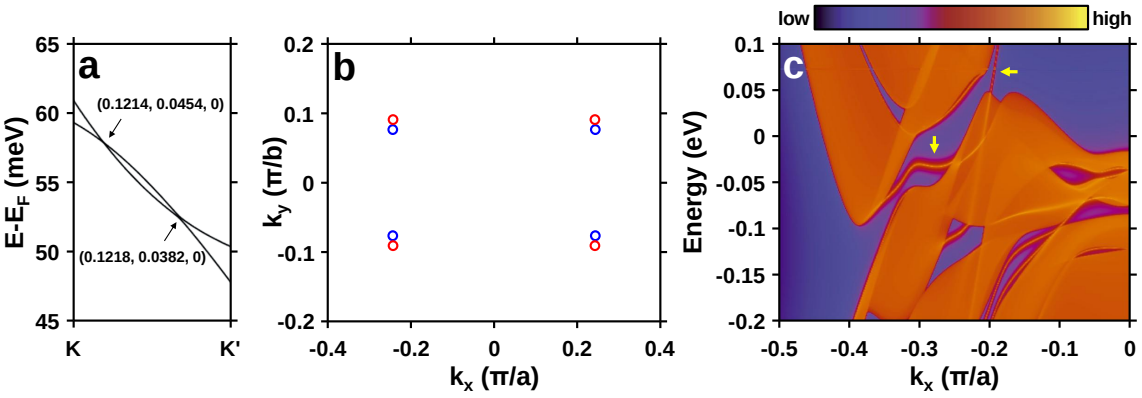

Figure 4.4: (a) Adapted from [156]. Zoom into the calculated bulk band structure of WTe_2 along the line K-K′ showing one of the four pairs of Weyl points. K = (0.1208, 0.0562, 0) and K′ = (0.1226, 0.0238, 0) in units of reciprocal lattice constants. (b) Location of the four pairs of Weyl points in the $k_z = 0$ plane. Positive and negative chirality points are depicted in blue and red, respectively. (c) Adapted from [156]. Calculated spectral density function of the (001) surface of WTe_2. The bulk band structure is given by the orange shaded areas. The surface states join different parts of the band structure giving the thin lines. Yellow arrows mark some of those surface states.

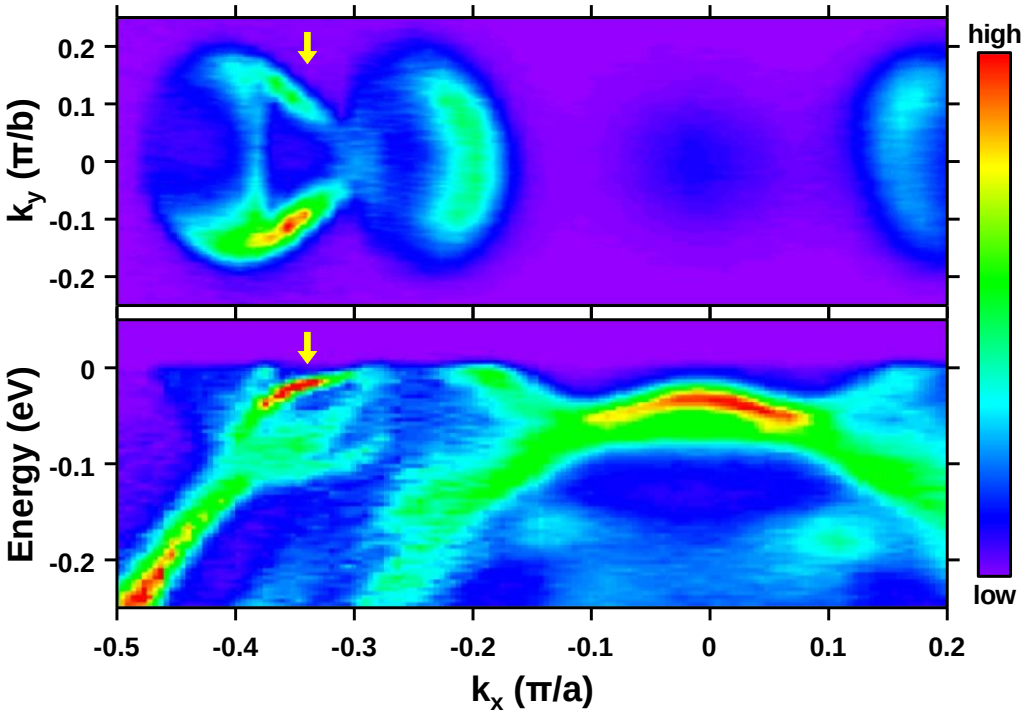

Figure 4.5: Adapted from [186]. ARPES intensity measured at 16 K in WTe_2 showing a surface state (yellow arrows) connecting the electron and hole pockets.

Along with WTe_2, some other transition metal dichalcogenides as $MoTe_2$ [172, 173] and $Mo_xW_{1-x}Te_2$ [174] have recently been proposed as type II Weyl semimetals.

Weyl points act as topological charges, being either sources or sinks of Berry curvature. As the net topological charge (or Chern number) must be zero inside the Brillouin zone, Weyl points always appear in pairs of opposite chirality. The projections of these Weyl points into the surface are connected by a surface state called Fermi arc (fig. 4.3c). It appears as an open contour in the surface Fermi surface, with the edges of the arcs located at the Weyl points. Such open contours were first observed in 3D Dirac systems [175].

As the surface Fermi arcs are directly related to the topologically nontrival features of the bulk bands, the presence of such states in the surface is the main fingerprint to seek for when studying Weyl semimetals. Angle resolved photoemission spectroscopy (ARPES) has revealed the presence of arc-like surface states in TaAs [169, 170], TaP [176] and $MoTe_2$ [177, 178, 179]. However, it is often not easy to prove the nontriviality of these surface states. STM quasiparticle interference measurements (QPI) have also been established as a powerful technique to identify topological surface states in Dirac and Weyl semimetals above and below the Fermi level [180, 181]. QPI has found surface states in several semimetals such as TaAs [182, 183], NbP [184] or $MoTe_2$ [177, 185], but additional signatures of the Weyl state are still needed to dismiss topologically trivial interpretations for the surface states.

In WTe_2, four pairs of type II Weyl points have been predicted to occur at 52 meV and 58 meV above the Fermi level [156] (fig. 4.4a). The location of the different

Weyl points in reciprocal space is shown in fig. 4.4b. Figure 4.3c shows the Fermi arcs expected to emerge in the surface connecting the electron and hole pockets. ARPES measurementes made up to the Fermi level in the occupied states show the electron and hole pockets below the Fermi level and a surface state joining them. It is known from ARPES measurements that the band structure is strongly temperature dependent. A Lifshitz transition where a temperature induced shift of the chemical potential leads to hole pockets disappearing from the Fermi surface at about 160 K has been reported [187]. Arc-like surface states have also been reported in this material below the Fermi level by ARPES [186]. These surface states are clearly connecting the electron and hole pockets as shown in fig. 4.5. However, the question about the nontriviality of the surface states remains unsolved. In fact, ARPES data seems to be well described by a topologically trivial model [188]. High temperature ARPES measurements reveal features within the band structure of empty states that have been associated to type II Weyl fermions [189]. Nevertheless, these are obtained thanks to a large temperature induced smearing, which might considerably influence the band structure [187]. QPI measurements have also attempted to explore the surface states in WTe_2 at zero magnetic field [153, 154, 155]. Some features above the Fermi energy have been associated to the scattering between arc-like surface states, but the relation between the features of the bulk band structure and STM results is not clear yet.

In this chapter, I will present some STM measurements we performed for different values of the magnetic field up to 14 T. I will also present the measured band structure from QPI measurements and compare it with the bulk calculations. I will also discuss some features that can be related to topologically nontrivial surface states in WTe_2.

4.2 Atomic structure

WTe_2 crystallizes in an orthorhombic structure belonging to the noncentrosymmetric $Pmn2_1$ space group [190]. The primitive unit cell contains four formula units and the lattice parameters are a = 3.477 Å, b = 6.249 Å and c = 14.018 Å. As shown in fig. 4.6a, WTe_2 has the typical layered structure of transition metal dichalcogenides, with strong covalent intra-layer bonding and weak van der Waals inter-layer interactions. Each layer consists of a Te-W-Te sandwich with W atoms forming zigzag chains along a-axis. The distance between two consecutive W atoms is significantly smaller along a-axis than along b-axis or c-axis, what gives the material a quite one-dimensional behavior.

The lack of inversion symmetry in this system results in a difference between the two (001) terminations of the crystal [188]. Both inequivalent surfaces have identical chemical composition and they even present the same buckling patterns for W and Te atoms. Figure 4.6c compares a side view of the so-called top and bottom surfaces. The position of top Te atoms is the same in both terminations, but the average distance to the underlying W plane differs between both terminations. Depending

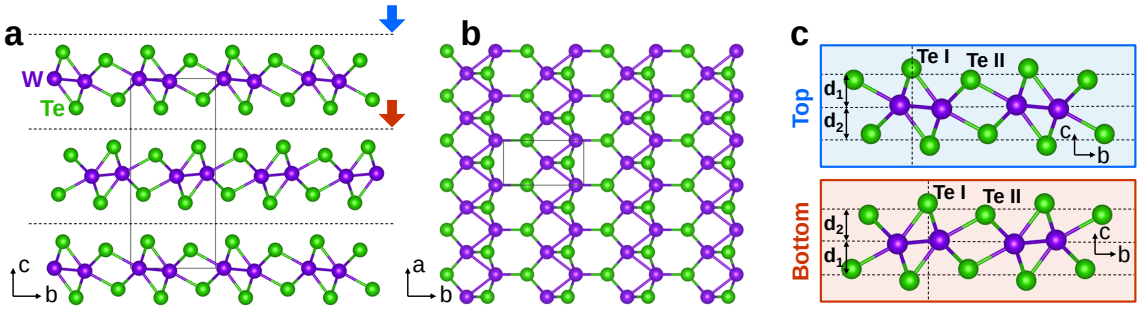

Figure 4.6: Side view (a) and top view (b) of the atomic structure of WTe_2. W atoms are depicted in purple and Te atoms, in green. Black rectangle shows the unit cell. (c) Comparison between the two possible terminations of the crystal. The position of top Te atoms is the same for top and bottom terminations, but the distance to the underlying W plane is different. Depending on the cleaving plane (blue and orange arrows in (a)) we can access one termination or the other. Inequivalent positions of Te atoms are marked as Te I and Te II in (c).

on the cleaving plane we can access one termination or the other. Surface states are predicted to be slightly different in both terminations of the crystal.

High quality surfaces for STM can be found in WTe_2 [154, 155, 191, 192]. STM experiments show changes in the topographical structure at the surface when cooling down to 4.2 K [191]. In this thesis, we measured WTe_2 single crystals provided by the group of Prof. Paul C. Canfield. They were grown from a Te-rich binary melt following the procedure described in Refs. [187, 193]. The crystals were plate-like with typical dimensions of 2 mm × 0.1 mm × 0.01 mm (fig. 4.7a). The crystallographic *c*-axis was perpendicular to the largest crystal surface. Figure 4.7b

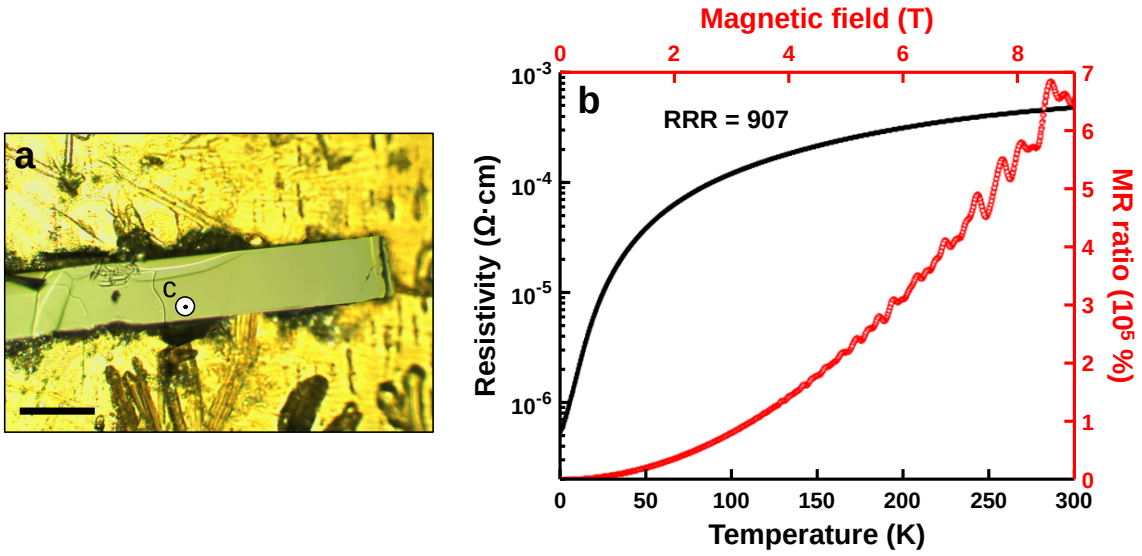

Figure 4.7: (a) Optical microscope image of one of the measured WTe_2 samples. Scale bar is 100 μm long. (b) Adapted from [187]. Measured resistivity versus temperature (black) and magnetoresistance ratio versus magnetic field (red) in one of the crystals from the same batch we took our STM samples from.

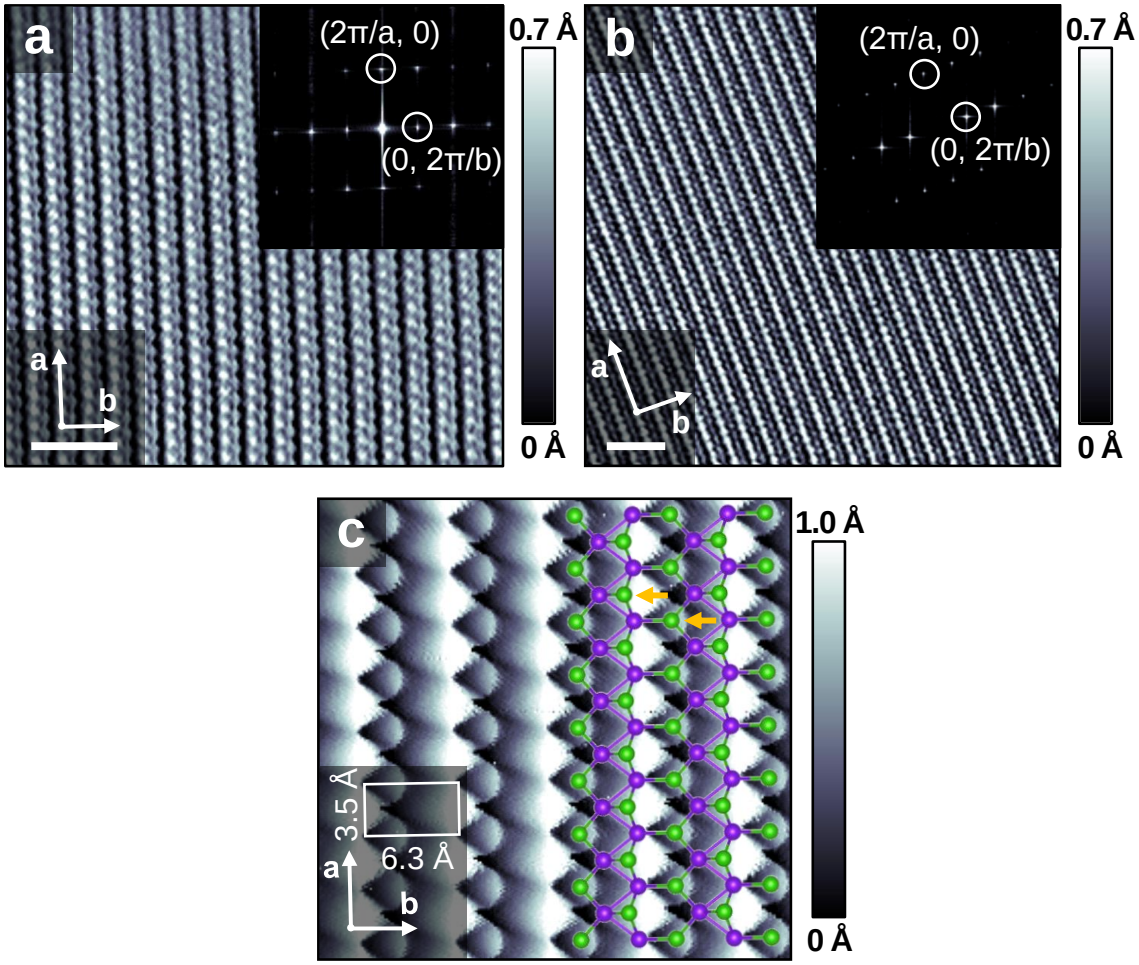

Figure 4.8: (a) STM topographic image of WTe_2 taken at 100 mV with a setpoint current of 6 nA (T = 100 mK, B = 0 T). Fourier transform of the topography with highlighted first order Bragg peaks is shown in the inset. (b) 14 T STM topography measured at 100 mV with a setpoint current of 4 nA displaying the same zero magnetic field atomic arrangement (T = 4.2 K). Fourier transform is shown in the inset. (c) High resolution topography of a smaller area where the two inequivalent positions of Te atoms are perfectly resolved. The white rectangle defines the unit cell dimensions. Orange arrows mark the two inequivalent positions of Te atoms. A diagram of the atomic structure for bottom termination is plotted over the topography. Top Te atoms are depicted in green and subsurface W atoms, in purple. White arrows indicate the orientation of a and b crystalline axes. Horizontal scale bars in (a, b) are 2 nm long.

shows resistivity and magnetoresistance measurements in these crystals [187]. The extremely high residual resistance ratio (RRR) of 907 reflects the high quality of the crystals. Magnetoresistance goes up to 6.5×10^5 % at 9 T, confirming the large quadratic response of resistivity to magnetic field previously reported by Ali *et al.* [125].

We performed scanning tunneling measurements using the setup mounted during this thesis (see chapter 2). We exfoliated the sample in-situ in cryogenic conditions by gluing a post on top of the sample and pushing the sample holder at low

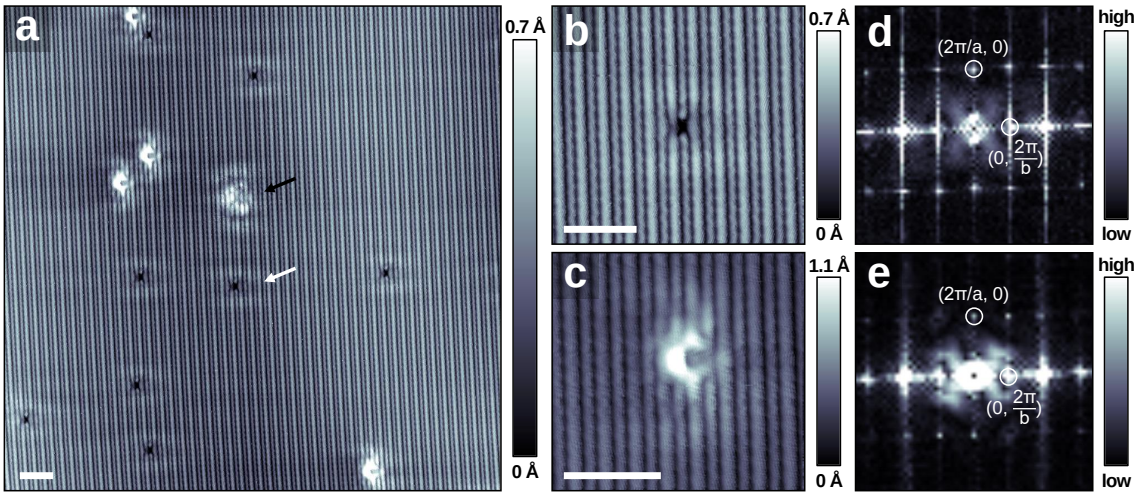

Figure 4.9: (a) Large STM topographic image showing a region with different types of defects. White and black arrows mark vacancy-like defects and interstitials, respectively. Wavelike patterns can be seen coming from the scattering around the defects. (b) Zoom into a vacancy-like defect showing the lack of a surface Te atom. The surface pattern caused by this disruption is slightly asymmetric along *b*-direction. (c) Zoom into an interstitial-like defect. The asymmetry along *b*-direction is more clear in this case. (d,e) Fourier transforms of the images in (b) and (c), respectively, with highlighted first order Bragg peaks. Topographies in (a, b, c) were measured at 100 mV with a setpoint current of 6 nA (T = 100 mK, B = 5 T). Horizontal scale bars in are 2 nm long.

temperatures as described in section 2.3.4. As a result of the cleaving process, clean surfaces of Te atoms were obtained. Figure 4.8a shows one of the STM topographic images we took at 100 mK and zero magnetic field. The obtained topography is equivalent to that found in previous works [153, 154, 155, 191, 192]. The surface atomic structure consists of arrangements of Te atoms in which we can identify the two inequivalent positions of these atoms. Te atoms order forming stripes along the *a*-direction, which is also the orientation of the underlying W zigzag chains. The patterns observed in STM images are exactly the same at 14 T (fig. 4.8b), advancing that there are no strong magnetic field induced modifications in the electronic structure of WTe_2. Figure 4.8c shows the schematic atomic structure for one the two possible terminations placed on top of a high resolution topographic image in which Te atoms are perfectly resolved. The measured unit cell dimensions are 3.5 Å along the *a*-axis and 6.3 Å along the *b*-axis.

As I introduced before, there is a difference between the two possible surface terminations. However, from the STM point of view, the distribution of Te atoms is completely identical in both situations. As shown in fig. 4.6c, the difference is in the distance between adjacent planes. This makes it almost impossible for STM topographic images to distinguish between the two unequal surfaces.

The mobility and the residual resistivity can be calculated from the density of defects, which is quite small in agreement with the high RRR value of the crystals. We can estimate a value for the density of defects of approximately 1.3×10^{12} cm^{-2} from the topographies we measured (fig. 4.9a). Using the lattice parameters a = 3.5 Å

and b = 6.3 Å, we can assume that electrons can move freely along ~ 350 unit cells, and thus estimate a mean free path of ~ 170 nm. Introducing these values in the Drude model for the conductivity, we obtain a residual resistivity of ~ 1.9 $\mu\Omega$·cm and a mobility of ~ 4.3 m^2/V·s. Although this is a very simple approximation, both values are consistent with those previously reported [187].

We identify two different types of defects on the surface of WTe_2 (fig. 4.9a). We find either small point vacancies (white arrow) or bump-like features that we refer to as interstitials (black arrow). High resolution topographies of a vacancy and an interstitial are shown in fig. 4.9b,c, respectively. Electrons scatter around the defects producing oscillating patterns that are clearly visible in the topography of fig. 4.9a. The wavelike scattering patterns around the defects are quite one-dimensional along a-direction and both types of defects produce asymmetric patterns along b-direction. This asymmetry is more obvious in the case of interstitials (see fig. 4.9d). Fourier transforms of the images in fig. 4.9b,c are shown in fig. 4.9d,e, respectively. The features at smaller $\vec{q}$ come from the electronic scattering around the defects and studying their energy evolution we can extract information about the band structure of the material as I will discuss below.

4.3 Bulk density of states

As introduced above, WTe_2 is a semimetallic compound with very low density of states around the Fermi level and a very weak overlap between conduction and valence bands (see fig. 4.10). Bulk band structure calculations predict a couple of hole pockets and a couple of electron pockets along the Γ-X direction [156, 187].

Figure 4.11a shows a zoom into the bulk calculated band structure along the Γ-X direction inside the energy range we explored in our STM measurements. Electron and hole bands are plotted in blue and red, respectively. Figure 4.11b shows some spatially averaged tunneling conductance versus bias voltage curves we measured

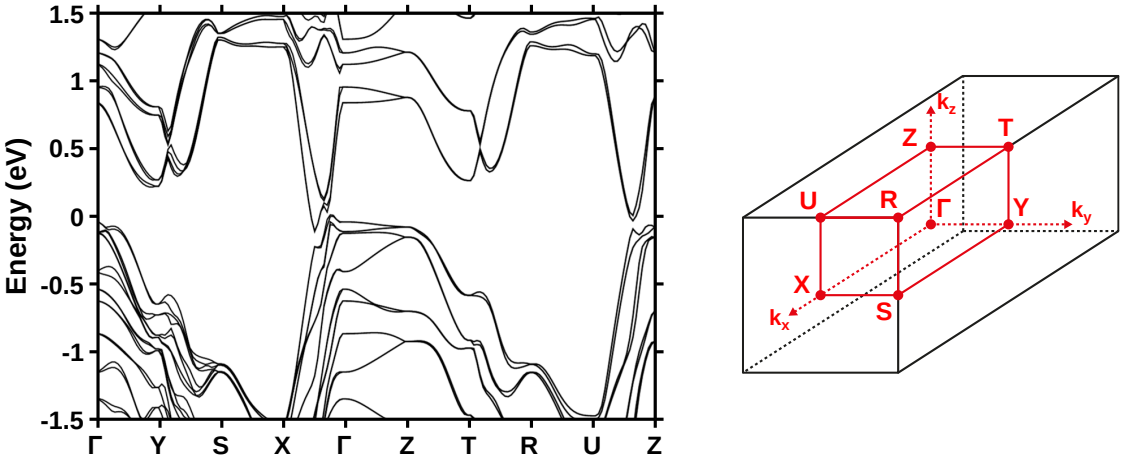

Figure 4.10: Adapted from [156]. Calculated bulk band structure of WTe_2 along high symmetry directions (left) together with the diagram of the Brillouin zone (right).

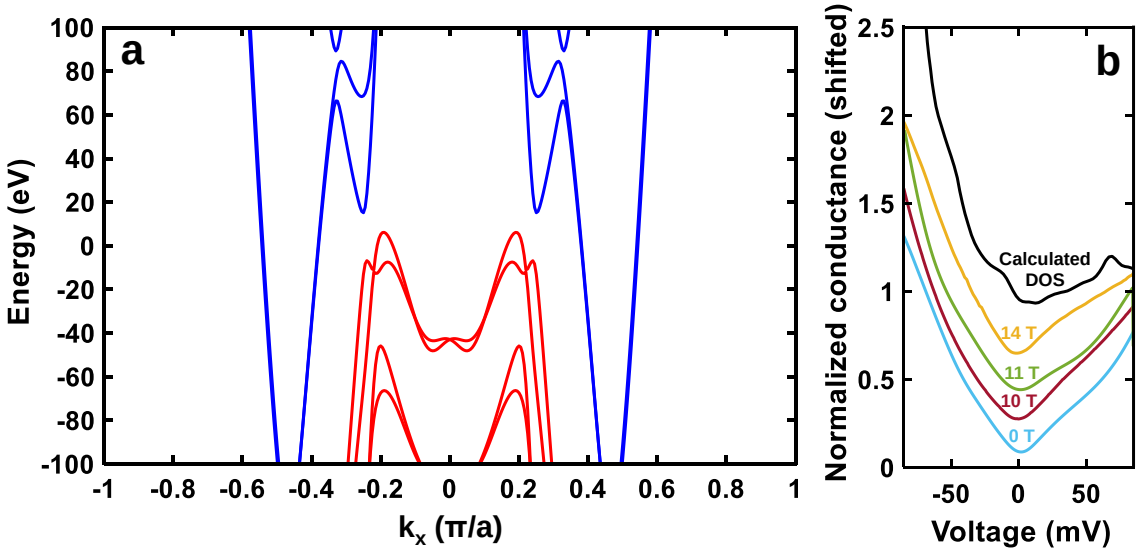

Figure 4.11: (a) Calculated bulk band structure along the Γ ($k_x = 0$) to X ($k_x = 1$) direction inside the energy range explored in the experiment. Electron and hole bands are depicted in blue and red, respectively. The calculations are shifted 45 meV downwards to match our experimental results. (b) Spatially averaged normalized tunneling conductance versus bias voltage curves measured at magnetic field ranging from 0 T to 14 T (colored lines). Normalized density of states obtained from the band structure in (a) is also plotted (black line) in the same range of energies for comparison. Curves are shifted upwards for better visualization.

for different values of the magnetic field together with the density of states expected from the density functional theory (DFT) bulk band structure calculations in the same energy range. The general shape of our measured conductance curves is similar to that of the calculated density of states after shifting it 45 meV downwards. The need of this shift comes from a certain ambiguity in the position of the Fermi level in DFT calculations combined with the common presence of small surface potentials in semimetals. The 45 mV shift is comparable to that of previous STM studies [154, 155, 191]. Magnetoresistance in WTe_2 is extremely high, so if this phenomenon was driven by changes in the band structure of the material, we would expect to see major modifications in the conductance curves when applying magnetic field. However, we do not appreciate any drastic change in these curves with magnetic field up to 14 T. This implies that the band structure in WTe_2 remains constant with magnetic field. Notice that Zeeman splitting is of the order of 1.6 meV at 14 T, without spin-orbit coupling. Clearly, spin-orbit coupling does not enhance Zeeman splitting enough to produce identifiable changes in the band structure.

Although we do not observe quantum oscillations in the high magnetic field conductance curves shown in fig. 4.11b, Shubnikov-de Haas oscillations in WTe_2 are observed at relatively low fields [152, 187]. This means that the high field band structure is Landau quantized. Assuming a parabolic dispersion, starting from the

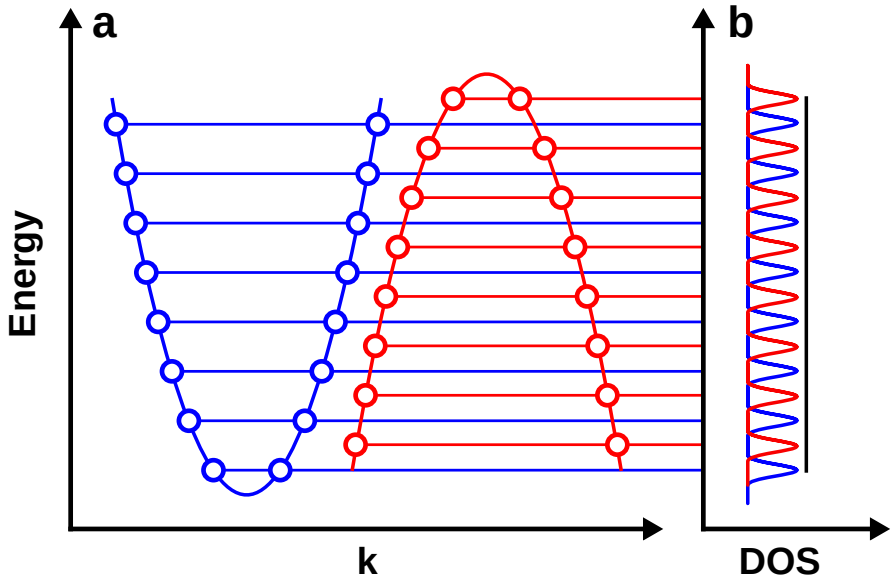

Figure 4.12: (a) Simple model of a system with two quantized parabolic bands. Landau levels are represented by blue and red circles in the electron and hole bands, respectively. (b) Density of states versus energy coming from the same color quantized bands in (a). Black line represent the smooth density of states curve that would measure an experiment unable to resolve the individual peaks.

bottom (or top) of an electron (or hole) band, the energy of the discrete Landau levels is given by

$$E_n = \hbar\omega_c(n + \frac{1}{2}), \tag{4.6}$$

where $\omega_c = eB/m^*$ is the cyclotron frequency, e is the electron charge, B is the magnitude of the applied magnetic field and m^* is the effective mass of the quantized band. If we were measuring a system with single quantized bands, the tunneling conductance curve would feature peaks at the energies corresponding to the different Landau levels. However, this is not the situation in WTe_2. Here, we have four different bands whose effective masses are of around 0.3 times the free electron mass [187]. Introducing this effective mass in eq. (4.6), we estimate an energy separation between consecutive Landau levels of around 0.39 meV/T. Thus, at 10 T, that separation will be 3.9 meV, what falls well within our resolution in energy. However, we observe a density of states which shows no features of Landau quantization. To explain this, we have to consider different possible smearing sources. First, we have to remind that we are measuring an average of the densities of states of a set of different bands. Actually, four. Their bottom and tops are slightly shifted with respect to each other. Therefore, the Landau levels are not located all at exactly the same energy. As we schematically show in fig. 4.12, already two bands produce a significant increase in the amount of observable Landau levels. If we add more bands with uncoordinated Landau levels to the model, the energy difference between two consecutive peaks in the density of states will reduce and eventually become smaller

than the finite energy resolution of a particular experiment. Thus, the experiment will not be able to resolve the individual peaks and the result of the measurement of the density of states will be a smooth curve (see black line in fig. 4.12b). In the case of WTe_2, increasing this to four bands may reduce the separation between consecutive peaks down to 1 meV at 10 T in the worst case scenario. Still, we should be able to resolve those features in our curves. Therefore, electronic scattering around impurities may induce an energy smearing in the density of states that explains the smooth curves we measure at high magnetic fields. Additionally, the curves we show in fig. 4.11b are spatially averaged inside a region of around 20×20 nm^2. Hence, any eventual spatial dependence in the Landau oscillations might further contribute to the energy smearing.

4.4 Band structure from QPI experiments

To explore the Fermi surface of WTe_2 we performed some quasiparticle interference measurements. For this technique to work it is necessary to have impurities or defects in the surface to act as scattering points. The method is described in section 2.1.4. As seen in fig. 4.9a, the scattering around the defects produce oscillating patterns in the surface that, in the case of WTe_2, are mainly one-dimensional along a-direction.

Figure 4.13 shows the topography (a), the normalized conductance map at 35 mV (b) and its corresponding fast Fourier transform (FFT) inside the first Brillouin zone (c) in a region showing some vacancy-like defects and one interstitial. FFT maps are mirror symetrized along the two in-plane crystalline axes. We applied a 3×3 pixel average filter to further increase the signal to noise ratio, and we eliminated results for low $\vec{q}$ by subtracting a Gaussian core as described in section 2.1.4.

A typical image of the quasiparticle interference is given in fig. 4.13c. We observe mostly a one-dimensional pattern along q_x, with several scattering vectors along the $q_y = 0$ line. When leaving the $q_y = 0$ line, scattering provides either opened bow tie ("⊃⊂" shape with respect to $q_x = 0$) or closed infinity-like ("⊂⊃" with respect to $q_x = 0$) shaped patterns. The position in q_x and their shape along q_y changes considerably when modifying the bias voltage. Let us first focus on discussing the energy dependence of the features using their position in q_x.

4.4.1 Bulk band structure

Let us analyze the scattering patterns and the energy dependence of the bands at $q_y = 0$. QPI maps measured in the region shown in fig. 4.13 are shown in fig. 4.14a for some representative energies. Colored circles in fig. 4.14a mark the position of the main scattering vectors we observe at $q_y = 0$. We use the same colors in fig. 4.15a, where we show the $q_y = 0$ profiles from our QPI maps for all the energies of the study, and in fig. 4.15a, where we plot the different vectors we identify on top of the calculated bulk band structure.

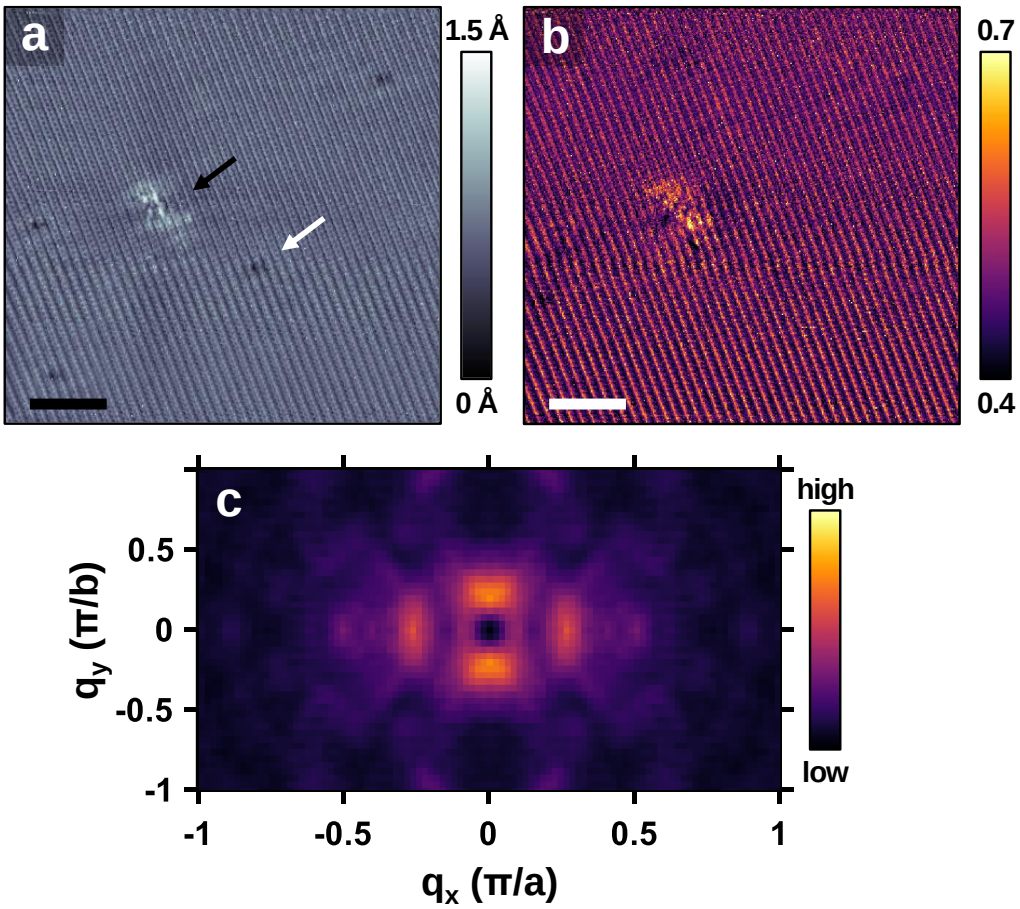

Figure 4.13: (a) STM topographic images of the regions where we studied the QPI scattering. It shows both vacancies (white arrow) and interstitials (black arrow). (b) Normalized tunneling conductance map at 35 mV inside the region shown in (a). Symmetrized FFT of this map inside the first Brillouin zone is shown in (c). Main scattering $\vec{q}$ vectors are obtained from the FFTs of the conductance maps. Horizontal scale bars in (a) and (b) are 5 nm long.

Starting at positive energies, at 75 meV we can identify three main scattering points given by the orange, green and pink points in fig. 4.14a. When decreasing energy, the three scattering vectors reduce their size. At zero bias, the intensity is smallest as the overall density of states is small. When reaching negative bias, we can identify two spots (pink and green points in fig. 4.14a at −50 meV) and one additional spot (light blue point). When looking on the $q_y = 0$ profiles as a function of the energy (fig. 4.15a), we can see more clearly the evolution of these spots as bright nearly vertical stripes.

We can now compare our data with band structure calculations and identify the most likely scattering patterns. Figure 4.14b shows the calculated constant energy contours of the Fermi surface inside the first Brillouin zone for the same representative energies. Calculations were performed by the group of R. Arita. We should note from the start that nearly all bands are spin degenerate [194]. However, the degeneracy is very small and the Zeeman effect of the magnetic field occurs

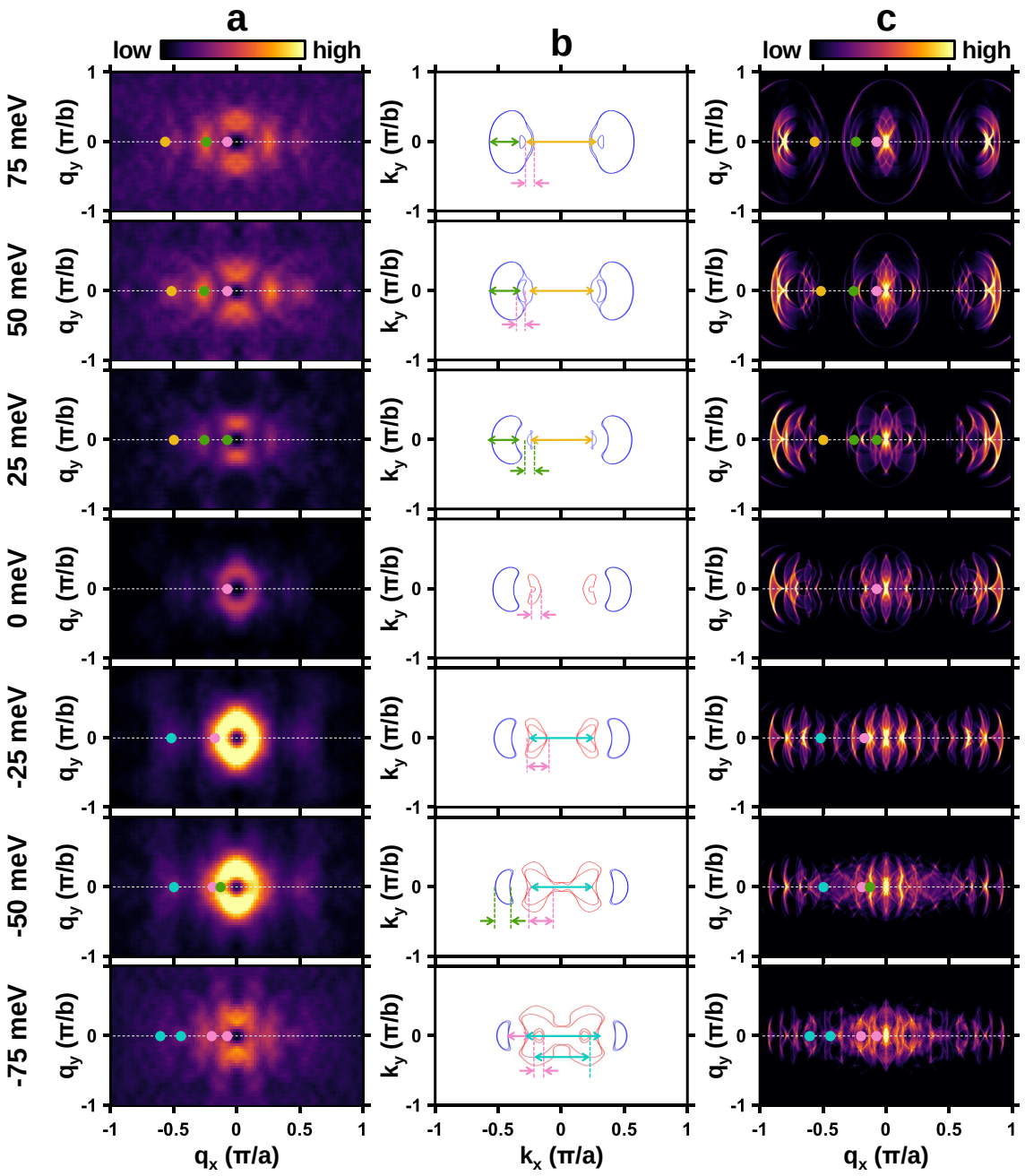

Figure 4.14: (a) QPI maps at the some representative energies measured at zero field in the region shown in fig. 4.13. Colored circles indicate the main scattering vectors we identify for each energy. (b) Constant energy contours of the Fermi surface inside the first Brillouin zone extracted from the calculated bulk band structure for the same energies. Electron and hole pockets are plotted in blue and red, respectively. Same color arrows indicate the regions of the Fermi surface connected by each of the scattering vectors we identify in the (a). (c) Bulk scattering probability maps obtained from the 2D-autocorrelation of the contours in (b). Scattering vectors identified in (a) are plotted in the same color over the maps in (c). White horizontal dashed lines mark the $q_y = 0$ profiles plotted in fig. 4.15a.

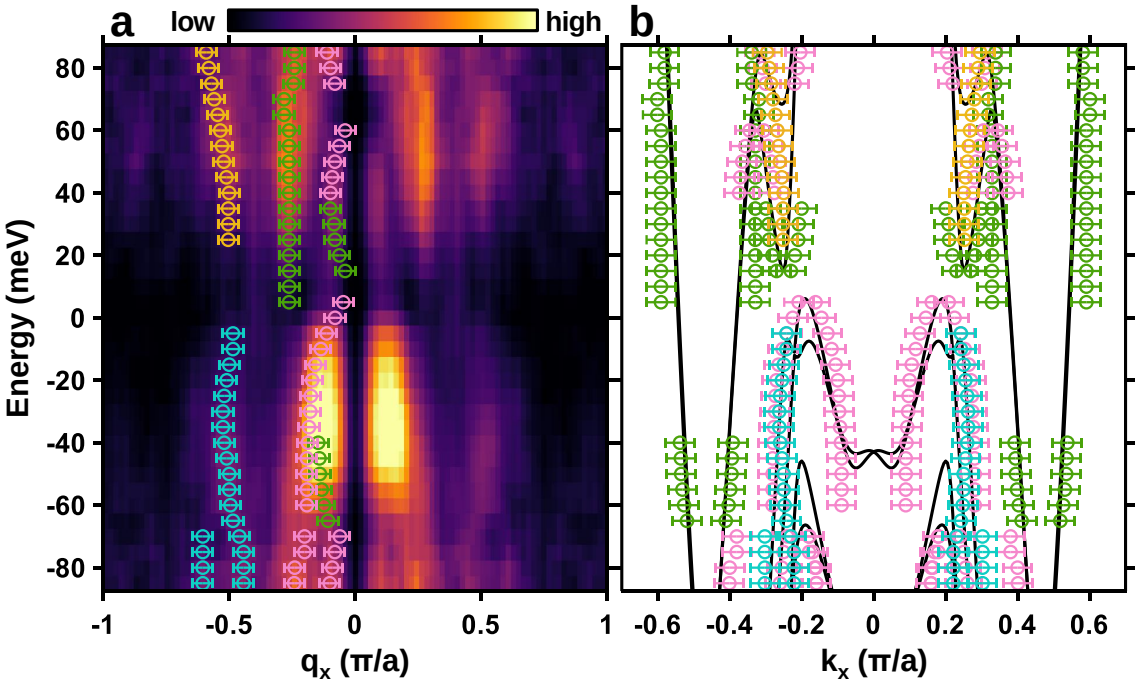

Figure 4.15: (a) $q_y = 0$ profiles along q_x-direction from the QPI maps (see horizontal dashed lines in fig. 4.14) stacked for all the energies of the study. Colored points with errorbars show the evolution of the main scattering $\vec{q}$ vectors we observe. (b) Measured scattering $\vec{q}$ vectors from the profiles in (a) plotted over the calculated bulk band structure (black lines in the background) in the energy range.

on a negligible energy range [194]. In principle, defects can be magnetic and favor or impede scattering among bands with different spin texture. However, as the degeneracy is very small, this effect can be neglected by now.

With these caveats in mind, we plot the scattering vectors we identify in fig. 4.14a as same color arrows on top the calculated bulk Fermi surface in fig. 4.14b. We note that the large orange scattering vector observed at 75 meV in fig. 4.14a is due to scattering between the inner sides of the small electron pockets (see orange arrow in fig. 4.14b). This vector decreases in size when decreasing energy and disappears for negative bias, as the bottom of the electron band is close to 0 meV (see fig. 4.15b).

The green vector at 75 meV in fig. 4.14a is adscribed to intra-band scattering inside the small electron pockets located at large k_x. This vector decreases slightly in size and continues below the Fermi level (see fig. 4.15b).

Finally, we identify the pink vector, which corresponds to small $\vec{q}$ scattering between different portions of the electron-like bands. Above 60 meV, this is due to scattering inside a small electron band, and below, to scattering between locally hole-like portions of the bands (see fig. 4.15b).

The pattern marked by pink dots below −25 meV in fig. 4.14a is due to intra-band scattering in the hole band (see fig. 4.15b). At −75 meV we identify an additional pink vector in fig. 4.14a due to the inter-band scattering between the electron and hole pockets (see fig. 4.15b).

Between −25 meV and +25 meV, we notice a strongly increased intensity for low $\vec{q}$ (see fig. 4.14a and fig. 4.15a). This can be attributed to the presence of flat portions of the band structure due to the hole bands in this energy range (fig. 4.15b).

Now we can discuss the scattering patterns along q_y expected from band structure calculations. These scattering probability maps are shown in fig. 4.14c and were calculated by applying a 2D-autocorrelation function to the calculated Fermi surface maps in fig. 4.14b. Scattering $\vec{q}$ vectors with higher intensity in the autocorrelated maps connect states with large joint density of states (JDOS) [180]. We see that there is a considerable amount of patterns. In the experiments, only a few of them are observed. This might be due to the scattering potential or to smearing by scattering. We can however qualitatively discuss the q_y dependence of those spots that we identified in fig. 4.14a, which are plotted on top of the scattering probability maps in fig. 4.14c.

Generally, an opened bow tie shape ("⊃⊂" shape with respect to $q_x = 0$) in the scattering pattern implies scattering between two bands that draw two closed circular patterns in q_x-q_y, while and infinity-like shape ("⊂⊃" shape with respect to $q_x = 0$) in the scattering pattern implies scattering inside a circularly shaped band in q_x-q_y. The orange spot at 75 meV in fig. 4.14c provides a bow tie shape. The green spot should provide the opposite, an infinity-like shape, at 75 meV. However, it also provides a bow tie shape. This discrepancy will be discussed below. For energies below the Fermi level, the patterns are nearly independent of q_y, although a slight bow tie shape can be identified for the light blue spot corresponding to the scattering between the edges of the hole band at −25 meV and −50 meV.

Thus, we can make a rather detailed account of the the full band structure of WTe_2 from our QPI analysis. Our QPI data proves to be robustly consistent with the calculations as every scattering $\vec{q}$ vector we observe connects two intra-band or inter-band points of the bulk calculated band structure in this range of energies.

4.4.2 Surface states

As bulk electron and hole bands also contribute to the scattering on the surface, it is convenient to compare our QPI data with first-principles surface calculations to try to distinguish the features coming from the surface states from those coming from the bulk bands.

Surface calculations predict arc-like surface states connecting the electron and hole pockets. Figure 4.16a shows the calculated spectral density maps at the surface at −50 meV, with yellow arrows indicating the position of the arc states. We isolate these arc states for better visualization and plot them in fig. 4.16b without the contribution of the bulk bands to the spectral density at the surface. Same way we proceeded with bulk calculations, 2D-autocorrelating the map with the two isolated arc states we obtain the JDOS map associated to these surface states (fig. 4.16c). When there are open contours in the surface Fermi surface, these surface scattering probability maps are expected to show some characteristic features. For arc-like states like those predicted in WTe_2, the scattering of one of the arcs with itself

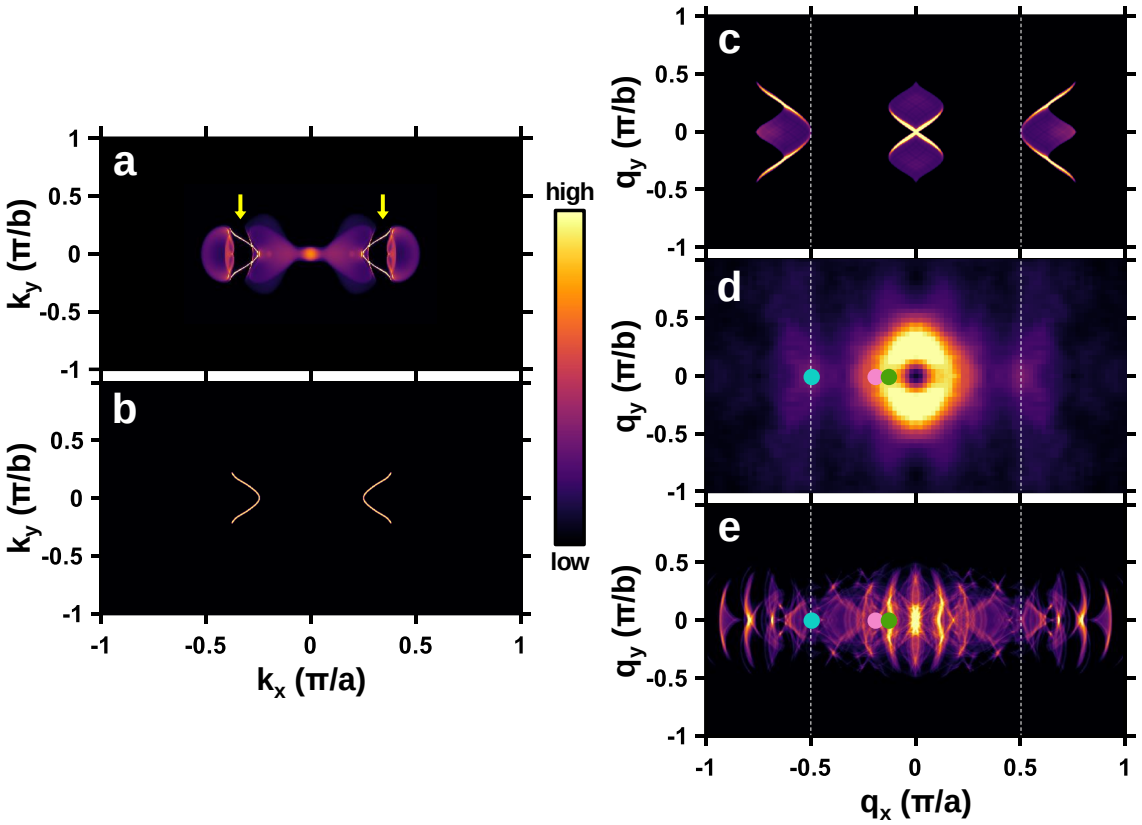

Figure 4.16: (a) Calculated spectral density function at the surface of WTe_2 at -50 meV. Yellow arrows mark the surface states between the electron and hole pockets that are plotted in (b) isolated from the contribution of the bulk bands to the spectral density. (c) JDOS associated to the surface states in (b). (d) Measured QPI map at -50 meV. Colored circles mark the bulk scattering vectors we identify at this energy. (e) Bulk JDOS obtained from the calculated Fermi surface at -50 meV. Vertical dashed lines at q_x = ±0.5 π/a indicate the expected position of the features coming from the scattering between the two arc states.

produces a cross-shaped pattern centered around q_x = 0, and the scattering between one arc and the other gives rise to arc-like features at a q_x value that equals the k_x separation between the arc states in reciprocal space [180, 195].

Our QPI map at −50 meV is shown in fig. 4.16d. Looking for signatures of the arc-like surface states in our QPI data, we observe a higher scattering intensity in the center of the map in a $\vec{q}$ range compatible with that of the expected cross-shaped pattern in fig. 4.16c. In fact, the eventual cross coming from the arc state is resolved at higher q_y in our QPI map. Vertical dashed lines in fig. 4.16d indicate the expected q_x-position of the patterns shown in fig. 4.16c corresponding to the scattering between the arcs. We find some features in our data that could correspond to the inter-arc scattering. We can even identify how the scattering intensity draws an arc shape in the q_x-q_y plane comparable to that predicted in fig. 4.16c. Notwithstanding, there are very similar shapes in the bulk predicted scattering maps (fig. 4.16e) at the same $\vec{q}$ vectors, so it is very difficult to tell whether these scattering vectors we see in our data come from the surface state or from the

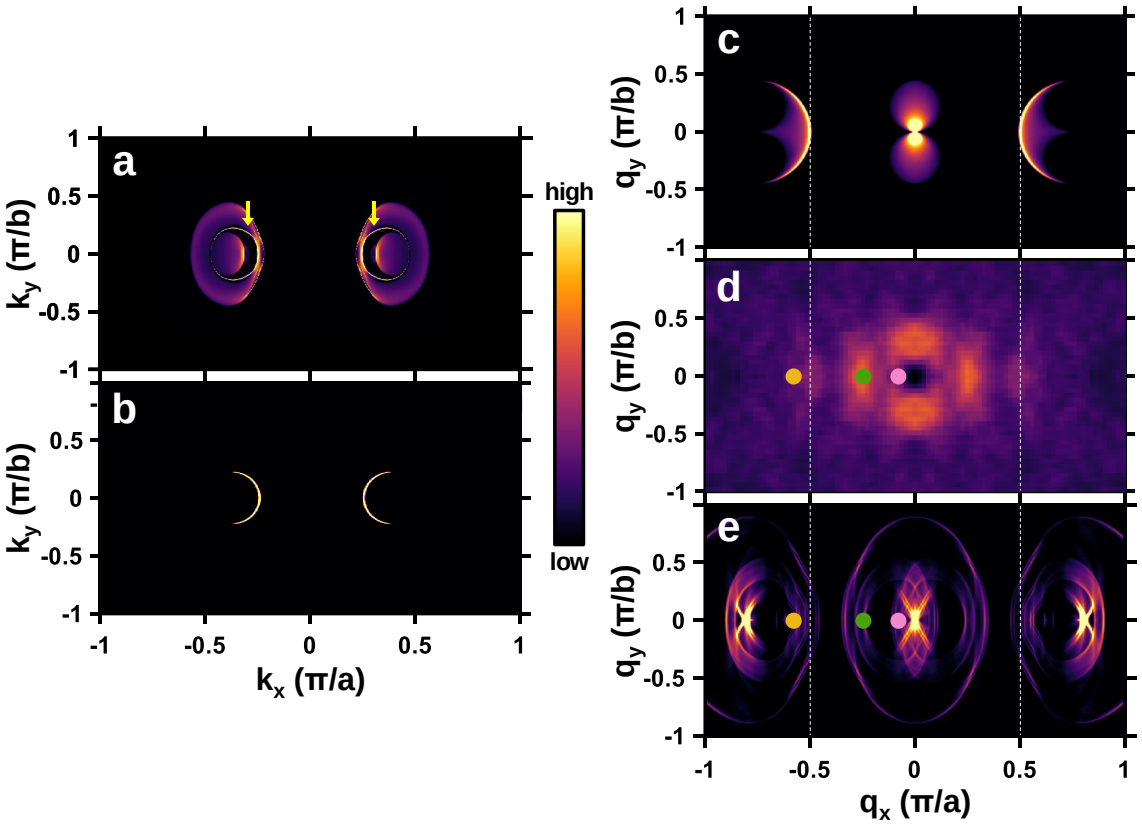

Figure 4.17: (a) Calculated spectral density function at the surface of WTe_2 at 75 meV. Yellow arrows mark the surface states. (b) Surface states isolated from the contribution of the bulk bands to the spectral density. (c) JDOS associated to the surface states in (b). (d) Measured QPI map at 75 meV. Colored circles mark the bulk scattering vectors we identify at this energy. (e) Bulk JDOS obtained from the calculated Fermi surface at 75 meV. Vertical dashed lines at $q_x = \pm 0.5\ \pi/a$ indicate the expected position of the bow tie features coming from the scattering between the two surface states.

bulk bands. In fact, in the previous section I discussed how all the scattering vectors we observe at −50 meV can be attributed to the scattering between different parts of the bulk bands (colored circles in fig. 4.16d,e).

Calculations also predict a surface state above the Fermi level (see fig. 4.4c). Figure 4.17a shows the calculated spectral density at the surface at 75 meV. Yellow arrows mark the position of the surface states. These surface states are isolated in fig. 4.17b, and fig. 4.17c shows the JDOS map associated to them. Similar to the previous case at −50 meV, the expected patterns from these surface states are an arc-like bow tie shape due to the scattering between one surface state and the other, and an eight-shaped pattern centered at $\vec{q} = 0$ accounting for the scattering of each surface state with itself. Our QPI map at 75 meV is shown in fig. 4.17d together with the scattering vectors we identified above. It shows bow tie features at the q_x position where the arc-like scattering features from the calculated surface state are expected to occur (see vertical dashed lines). The shape of the features we see in our data is very similar to that predicted by the calculations (see fig. 4.17c). This might be indeed indicating the presence of a surface state at positive energies.

However, here, bulk predicted scattering maps show similar features at the same $\vec{q}$ (see fig. 4.17e).

As I introduced above, we identified a scattering vector in our QPI data at 75 meV marked in green in fig. 4.17d whose size is consistent with an intra-band scattering vector inside the electron pockets. However, although this would imply an infinity-like shape in the q_x-q_y map, we rather observe a bow tie shape similar to those in fig. 4.17c, but located at smaller q_x. Such features are not present in the calculated bulk scattering predictions around the green vector we identify (fig. 4.17e). Therefore, our green vector might be a signature of a different surface state located at smaller k_x at 75 meV.

Extensive debates have been recently taking place regarding the nontriviality of the surface states in this material. In principle, nontrivial Fermi arcs connecting the projection of Weyl points into the surface should be much smaller accounting the near k-space location of opposite chirality Weyl points in this material (see fig. 4.4b). Therefore, the wide surface states joining the electron and hole pockets would be topologically trivial [156, 188]. Although some works claim the experimental detection of hallmark signatures of the smaller topological Fermi arcs through QPI [153, 155], we believe that this is not yet settled. From our data, we identify a possible surface state at 75 meV, and most likely another one at −50 meV. To discuss the features of these states, we hope for further insight from the magnetic properties of defects and their influence on the scattering by José J. Baldoví and coworkers at Instituto de Ciencia Molecular (ICMol), Valencia.

4.5 Conclusions

In summary, we have made a careful study of atomically resolved surfaces in WTe_2 using very low temperature and high magnetic field STM. The surface is characterized by chains of Te atoms. We have measured the spatially averaged density of states as a function of the magnetic field and found no variation with the magnetic field. This shows that the band structure does not show sizable Zeeman splitting or any other significant modification when applying a magnetic field. The absence of Landau quantization is a peculiar feature, possibly associated to the presence of many bands in the energy range we have studied. It remains to be seen how the density of states versus magnetic field behaves at atomic scale. There, it might show Landau quantization.

On the other hand, there are intense scattering patterns due to the presence of sparse defects, consisting essentially in interstitials and vacancies. Particularly, interstitials provide a sizable scattering signal. From the quasiparticle interference, and thanks to detailed comparison with band structure calculations, we can identify the main electron and hole bands at energies close to the Fermi level. Furthermore, I have discussed the possible appearance of surface states, identifying features of such states at −50 and at 75 meV. The features at 75 meV can be better viewed in the scattering signal, as these are distinguishable from bulk band structure features. It

is yet to be seen if a more careful analysis, possibly taking into account magnetic scattering, can lead to further insight in the possible topological features of the surface states.

5

States at very low energies inside the superconducting gap of Au_2Pb

5.1 Au_2Pb: a topological superconductor candidate

Since the discovery of the quantum Hall state in 1980 [196], topological materials and their novel and unique quantum states have attracted lots of attention. Recent efforts in band structure calculations have revealed a considerable amount of intermetallic compounds displaying nontrivial topological properties [197, 198, 199]. Some of these compounds become superconductors at low temperatures while possibly hosting topologically nontrivial excitations.

Similar to topological insulators, topological superconductors are characterized by a fully gapped state in the bulk and gapless conduction modes on the surface. But surface excitations in topological superconductors involve Bogoliubov quasiparticles that might display properties of Majorana fermions [200, 201]. The nonabelian statistics of these protected Majorana surface states gives these materials interesting potential applications in quantum computation [202]. Topological superconductors are rather rare as they require unconventional pairing mechanisms for a topologically nontrivial state. Some triplet superconductors, introduced in section 1.3, are actually topological superconductors too. Here, the focus is on the properties of the surface. The bulk might be a superconductor with a fully opened gap while unconventional properties are expected to manifest just at the surface.

Topological superconductivity appears naturally in ferromagnetic, spin-triplet superconductors such as UTe_2 and other heavy fermion compounds [35, 36, 203]. There has been, however, an intense activity in trying to obtain unconventional or topological superconducting properties in a number of other intermetallic compounds without rare earths in the crystal structure. Topological superconductor candidates can be obtained in artificial topological insulator-superconductor heterostructures [204, 205]. Another recipe consists in doping or pressurizing a topological material. One of the most studied cases is the topological insulator

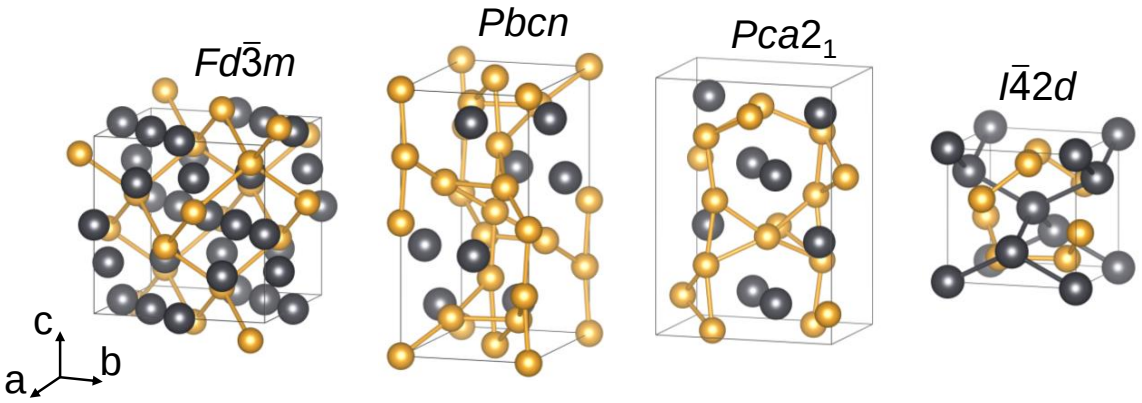

Figure 5.1: Schematic representation of the Au_2Pb crystalline structures. Au atoms are depicted in gold color and Pb atoms, in grey. Grey lines delimit the unit cell dimensions. The room temperature Laves phase $Fd\bar{3}m$ is shown at the left followed by the proposed low temperature phase, *Pbcn*, and other structures proposed to occur under pressure. All structures derive from the room temperature cubic Laves phase by small distortions of atomic positions.

Bi_2Se_3, which becomes metallic and superconductor upon Cu doping [206, 207, 208]. Bulk specific heat measurements unveil a full gap [209] and point contact spectroscopy shows an anomalous zero bias conductance peak that seems to be a signature of 2D Majorana fermions [207]. However, STM results reveal a fully opened gap across terraces and in different regions of the surface [210]. These properties are compatible with simple s-wave superconductivity. The latter experiments also show a strong tendency to have spatially inhomogeneous superconducting properties, with regions on the surface that are normal. Similar results are observed in Sr doped Bi_2Se_3 [211]. On the contrary, Nb and Tl doping does not induce surface superconductivity in Bi_2Se_3 [212]. Some other topological insulators become superconductors upon pressure [213, 214, 215, 216, 217, 218]. Nonetheless, in these cases the pressure-induced superconductivity is sometimes associated to changes in the crystalline structure. Thus, it is important to determine the gap structure and identify the Majorana surface states to label a superconductor as topological.

Topological superconductivity can also be found in natural stoichiometric compounds at ambient pressure. That is the case of $PbTaSe_2$, a noncentrosymmetric superconductor with T_c = 3.72 K [219]. $PbTaSe_2$ fulfills the two required conditions to be considered a topological superconductor candidate. It displays surface states associated to nodal-line semimetallic states [220, 221] as well as a fully gapped bulk superconducting state [222, 223, 224].

Among stoichiometric topological superconductor candidates, Au_2Pb stands out because of the presence of a 3D Dirac cone [225]. Au_2Pb crystallizes at room temperature in a cubic Laves phase[1] [226, 227]. Upon cooling, Au_2Pb undergoes

[1]Named after the German crystallographer Fritz Laves (1906 - 1978), Laves phases are intermetallic phases with composition AB_2 where A atoms arrange in a diamond-like structure an B atoms build tetrahedral structures around A atoms.

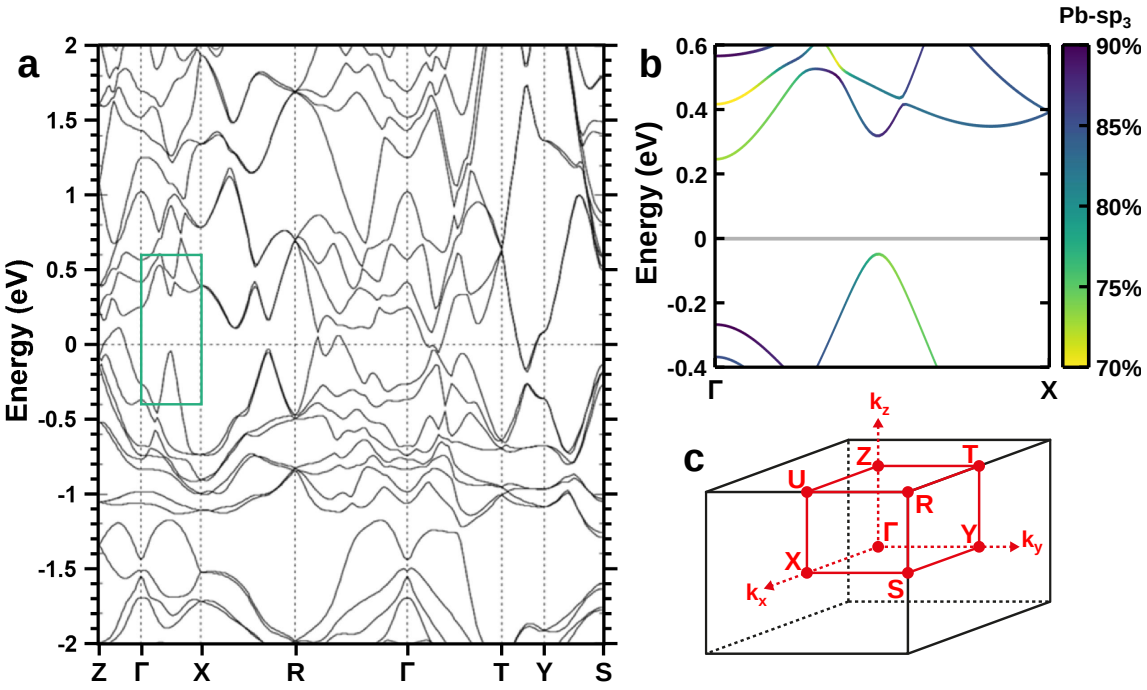

Figure 5.2: (a) Calculated electronic band structure of the low temperature orthorhombic *Pbcn* phase of Au_2Pb including spin-orbit coupling. Calculations were performed by José J. Baldoví at ICMol, Valencia. (b) Zoom into the gaped Dirac cone along the Γ-X direction showing the Pb-sp_3 character of the bands as a color code. (c) Schematic diagram of the Brillouin zone.

a series of structural phase transitions, and enters an orthorhombic structure at temperatures below 40 K. Calculations show that there are different crystalline structures for Au_2Pb that are energetically favorable at low temperatures [228] (see fig. 5.1). At room temperature, the crystal structure is the cubic Laves phase $Fd\bar{3}m$ (no. 227) with a cell parameter a = 7.9141 Å [227]. It is based on the pyrochlore lattice, with Au atoms presenting a tetrahedral arrangement distributed inside a face centered cubic lattice of Pb atoms. The structure of the low temperature phase is derived from the cubic room temperature phase by small atomic distortions [226]. The structure is orthorhombic (*Pbcn*, no. 60). The structure of the intermediate temperature phases is unknown. The ground state crystalline structure under pressure was analyzed by Wu *et al.* [228]. It was found that $Pba2_1$ phase, with slighly distorted atomic positions, is energetically more favorable than *Pbcn* at ambient pressure. Furthermore, under pressure, the structure $I\bar{4}2d$, which results from further small atomic distortions, was also proposed.

Band structure calculations predict a 3D Dirac cone [226, 227] in the room temperature cubic phase due to symmetry allowed band crossings. Angle resolved photoemission studies (ARPES) confirm the presence of the bulk Dirac cone [225]. In the low temperature phase below 40 K, the lowering of the crystal symmetry lifts the band degeneracy that allows crossing and the bands gap at the Dirac cone. Figure 5.2a shows the calculated bulk band structure on the low temperature phase of Au_2Pb, and fig. 5.2b shows a zoom into the gapped Dirac cone along the

Γ-X direction. The Pb-sp_3 character of the bands is given as a color code, with the remaining percentage until 100 % showing Au-d orbital character. Calculations were performed by José J. Baldoví at ICMol, Valencia. The gapped phase is expected to host topologically nontrivial edge states at the surface [226, 225]. These surface states coexist with electron and hole bands crossing the Fermi energy and the latter dominate the optical conductivity [226, 225, 229]. At a temperature below T_c = 1.1 K, orthorhombic Au_2Pb becomes superconductor [230]. Superconductivity is expected to show nontrivial topological properties related to those of the band structure [225, 231]. Low temperature specific heat and thermal conductivity measurements suggest that the bulk superconducting state of Au_2Pb is fully gapped [226, 232]. Point contact spectroscopy measurements reveal a superconducting gap and upper critical field that strongly increases due to the pressure exerted by the tip [231]. Experiments in single crystals under pressures of a few GPa show that T_c is slightly suppressed [227]. At higher pressures, above 5 GPa, an incomplete transition is found in the resistivity of powder samples with a $T_c \approx 4$ K. T_c decreases down to 2 K at 24 GPa [228].

In this chapter, I present STM experiments on the surface of Au_2Pb to study the behavior of the superconducting density of states as a function of temperature and magnetic field.

5.1.1 Crystal growth and characterization

Au_2Pb samples were synthesized in our laboratory with a Pb flux growth method [193, 226, 225, 233]. The obtained crystals typically had sizes of a few millimeters and showed clean triangular dark-silvered facets. Figure 5.3 shows a picture of one of the crystals we obtained, together with the x-ray data indexed with the crystallographic planes. The peaks in the x-ray data match the expected reflections for the room temperature $Fd\bar{3}m$ phase.

The resistivity and specific heat of the samples we obtained from this growth were characterized at Instituto de Ciencias de Materiales de Madrid of the Spanish National Research Council (ICMM-CSIC) from room temperature down to 2 K. For the resistivity measurements, the usual four-probe AC method was used, with electrical contacts made by gluing gold wires with silver epoxy. Specific heat was measured using a PPMS system of Quantum Design. In fig. 5.4 we show the resistivity as a function of temperature highlighting with colors the different structures found when cooling. The specific heat is shown in the inset, displaying three visible anomalies at the structural transitions. These data coincide with previous results in high quality single crystal Au_2Pb [226, 225].

We performed STM measurements using the setup mounted during this thesis and already presented in chapter 2. We cut single crystalline samples in rectangular bars that were a few mm long and a fraction of a mm wide. One of these bars was inserted in a hole in our sample holder and fixed there with silver epoxy, leaving one of the plane facets of the cubic structure facing upwards. After cooling down to 4 K, we moved the sample holder using the slider described in section 2.3.4 and approached

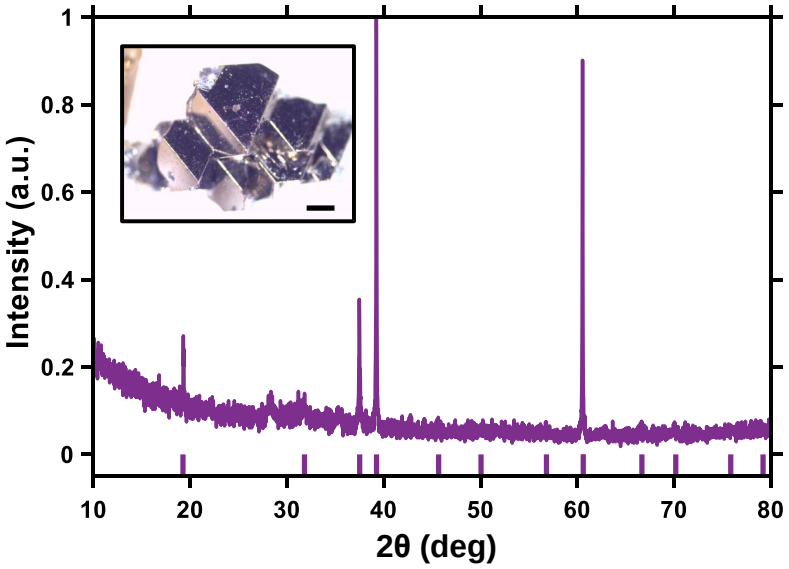

Figure 5.3: X-ray scattering data of Au_2Pb measured at room temperature. Vertical lines over the horizontal axes provide the expected reflections for the room temperature $Fd\bar{3}m$ crystal structure. Inset shows a picture of the Au_2Pb single crystals obtained after the growth. Horizontal scale bar is 1 mm long.

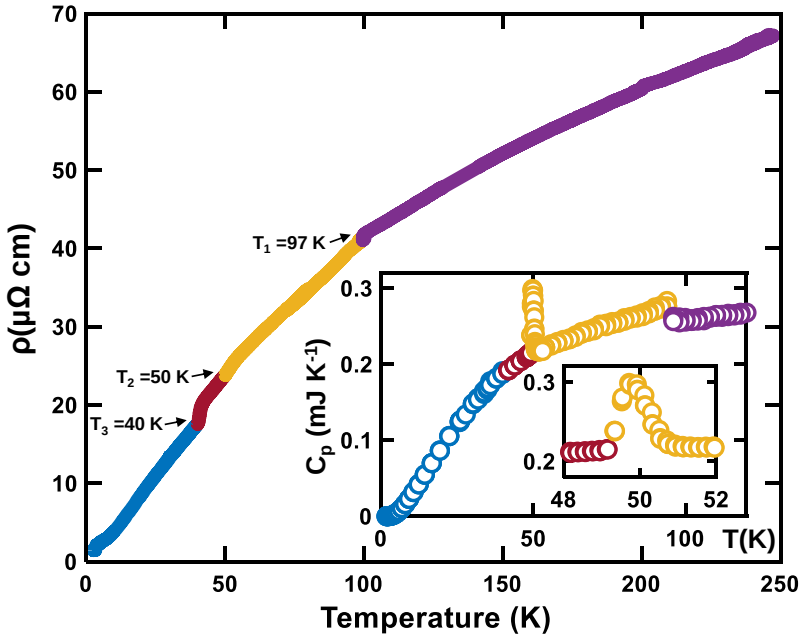

Figure 5.4: Temperature dependent resistivity. Different colors highlight the different crystalline structures obtained when cooling. Transition temperatures at 40 K, 50 K and 97 K are indicated. Inset shows the specific heat as a function of temperature displaying a noticeable anomaly at the 97 K transition and a high peak at the 50 K transition.

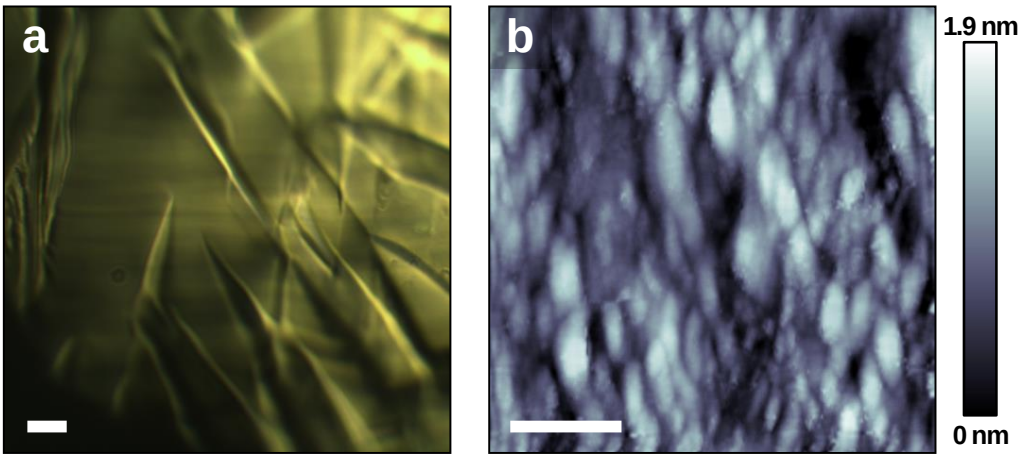

Figure 5.5: (a) Optical microscope image of one of the measured Au_2Pb samples (scale bar: 10 μm). (b) STM 200×200 nm^2 topographic image taken at 100 mK and zero magnetic field with a bias voltage of 1 mV and a setpoint current of 4 nA. Horizontal scale bar is 50 nm long and color scale bar provided at the right ranges from zero (black) to 1.9 nm (white).

the bar to a ceramic blade to break the sample. We then measured the surface of the broken sample. Ex-situ optical analysis made after finishing the experiment showed rough surfaces with linear elongated facets (fig. 5.5a), indicating that we could not break the sample on a clear cleaving plane. Figure 5.5b shows one of the STM topographies we obtained in a 200×200 nm^2 window. Typical corrugation found on the surface was of the order of 2 nm and individual atoms were not resolved in any of the locations we explored. We measured two in-situ broken samples and analyzed in each up to 20 different fields of view accessed by moving the sample holder in-situ at mK temperatures.

5.2 Superconducting gap characterization

As I discussed above, unveiling the gap structure of a superconductor is key to identify its topological properties. Due to the small expected size of the superconducting gap in Au_2Pb, it is important to make sure that the energy resolution of the tunneling conductance measurement setup is very high, of 9 μeV in our case, and that previous measurements using the same equipment lead to fully opened superconducting gap in conventional superconductors with similar T_c such as Al (see section 2.3.3).

Figure 5.6 shows our scanning tunneling spectroscopy measurements of the superconducting gap of Au_2Pb as a function of temperature. At 0.1 K, we do not observe a fully opened superconducting gap, but instead a large amount of states at the Fermi level. As temperature increases, the zero bias conductance increases. The quasiparticle peaks are already highly suppressed at low temperatures and not noticed at all above 0.6 K. We can obtain the superconducting density of states,

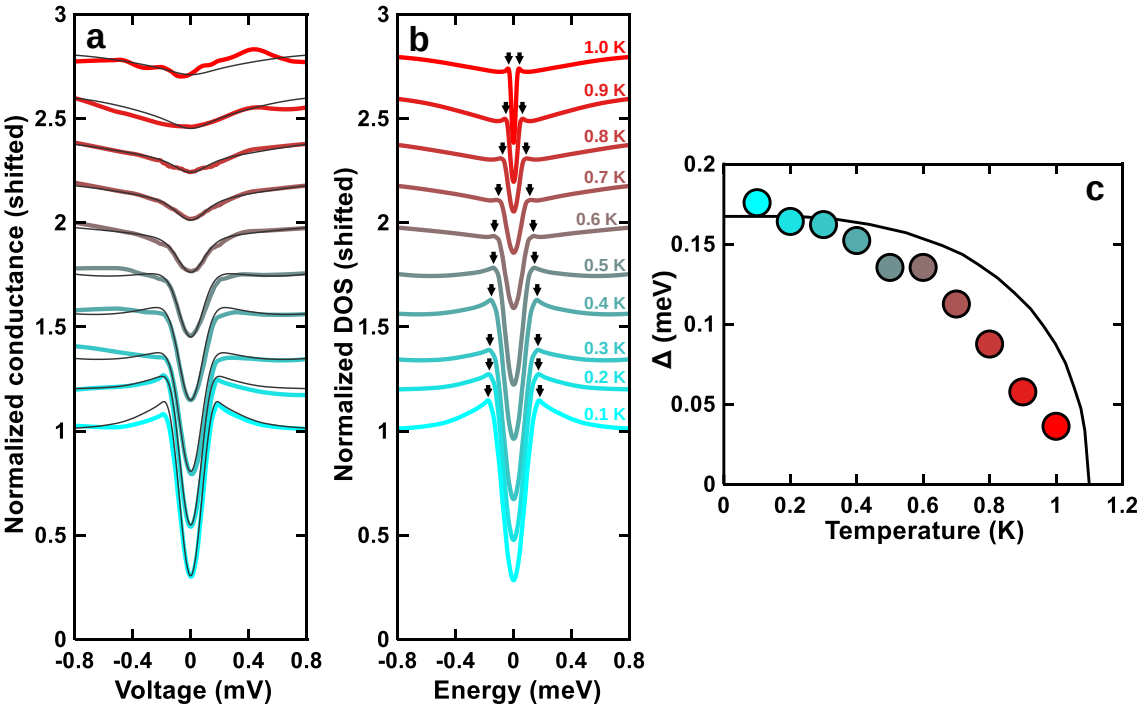

Figure 5.6: (a) Normalized tunneling conductance measured in Au_2Pb as a function of the bias voltage shown for increasing temperatures as colored lines. Curves are shifted upwards for better visualization. Bottom curve is at 100 mK (cyan) and top one is at 1 K (red), with 100 mK increments. Black lines over conductance curves show the result of the convolution of the density of states with the derivative of the Fermi distribution at each temperature. The density of states used at each temperature are shown in (b). (c) Temperature dependence of the position of quasiparticle peaks in the density of states (black arrows in (b)). BCS prediction for the gap size with T_c = 1.1 K is depicted in black.

$N(E)$, versus temperature by seeking for the $N(E)$ curve whose convolution with the derivative of the Fermi function at each temperature best fits the tunneling conductance (see eq. (2.9)). The resulting $N(E)$ is shown in fig. 5.6b. We determine the size of the superconducting gap, Δ, and its temperature dependence from the position of the quasiparticle peaks in the density of states. The temperature dependence of the gap size is shown in fig. 5.6c. We find a value for the superconducting gap of $\Delta(T = 0) = 0.17$ meV that decreases with increasing temperature slightly deviating from BCS prediction (black line in fig. 5.6c). The gap disappears at about 1.1 K, close to the temperature of the superconducting specific heat anomaly and the temperature at which the resistivity becomes zero in previous reports [226, 225, 231]. Despite the deviation of our data from BCS predictions for the gap size in the intermediate temperature range, BCS expression $\Delta(T = 0) = 1.76 k_B T_c$ provides $\Delta(T = 0) \approx 0.17$ meV using $T_c = 1.1$ K, which is in perfect agreement with the value found in the experiment.

The shape of the superconducting density of states is reproducibly found over large areas of the surface, covering several hundreds of nm. These areas are not atomically flat, but present a certain corrugation. Figure 5.7a shows a topographic image taken in a region of 345×345 nm^2 with a corrugation of ~ 2 nm. The topography presents

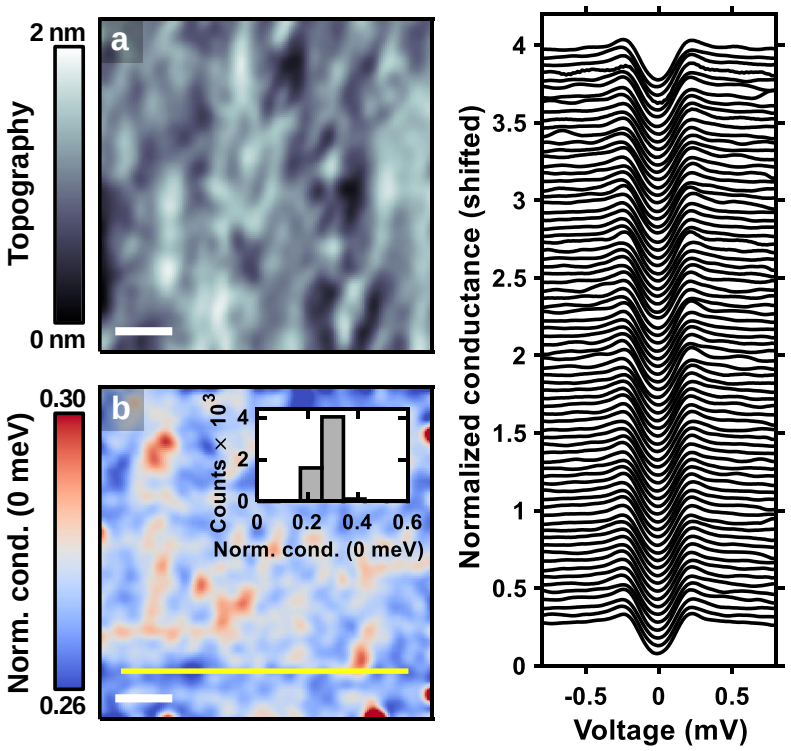

Figure 5.7: (a) STM topographic image measured at 100 mK and zero magnetic field in a 345×345 nm^2 region of the Au_2Pb sample. (b) Normalized zero bias conductance inside the same region of (a) 60 nm white scale bar is printed in the bottom-left corner of (a, b). Vertical color scale bars are provided at the left of each panel. Inset in (b) shows a histogram of the normalized conductance values. (c) Offset plot of the tunneling conductance curves measured along the yellow line in (a, b).

ellipsoidal features of the order of a few nm height, indicating that the sample does not easily break on an atomic plane. The zero bias conductance measured at 100 mK and zero magnetic field as a function of the position in the same field of view is mapped in fig. 5.7b. The tunneling conductance at zero bias presents small variations around 30 % of the conductance at bias voltages well above the superconducting gap, but it is always between 20 % and 30 % (see histogram in fig. 5.7b). Although some patterns in the conductance map can be related some features in the topography, there is no clear correlation between the two images. Figure 5.7d presents an offset plot of the tunneling conductance curves along the yellow line in fig. 5.7a,b,c evidencing that the measured superconducting gap size remains basically unchanged over the image.

The zero bias conductance, $\sigma(V = 0)$, is of around 0.3 times the normal state conductance at 100 mK and it increases with temperature as expected, but the obtained zero energy density of states, $N(E = 0)$, is also nonzero (about a third of the normal state density of states). In a usual s-wave BCS superconductor, $N(E)$ is exactly zero at zero energy and remains this way when increasing temperature as long as the superconducting critical temperature is not surpassed. The effect of temperature is just to decrease the distance between the quasiparticle peaks as the superconducting gap size, $\Delta(T)$, decreases with increasing temperature. To

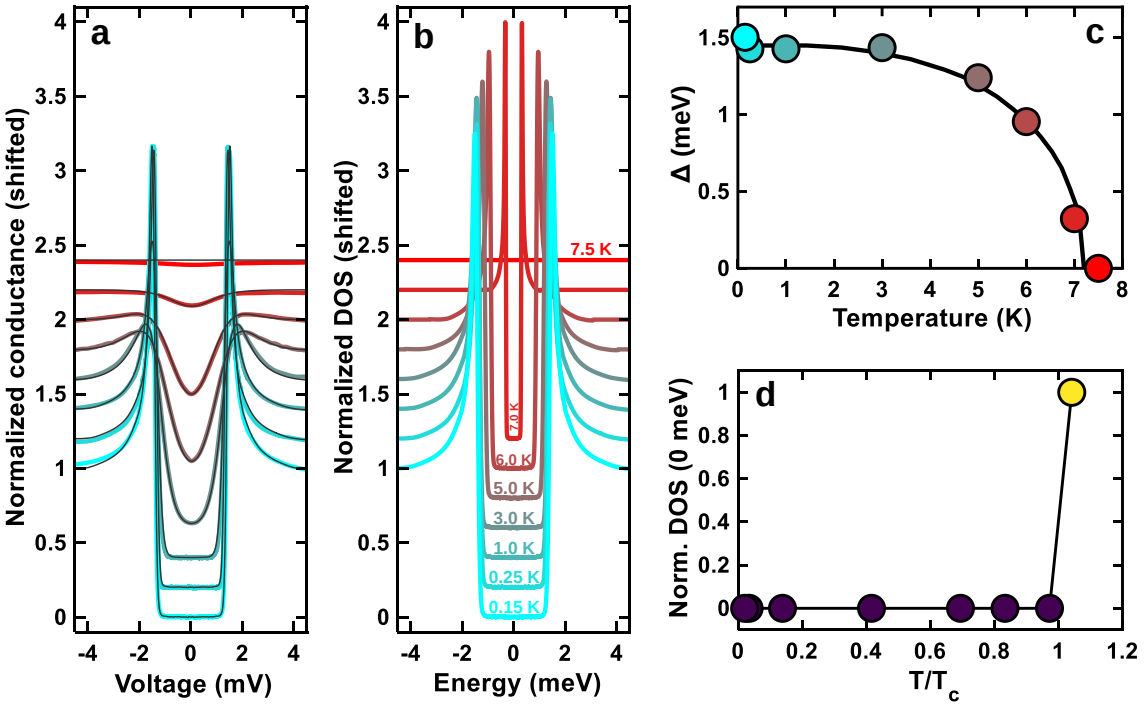

Figure 5.8: (a) Normalized tunneling conductance measured in Pb as a function of the bias voltage shown for increasing temperatures as colored lines. Curves are shifted upwards for better visualization. From bottom to top, the temperatures of the curves are 150 mK, 250 mK, 1 K, 3 K, 5 K, 6 K, 7 K and 7.5 K, respectively. Black lines are the density of states convoluted with the derivative of the Fermi function at the corresponding temperature. The density of states used at each temperature are shown in (b). (c) Temperature dependence of the gap size obtained from the position of the quasiparticle peaks in (b). BCS prediction for the gap size with T_c = 7.2 K is depicted in black. (d) Zero energy density of states versus temperature as obtained from (b). Temperature is normalized to T_c.

illustrate this, we measured a set of tunneling conductance curves from 0.15 K up to 7.5 K on a pure Pb surface (fig. 5.8). In this case, the energy position of the quasiparticle peaks is closer to zero as temperature increases (fig. 5.8b,c), but fig. 5.8d shows how the zero energy density of states remains strictly equal to zero until we go beyond the superconducting critical temperature of Pb (T_c = 7.2 K). In Au_2Pb, however, our data show that the zero energy density of states is already finite at low temperatures far from T_c.

It is quite clear from our data that we can identify large areas on the sample (fig. 5.7) that present the same homogeneous critical temperature of bulk measurements. The value of the superconducting gap and, as we will describe in section 5.3, the qualitative magnetic field behavior, are as expected from the properties that we know from the the bulk. The finite density of states at the Fermi level is however different from the Fermi energy density of states found in bulk measurements in the superconducting phase, what is probably the most intriguing finding of our experiments.

The finite zero energy density of states observed in our experiments evidences that the surface superconductivity is radically different from the bulk one. This difference could be attributed to the presence of a trivial normal layer due to surface degradation, but the huge coherence length, ξ, of bulk Au_2Pb, of 60 nm or larger (see magnetic field behavior in section 5.3), implies however that the normal layer should be tens of nm thick to sufficiently disturb the superconducting density of states at the surface and provide a sizable zero energy density of states. Having cleaved the sample at low temperatures in cryogenic vacuum conditions eliminates the appearance of oxides or chemical decomposition.

As I introduced above, there are Dirac cones in the high temperature phase along the Γ-X line of the Brillouin zone. In the low temperature phase, symmetry breaking allows band mixing and the Dirac cone gaps out. As shown by Cheon *et al.* [234], the structural distortion can lead to a fully gapped bulk superconductor with surface states that show topologically nontrivial properties. Cheon *et al.* [234] analyze the irreducible representations of the point group of Au_2Pb and derive from these the possible superconducting gap symmetries. They start assuming a high temperature D_{4h} phase with a Dirac cone. When cooling, this phase distorts into a D_{2h} phase and the Dirac cone gaps out, leaving surface states. The nature of superconductivity in these surface states is analyzed depending on the irreducible representation of the superconducting order parameter. In particular, it is found that, if the initial D_{4h} phase is an odd superconductor with B_{1u} symmetry and nodes in the superconducting gap, the distorted phase will have A_u symmetry, and thus, no nodes in the bulk band structure. The surface, on the contrary, will show the closed Dirac gap, and thus, a closed gap and a linear dispersion relation. A schematic representation of this situation is shown in fig. 5.9.

This would explain some of our observations. The analysis of other changes in the surface properties in the structural transition lead to superconducting properties with nodes in the bulk, or to a fully gapped trivial superconductor. The presence of nodes is not compatible with macroscopic specific heat measurementes. The linear dispersion in the density of states (fig. 5.6b) suggests a connection to the expected Dirac-like linear dispersion of the surface state discussed above. However, there is a large amount of states inside the superconducting gap. It has been shown by Wehling *et al.* [235] that a Dirac dispersion relation is strongly affected by disorder, which induces states inside the gap (see fig. 5.9b). The presence of a large amount of such in-gap states at different energies could explain the observed finite density of states at low energies.

Figure 5.10 shows some first-principles calculations of the band structure on the (010) surface of the low temperatures phase of Au_2Pb. Calculations were performed by José J. Baldoví at ICMol, Valencia. We observe several surface states inside the gapped bulk band structure along Γ-X line. Some of them show a linear energy dispersion forming Dirac cones at the surface (see green box in fig. 5.10a). Figure 5.10b shows the calculated surface Fermi surface in the k_x-k_z plane, and spin texture of the surface states is added as green arrows in fig. 5.10c. The Berry flux computed along closed paths of the surface states in the Γ-X line

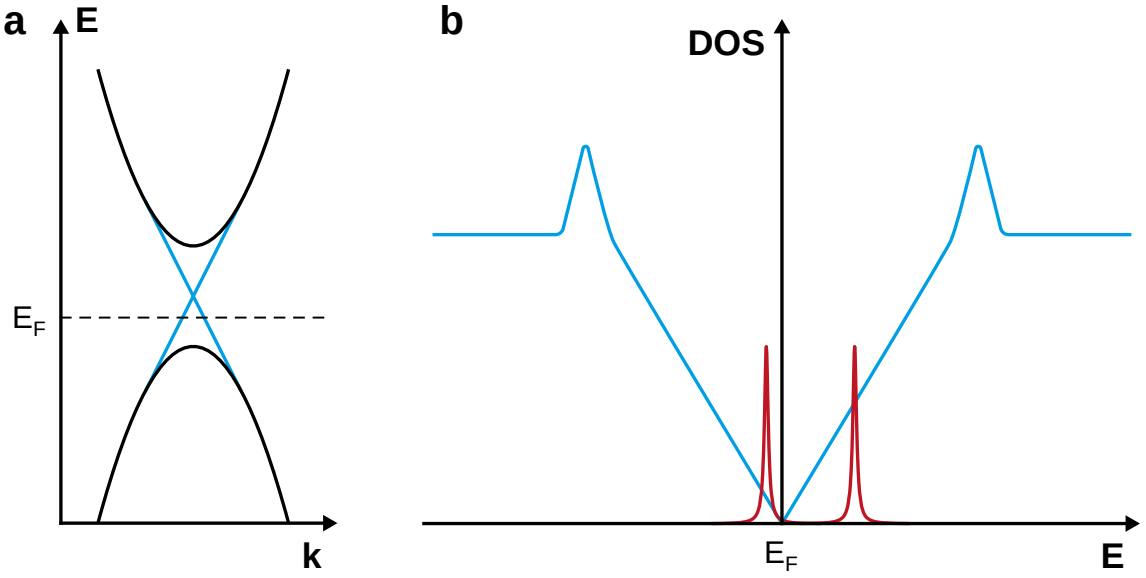

Figure 5.9: (a) Schematic representation of the band structure of a gapped system (black lines) with two relativistic surface states (blue lines) inside the energy gap which may show superconductivity. (b) Superconducting density of states in the surface states in (a), with no states at the Fermi level (blue). Disorder introduces states inside the superconducting gap (red) which can lead to a finite density of states at the Fermi level in strongly disordered surfaces [235].

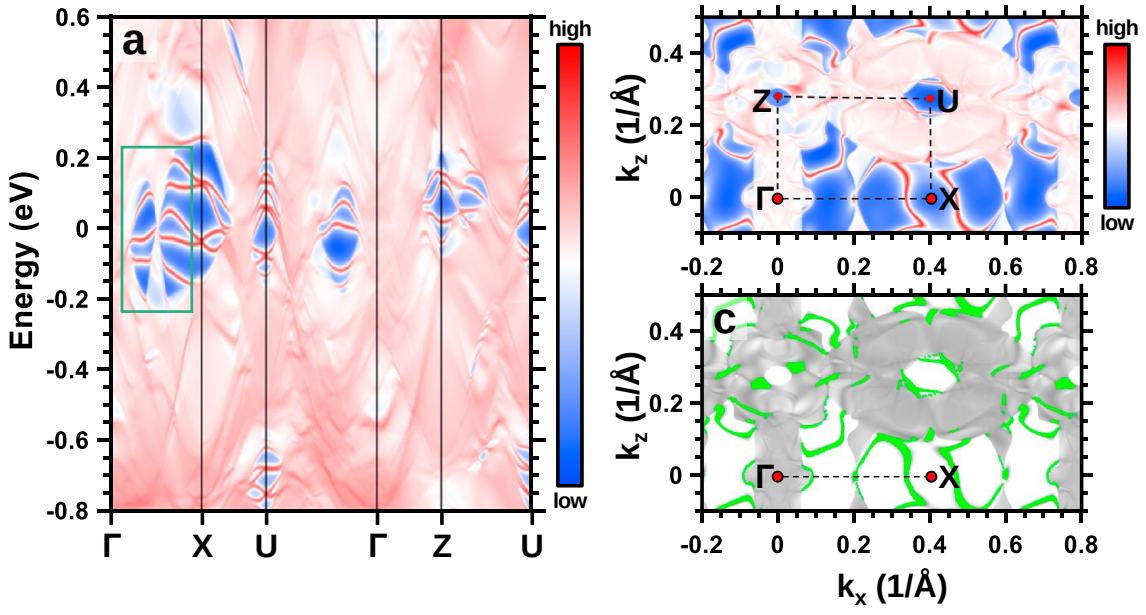

Figure 5.10: (a) Projected energy spectrum for the right-side termination of the (010) surface calculated for the low temperature structure of Au_2Pb. Surface states arise inside the gapped bulk band structure along the Γ-X direction. Green square marks the cone-like dispersion of some surface states. (b) Calculated Fermi surface for the right termination of the (010) surface of Au_2Pb showing several surface states inside the first Brillouin zone. (c) Same as (b) adding green arrows marking the spin texture of the surface states. Calculations were performed by José J. Baldoví at ICMol, Valencia.

gives a topological invariant $Z_2 = 1$, meaning that the cone-like surface states are topologically nontrivial.

Thus, we can conclude that our results are compatible with fully gapped odd paring in Au_2Pb giving a surface state with a Dirac dispersion inside the superconducting gap. Of course, to get bulk odd superconducting pairing with A_u symmetry, we do need electronic correlations [234]. This possibility has to be studied with more measurements of the bulk properties of Au_2Pb, for instance Knight shift or neutron scattering. By now, there is no evidence for the needed electronic correlations that could lead to such a peculiar superconducting state.

It is now useful to remind the situation in other compounds such as β-Bi_2Pd or BiPd [236, 237]. The latter is a noncentrosymmetric system expected to show spin polarization as a consequence of broken inversion symmetry and spin-orbit coupling. Nonetheless, it was shown that spin polarization induced by spin-orbit coupling can also occur in centrosymmetric compounds, such as β-Bi_2Pd [238]. Both compounds show a largely opened superconducting gap at the surface [239], although there are also reports of unconventional behavior at the surface of β-Bi_2Pd [240, 241, 242]. In β-Bi_2Pd, at about 2 eV below the Fermi level, a bulk gap is closed at the surface by a surface Dirac cone as shown by band structure calculations involving just a few layers [236]. Spin resolved ARPES measurements showed that the Dirac cone is spin-polarized, resembling the helical surface state of topological insulators [236]. The topological invariant for the corresponding gap is $Z_2 = 1$, which requires an odd number of surface states, and thus spin-polarized surface bands [236]. Furthermore, there are two surface states appearing at the Fermi level, one of which is also topologically nontrivial and lies very close to the bulk bands in k-space. ARPES identified spin polarization in both topologically trivial and nontrivial surface states. STM shows a spin arrangement from scattering that supports the presence of spin-polarized bands [240]. However, the superconducting gap is fully open [239, 240].

5.3 Magnetic field behavior

To further explore the superconducting properties of Au_2Pb, we studied the tunneling spectroscopy in a magnetic field. Previous bulk measurements have found a first critical field, H_{c_1}, of about 30 mT, a second critical field, H_{c_2}, of the same order, with values ranging between 20 and 80 mT, and a coherence length of $\xi \approx 60$ nm. This value was extracted from the temperature dependence of the second critical field [226, 225, 231, 232]. There is clear Meissner field expulsion until several tens of mT at low temperatures [231]. Hence, we can expect nearly type I superconductivity with strong field expulsion and concomitant demagnetizing effects, similar to those that can be found in elemental Pb or in Nb at small magnetic fields [243, 244, 245]. Our sample is nearly plate-like, with demagnetizing factor close to one, which implies extreme field enhancement at the edges of the sample and that the sample almost immediately enters a state with a highly inhomogeneous magnetic field [246, 247, 248, 249, 250]. This leads

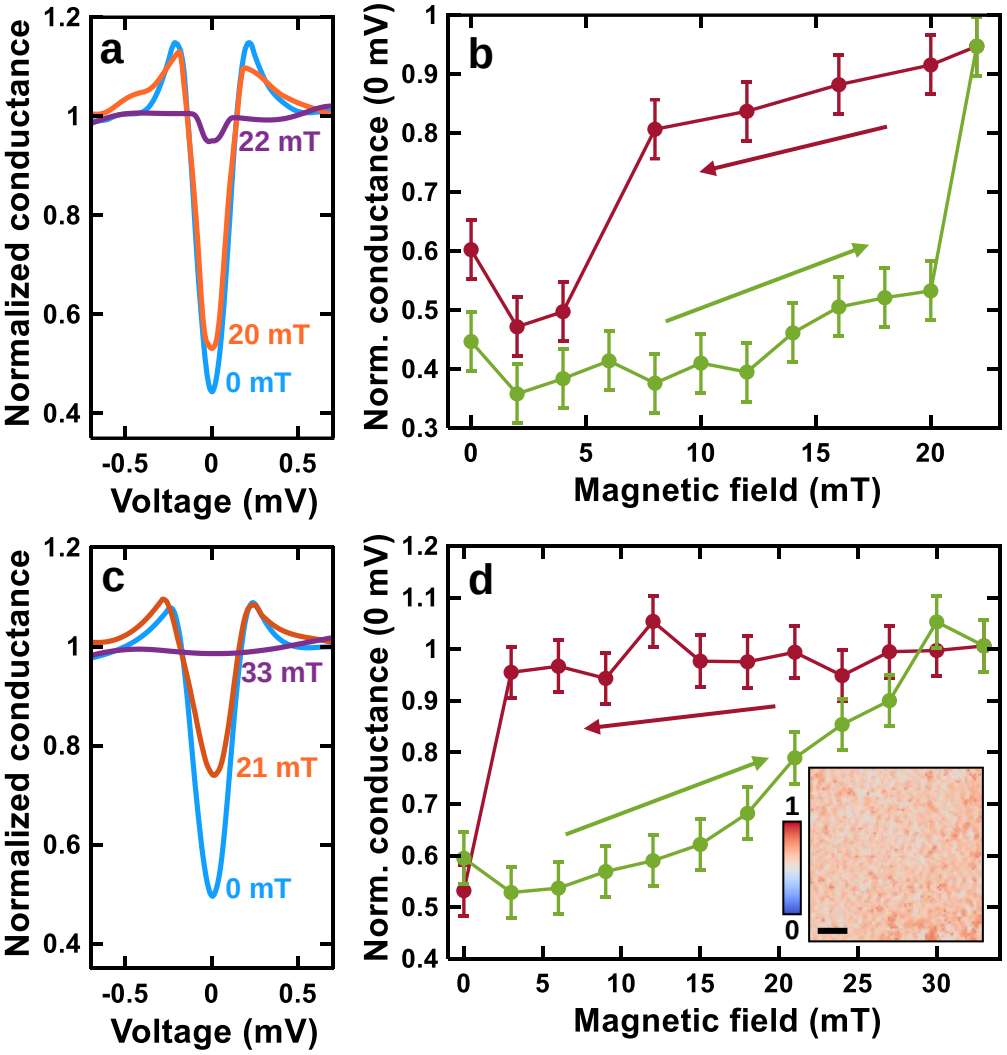

Figure 5.11: (a) Magnetic field dependence of the superconducting tunneling conductance. The values of the magnetic field are indicated in the panel. (b) Zero bias conductance as a function of magnetic field for increasing (dark red) and decreasing (green) magnetic fields. (c, d) Same panels for a different magnetic field ramp. Error bars are indicative of the dispersion of the zero bias conductance value found over areas covering a few hundred of nm. Inset of (d) shows a representative image of the zero bias tunneling conductance measured at 100 mK at an applied field of 10 mT inside a 305×305 nm^2 area. Horizontal scale bar is 50 nm long and vertical scale bar ranges between zero (blue) and 1 (red).

to the so-called intermediate state, which consists of normal and superconducting areas of macroscopic sizes. Eventually, in areas of the sample with a reduced mean free path, one might also expect the intermediate mixed state, consisting of superconducting and mixed state vortex areas that appear between the Meissner phase and the complete suppression of superconductivity [251]. Nevertheless, in all cases, we expect macroscopically differing areas with fully superconducting and normal properties, being each respectively at zero magnetic field and at the critical field, and a strong hysteretic dependence on the magnetic field history due

to pinned normal areas that move through the sample at each modification of the magnetic field [246, 247, 248, 249, 250, 251].

We indeed observe strongly hysteretic behavior, as shown in fig. 5.11. Superconductivity disappears most often between 20 mT and 30 mT depending on the area over the sample where we are scanning, in agreement with bulk superconducting properties. We could find no indications of separated normal and superconducting areas within our fields of view. Inset in fig. 5.11d displays the homogeneous zero bias conductance map taken at 10 mT inside a 305 nm × 305 nm area. Therefore, as the normal and superconducting areas of the intermediate state form over length scales of the order of the coherence length, ξ, our measurements confirm that its value is certainly as estimated from bulk measurements (60 nm) or even larger. We also found no evidence for vortices, although this is not surprising given the demagnetizing effects and our limited field of view of about 2 μm × 2 μm.

Interestingly, the zero bias conductance in the superconducting areas does not remain constant with magnetic field but shows a clear variation. For example, in fig. 5.11a,b we observe an increase of the zero bias conductance when increasing the magnetic field and a decrease when decreasing the magnetic field. In this field ramp we did not reach full suppression of superconductivity. In fig. 5.11c,d we measure up to slightly higher fields and observe again an increasing zero bias conductance when increasing the magnetic field. Here, in contrast to the previous case, the field remains trapped with the system in the normal phase down to very small magnetic fields. Actually, after applying a magnetic field, we often observed zero bias conductance larger than those shown in fig. 5.6.

We can discuss this behavior in terms of the Dirac cone at the surface. As shown by the hysteretic behavior (fig. 5.11b,c), when applying a magnetic field, there are certainly normal areas that nucleate close to our field of view. Given the large value of the coherence length, these normal areas broaden localized states inside the Dirac dispersion relation. This broadening can lead to an increased zero energy density of states with magnetic field.

5.4 Conclusions

In summary, we have studied the surface of Au_2Pb with STM measuring the superconducting gap as a function of the temperature and magnetic field. We find a superconducting gap compatible with a critical temperature of 1.1 K in agreement with bulk transport measurements. When applying magnetic field, we observe a small critical field over large areas on the surface as well as an hysteretic behavior of the zero bias conductance. This serves us to identify Au_2Pb as a type I or very weak type II superconductor.

The superconducting gap is not fully opened, but we have found a finite residual density of states at the surface that remains larger than about a third of the normal phase value. Besides, the measured superconducting gap is homogeneous over large areas of the sample. We discussed possible explanations, including sample

inhomogeneities and the presence of in-gap states on a surface Dirac cone. The large value of the bulk coherence length favors the latter option.

It would be great to find atomically flat surfaces and study the superconducting behavior on such surfaces. Spin resolved measurements of the bulk properties should also provide further insight into the bulk superconductivity, which is key to understand the effects of the surface. In all, Au_2Pb is an intriguing superconductor. As compared to all other intermetallic superconductors where topological properties are discussed in the literature in absence of strong correlations (such as heavy fermions or proximity to a magnetic phase), Au_2Pb is the only one (to our knowledge) which shows a robust zero energy density of states covering the whole surface. This in itself is an indication of a bulk state with different properties, although it requires further study by spin sensitive bulk techniques.

6

High magnetic field vortex lattice in the iron based superconductor FeSe

6.1 Iron based superconductivity

Two decades after the first report of high-T_c superconductivity, unconventional superconductivity was also observed in a family of iron based materials. It was first discovered in LaFePO with T_c = 4 K [252] and in LaNiAsO with T_c = 2.4 K [253], but the first report of an iron based high-T_c superconductor was $LaFeAsO_{1-x}F_x$ with a T_c of 26 K [24]. Magnetism and superconductivity were considered to be competing phenomena, so the discovery of superconductivity in materials based on Fe, which is a well known magnetic element, was indeed surprising, and iron based compounds were soon considered as the perfect candidates to study the interplay between magnetic correlations and the formation of superconducting Cooper pairs. Besides, the normal state of these materials is metallic, what makes iron based superconductors interesting for applications as compared with cuprates, which are ceramic materials that are not easily workable and typically require higher manufacturing costs.

There is a wide variety of different iron based superconductors. They are all obtained by combining Fe with elements from the group 15 (pnictogens) or the group 16 (chalcogens) of the periodic table. They can be classified in families by the stoichiometric relations between the different elements (11, 111, 122, *etc.*). All the families have a common building block that consists of a Fe-As plane for the pnictides and a Fe-Se/Te plane for the chalcogenides [254, 255].

Iron based superconductors are strongly correlated systems that present very particular properties such as multiband superconductivity with a unique situation having a Cooper pair wavefunction that changes sign in different sheets of the Fermi surface. Their phase diagrams feature magnetic ordered phases, superconductivity, electronic nematicity and quantum criticality [255]. Similar to cuprates, superconducting regions in the phase diagram appear close to antiferromagnetism. In fact, in the most accepted scenario, pairing is mediated by

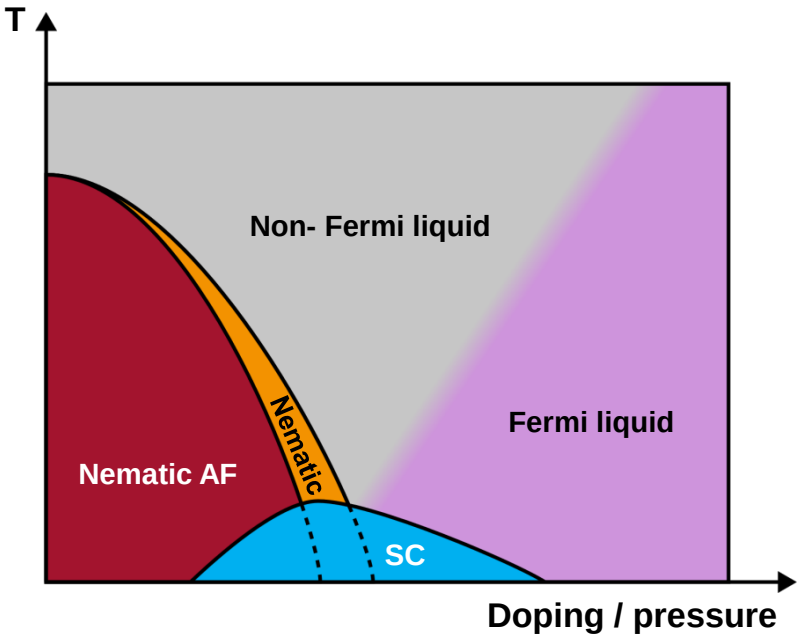

Figure 6.1: Generic temperature versus pressure or doping phase diagram for iron based superconductors. The ground state is an antiferromagnet with strong nematic properties (red region). Depending on the particular compound, the magnetic phase transition can be coupled to or separated from the structural transition. Above these transitions there is a nematic phase (orange region) usually coupled to the magnetic and structural transitions. Upon doping or pressure, a superconducting dome emerges (blue region). The highest critical temperature for the superconducting state is reached at the optimal doping, which usually coincides with the extrapolation of the magnetic phase transition to zero temperature.

spin fluctuations with the antiferromagnetic vector connecting electron and hole pockets. The highest superconducting critical temperatures in single crystal iron based superconductors are close to 60 K [254, 255], while monolayer FeSe displays a T_c above 100 K [256].

Figure 6.1 shows the generic temperature versus pressure (or doping) phase diagram for iron based superconductors. The ground state of the parent compound is antiferromagnetic and sometimes shows nematic properties [257]. There is a structural phase transition that is many times coupled to the magnetic transition. In compounds showing nematic properties, the nematic phase transition lies very close to the structural and magnetic transitions. These three transitions are strongly coupled to each other and it is thus very difficult to disentangle their origin [258]. With increasing doping (or pressure), a superconducting dome emerges. The optimal doping at which the superconducting critical temperature is higher is reached close to the extrapolation of the magnetic transition at zero temperature. Magnetic order and superconductivity coexist in a small region of the phase diagram of some materials.

Two months after the discovery of superconductivity in the 122 systems, superconductivity was reported in FeSe below a critical temperature of about 8-9 K

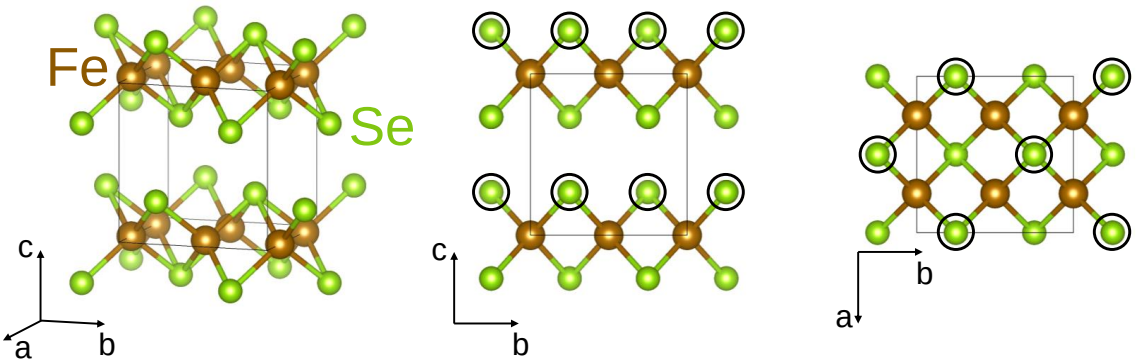

Figure 6.2: Schematic representation of the low temperature *Cmma* orthorhombic atomic structure of FeSe. Fe atoms are depicted in brown and Se atoms, in green. General, lateral and top points of view are shown in left, middle and right panels, respectively. Light grey lines delimit the unit cell dimensions (a = 5.318 Å, b = 5.343 Å and c = 5.495 Å). Black circles mark the top Se atoms accessible with the STM tip after the cleaving process. The square arrangement of top Se atoms is tilted 45° with respect to the orthorhombic a and b axes.

[259]. This report attracted lot of attention regarding the unusual simplicity of this compound, which consists only of two different elements in the same stoichiometric proportion. The critical temperature of FeSe is not as high as that of other iron based superconductors, but by applying pressure or doping, T_c can be considerably increased. FeSe is a good system to study the interplay between nematicity, magnetism and superconductivity given the unusual correlations between these three phenomena.

In this chapter, I will show our STM results in high quality FeSe single crystals grown by the group of Paul C. Canfield. Among the iron based superconductors, FeSe has a peculiar band structure with small Fermi surface pockets and Fermi energies. Furthermore, since the critical field is of about 17 T [260], we can nearly access the whole magnetic field range.

6.1.1 Atomic structure

FeSe crystallizes in a tetragonal phase at room temperature. It undergoes a structural transition below ~ 90 K to an orthorhombic phase in which the symmetry between a and b axes is broken [259, 261, 262] and nematicity appears [263]. The lattice parameters of this orthorhombic phase belonging to the space group *Cmma* are a = 5.318 Å, b = 5.343 Å and c = 5.495 Å.

FeSe is an easily exfoliable layered material with layers van der Waals-stacked along the crystallographic c-axis. Each layer consists of an Fe plane sandwiched by two Se planes (see fig. 6.2). Inside the Fe plane, the distance between consecutive Fe atoms is a_{Fe} = 2.659 Å along a-direction and b_{Fe} = 2.672 Å along b-direction. On the other hand, Se planes comprise a square lattice of Se atoms separated 3.769 Å whose orientation is tilted 45° with respect to a_{Fe} and b_{Fe}. Unlike WTe_2, the other layered

compound studied in this thesis, in FeSe the inversion symmetry is not broken. The top Se plane presents a two-dimensional structure in contrast to that of top Te atoms in WTe_2, which arrange in stripes along one of the crystalline axes giving rise to quasi-one-dimensional electronic properties (see chapter 4).

Nematicity in this compound concerns a difference in the electronic properties along a and b crystalline axes. For instance, superconducting vortices in FeSe are observed as ellipsoidal features with the bigger axis of the ellipse pointing to one of the two orthorhombic axes. The ab reference plane rotates 90° every time a nematic twin boundary is crossed as I will discuss in section 6.3.

6.1.2 Superconductivity and nematicity in FeSe

The atomic structure of bulk FeSe at room temperature is tetragonal. Lowering the temperature, it enters an orthorhombic phase below $T_s \approx 90$ K [259, 261, 262]. This phase transition is analogous to the nematic transtion observed in many other iron based materials. The parent compound is paramagnetic at ambient pressure [262, 264] and spin fluctuations are found to be enhanced only at low temperatures, which raises the question about the origin of the structural transition [264]. Unlike other iron based superconductors, FeSe does not show antiferromagnetic ordering at low temperatures and ambient pressure. When applying pressure, the system becomes magnetically ordered at ~ 1 GPa [264, 265] and there is a significant increase of the superconducting critical temperature, that reaches a maximum of $T_c \approx 37$ K at ~ 6 GPa [266, 267, 268, 269].

The unconventional pairing mechanism in FeSe seems to be sign-changing spin-fluctuation-mediated as pointed by the observation of a spin-resonance mode [270]. The change of sign in the superconducting pair wavefunction between the electron and hole pockets of the Fermi surface has been confirmed by STM experiments [271, 272, 273]. Strong electron-phonon interaction has also been recently reported exposing the importance of the interplay between the electron-electron and the electron-phonon interactions [274].

The Fermi surface of FeSe obtained by tight binding models consists of three bands, α, ϵ and δ [276, 277]. The hole-like α-band produces an ellipsoidal pocket centered at the $\Gamma = (0, 0)$ point of the Brillouin Zone, with its major axis aligned to the orthorhombic b axis. The electron-like ϵ-band is located around the $X = (\pi/a, 0)$ point. This band is even more elongated than the α-band, but in this case the major axis is oriented along the orthorhombic a axis. Finally, a δ-band pocket has been also predicted at the $Y = (\pi/b, 0)$ point with its major axes aligned to the orthorhombic b axis. Figure 6.3 shows a schematic representation of the three bands, with the orbital character as a color code. The calculated α-band and ϵ-band Fermi surface pockets agree with Fermi surface size and geometry obtained from angle resolved photoemission spectroscopy (ARPES) [278, 279] and quantum oscillations [280, 281]. The δ-band has not been observed experimentally yet. Recent ARPES studies suggest that the single hole pocket around Γ splits into two pockets at the surface, leading to spinful surface bands [282].

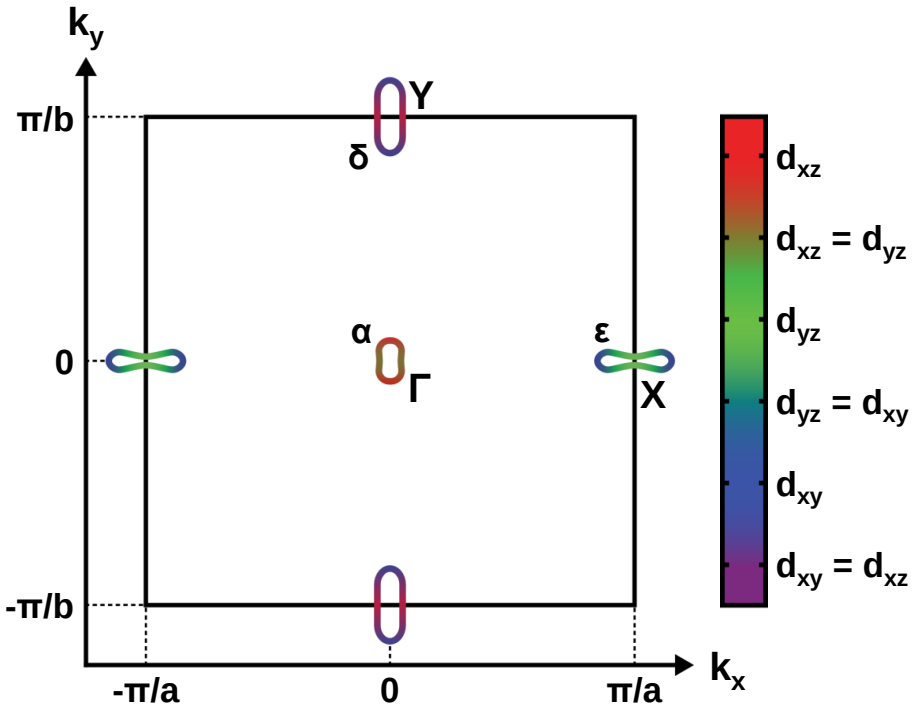

Figure 6.3: Adapted from [271]. Schematic diagram of the FeSe Fermi surface. The black square marks the limits of the first Brillouin zone. Hole-like α-band is shown around the Γ point, electron-like ϵ-band, around the X point, and δ-band, around the Y point. Orbital character of the bands is given by the color code (see Ref. [275]).

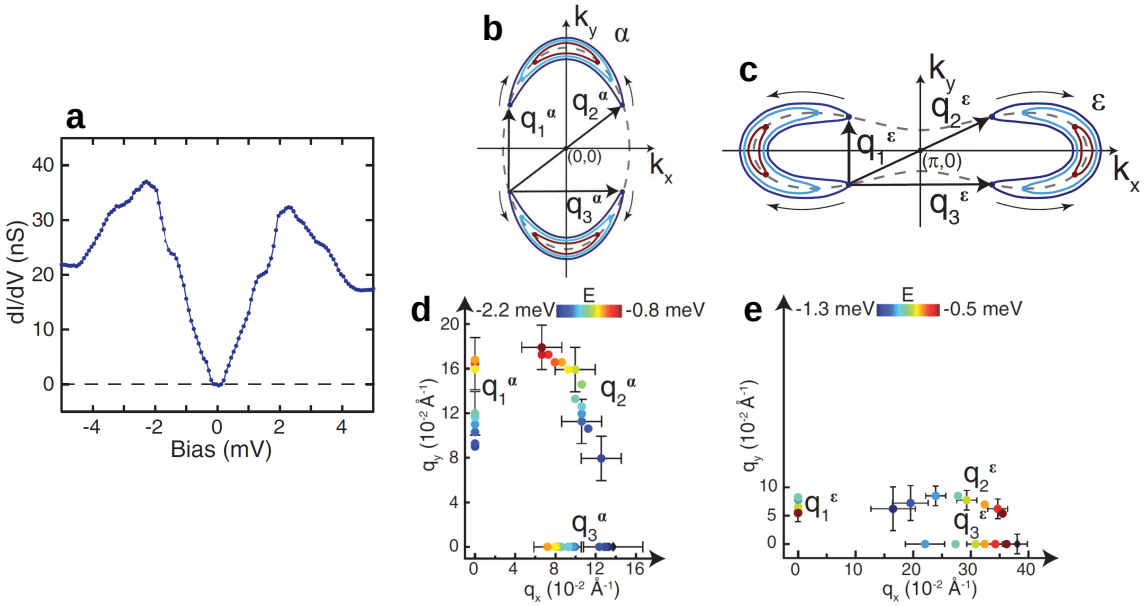

Figure 6.4: QPI results obtained by Sprau *et al.* [271]. (a) Tunneling conductance versus bias voltage. (b) Increasing energy (red to purple) constant energy contours of the gapped α-band showing the three scattering vectors they identify as black arrows. Dashed line sketches the ellipsoidal shape of the normal state Fermi surface. (c) Same for the scattering vectors identified in the gapped ϵ-band. (d) Energy evolution of the α-band scattering vectors in (b). (e) Energy evolution of the ϵ-band scattering vectors in (c).

The shape of α and ϵ bands at the Fermi level has been measured by Sprau *et al.* [271] through quasiparticle interference imaging. Figure 6.4a shows the tunneling conductance curve measured in this work, which is very similar to the curves we measure in our FeSe sample (see section 6.2.1 and fig. 6.8). Authors show that, depending on the coupling between the STM tip and the sample, they can either access some scattering vectors inside the α-band or inside the ϵ-band. They identify three vectors due to the scattering in the α-band (fig. 6.4b,d) and another three vectors due to the scattering in the ϵ-band (fig. 6.4c,e), and resolve the elongated shapes of the α and ϵ bands along k_y and k_x, respectively. These results show that superconducting paring in FeSe is orbital selective [271], what has been confirmed by calculations [283, 284].

Figure 6.5 plots the magnetic field parallel to c-axis versus temperature phase diagram showing the superconducting region below $H_{c2}(T = 0) \sim 17$ T and $T_c(H = 0) \sim 9$ K. Figure 6.6 shows the superconducting vortex lattice measured up to 8 T by Song *et al.* [285]. Nematicity in this material results in the observation of elongated vortices along the orthorhombic a-direction.

A new high magnetic field phase has been proposed related to features observed in the thermal conductivity versus magnetic field [260, 286] (see fig. 6.5). The upper critical field of FeSe is so large that the Zeeman induced spin splitting of the superconducting density of states is of the order of the superconducting gap at about 15 T. Actually, taking a Landé factor $g = 2$, we can estimate the Zeeman splitting to be 1.74 meV at 15 T, which is of the order of the size of the superconducting gap ($\sim$ 2 meV). This suggests that the putative high magnetic field superconducting phase is related to the Zeeman spin polarization. In presence of a large spin polarization, Fulde, Ferrel, Larkin and Ovchinnikov (FFLO, [287, 288]) proposed that a superconductor might show a spatial modulation of the superconducting pair wavefunction. This leads to a sort of modulated order parameter with a spin and orbital structure that is intricate and has not been resolved yet. The FFLO modulation coexists with the vortex lattice. Some calculations propose, for example, coupled in and out of plane modulations as a result of Zeeman splitting and in-plane supercurrent quantization. The authors of Refs. [260, 286, 289] propose that the high field superconducting phase might be related to the FFLO prediction. A recent striking result by Hanaguri *et al.* [290] shows that the vortex lattice vanishes in the high magnetic field phase.

As I have discussed above, the Fermi surfaces and Fermi energy of FeSe are extremely small. This leads to a very peculiar situation in which the superconducting gap is of the order of the Fermi energy. The small value of the superconducting gap with respect to the Fermi energy is probably the main postulate of BCS theory. The influence of such a situation in a superconductor is under debate. Some authors propose that it could lead to a more Bose-Einstein like condensation (BEC) of Cooper pairs instead of BCS theory [260, 291].

Here, I will present a comprehensive STM study of the superconducting properties of FeSe. First, I will discuss the gap structure as obtained from tunneling spectroscopy using normal and superconducting tips. With the latter, we could

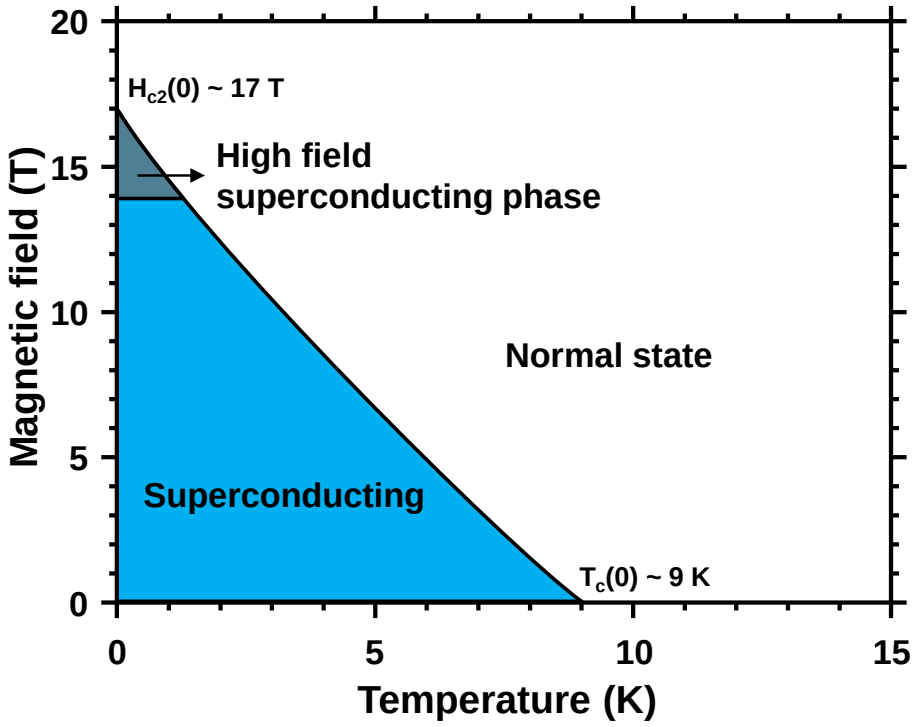

Figure 6.5: Magnetic field parallel to *c*-axis versus temperature phase diagram for FeSe according to Kasahara *et al.* [260]

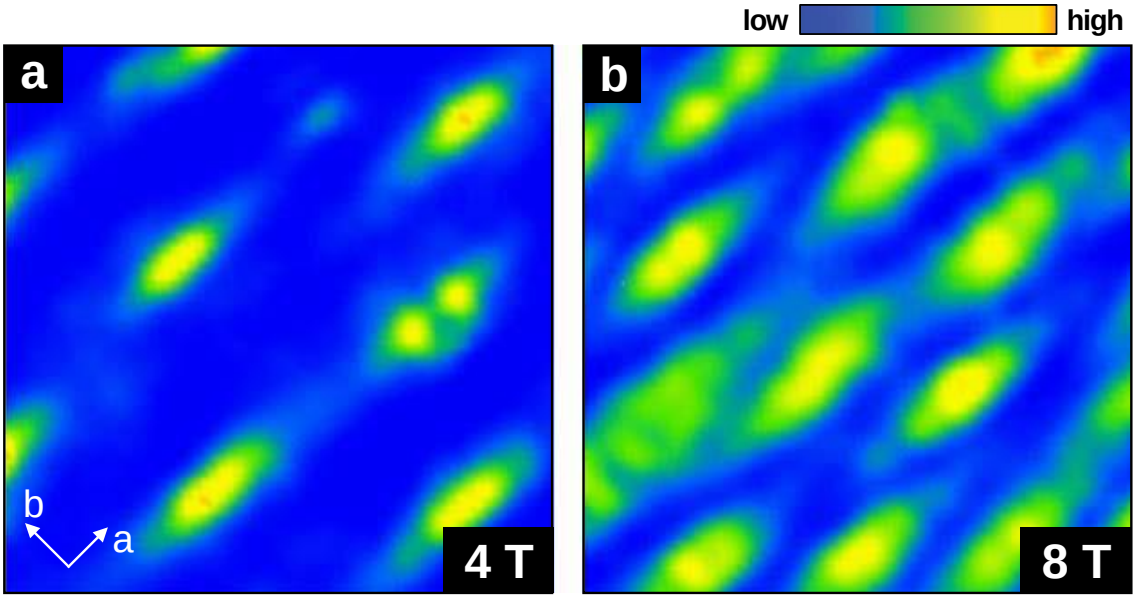

Figure 6.6: FeSe vortex lattice measured by Song *et al.* [285] at 0.4 K and (a) 4 T and (b) 8 T in a 60×60 nm^2 region. Vortices show elongated shapes along *a*-axis.

obtain an improved energy resolution with respect to previous work. Finally, and probably most importantly, we observed the vortex lattice in the whole magnetic field range and found a new charge density wave at very high magnetic fields.

6.2 Characterization of the FeSe surface

FeSe single crystals were grown by the group of Paul C. Canfield following the method described in Ref. [193]. Resulting crystals are plate-like with the c-axis perpendicular to the flat surface. Crystals are ~ 0.05 mm thick with typical in-plane dimensions of ~ 1 mm. We used the experimental setup developed during this thesis to measure two different FeSe samples, one using a normal Au tip and other one using a superconducting Pb tip. Samples were in-situ exfoliated at 5 K by gluing a piece of alumina on top of them and pushing the sample holder towards a transversely placed copper bar as described in section 2.3.4. The cleaving process resulted in very clean flat Se surfaces extended over several tens of μm. Figure 6.7a shows an optical microscope image taken on one of the FeSe samples after the cleaving process. We can find large flat areas all over the sample with some perpendicular breaking-lines following the square lattice of Se atoms.

Figure 6.7b shows an 218×218 nm^2 STM topographic image taken in one of the flat areas where we found some atomic steps. Inset in fig. 6.7b displays a height profile along the orange line in fig. 6.7b perpendicular to the steps. Each height step corresponds to either one (~ 5.5 Å) or two (~ 11 Å) unit cells in c-direction, proving that the cleaving always occurs between layers and that we can only access the top Se planes marked with black arrows in fig. 6.2. If we zoom into one of the atomic terraces, our STM topographic images clearly resolve the square lattice of Se atoms (fig. 6.7c). All over the surface we find some randomly distributed defects that appear as bump-like features in the topography.

6.2.1 Superconducting gap structure

Let us start presenting the tunneling conductance curve we measured in FeSe. Figure 6.8a shows a conductance curve acquired at 100 mK and zero magnetic field normalized to the conductance value at higher voltages outside the superconducting gap. The conductance curve displays a V-shape with two maxima that correspond to the position of the quasiparticles peaks of the bigger gap (at around ±2 mV, purple arrows in fig. 6.8a). Inside the bigger gap, we observe two additional features at around ±1 mV (green arrows in fig. 6.8a) coming from the quasiparticle peaks of a smaller superconducting gap, evidencing the double gap structure of FeSe. The sizes of the two superconducting gaps are Δ_1 = 1.9 meV and Δ_2 = 0.9 meV (measured from the position of the maxima in the dN/dE curve). The V-shape of the density of states and the multigap structure we observe is similar to that reported in previous STM studies [260, 292, 271].

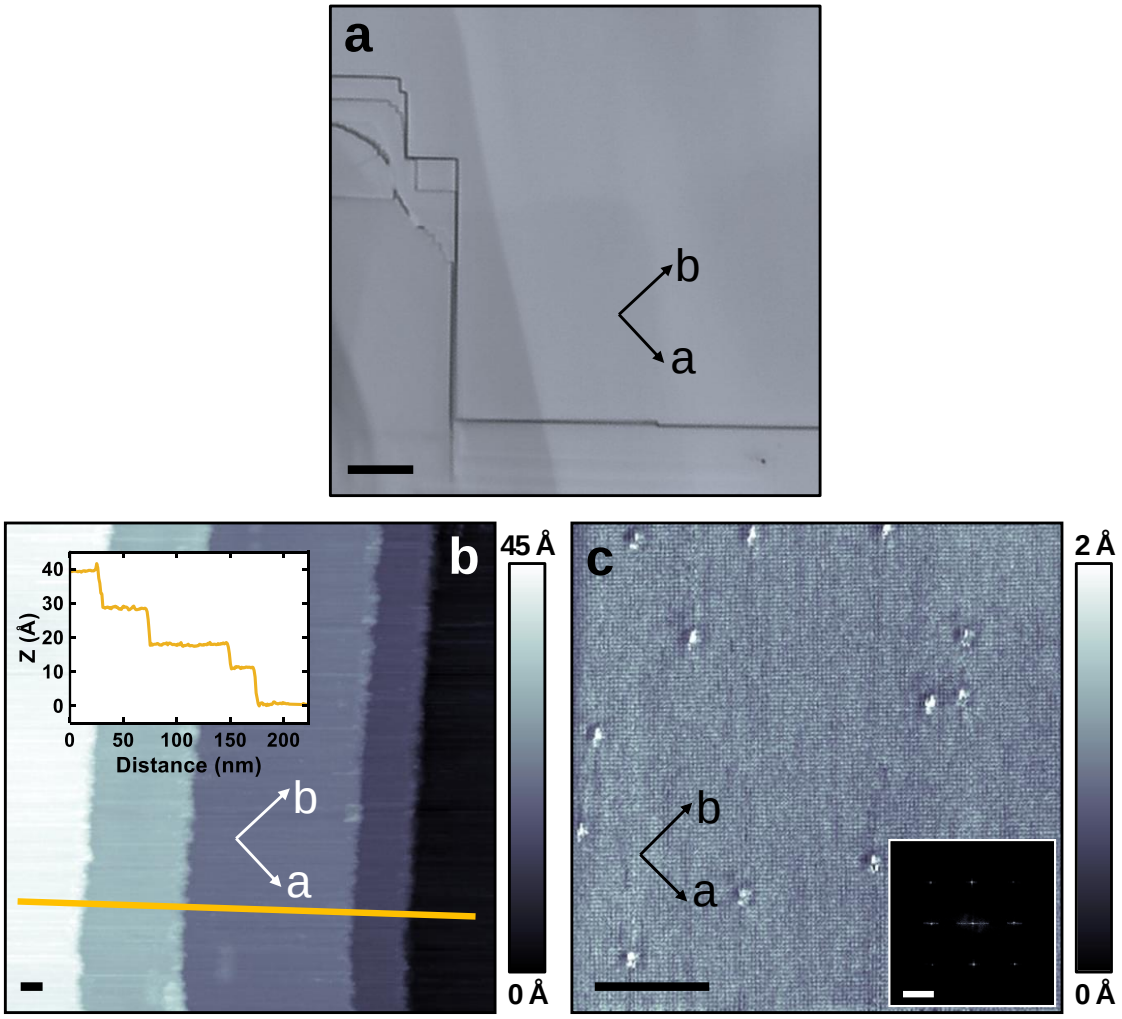

Figure 6.7: (a) Optical microscope image on one of the FeSe samples we measured after the cleaving process at cryogenic conditions. Perpendicular breaking-lines in the surface reveal the orientation of the square lattice of Se atoms. Scale bar: 10 μm. (b) 218×218 nm^2 STM topographic image of FeSe showing subsequent atomic terraces separated by steps. Inset displays a height profile along the orange line across the steps. The height jump between steps is always of one or two unit cells in c-direction. (c) 42.5 × 42.5 nm^2 STM topography showing square Se lattice with atomic resolution and several bump-like defects. The Fourier transform of the image in the inset shows the Bragg peaks corresponding to the observed Se lattice (scale bar is 2 nm^{-1} long). Topographic images in (b, c) were measured with Au tip at 100 mK with a bias voltage of 10 mV at a setpoint current of 4 nA. Scale bars in (b, c) are 10 nm long. Vertical color scale is given at the right of each panel. The orientation of a and b orthorhombic axes is indicated by black or white arrows in each image.

The evolution of the measured conductance curves with increasing temperature is shown in fig. 6.8b from 0.1 K up to 9.4 K as colored lines. The zero bias conductance value gradually increases and the height of the quasiparticle peaks gradually decreases until the curves eventually become flat above 8.6 K. To obtain the dependence of the density of states, $N(E)$, with the temperature we

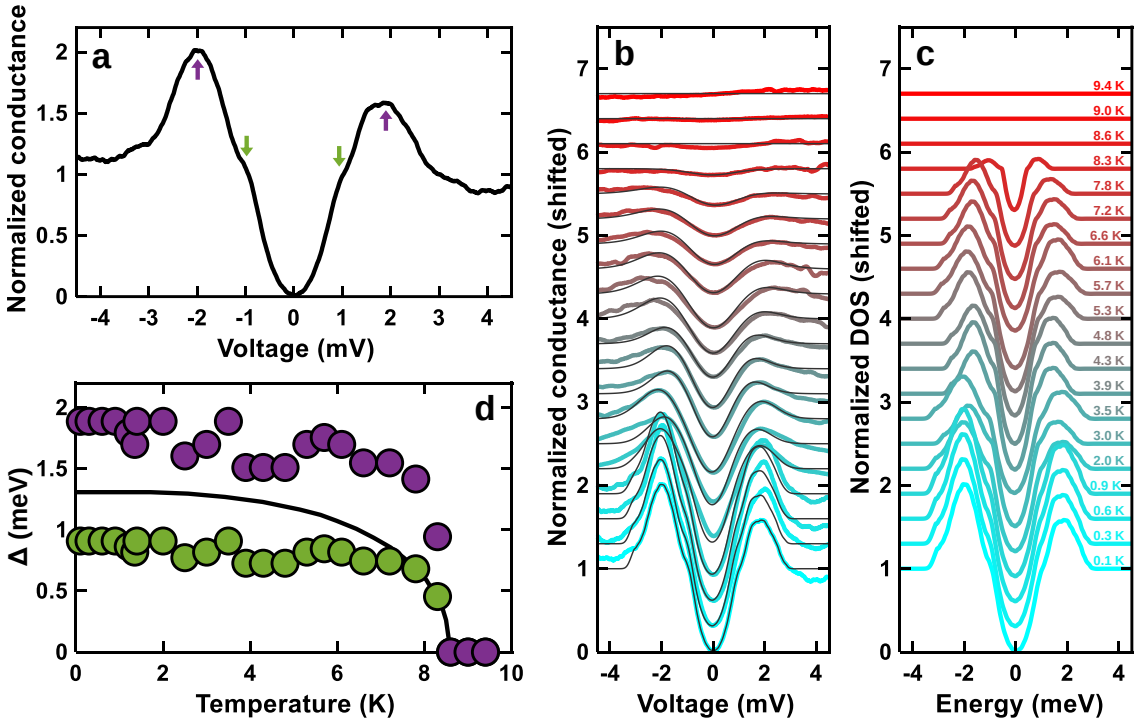

Figure 6.8: (a) Tunneling conductance versus voltage curve measured with Au tip on the FeSe surface using a setpoint current of 4 nA. The curve shows a double gap structure identified by the quasiparticle peaks of the bigger gap (purple arrows) and two additional in-gap features (green arrows). Conductance curves are normalized to the conductance outside the superconducting gap. (b) Normalized conductance curves measured in FeSe as a function of the bias voltage shown for increasing temperatures as colored lines. Curves are shifted upwards for better visualization. Black lines account for the result of the convolution of the density of states in (c) with the derivative of the Fermi distribution at each temperature. The temperature of each curve is printed in (c). (d) Temperature dependence of the gap size of the two gaps we spot in (a). The gap size is measured from the position of the peaks in dN/dE and is depicted in purple for the bigger gap and in green for the smaller one. BCS expected evolution of the gap size with temperature is plotted in black for T_c = 8.6 K.

search for the $N(E)$ curve that best recovers the measured conductance curve after being convoluted with the corresponding derivative of the Fermi function at each temperature (see eq. (2.9)). The $N(E)$ curves we obtained are shown in fig. 6.8c and their convolutions with the derivative of the Fermi distribution at each temperature are plotted in black in fig. 6.8b on top of the corresponding conductance curve.

From the density of states versus energy curves in fig. 6.8c we can obtain the evolution of the gap size with temperature for both superconducting gaps (fig. 6.8d). Values for the gap size determined from the position of the peaks in the dN/dE curves for the bigger (Δ_1) and the smaller (Δ_2) gaps are depicted as purple and green circles, respectively. The BCS expected behavior for the gap size as a function of the temperature is shown as a black line in fig. 6.8d for a T_c of 8.6 K. The gap size at low temperatures is slightly bigger than the BCS prediction for Δ_1 and sligthly

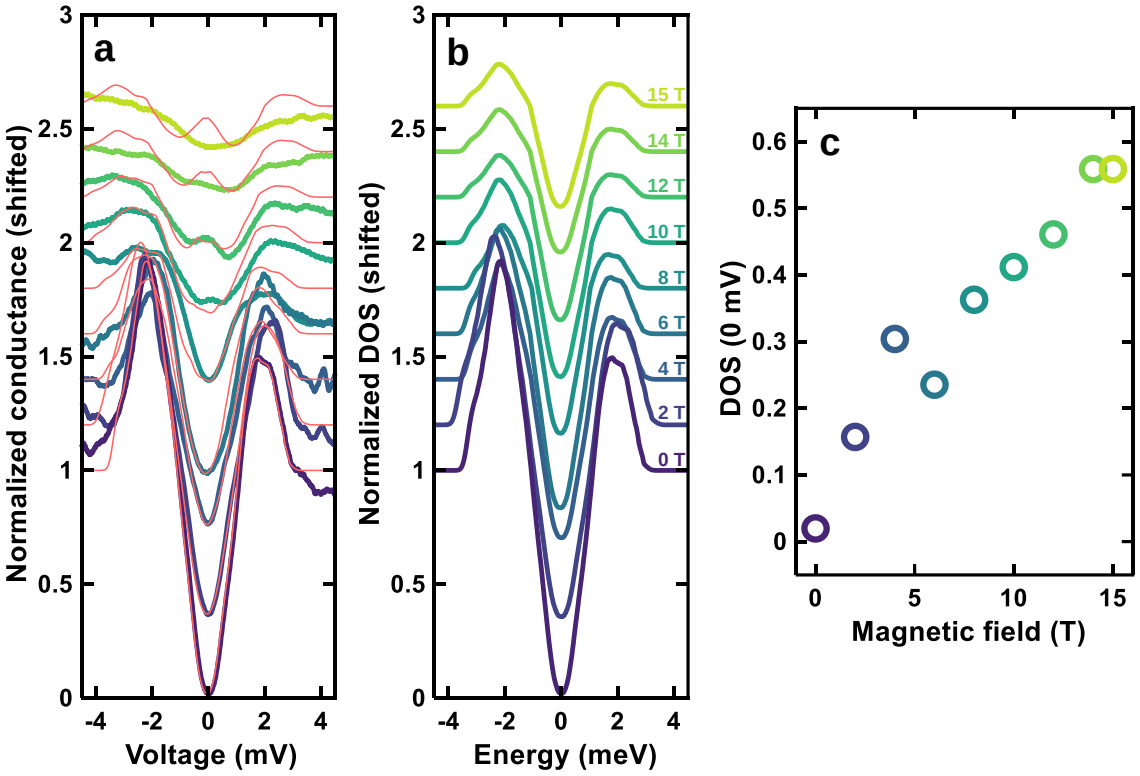

Figure 6.9: (a) Normalized tunneling conductance curves measured in FeSe as a function of the bias voltage for different values of the magnetic field (thick colored lines). Curves are shifted upwards for better visualization. (b) Density of states curves as a function of the energy inferred from the conductance curves in (a). Magnetic field value of each curve is printed in (c). For each magnetic field, light red lines in (a) show the result of the convolution of the density of states curves in (b) with a Zeeman energy splitting of 0.067 meV/T with the derivative of the Fermi distribution at 100 mK. (c) Zero energy density of states as a function of applied magnetic field showing a roughly linear behavior.

smaller for Δ_2. The temperature dependence of the superconducting gaps roughly follows BCS theory.

6.2.2 Zeeman splitting

As I introduced above, Zeeman energy in FeSe is comparable with the Fermi energy of the bands and with the superconducting gap size. Assuming a typical g-factor of 2, the estimation for the Zeeman energy (E_Z) of FeSe at 15 T is of $E_Z \approx \mu_B g B \approx 1.74$ meV, where μ_B is the Bohr magneton. Thus, as the bigger superconducting gap size we measure is Δ_1 = 1.9 meV, it is reasonable to expect that a band splitting of the order of the superconducting gap would considerably alter the density of states at high magnetic fields.

Figure 6.9a shows the normalized conductance versus voltage curves we measured at 100 mK with the Au STM tip in FeSe as thick colored lines for different values of the magnetic field from 0 T to 15 T. To make sure that the curves belong to the

superconducting phase, we took vortex images at each field and positioned the STM tip in a space between vortices. At lower magnetic field, the zero bias conductance is smaller and the quasiparticle peaks are higher. As magnetic field increases, the quasiparticle peaks become wider and the zero bias conductance rises. To obtain the density of states versus the energy we tried to find the $N(E)$ curve whose convolution with the derivative of the Fermi distribution at 100 mK best fit the measured conductance at each field. However, we were not able to fit the curves at higher magnetic fields without completely distorting the shape of the $N(E)$ curves used at lower magnetic fields. Thus, we introduced an energy splitting in the $N(E)$ curves that increases linearly with magnetic field. This way, when convoluting the $N(E)$ curve after being energy-split by a certain Zeeman energy with the derivative of the Fermi distribution, we can reproduce the broadening of the quasiparticle peaks observed in the conductance curves as magnetic field increases. After this fitting process, we found this Zeeman energy to be 1 meV at 15 T, slightly smaller but of the same order of the estimation made above. The resulting density of states curves are plotted in fig. 6.9b and the corresponding energy-split and temperature convoluted curves are plotted in light red on top of the corresponding conductance curves in fig. 6.9a. Interestingly, the position of the quasiparticle peaks, and thus, the gap size, remains constant up to 15 T, but the zero energy density of states increases with magnetic field following an almost linear trend (see fig. 6.9c). Such a behavior is a consequence of a Zeeman splitted density of states with a linear density of states at low energies.

With this simple analysis, we see how Zeeman splitting can explain the broadening of the quasiparticle peaks at higher magnetic field. However, it does not destroy completely superconductivity even at 15 T and we have relatively deep superconducting gaps that allow us to see vortices at very high magnetic fields.

6.3 High magnetic field vortex lattice

Superconducting vortices in FeSe have been extensively studied with STM at relatively low magnetic fields (lower than 8 T) [285, 293, 294]. However, an analysis of the vortex lattice near $H_{c2} \approx 17$ T was still lacking. A high magnetic field superconducting phase has been proposed above 13-14 T arising from the BCS-BEC crossover regime given the comparable scales of the Zeeman energy, the Fermi energy and the superconducting gap size in this material [260, 286], but no experimental observation of the vortex lattice has been reported in the vicinities of that proposed transition.

Vortices in FeSe appear as elongated features as a result of the difference between coherence lengths, ξ, along the a and b directions, what mainly reflects the twofold symmetry of the gap function. The major axis of the ellipsoidal shape of the vortex cores lies along two perpendicular directions in different areas separated by twin boundaries. The presence of this twinned domains is well noticed in our STM vortex images. Figure 6.10a shows a topographic image taken at 100 mK and 8 T in a region where we found two line defects crossing the image from bottom to top.

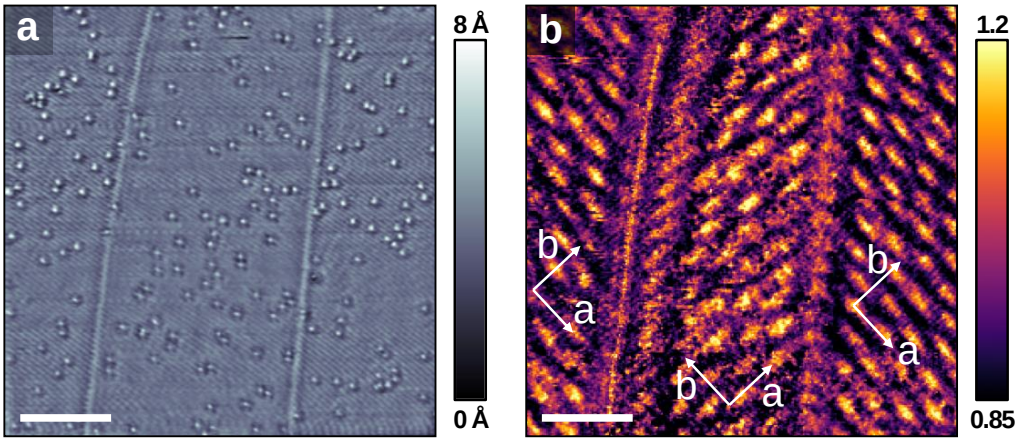

Figure 6.10: (a) 236.3×236.3 nm^2 STM topographic image measured at 8 T and 100 mK showing several bump-like defects and two line defects (V_{bias} = 5 mV, $I_{setpoint}$ = 4 nA). (b) Zero bias normalized conductance map in the same field of view at 8 T showing the superconducting vortex lattice. Vortices are elongated along orthorhombic *a*-direction and line defects act as twin boundaries rotating the reference *ab*-plane 90°. The orientation of *a* and *b* axes is marked with white arrows in (b) for each twinned domain. Horizontal scale bar is 50 nm long and vertical color scale bars are provided at the right of each panel.

The zero bias normalized conductance at 8 T in the same field of view is mapped in fig. 6.10b. The shape of the superconducting vortices we see is ellipsoidal as reported in previous works [285] (see fig. 6.6), but our field of view is significantly larger. The line defects we observed in the topography act as twin boundaries that change 90° the direction of the nematic domain [285]. The reference *ab*-plane rotates 90° every time a twin boundary is crossed so that vortices are always elongated along *a*-direction (see *a* and *b* axes reference in fig. 6.10b). In each twinned domain, the inter-vortex distance is that expected for a typical Abrikosov vortex lattice at 8 T (≈ 17.7 nm). Inside the twin boundaries pair-breaking intensifies and the vortex density becomes much higher. This shows that the twin boundaries act as pinning centers.

Far from the influence of any twin boundary we can resolve individual vortices and thus we chose these regions study the vortex lattice at high magnetic fields. Figure 6.11 shows a series of 71.3 × 71.3 nm^2 vortex images acquired at different values of the magnetic field ranging from 8 to 15 T. Vortex density increases with magnetic field and the inter-vortex distance matches the expected one for an Abrikosov lattice at each field (see fig. 6.11g). The contrast between superconducting and non-superconducting areas decreases with increasing magnetic field as a consequence of the increase of the zero bias conductance with magnetic field I discussed above. However, to enhance the visibility of the vortex lattice, we applied individual contrast to each image (see color scale bars in fig. 6.11).

With these results we prove that superconducting vortices are observable in FeSe very close to H_{c2} (at least up to 15 T) and that in case there is a high magnetic field superconducting phase somehow different than the low field phase, it does not really affect the vortex behavior.

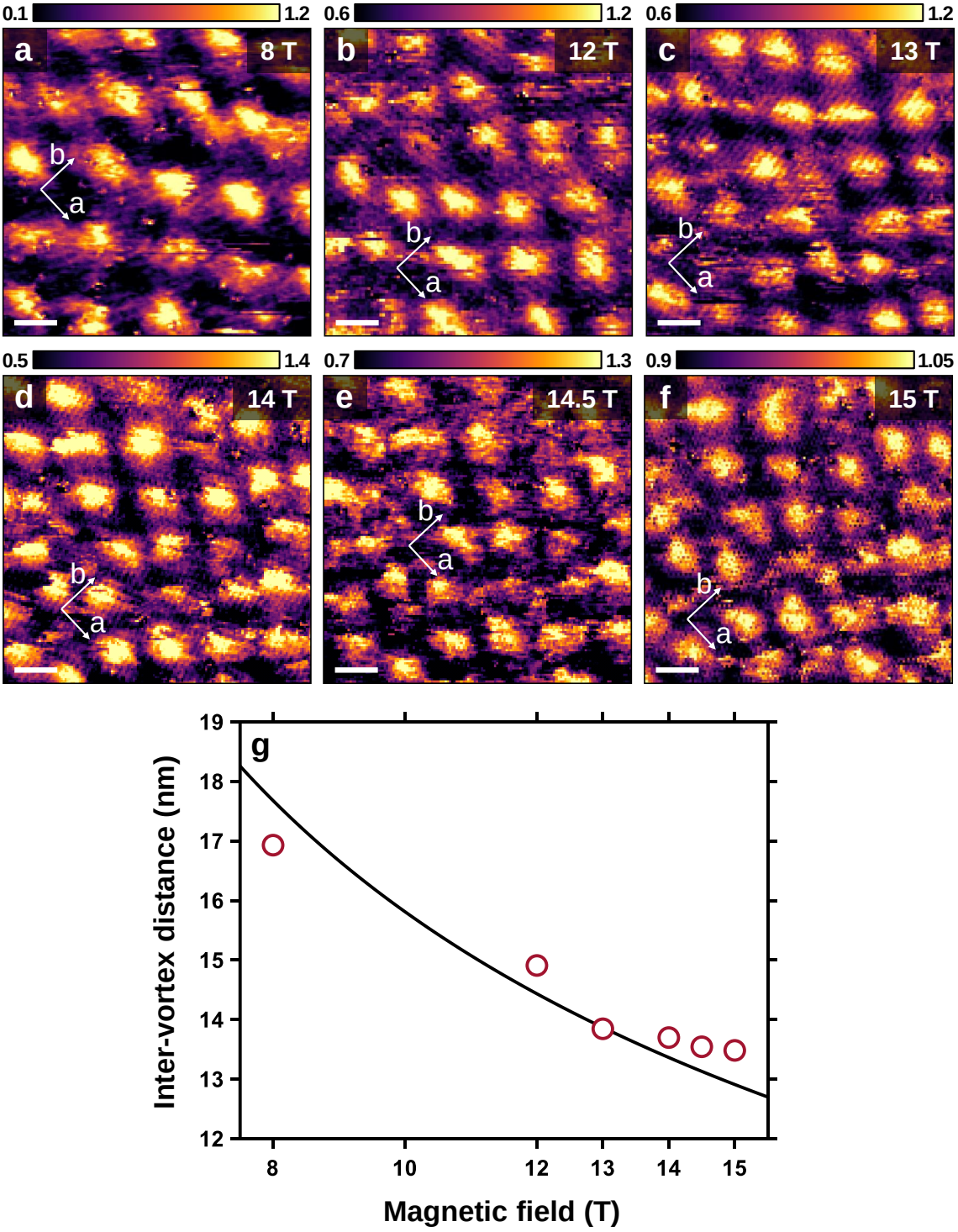

Figure 6.11: Zero bias normalized conductance maps showing the vortex lattice in FeSe at 100 mK inside a 71.3×71.3 nm^2 region at (a) 8 T, (b) 12 T, (c) 13 T, (d) 14 T, (e) 14.5 T and (f) 15 T. White arrows mark the orientation of the orthorhombic a and b axes. Horizontal scale bar is 10 nm long and the normalized conductance is given by the color code provided at the top of each panel. (g) Measured average inter-vortex distance versus magnetic field. We have applied the Delaunay triangulation algorithm described in Ref. [68] to the images in (a-f) to obtain the red data points. Black line represents the Abrikosov inter-vortex distance as a function of magnetic field.

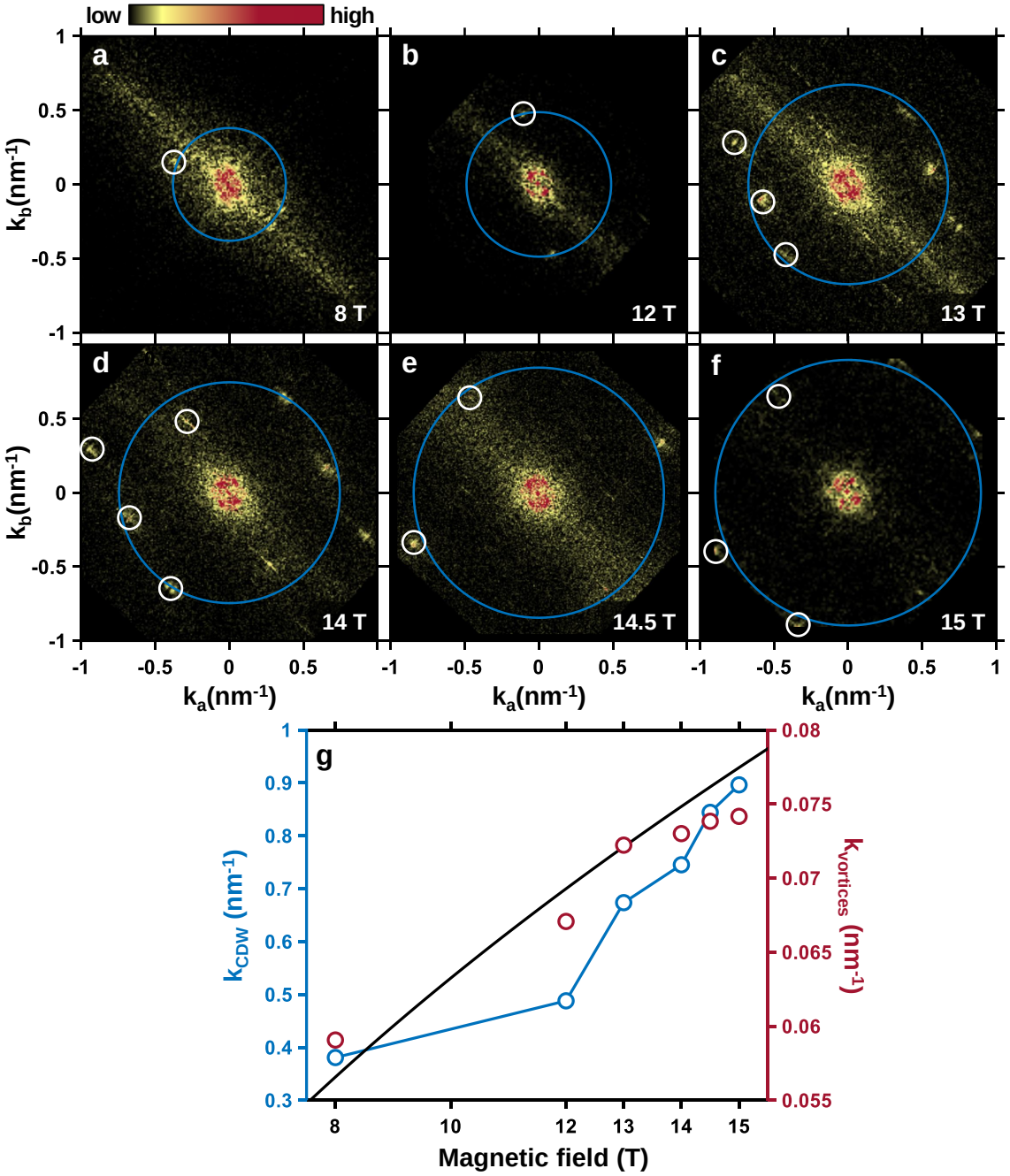

Figure 6.12: Fourier transforms of the conductance maps in fig. 6.11 at (a) 8 T, (b) 12 T, (c) 13 T, (d) 14 T, (e) 14.5 T and (f) 15 T. White circles highlight the characteristic wavevectors we observe at each field and blue circles mark the average position of these wavevectors. (g) Average size of the wavevectors at each field (blue) and size of the wavevector of the vortex lattice (red) versus magnetic field. Black line indicates the size of the characteristic wavevector of an Abrikosov lattice.

At high magnetic fields, together with the vortex lattice, in the zero bias conductance maps we spot some stripe-like features that are clearly noticeable in the images of fig. 6.11. The Fourier transforms of the images in fig. 6.11 are shown in fig. 6.12a-f. Fourier transforms show several hot spots at the characteristic

wavevectors of the stripe-like features (white circles in fig. 6.12a-f). These hot spots are not aligned with any of the crystalline axes, and their magnetic field evolution is quite strong. The average size of the wavevectors of these spots, indicated by the blue circles in fig. 6.12a-f, increases with magnetic field. The characteristic wavevectors of these modulations are significantly smaller than that of the atomic periodicity ($1/a = 1.87$ nm^{-1}). Red spots at smaller $\vec{q}$ in fig. 6.12a-f are due to the characteristic wavevectors of the vortex lattice.

Figure 6.12g plots this average size as a function of the magnetic field (blue), together with the characteristic wavevector of the vortex lattice (red). These modulations might be the signature of a strongly magnetic field dependent charge density wave. As I will discuss in the following section, the band structure in FeSe shows some bands that terminate very close to the Fermi level. This allows scattering with wavevectors whose size is comparable to those of the Abrikosov vortex lattice. The interaction between those scattering vectors and the vortex lattice could lead to significant modifications in the band structure, and thus favor the appearance of charge modulations. Due to the Zeeman shift of the band structure, the periodicity of the charge density wave shows a strong magnetic field dependence. In fact, if we assume that the bands follow a parabolic dispersion, the k-dependence of the energy of the Zeeman split bands will be given by

$$E_k \pm E_z \propto \frac{\hbar^2 k^2}{2m^*}, \tag{6.1}$$

where m^* is the effective mass of the band. Isolating k, we obtain the following relation between k and E_z:

$$k \propto \sqrt{E_k \pm E_z} \tag{6.2}$$

Therefore, as the Zeeman energy E_z increases linearly with the applied magnetic field, H, the changes in k introduced by the Zeeman splitting of the bands will go as $k \propto \sqrt{H}$. On the other hand, since the Abrikosov inter-vortex distance goes as $d_{vortices} \propto 1/\sqrt{H}$, the wavevector associated to the vortex lattice will feature the same field dependence as that of the Zeeman shifted band structure, $k_{vortices} \propto \sqrt{H}$. Both wavevectors show a similar magnetic field dependence and, when there are bands terminating very close to the Fermi level, the size of the k wavevector of such bands can become comparable with the wavevector of the high magnetic field vortex lattice. Thus, the interference of two modulations with very similar but not exactly equal wavevector might produce a supermodulation similar to a Moiré pattern with a much larger wavevector. Although we do not have a theoretical explanation for these observations, there seems to be a link between charge modulations and the vortex lattice which has been, to our knowledge, never observed before.

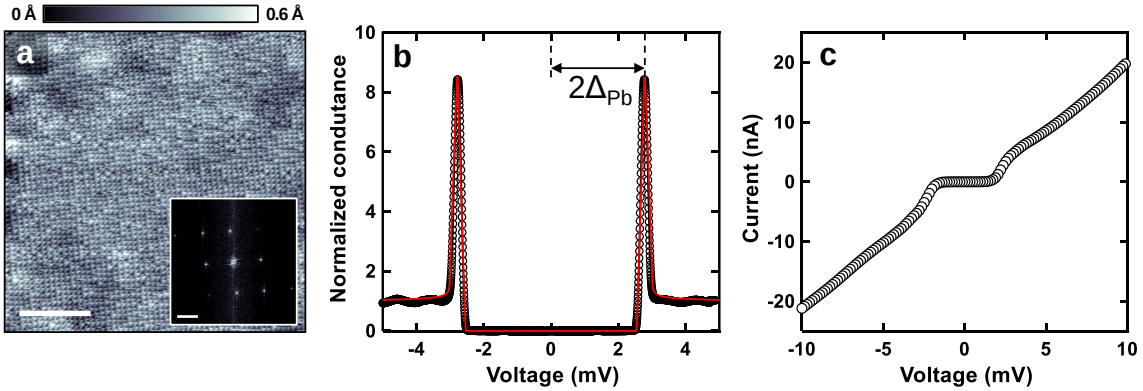

Figure 6.13: (a) STM topographic image taken at 100 mK and zero magnetic field in a 21.2 × 21.2 nm^2 area where we studied the quasiparticle interference scattering (Pb tip, V_{bias} = 10 mV, $I_{setpoint}$ = 20 nA). We observe a height modulation over the square lattice of Se atoms coming from the electronic scattering around defects outside this scanning window. Scale bar: 5 nm. Inset: Fourier transform of the image showing the Bragg peaks of the square Se lattice and the long wavelength scattering signal around the central point. Scale bar: 2 nm^{-1}. (b) Normalized tunneling conductance versus bias voltage curve (black circles) measured in a Pb sample with the same Pb tip used in the topography shown in (a). Red line on top of the data points shows a BCS fitting of the gap using Δ_{Pb} = 1.4 meV. (c) Average tunneling current versus voltage curve measured in FeSe inside the region shown in (a) with a Pb tip.

6.4 QPI: band structure and superconducting gap symmetry

We performed QPI measurements in the 21.2×21.2 nm^2 region with atomic resolution shown in the topography of fig. 6.13a. The square lattice of Se atoms is clearly resolved in this area. Although there are no defects in this particular scanning window, the presence of nearby defects provides sufficient scattering signal for the QPI analysis.

Unlike other QPI studies presented in this thesis, here we used a superconducting Pb tip to increase the energy resolution. In this situation, the density of states of the tip, $N_t(E)$, is not constant with energy but presents two very sharp peaks at the position of the quasiparticle peaks in Pb (see fig. 6.13b). In a simplified picture, $N_t(E)$ can be approached by a function consisting of two δ-functions centered at the position of the quasiparticle peaks of Pb and being exactly zero in between. Introducing such $N_t(E)$ in eq. (2.7), we will obtain that, at low temperatures, the tunneling current measured with a superconducting tip is proportional to the density of states of the sample with an energy offset equal to the superconducting gap of the tip [50]. Thus, the QPI signal will be observed in the current maps instead of the conductance maps. To correct for the energy offset introduced by the superconducting Pb tip, we have to subtract Δ_{Pb} to the data at positive energies and add Δ_{Pb} to the data at negative energies. This means that, for instance, as we measure a value of Δ_{Pb} = 1.4 mV from the Pb-Pb junction between the same Pb

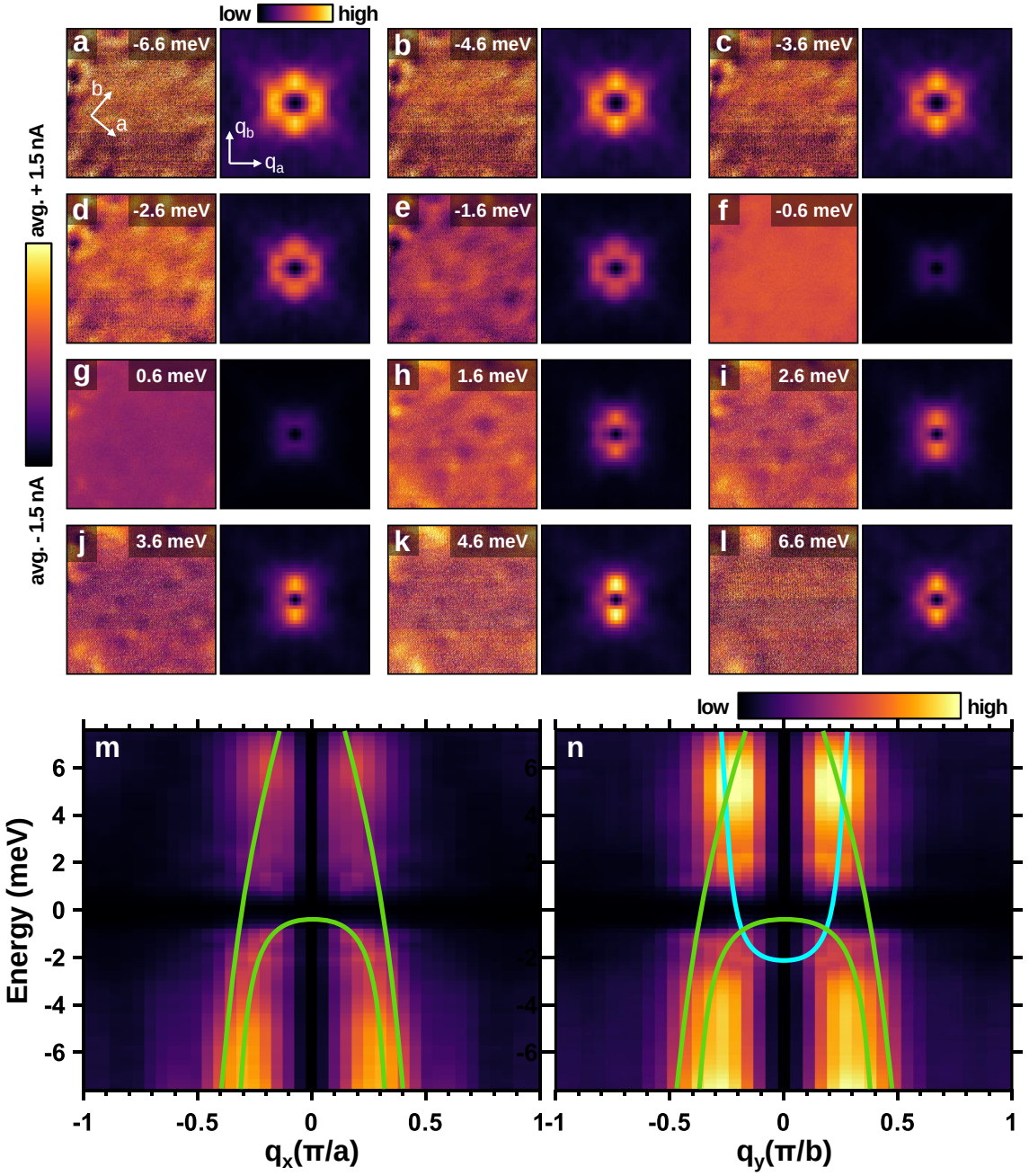

Figure 6.14: (a-l) Current maps (left) in the same field of view of the topography in fig. 6.13a and their 2D-Fourier transform (FFT) maps inside the 1BZ (right) for some representative energies from -6.6 meV to +6.6 meV (energy offset coming from the superconducting Pb tip already corrected). Energy values are indicated in the top-right corner of each current map. For better visualization, vertical color scale bar for current maps covers a ±1.5 nA range around the average current value of each map. The orientation of the orthorhombic a and b axes is marked with white arrows in the left panel of (a). FFT maps are shown from $-\pi/a$ to $+\pi/a$ along q_a and from $-\pi/b$ to $+\pi/b$ along q_b. q_a and q_b directions are marked in the right panel of (a). (m) q_b = 0 profiles for all the energies of the study showing the scattering intensity of the FFT maps along q_a. (n) Same for the q_a = 0 profiles along q_b. Green and cyan bands plotted over the profiles mark, respectively, the hole-like and electron-like dispersion of the scattering vectors we observe in our data.

tip and a Pb sample (see fig. 6.13b), the scattering features that we observe in the current when we apply a bias voltage of +3 mV will give as information about the band structure of the sample at E = 3 mV − Δ_{Pb} = 1.6 mV. Using a superconducting Pb tip, at each nominal value of the energy, we are essentially probing the sample with a narrower function in energy (with the width of the quasiparticle peaks of Pb), what allows for smaller energy steps, and thus provides a higher energy resolution of the measured density of states of the sample.

We took current versus voltage curves between ±10 mV at every pixel of the simultaneously acquired topography shown in fig. 6.13a. The average current curve in the whole image is plotted in fig. 6.13c. From the current curves, we built spatially resolved current maps for all the energies of the study and Fourier transform them to access the main scattering $\vec{q}$ vectors in reciprocal space. Fourier transform (FFT) maps are mirror-symmetrized along the orthorhombic a and b axes to increase the signal to noise ratio. Current maps and FFT maps inside the first Brillouin zone (1BZ) are shown in fig. 6.14a-l for some representative energies. We applied a 3 × 3 pixel average filter to further increase the signal to noise ratio and we subtracted a Gaussian core centered at $\vec{q}$ = 0 to filter out the smallest wavevectors and increase the contrast of the images. Real space current maps show some modulations that evolve with energy and decrease in intensity around the Fermi energy as the superconducting gap of FeSe appears. FFT maps display a roughly round intensity cloud around the central point at negative energies that shrinks and changes its shape with increasing energy to end up as a more ellipsoidal feature along q_b at positive energies.

Seeking for signatures of the Fermi surface of FeSe described above, we plot profiles of the FFT maps along a and b high symmetry directions for all the energies of the study (see fig. 6.14m,n). Both profiles present a drop of the intensity around the Fermi level as a consequence of the FeSe superconducting gap. The scattering patterns along q_a and q_b are very similar, but the profile along q_a shows higher intensity for negative energies, while the scattering intensities in the q_b profile are of the same order at negative and positive energies. In both profiles, the enhanced scattering cloud is centered at around 0.35 π/a at −7 meV and evolves to smaller $\vec{q}$ with increasing energy.

The fact that the scattering intensity along q_a is higher at negative energies can be understood if there are two hole pockets at the Γ point instead of just one, as pointed out by Li *et al.* [282]. In this picture, one of the hole bands terminates very close to the Fermi level. At negative energies we observe scattering vectors coming from both bands, while the scattering intensity at positive energies is only due to the scattering inside the remaining band. Such a situation is qualitatively plotted in green in fig. 6.14m on top of the QPI profiles. This scheme is also compatible with our QPI data along q_b (fig. 6.14n), but there, the scattering clouds appear at slightly higher $\vec{q}$. If we take a look at the shape of the hole-like α-band shown in fig. 6.3, it has a rather ellipsoidal shape with its mayor axis aligned to the orthorhombic b axis. Thus, we expect to observe scattering features along q_a to be at slightly smaller $\vec{q}$ than that along q_b. This is exactly what we observe in our QPI data. However, the scattering signal along q_b at positive energies is much more intense.

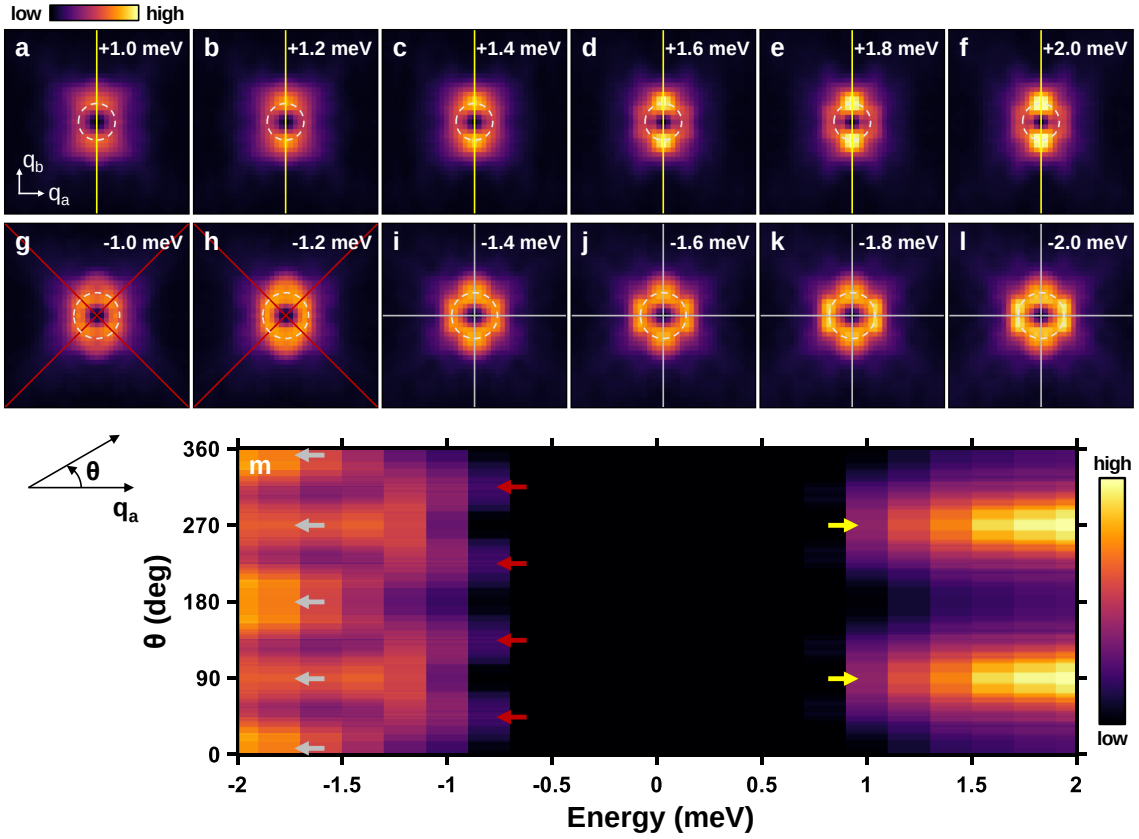

Figure 6.15: Measured QPI maps inside the first Brillouin zone between +1 meV and +2 meV (a-f) and between -1 meV and -2 meV (g-l). White arrows in (a) mark q_a and q_b directions. (m) Scattering intensity profile along the white circle in (a-l) as a function of the energy and the angle measured from q_a. Grey arrows mark the four-fold symmetric bright spots at around −2 meV along the crystallographic axes, red arrows mark the four bright spots along the diagonals at around −1 meV and yellow arrows mark the two-fold symmetric bright spots along q_b at positive energies. Colored lines in (a-l) indicate the angles marked by colored arrows in (m).

To account for this enhanced scattering we have to consider a new contribution to the scattering. Figure 6.14n shows a scattering cloud centered at around 0.25 π/a at 7 meV that evolves to smaller $\vec{q}$ as energy decreases and terminates at around −2 meV (cyan line in fig. 6.14n). Coming back to the band scheme in fig. 6.3, the electron-like ϵ-band centered at the X point is very elongated along the a axis, so we expect higher scattering intensity along q_b connecting the flatter regions of the band, that lie parallel to b-direction. Therefore, the electron-like scattering features are expected to be much more intense along q_b than along q_a, what explains the difference in intensity in our QPI profiles along q_a and q_b at positive energies. Notice that the size at E = 0 of the hole and electron bands we measure is in agreement with α and ϵ bands obtained by ARPES [278, 279] or QPI [271, 260].

We observe a symmetry change with energy in our QPI maps (fig. 6.14a-l). At negative energies, the maps are nearly four-fold symmetric, while at positive energies the symmetry is clearly two-fold. In the band scheme we inferred from our QPI data,

at negative energies we only have two hole bands whose size is just slightly higher along q_b than along q_a. This explains the nearly four-fold symmetry in our maps at negative energies. Conversely, at positive energies the presence of the directional electron-band introduces another contribution to the scattering only along q_b that reduces the symmetry in our maps from four-fold to two-fold.

Figure 6.15 shows the QPI maps inside the first Brillouin zone between +1 meV and +2 meV (a-f) and between −1 meV and −2 meV (g-l). At positive energies, the symmetry of the scattering patterns is two-fold, with two brighter spots along q_b. At negative energies, the ellipsoidal patterns at −1 meV and −1.2 meV evolve to a nearly four-fold symmetric pattern below −1.6 meV.

To better characterize the changes in the superconducting gap symmetry, fig. 6.15m plots a profile of the QPI maps along the white circles in fig. 6.15a-l as a function of the angle and the energy. The radius of the white circle is 0.2 π/a for positive energies and 0.25 π/a for negative energies. Starting at −2 meV, the symmetry is four-fold with the symmetry axes along the crystallographic a and b axes (grey arrows in fig. 6.15m). Around −1 meV, the symmetry is still four-fold, but the symmetry axes are no longer along the crystallographic axes, but along the diagonals (red arrows). Finally, at positive energies the gap shows two-fold symmetry with the more intense spots along q_b (yellow arrows). As discussed above, this symmetry change can be understood from the presence of bands that terminate very close to the Fermi level, specially the electron-like ϵ-band, which is very directional along q_b.

6.5 Conclusions

In summary, we have probed the surface of the iron based superconductor FeSe. Low temperature cleaving results in clean flat surfaces where we can clearly resolve the square Se lattice. We have measured the density of states around the Fermi energy at 100 mK spotting the double gap structure. We followed it up to 9.4 K finding a superconducting critical temperature of around 8.6 K, in agreement with previous results from macroscopic transport measurements in bulk FeSe single crystals. We studied the shape of the superconducting gap with magnetic field up to 15 T and show how a Zeeman splitting in the density of states can explain the broadening of the quasiparticle peaks we observe as magnetic field increases.

We have also studied the vortex lattice up to 15 T. In some regions of the sample, we observed ellipsoidal nematic vortices whose bigger axis rotates 90° in the nematic twin boundaries. In areas of the sample far from any domain boundary we clearly spot the vortex lattice and tracked it up to 15 T. We observe a charge density wave at high magnetic fields that depends strongly on magnetic field possibly originating from the interaction between the vortex lattice and the low energy band structure.

We have performed QPI measurements inside a ±8 meV energy range around the Fermi level using a superconducting tip. From the QPI data we resolve two hole pockets, and one electron pocket. One of the hole pockets and the highly anisotropic

electron pocket terminate very close to the Fermi level. We have also been able to measure the superconducting gap symmetry from our QPI data, noticing a change from a nearly four-fold symmetry at negative energies to a two-fold symmetry at positive energies.

General conclusions

In summary, I have covered the aspects which I believe are most interesting to understand superconductivity in topical systems. I have taken two model systems, $Ce(Ru_{0.92}Rh_{0.08})_2Si_2$ and WTe_2, and studied, respectively, magnetism and low energy band structure in these systems. I have then taken two superconductors, Au_2Pb and FeSe, and analyzed their low energy properties.

In $Ce(Ru_{0.92}Rh_{0.08})_2Si_2$, I have analyzed the problem of vanishing magnetic order. I have shown that the Zeeman splitting of the band structure produces the different magnetic transitions and eventually eliminates magnetism. The low energy band structure is not radically affected by magnetic field and it is dominated by Kondo hybridization between the heavy $4f$-electrons of Ce and the light conduction electrons. This hybridization is present in the whole phase diagram. Future experiments should probably address the behavior of La-doped $CeRu_2Si_2$ just at the verge of magnetism at zero field. The low energy band structure should show features related to magnetism in absence of a magnetic field.

In WTe_2, I determined the band structure, finding a good match between calculations and experiments. The magnetic field does not significantly influence the band structure. A more careful, atomic size study of the band structure is needed to address issues like Landau quantization. Furthermore, I have addressed the properties of surface states. I have found two energy ranges where scattering possibly shows surface states. Their topological properties remain to be analyzed using further experiments and calculations. In all, the determination of the low energy band structure of WTe_2 is quite complete and highlights the peculiar aspects that arise in an electronic band structure when looking on the detailed features at low energies.

In Au_2Pb, I have characterized the superconducting properties as a function of temperature and magnetic field. I have shown that there is a finite density of states at the Fermi level and discussed how these states could be related to the closing of a Dirac cone at the surface. Au_2Pb, being in principle a simple compound, shows a rare situation with many structural phase transitions below room temperature, indicating a considerable sensitivity to stress. Probably, modifying the cleaving mechanism, or cleaving at another crystalline phase, could lead to the desired observation of an atomically resolved surface. By now, the picture is that Au_2Pb is the only system with topologically nontrivial excitations showing a finite density of states at the Fermi level over large areas at the surface.

Finally, I have studied in great detail FeSe, finding radically new features. I have imaged for the first time the vortex lattice at high magnetic fields and tracked it up to 15 T. I found that the bottom of an electron band lies inside the superconducting gap, what leads to an electron-hole asymmetry in the superconducting density of states that had not been observed before. Besides, I observed a new charge density

wave. The wavevector of this modulation follow a magnetic field dependence similar to the wavevector of the vortex lattice. The origin of this charge density wave might be related to the unique features of the low energy band structure in this material. Exploring the phase diagrams by doping with Te and S should probably help better understand the surface properties of this high temperature superconductor. It would be important to perform syncroton or neutron scattering experiments to see if the charge density wave is a feature of the surface or if it is related to the features observed in the thermal conductivity at high magnetic fields.

Conclusiones generales

En resumen, a lo largo de esta tesis he tratado los aspectos que considero más interesantes para entender el fenómeno de la superconductividad en distintos sistemas. He utilizado dos sistemas modelo, $Ce(Ru_{0.92}Rh_{0.08})_2Si_2$ y WTe_2, y he estudiado, respectivamente, el magnetismo y la estructura de bandas a bajas energías en estos sistemas. Posteriormente, he caracterizado dos materiales superconductores, Au_2Pb y FeSe, y he analizado sus propiedades a bajas energías.

En $Ce(Ru_{0.92}Rh_{0.08})_2Si_2$, he analizado el fenómeno de la desaparición del orden magnético. He mostrado cómo el desplazamiento Zeeman de la estructura de bandas da lugar a las diferentes fases magnéticas y acaba eventualmente con el magnetismo. La estructura de bandas a bajas energías, dominada por la hibridación Kondo entre los electrones pesados $4f$ del Ce y los electrones ligeros de conducción, no se ve afectada en gran medida por el campo magnético. El esquema de hibridación está presente en todo el diagrama de fases. Probablemente, trabajos futuros deberían estudiar el comportamiento del $CeRu_2Si_2$ dopado con La en la frontera del magnetismo a campo cero. La estructura de bandas a bajas energías debería mostrar características relacionadas con el magnetismo en ausencia de campo magnético.

En WTe_2, he determinado la estructura de bandas, encontrando un buen acuerdo entre los cálculos y los experimentos. El campo magnético no afecta significativamente a la estructura de bandas, de acuerdo con previas sugerencias. En el futuro, un estudio más detallado podría revelar algunos aspectos importantes como la cuantización de Landau. Por otro lado, he estudiado las propiedades de los estados de superficie. He encontrado dos rangos de energía en los que el scattering electrónico puede estar relacionado con la presencia de estados de superficie. Las propiedades topológicas de dichos estados deben ser aún analizadas usando experimentos y cálculos más específicos. Pese a todo, se ha logrado una determinación bastante completa de la estructura de bandas en WTe_2 a bajas energías, discutiendo los aspectos específicos que aparecen en una estructura de bandas cuando se estudia a bajas energías.

En Au_2Pb, he caracterizado las propiedades superconductoras en función de la temperatura y del campo magnético. He observado una densidad de estados finita al nivel de Fermi y he discutido cómo estos estados sugieren la presencia de un cono de Dirac en la superficie. A pesar de que, en principio, el Au_2Pb es un compuesto sencillo, muestra un comportamiento singular con varias transiciones de fase estructurales a bajas temperaturas, lo que indica una particular sensibilidad a las tensiones. Posiblemente, modificando el mecanismo de clivaje o clivando en otra fase cristalina se pueda tener acceso a superficies con resolución atómica. Por ahora, la conclusión es que el Au_2Pb es el único sistema con excitaciones topológicamente no

triviales cuya densidad de estados es finita al nivel de Fermi a lo largo de superficies extensas.

Por último, he estudiado con mucho detalle el superconductor FeSe, encontrando características muy novedosas. He realizado por primera vez imágenes de la red de vórtices a altos campos magnéticos y he seguido su evolución hasta 15 T. Por otro lado, he observado que el fondo de una banda de electrones está situado dentro del gap superconductor, lo que da origen a una asimetría electrón-hueco que no había sido observada antes. Adicionalmente, he observado una nueva onda de densidad de carga. El vector de onda de esta modulación sigue una dependencia con el campo magnético muy similar a la del vector de onda de la red de vórtices. El origen de esta onda de densidad de carga puede estar relacionado con las propiedades singulares de la estructura de bandas a bajas energías en este material. Explorar el diagrama de fases dopando con Te y S podría ayudar a entender mejor las propiedades de la superficie en este superconductor de alta temperatura crítica. Sería importante llevar a cabo experimentos de sincrotrón o de scattering de neutrones para ver si la onda de densidad de carga es una característica de la superficie o si está relacionada con propiedades observadas en la conductividad térmica a campos magnéticos elevados.

Publications

M. Fernández-Lomana, B. Wu, **F. Martín-Vega**, R. Sánchez-Barquilla, R. Álvarez-Montoya, J.M. Castilla, J. Navarrete, J.R. Marijuán, E. Herrera, H. Suderow and I. Guillamón, *Millikelvin scanning tunneling microscope at 20/22 T with a graphite enabled stick-slip approach and an energy resolution below 8 μeV: Application to conductance quantization at 20 T in single atom point contacts of Al and Au and to the charge density wave of 2H-$NbSe_2$*, Review of Scientific Instruments **92**, 093701 (2021).

F. Martín-Vega, V. Barrena, R. Sánchez-Barquilla, M. Fernández-Lomana, J. Benito-Llorens, B. Wu, A. Fente, D. Perconte-Duplain, I. Horcas, R. López, J. Blanco, J.A. Higuera, S. Mañas-Valero, N.H. Jo, J. Schmidt, P. C. Canfield, G. Rubio-Bollinger, J.G. Rodrigo, E. Herrera, I. Guillamón and H. Suderow, *Simplified feedback control system for scanning tunneling microscopy*, Review of Scientific Instruments **92**, 103705 (2021).

F. Martín-Vega, R. Sánchez-Barquilla, E. Herrera, H. Suderow, I. Guillamón, J.J. Baldoví, M. Ochi, R. Arita, N.H. Jo, S.L. Bud'ko and P.C. Canfield, *High magnetic field band structure in the topological semimetal WTe_2*. In preparation.

F. Martín-Vega, E. Herrera, G. Knebel, J.P. Brison, J. Flouquet, D. Aoki, D. Morr, H. Suderow and I. Guillamón, *Magnetic correlations through quantum criticality in Rh-doped $CeRu_2Si_2$*. In preparation.

F. Martín-Vega, J.J. Baldoví, B. Wu, V. Barrena, F. Mompeán, M. García-Hernández, P.C. Canfield, A. Black Schaffer, I. Guillamón and H. Suderow, *Superconducting density of states and band structure at the surface of the candidate topological superconductor Au_2Pb*. In preparation.

F. Martín-Vega, H. Suderow, I. Guillamón, J. Schmidt, S. Bud'ko and P.C. Canfield, *Electronic correlations in the nematic iron based superconductor FeSe*. In preparation.

Bibliography

[1] H. Onnes, *Further experiments with liquid helium. g. on the change ofelectrical resistance of pure metals at very low temperatures, etc. vi. on thesudden change in the rate at which the resistance of mercury disappears*, Comm. Phys. Lab. Univ. Leiden **29** (1911).

[2] W. Meissner and R. Ochsenfeld, *Ein neuer Effekt bei Eintritt der Supraleitfähigkeit*, Naturwissenschaften **21**, 787 (1933).

[3] F. London, H. London, and F. A. Lindemann, *The electromagnetic equations of the supraconductor*, Proceedings of the Royal Society of London. Series A - Mathematical and Physical Sciences **149**, 71 (1935).

[4] A. A. Abrikosov, *On the Magnetic properties of superconductors of the second group*, Sov. Phys. JETP **5**, 1174 (1957).

[5] L. Shubnikov, V. Khotkevich, Y. D. Shepelev, and Y. N. Ryabinin, *Magnetic properties of superconducting metals and alloys*, Zh. Eksp. Teor. Fiz **7**, 221 (1937).

[6] N. R. Werthamer, E. Helfand, and P. C. Hohenberg, *Temperature and Purity Dependence of the Superconducting Critical Field, H_{c2}. III. Electron Spin and Spin-Orbit Effects*, Phys. Rev. **147**, 295 (1966).

[7] P. C. Canfield, P. L. Gammel, and D. J. Bishop, *New Magnetic Superconductors: A Toy Box for Solid-State Physicists*, Physics Today **51**, 40 (1998).

[8] Y. Fasano and M. Menghini, *Magnetic-decoration imaging of structural transitions induced in vortex matter*, Superconductor Science and Technology **21**, 023001 (2008).

[9] D. Vasyukov, Y. Anahory, L. Embon, D. Halbertal, J. Cuppens, L. Neeman, A. Finkler, Y. Segev, Y. Myasoedov, M. L. Rappaport, M. E. Huber, and E. Zeldov, *A scanning superconducting quantum interference device with single electron spin sensitivity*, Nature Nanotechnology **8**, 639 (2013).

[10] J. R. Kirtley, *Fundamental studies of superconductors using scanning magnetic imaging*, Reports on Progress in Physics **73**, 126501 (2010).

[11] H. Suderow, I. Guillamón, J. G. Rodrigo, and S. Vieira, *Imaging superconducting vortex cores and lattices with a scanning tunneling microscope*, Superconductor Science and Technology **27**, 063001 (2014).

[12] O. Fischer, M. Kugler, I. Maggio-Aprile, C. Berthod, and C. Renner, *Scanning tunneling spectroscopy of high-temperature superconductors*, Rev. Mod. Phys. **79**, 353 (2007).

[13] J. Bardeen, L. N. Cooper, and J. R. Schrieffer, *Microscopic Theory of Superconductivity*, Phys. Rev. **106**, 162 (1957).

[14] J. Bardeen, L. N. Cooper, and J. R. Schrieffer, *Theory of Superconductivity*, Phys. Rev. **108**, 1175 (1957).

[15] E. Maxwell, *Isotope Effect in the Superconductivity of Mercury*, Phys. Rev. **78**, 477 (1950).

[16] C. A. Reynolds, B. Serin, W. H. Wright, and L. B. Nesbitt, *Superconductivity of Isotopes of Mercury*, Phys. Rev. **78**, 487 (1950).

[17] H. Fröhlich, *Theory of the Superconducting State. I. The Ground State at the Absolute Zero of Temperature*, Phys. Rev. **79**, 845 (1950).

[18] L. N. Cooper, *Bound Electron Pairs in a Degenerate Fermi Gas*, Phys. Rev. **104**, 1189 (1956).

[19] L. P. Gor'kov, *Microscopic derivation of the Ginzburg-Landau equations in the theory of superconductivity*, Sov. Phys. - JETP (Engl. Transl.); (United States) **9:6** (1959).

[20] H. Suhl, B. T. Matthias, and L. R. Walker, *Bardeen-Cooper-Schrieffer Theory of Superconductivity in the Case of Overlapping Bands*, Phys. Rev. Lett. **3**, 552 (1959).

[21] J. G. Bednorz and K. A. Müller, *Possible highTc superconductivity in the Ba-La-Cu-O system*, Zeitschrift für Physik B Condensed Matter **64**, 189 (1986).

[22] Z. Z. Sheng and A. M. Hermann, *Bulk superconductivity at 120 K in the Tl-Ca/Ba-Cu-O system*, Nature **332**, 138 (1988).

[23] A. Schilling, M. Cantoni, J. D. Guo, and H. R. Ott, *Superconductivity above 130 K in the Hg-Ba-Ca-Cu-O system*, Nature **363**, 56 (1993).

[24] Y. Kamihara, T. Watanabe, M. Hirano, and H. Hosono, *Iron-Based Layered Superconductor La($O_{1-x}F_x$)FeAs (x = 0.05-0.12) with T_c = 26 K*, J. Am. Chem. Soc. **130**, 3296 (2008).

[25] K. A. Brueckner, T. Soda, P. W. Anderson, and P. Morel, *Level Structure of Nuclear Matter and Liquid* He^3, Phys. Rev. **118**, 1442 (1960).

[26] V. J. Emery and A. M. Sessler, *Possible Phase Transition in Liquid* He^3, Phys. Rev. **119**, 43 (1960).

[27] P. W. Anderson and P. Morel, *Generalized Bardeen-Cooper-Schrieffer States and the Proposed Low-Temperature Phase of Liquid* He^3, Phys. Rev. **123**, 1911 (1961).

[28] W. Kohn and J. M. Luttinger, *New Mechanism for Superconductivity*, Phys. Rev. Lett. **15**, 524 (1965).

[29] M. Sigrist and K. Ueda, *Phenomenological theory of unconventional superconductivity*, Rev. Mod. Phys. **63**, 239 (1991).

[30] D. Scalapino, *The case for dx^2 - y^2 pairing in the cuprate superconductors*, Physics Reports **250**, 329 (1995).

[31] C. C. Tsuei and J. R. Kirtley, *Pairing symmetry in cuprate superconductors*, Rev. Mod. Phys. **72**, 969 (2000).

[32] E. M. Nica and Q. Si, *Multiorbital singlet pairing and d+d superconductivity*, npj Quantum Materials **6**, 3 (2021).

[33] D. S. Inosov, J. T. Park, P. Bourges, D. L. Sun, Y. Sidis, A. Schneidewind, K. Hradil, D. Haug, C. T. Lin, B. Keimer, and V. Hinkov, *Normal-state spin dynamics and temperature-dependent spin-resonance energy in optimally doped BaFe1.85Co0.15As2*, Nature Physics **6**, 178 (2010).

[34] A. P. Mackenzie and Y. Maeno, *The superconductivity of* Sr_2RuO_4 *and the physics of spin-triplet pairing*, Rev. Mod. Phys. **75**, 657 (2003).

[35] S. Ran, C. Eckberg, Q.-P. Ding, Y. Furukawa, T. Metz, S. R. Saha, I.-L. Liu, M. Zic, H. Kim, J. Paglione, and N. P. Butch, *Nearly ferromagnetic spin-triplet superconductivity*, Science **365**, 684 (2019).

[36] D. Aoki, A. Nakamura, F. Honda, D. Li, Y. Homma, Y. Shimizu, Y. J. Sato, G. Knebel, J.-P. Brison, A. Pourret, D. Braithwaite, G. Lapertot, Q. Niu, M. Vališka, H. Harima, and J. Flouquet, *Unconventional Superconductivity in Heavy Fermion UTe2*, Journal of the Physical Society of Japan **88**, 043702 (2019).

[37] D. Shoenberg, *Magnetic Oscillations in Metals*, Cambridge Monographs on Physics (Cambridge University Press, 1984).

[38] M. Fernández-Lomana, B. Wu, F. Martín-Vega, R. Sánchez-Barquilla, R. Álvarez Montoya, J. M. Castilla, J. Navarrete, J. R. Marijuan, E. Herrera, H. Suderow, and I. Guillamón, *Millikelvin scanning tunneling microscope at 20/22 T with a graphite enabled stick-slip approach and an energy resolution below 8 μeV: Application to conductance quantization at 20 T in single atom point contacts of Al and Au and to the charge density wave of 2H-NbSe2*, Review of Scientific Instruments **92**, 093701 (2021).

[39] F. Martín-Vega, V. Barrena, R. Sánchez-Barquilla, M. Fernández-Lomana, J. Benito Llorens, B. Wu, A. Fente, D. Perconte Duplain, I. Horcas, R. López, J. Blanco, J. A. Higuera, S. Mañas-Valero, N. H. Jo, J. Schmidt, P. C. Canfield, G. Rubio-Bollinger, J. G. Rodrigo, E. Herrera, I. Guillamón, and H. Suderow, *Simplified feedback control system for scanning tunneling microscopy*, Review of Scientific Instruments **92**, 103705 (2021).

[40] Y. J. Song, A. F. Otte, V. Shvarts, Z. Zhao, Y. Kuk, S. R. Blankenship, A. Band, F. M. Hess, and J. A. Stroscio, *Invited Review Article: A 10 mK scanning probe microscopy facility*, Review of Scientific Instruments **81**, 121101 (2010).

[41] G. Binnig, H. Rohrer, C. Gerber, and E. Weibel, *Tunneling through a controllable vacuum gap*, Applied Physics Letters **40**, 178 (1982).

[42] J. Bardeen, *Tunnelling from a Many-Particle Point of View*, Phys. Rev. Lett. **6**, 57 (1961).

[43] J. Tersoff and D. R. Hamann, *Theory and Application for the Scanning Tunneling Microscope*, Phys. Rev. Lett. **50**, 1998 (1983).

[44] J. Tersoff and D. R. Hamann, *Theory of the scanning tunneling microscope*, Phys. Rev. B **31**, 805 (1985).

[45] *Segainvex, Universidad Autónoma de Madrid*.

[46] *SENSOR Nederland b.v., AP Voorschoten, The Netherlands*.

[47] *Newport Corporation, Irvine, California, USA*.

[48] *TMC Vibration Control, Peabody, Massachusetts, USA*.

[49] J. G. Rodrigo, H. Suderow, and S. Vieira, *On the use of STM superconducting tips at very low temperatures*, The European Physical Journal B - Condensed Matter and Complex Systems **40**, 483 (2004).

[50] V. Crespo, A. Maldonado, J. Galvis, P. Kulkarni, I. Guillamon, J. Rodrigo, H. Suderow, S. Vieira, S. Banerjee, and P. Rodiere, *Scanning microscopies of superconductors at very low temperatures*, Physica C: Superconductivity **479**, 19 (2012), proceedings of VORTEX VII Conference.

[51] J. Lee, K. Fujita, A. R. Schmidt, C. K. Kim, H. Eisaki, S. Uchida, and J. C. Davis, *Spectroscopic Fingerprint of Phase-Incoherent Superconductivity in the Underdoped Bi2Sr2CaCu2O8+Δ*, Science **325**, 1099 (2009).

[52] M. J. Lawler, K. Fujita, J. Lee, A. R. Schmidt, Y. Kohsaka, C. K. Kim, H. Eisaki, S. Uchida, J. C. Davis, J. P. Sethna, and E.-A. Kim, *Intra-unit-cell electronic nematicity of the high-Tc copper-oxide pseudogap states*, Nature **466**, 347 (2010).

[53] L. Petersen, P. T. Sprunger, P. Hofmann, E. Lægsgaard, B. G. Briner, M. Doering, H.-P. Rust, A. M. Bradshaw, F. Besenbacher, and E. W. Plummer, *Direct imaging of the two-dimensional Fermi contour: Fourier-transform STM*, Phys. Rev. B **57**, R6858 (1998).

[54] P. J. Hirschfeld, D. Altenfeld, I. Eremin, and I. I. Mazin, *Robust determination of the superconducting gap sign structure via quasiparticle interference*, Phys. Rev. B **92**, 184513 (2015).

[55] M. P. Allan, F. Massee, D. K. Morr, J. Van Dyke, A. W. Rost, A. P. Mackenzie, C. Petrovic, and J. C. Davis, *Imaging Cooper pairing of heavy fermions in CeCoIn5*, Nature Physics **9**, 468 (2013).

[56] O. Lounasmaa, *Experimental principles and methods below 1 K* (Academic Press, 1974).

[57] H. London, G. R. Clarke, and E. Mendoza, *Osmotic Pressure of* He^3 *in Liquid* He^4*, with Proposals for a Refrigerator to Work below 1°K*, Phys. Rev. **128**, 1992 (1962).

[58] D. O. Edwards, D. F. Brewer, P. Seligman, M. Skertic, and M. Yaqub, *Solubility of* He^3 *in Liquid* He^4 *at 0°K*, Phys. Rev. Lett. **15**, 773 (1965).

[59] *Oxford Instruments plc, Tubney Woods, Abingdon, UK*.

[60] M. Wilson, *Superconducting magnets*, Monographs on cryogenics (Clarendon Press, 1983).

[61] P. Lebrun and L. Tavian, *Cooling with Superfluid Helium*, , 453 (2014), comments: 24 pages, contribution to the CAS-CERN Accelerator School: Superconductivity for Accelerators, Erice, Italy, 24 April - 4 May 2013, edited by R. Bailey.

[62] K. Bladh, D. Gunnarsson, E. Hürfeld, S. Devi, C. Kristoffersson, B. Smålander, S. Pehrson, T. Claeson, P. Delsing, and M. Taslakov, *Comparison of cryogenic filters for use in single electronics experiments*, Review of Scientific Instruments **74**, 1323 (2003).

[63] A. Lukashenko and A. V. Ustinov, *Improved powder filters for qubit measurements*, Review of Scientific Instruments **79**, 014701 (2008).

[64] J. M. Martinis, M. H. Devoret, and J. Clarke, *Experimental tests for the quantum behavior of a macroscopic degree of freedom: The phase difference across a Josephson junction*, Phys. Rev. B **35**, 4682 (1987).

[65] J. A. Galvis, E. Herrera, I. Guillamón, J. Azpeitia, R. F. Luccas, C. Munuera, M. Cuenca, J. A. Higuera, N. Díaz, M. Pazos, M. García-Hernandez, A. Buendía, S. Vieira, and H. Suderow, *Three axis vector magnet set-up for cryogenic scanning probe microscopy*, Review of Scientific Instruments **86**, 013706 (2015).

[66] *Lake Shore Cryotronics, Inc, Westerville, Ohio, USA*.

[67] H. Suderow, I. Guillamon, and S. Vieira, *Compact very low temperature scanning tunneling microscope with mechanically driven horizontal linear positioning stage*, Review of Scientific Instruments **82**, 033711 (2011).

[68] J. Benito-Llorens, *Vortex lattices under stress*, Ph.D. thesis, Universidad Autónoma de Madrid (2020).

[69] C. J. Chen, *Electromechanical deflections of piezoelectric tubes with quartered electrodes*, Applied Physics Letters **60**, 132 (1992).

[70] A. Woronko, J. Huang, and Y. Altintas, *Piezoelectric tool actuator for precision machining on conventional CNC turning centers*, Precision Engineering-journal of The International Societies for Precision Engineering and Nanotechnology **27**, 335 (2003).

[71] D. W. Pohl, *Dynamic piezoelectric translation devices*, Review of Scientific Instruments **58**, 54 (1987).

[72] C. Renner, P. Niedermann, A. D. Kent, and O. Fischer, *A vertical piezoelectric inertial slider*, Review of Scientific Instruments **61**, 965 (1990).

[73] K.-F. Hii, R. R. Vallance, and M. Pinar Mengüç, *Design, operation, and motion characteristics of a precise piezoelectric linear motor*, Precision Engineering **34**, 231 (2010).

[74] S. H. Pan, E. W. Hudson, and J. C. Davis, *3He refrigerator based very low temperature scanning tunneling microscope*, Review of Scientific Instruments **70**, 1459 (1999).

[75] J. G. Rodrigo, H. Suderow, S. Vieira, E. Bascones, and F. Guinea, *Superconducting nanostructures fabricated with the scanning tunnelling microscope*, Journal of Physics: Condensed Matter **16**, R1151 (2004).

[76] E. Scheer, N. Agraït, J. C. Cuevas, A. L. Yeyati, B. Ludoph, A. Martín-Rodero, G. R. Bollinger, J. M. van Ruitenbeek, and C. Urbina, *The signature of chemical valence in the electrical conduction through a single-atom contact*, Nature **394**, 154 (1998).

[77] N. Agraït, A. L. Yeyati, and J. M. van Ruitenbeek, *Quantum properties of atomic-sized conductors*, Physics Reports **377**, 81 (2003).

[78] E. Wolf, *Principles of Electron Tunneling Spectroscopy: Second Edition*, International Series of Monographs on Physics (OUP Oxford, 2011).

[79] J. Schwenk, S. Kim, J. Berwanger, F. Ghahari, D. Walkup, M. R. Slot, S. T. Le, W. G. Cullen, S. R. Blankenship, S. Vranjkovic, H. J. Hug, Y. Kuk, F. J. Giessibl, and J. A. Stroscio, *Achieving μeV tunneling resolution in an in-operando scanning tunneling microscopy, atomic force microscopy, and magnetotransport system for quantum materials research*, Review of Scientific Instruments **91**, 071101 (2020).

[80] S. Misra, B. B. Zhou, I. K. Drozdov, J. Seo, L. Urban, A. Gyenis, S. C. J. Kingsley, H. Jones, and A. Yazdani, *Design and performance of an ultra-high vacuum scanning tunneling microscope operating at dilution refrigerator temperatures and high magnetic fields*, Review of Scientific Instruments **84**, 103903 (2013).

[81] M. Assig, M. Etzkorn, A. Enders, W. Stiepany, C. R. Ast, and K. Kern, *A 10 mK scanning tunneling microscope operating in ultra high vacuum and high magnetic fields*, Review of Scientific Instruments **84**, 033903 (2013).

[82] U. R. Singh, M. Enayat, S. C. White, and P. Wahl, *Construction and performance of a dilution-refrigerator based spectroscopic-imaging scanning tunneling microscope*, Review of Scientific Instruments **84**, 013708 (2013).

[83] H. von Allwörden, A. Eich, E. J. Knol, J. Hermenau, A. Sonntag, J. W. Gerritsen, D. Wegner, and A. A. Khajetoorians, *Design and performance of an ultra-high vacuum spin-polarized scanning tunneling microscope operating at 30 mK and in a vector magnetic field*, Review of Scientific Instruments **89**, 033902 (2018).

[84] D. Wong, S. Jeon, K. P. Nuckolls, M. Oh, S. C. J. Kingsley, and A. Yazdani, *A modular ultra-high vacuum millikelvin scanning tunneling microscope*, Review of Scientific Instruments **91**, 023703 (2020).

[85] H. Baek, J. Ha, D. Zhang, B. Natarajan, J. P. Winterstein, R. Sharma, R. Hu, K. Wang, S. Ziemak, J. Paglione, Y. Kuk, N. B. Zhitenev, and J. A. Stroscio, *Creating nanostructured superconductors on demand by local current annealing*, Phys. Rev. B **92**, 094510 (2015).

[86] T. Machida, Y. Kohsaka, and T. Hanaguri, *A scanning tunneling microscope for spectroscopic imaging below 90 mK in magnetic fields up to 17.5 T*, Review of Scientific Instruments **89**, 093707 (2018).

[87] *Delphi, Embarcadero, Inc, Austin, Texas, USA*.

[88] I. Horcas, R. Fernández, J. M. Gómez-Rodríguez, J. Colchero, J. Gómez-Herrero, and A. M. Baro, *WSXM: A software for scanning probe microscopy and a tool for nanotechnology*, Review of Scientific Instruments **78**, 013705 (2007).

[89] *MATLAB, The Mathworks, Inc., Natick, Massachusetts, USA*.

[90] R. A. Gordon, *A Least Squares Approach to Differentiation*, Real Anal. Exchange **35**, 205 (2009).

[91] E. Fawcett, *Spin-density-wave antiferromagnetism in chromium*, Rev. Mod. Phys. **60**, 209 (1988).

[92] R. K. Kummamuru and Y.-A. Soh, *Electrical effects of spin density wave quantization and magnetic domain walls in chromium*, Nature **452**, 859 (2008).

[93] A. L. Trego, *Antiferromagnetism in dilute chromium alloys*, Ph.D. thesis (1965).

[94] P. W. Anderson, *Antiferromagnetism. Theory of Superexchange Interaction*, Phys. Rev. **79**, 350 (1950).

[95] P. W. Anderson, *Localized Magnetic States in Metals*, Phys. Rev. **124**, 41 (1961).

[96] J. R. Iglesias, C. Lacroix, and B. Coqblin, *Revisited Doniach diagram: Influence of short-range antiferromagnetic correlations in the Kondo lattice*, Phys. Rev. B **56**, 11820 (1997).

[97] S. Doniach, *The Kondo lattice and weak antiferromagnetism*, Physica B+C **91**, 231 (1977).

[98] D. V. Averin and Y. V. Nazarov, *Virtual electron diffusion during quantum tunneling of the electric charge*, Phys. Rev. Lett. **65**, 2446 (1990).

[99] M. Pustilnik and L. I. Glazman, *Kondo Effect in Real Quantum Dots*, Phys. Rev. Lett. **87**, 216601 (2001).

[100] M. Plihal and J. W. Gadzuk, *Nonequilibrium theory of scanning tunneling spectroscopy via adsorbate resonances: Nonmagnetic and Kondo impurities*, Phys. Rev. B **63**, 085404 (2001).

[101] M. Ternes, A. J. Heinrich, and W.-D. Schneider, *Spectroscopic manifestations of the Kondo effect on single adatoms*, Journal of Physics: Condensed Matter **21**, 053001 (2008).

[102] U. Fano, *Effects of Configuration Interaction on Intensities and Phase Shifts*, Phys. Rev. **124**, 1866 (1961).

[103] P. Coleman, *Handbook of Magnetism and Advanced Magnetic Materials* (John Wiley and Sons, New York, 2007).

[104] M. Maltseva, M. Dzero, and P. Coleman, *Electron Cotunneling into a Kondo Lattice*, Phys. Rev. Lett. **103**, 206402 (2009).

[105] S. Seiro, L. Jiao, S. Kirchner, S. Hartmann, S. Friedemann, C. Krellner, C. Geibel, Q. Si, F. Steglich, and S. Wirth, *Evolution of the Kondo lattice and non-Fermi liquid excitations in a heavy-fermion metal*, Nature Communications **9**, 3324 (2018).

[106] W. Knafo, D. Aoki, D. Vignolles, B. Vignolle, Y. Klein, C. Jaudet, A. Villaume, C. Proust, and J. Flouquet, *High-field metamagnetism in the antiferromagnet $CeRh_2Si_2$*, Phys. Rev. B **81**, 094403 (2010).

[107] J. Flouquet, P. Haen, S. Raymond, D. Aoki, and G. Knebel, *Itinerant metamagnetism of CeRu2Si2: bringing out the dead. Comparison with the new Sr3Ru2O7 case*, Physica B: Condensed Matter **319**, 251 (2002).

[108] J. Flouquet, *Progress in Low Temperature Physics,* Vol. 15, p. 139., edited by M. Tsubota and W. Halperin (Amsterdam, 2005).

[109] P. Haen, H. Bioud, and T. Fukuhara, *Evolution of the magnetic phase diagram in $CeRu_2(Si_{1-x}Ge_x)_2$*, Physica B: Condensed Matter **259-261**, 85 (1999).

[110] H. Kadowaki, M. Sato, and S. Kawarazaki, *Spin Fluctuation in Heavy Fermion* $CeRu_2Si_2$, Phys. Rev. Lett. **92**, 097204 (2004).

[111] D. Aoki, C. Paulsen, H. Kotegawa, F. Hardy, C. Meingast, P. Haen, M. Boukahil, W. Knafo, E. Ressouche, S. Raymond, and J. Flouquet, *Decoupling between Field-Instabilities of Antiferromagnetism and Pseudo-Metamagnetism in Rh-Doped $CeRu_2Si_2$ Kondo Lattice*, J. Phys. Soc. Jpn. **81**, 034711 (2012).

[112] S. R. Julian, F. S. Tautz, G. J. McMullan, and G. G. Lonzarich, *Quantum oscillation measurements of band magnetism in UPt_3 and $CeRu_2Si_2$*, Physica B: Condensed Matter **199-200**, 63 (1994).

[113] J. Flouquet, Y. Haga, P. Haen, D. Braithwaite, G. Knebel, S. Raymond, and S. Kambe, *Phase diagram of heavy fermion systems*, Journal of Magnetism and Magnetic Materials **272-276**, 27 (2004).

[114] M. Sato, Y. Koike, S. Katano, N. Metoki, H. Kadowaki, and S. Kawarazaki, *Field-induced Ferromagnetic Correlation in the Metamagnetic Crossover in CeRu2Si2 as Studied by Neutron Scattering*, J. Phys. Soc. Jpn. **73**, 3418 (2004).

[115] J.-X. Boucherle, F. Givord, S. Raymond, J. Schweizer, E. Lelièvre-Berna, P. Lejay, and G. Fillion, *Magnetic form factor in CeRu2Si2on crossing its metamagnetic transition*, Journal of Physics: Condensed Matter **13**, 10901 (2001).

[116] E. Herrera, V. Barrena, I. Guillamón, J. A. Galvis, W. J. Herrera, J. Castilla, D. Aoki, J. Flouquet, and H. Suderow, *1D charge density wave in the hidden order state of URu2Si2*, Communications Physics **4**, 98 (2021).

[117] I. Zeljkovic, D. Walkup, B. A. Assaf, K. L. Scipioni, R. Sankar, F. Chou, and V. Madhavan, *Strain engineering Dirac surface states in heteroepitaxial topological crystalline insulator thin films*, Nature Nanotechnology **10**, 849 (2015).

[118] T. Willers, D. T. Adroja, B. D. Rainford, Z. Hu, N. Hollmann, P. O. Körner, Y.-Y. Chin, D. Schmitz, H. H. Hsieh, H.-J. Lin, C. T. Chen, E. D. Bauer, J. L. Sarrao, K. J. McClellan, D. Byler, C. Geibel, F. Steglich, H. Aoki, P. Lejay, A. Tanaka, L. H. Tjeng, and A. Severing, *Spectroscopic determination of crystal-field levels in $CeRh_2Si_2$ and $CeRu_2Si_2$ and of the $4f^0$ contributions in CeM_2Si_2 (M=Cu, Ru, Rh, Pd, and Au)*, Phys. Rev. B **85**, 035117 (2012).

[119] P. Hansmann, A. Severing, Z. Hu, M. W. Haverkort, C. F. Chang, S. Klein, A. Tanaka, H. H. Hsieh, H.-J. Lin, C. T. Chen, B. Fåk, P. Lejay, and L. H. Tjeng, *Determining the Crystal-Field Ground State in Rare Earth Heavy Fermion Materials Using Soft-X-Ray Absorption Spectroscopy*, Phys. Rev. Lett. **100**, 066405 (2008).

[120] L. P. Regnault, W. A. C. Erkelens, J. Rossat-Mignod, P. Lejay, and J. Flouquet, *Neutron scattering study of the heavy-fermion compound* $CeRu_2Si_2$, Phys. Rev. B **38**, 4481 (1988).

[121] A. Pourret, D. Aoki, M. Boukahil, J.-P. Brison, W. Knafo, G. Knebel, S. Raymond, M. Taupin, Y. Ōnuki, and J. Flouquet, *Quantum Criticality and Lifshitz Transition in the Ising System $CeRu_2Si_2$: Comparison with $YbRh_2Si_2$*, J. Phys. Soc. Jpn. **83**, 061002 (2014).

[122] S. Blundell, *Magnetism in Condensed Matter*, Oxford Master Series in Condensed Matter Physics (OUP Oxford, Oxford, 2001).

[123] P. J. W. Moll, T. Helm, S.-S. Zhang, C. D. Batista, N. Harrison, R. D. McDonald, L. E. Winter, B. J. Ramshaw, M. K. Chan, F. F. Balakirev, B. Batlogg, E. D. Bauer, and F. Ronning, *Emergent magnetic anisotropy in the cubic heavy-fermion metal CeIn3*, npj Quantum Materials **2**, 46 (2017).

[124] K. Nagaoka, T. Jamneala, M. Grobis, and M. F. Crommie, *Temperature Dependence of a Single Kondo Impurity*, Phys. Rev. Lett. **88**, 077205 (2002).

[125] M. N. Ali, J. Xiong, S. Flynn, J. Tao, Q. D. Gibson, L. M. Schoop, T. Liang, N. Haldolaarachchige, M. Hirschberger, N. P. Ong, and R. J. Cava, *Large, non-saturating magnetoresistance in WTe2*, Nature **514**, 205 (2014).

[126] A. Pippard, *Magnetoresistance in Metals*, edited by A. Goldman, P. McClintock, and M. Springford, Cambridge Studies in Low Temperature Physics (Cambridge University Press, 1989).

[127] A. Abrikosov, *Fundamentals of the Theory of Metals* (Dover Publications, 2017).

[128] P. Kapitza and E. Rutherford, *The change of electrical conductivity in strong magnetic fields. Part I. -Experimental results*, Proceedings of the Royal Society of London. Series A, Containing Papers of a Mathematical and Physical Character **123**, 292 (1929).

[129] Z. Zhu, B. Fauqué, K. Behnia, and Y. Fuseya, *Magnetoresistance and valley degree of freedom in bulk bismuth*, Journal of Physics: Condensed Matter **30**, 313001 (2018).

[130] P. B. Alers and R. T. Webber, *The Magnetoresistance of Bismuth Crystals at Low Temperatures*, Phys. Rev. **91**, 1060 (1953).

[131] F. Y. Yang, K. Liu, C. L. Chien, and P. C. Searson, *Large Magnetoresistance and Finite-Size Effects in Electrodeposited Single-Crystal Bi Thin Films*, Phys. Rev. Lett. **82**, 3328 (1999).

[132] X. Du, S.-W. Tsai, D. L. Maslov, and A. F. Hebard, *Metal-Insulator-Like Behavior in Semimetallic Bismuth and Graphite*, Phys. Rev. Lett. **94**, 166601 (2005).

[133] Y. Kopelevich, J. H. S. Torres, R. R. da Silva, F. Mrowka, H. Kempa, and P. Esquinazi, *Reentrant Metallic Behavior of Graphite in the Quantum Limit*, Phys. Rev. Lett. **90**, 156402 (2003).

[134] B. Fauqué, B. Vignolle, C. Proust, J.-P. Issi, and K. Behnia, *Electronic instability in bismuth far beyond the quantum limit*, New Journal of Physics **11**, 113012 (2009).

[135] F. F. Tafti, Q. D. Gibson, S. K. Kushwaha, N. Haldolaarachchige, and R. J. Cava, *Resistivity plateau and extreme magnetoresistance in LaSb*, Nature Physics **12**, 272 (2016).

[136] Y. Feng, Y. Wang, D. M. Silevitch, J.-Q. Yan, R. Kobayashi, M. Hedo, T. Nakama, Y. Onuki, A. V. Suslov, B. Mihaila, P. B. Littlewood, and T. F. Rosenbaum, *Linear magnetoresistance in the low-field limit in density-wave materials*, Proceedings of the National Academy of Sciences **116**, 11201 (2019).

[137] I. A. Leahy, Y.-P. Lin, P. E. Siegfried, A. C. Treglia, J. C. W. Song, R. M. Nandkishore, and M. Lee, *Nonsaturating large magnetoresistance in semimetals*, Proceedings of the National Academy of Sciences **115**, 10570 (2018).

[138] S. Mitra, J. G. S. Kang, J. Shin, J. Q. Ng, S. S. Sunku, T. Kong, P. C. Canfield, B. S. Shastry, P. Sengupta, and C. Panagopoulos, *Quadratic to linear magnetoresistance tuning in* TmB_4, Phys. Rev. B **99**, 045119 (2019).

[139] S. L. Bud'ko, P. C. Canfield, C. H. Mielke, and A. H. Lacerda, *Anisotropic magnetic properties of light rare-earth diantimonides*, Phys. Rev. B **57**, 13624 (1998).

[140] K. Myers, S. Bud'ko, I. Fisher, Z. Islam, H. Kleinke, A. Lacerda, and P. Canfield, *Systematic study of anisotropic transport and magnetic properties of RAgSb2 (R=Y, La–Nd, Sm, Gd–Tm)*, Journal of Magnetism and Magnetic

Materials **205**, 27 (1999).

[141] E. Mun, H. Ko, G. J. Miller, G. D. Samolyuk, S. L. Bud'ko, and P. C. Canfield, *Magnetic field effects on transport properties of $PtSn_4$*, Phys. Rev. B **85**, 035135 (2012).

[142] Y. Wu, L.-L. Wang, E. Mun, D. D. Johnson, D. Mou, L. Huang, Y. Lee, S. L. Bud'ko, P. C. Canfield, and A. Kaminski, *Dirac node arcs in PtSn4*, Nature Physics **12**, 667 (2016).

[143] R. F. Luccas, A. Fente, J. Hanko, A. Correa-Orellana, E. Herrera, E. Climent-Pascual, J. Azpeitia, T. Pérez-Castañeda, M. R. Osorio, E. Salas-Colera, N. M. Nemes, F. J. Mompean, M. García-Hernández, J. G. Rodrigo, M. A. Ramos, I. Guillamón, S. Vieira, and H. Suderow, *Charge density wave in layered* $La_{1-x}Ce_xSb_2$, Phys. Rev. B **92**, 235153 (2015).

[144] J. A. Galvis, H. Suderow, S. Vieira, S. L. Bud'ko, and P. C. Canfield, *Scanning tunneling microscopy in the superconductor $LaSb_2$*, Phys. Rev. B **87**, 214504 (2013).

[145] H.-Y. Yang, T. Nummy, H. Li, S. Jaszewski, M. Abramchuk, D. S. Dessau, and F. Tafti, *Extreme magnetoresistance in the topologically trivial lanthanum monopnictide LaAs*, Phys. Rev. B **96**, 235128 (2017).

[146] C. Shekhar, A. K. Nayak, Y. Sun, M. Schmidt, M. Nicklas, I. Leermakers, U. Zeitler, Y. Skourski, J. Wosnitza, Z. Liu, Y. Chen, W. Schnelle, H. Borrmann, Y. Grin, C. Felser, and B. Yan, *Extremely large magnetoresistance and ultrahigh mobility in the topological Weyl semimetal candidate NbP*, Nature Physics **11**, 645 (2015).

[147] B. Q. Lv, Z.-L. Feng, Q.-N. Xu, X. Gao, J.-Z. Ma, L.-Y. Kong, P. Richard, Y.-B. Huang, V. N. Strocov, C. Fang, H.-M. Weng, Y.-G. Shi, T. Qian, and H. Ding, *Observation of three-component fermions in the topological semimetal molybdenum phosphide*, Nature **546**, 627 (2017).

[148] J.-Z. Ma, J.-B. He, Y.-F. Xu, B. Q. Lv, D. Chen, W.-L. Zhu, S. Zhang, L.-Y. Kong, X. Gao, L.-Y. Rong, Y.-B. Huang, P. Richard, C.-Y. Xi, E. S. Choi, Y. Shao, Y.-L. Wang, H.-J. Gao, X. Dai, C. Fang, H.-M. Weng, G.-F. Chen, T. Qian, and H. Ding, *Three-component fermions with surface Fermi arcs in tungsten carbide*, Nature Physics **14**, 349 (2018).

[149] N. H. Jo, Y. Wu, L.-L. Wang, P. P. Orth, S. S. Downing, S. Manni, D. Mou, D. D. Johnson, A. Kaminski, S. L. Bud'ko, and P. C. Canfield, *Extremely large magnetoresistance and Kohler's rule in* $PdSn_4$*: A complete study of thermodynamic, transport, and band-structure properties*, Phys. Rev. B **96**, 165145 (2017).

[150] B. Wu, V. Barrena, H. Suderow, and I. Guillamón, *Huge linear magnetoresistance due to open orbits in* γ*–*$PtBi_2$, Phys. Rev. Research **2**, 022042 (2020).

[151] D. Kang, Y. Zhou, W. Yi, C. Yang, J. Guo, Y. Shi, S. Zhang, Z. Wang, C. Zhang, S. Jiang, A. Li, K. Yang, Q. Wu, G. Zhang, L. Sun, and Z. Zhao,

Superconductivity emerging from a suppressed large magnetoresistant state in tungsten ditelluride, Nature Communications **6**, 7804 (2015).

[152] Z. Zhu, X. Lin, J. Liu, B. Fauqué, Q. Tao, C. Yang, Y. Shi, and K. Behnia, *Quantum Oscillations, Thermoelectric Coefficients, and the Fermi Surface of Semimetallic* WTe_2, Phys. Rev. Lett. **114**, 176601 (2015).

[153] C.-L. Lin, R. Arafune, R.-Y. Liu, M. Yoshimura, B. Feng, K. Kawahara, Z. Ni, E. Minamitani, S. Watanabe, Y. Shi, M. Kawai, T.-C. Chiang, I. Matsuda, and N. Takagi, *Visualizing Type-II Weyl Points in Tungsten Ditelluride by Quasiparticle Interference*, ACS Nano **11**, 11459 (2017).

[154] W. Zhang, Q. Wu, L. Zhang, S.-W. Cheong, A. A. Soluyanov, and W. Wu, *Quasiparticle interference of surface states in the type-II Weyl semimetal* $\mathbf{WTe_2}$, Phys. Rev. B **96**, 165125 (2017).

[155] Y. Yuan, X. Yang, L. Peng, Z.-J. Wang, J. Li, C.-J. Yi, J.-J. Xian, Y.-G. Shi, and Y.-S. Fu, *Quasiparticle interference of Fermi arc states in the type-II Weyl semimetal candidate* WTe_2, Phys. Rev. B **97**, 165435 (2018).

[156] A. A. Soluyanov, D. Gresch, Z. Wang, Q. Wu, M. Troyer, X. Dai, and B. A. Bernevig, *Type-II Weyl semimetals*, Nature **527**, 495 (2015).

[157] H. Weng, C. Fang, Z. Fang, B. A. Bernevig, and X. Dai, *Weyl Semimetal Phase in Noncentrosymmetric Transition-Metal Monophosphides*, Phys. Rev. X **5**, 011029 (2015).

[158] H. Weyl, *Elektron und Gravitation. I*, Zeitschrift für Physik **56**, 330 (1929).

[159] H. Nielsen and M. Ninomiya, *The Adler-Bell-Jackiw anomaly and Weyl fermions in a crystal*, Physics Letters B **130**, 389 (1983).

[160] A. A. Zyuzin and A. A. Burkov, *Topological response in Weyl semimetals and the chiral anomaly*, Phys. Rev. B **86**, 115133 (2012).

[161] D. T. Son and B. Z. Spivak, *Chiral anomaly and classical negative magnetoresistance of Weyl metals*, Phys. Rev. B **88**, 104412 (2013).

[162] B. Z. Spivak and A. V. Andreev, *Magnetotransport phenomena related to the chiral anomaly in Weyl semimetals*, Phys. Rev. B **93**, 085107 (2016).

[163] P. Hosur and X. Qi, *Recent developments in transport phenomena in Weyl semimetals*, Comptes Rendus Physique **14**, 857 (2013), topological insulators / Isolants topologiques.

[164] S. A. Parameswaran, T. Grover, D. A. Abanin, D. A. Pesin, and A. Vishwanath, *Probing the Chiral Anomaly with Nonlocal Transport in Three-Dimensional Topological Semimetals*, Phys. Rev. X **4**, 031035 (2014).

[165] A. A. Burkov, *Chiral anomaly and transport in Weyl metals*, Journal of Physics: Condensed Matter **27**, 113201 (2015).

[166] S.-M. Huang, S.-Y. Xu, I. Belopolski, C.-C. Lee, G. Chang, B. Wang, N. Alidoust, G. Bian, M. Neupane, C. Zhang, S. Jia, A. Bansil, H. Lin, and M. Z. Hasan, *A Weyl Fermion semimetal with surface Fermi arcs in the*

transition metal monopnictide TaAs class, Nature Communications **6**, 7373 (2015).

[167] S.-Y. Xu, I. Belopolski, N. Alidoust, M. Neupane, G. Bian, C. Zhang, R. Sankar, G. Chang, Z. Yuan, C.-C. Lee, S.-M. Huang, H. Zheng, J. Ma, D. S. Sanchez, B. Wang, A. Bansil, F. Chou, P. P. Shibayev, H. Lin, S. Jia, and M. Z. Hasan, *Discovery of a Weyl fermion semimetal and topological Fermi arcs*, Science **349**, 613 (2015).

[168] B. Q. Lv, H. M. Weng, B. B. Fu, X. P. Wang, H. Miao, J. Ma, P. Richard, X. C. Huang, L. X. Zhao, G. F. Chen, Z. Fang, X. Dai, T. Qian, and H. Ding, *Experimental Discovery of Weyl Semimetal TaAs*, Phys. Rev. X **5**, 031013 (2015).

[169] S.-Y. Xu, N. Alidoust, I. Belopolski, Z. Yuan, G. Bian, T.-R. Chang, H. Zheng, V. N. Strocov, D. S. Sanchez, G. Chang, C. Zhang, D. Mou, Y. Wu, L. Huang, C.-C. Lee, S.-M. Huang, B. Wang, A. Bansil, H.-T. Jeng, T. Neupert, A. Kaminski, H. Lin, S. Jia, and M. Zahid Hasan, *Discovery of a Weyl fermion state with Fermi arcs in niobium arsenide*, Nature Physics **11**, 748 (2015).

[170] S.-Y. Xu, I. Belopolski, D. S. Sanchez, C. Zhang, G. Chang, C. Guo, G. Bian, Z. Yuan, H. Lu, T.-R. Chang, P. P. Shibayev, M. L. Prokopovych, N. Alidoust, H. Zheng, C.-C. Lee, S.-M. Huang, R. Sankar, F. Chou, C.-H. Hsu, H.-T. Jeng, A. Bansil, T. Neupert, V. N. Strocov, H. Lin, S. Jia, and M. Z. Hasan, *Experimental discovery of a topological Weyl semimetal state in TaP*, Science Advances **1** (2015), 10.1126/sciadv.1501092.

[171] D.-F. Xu, Y.-P. Du, Z. Wang, Y.-P. Li, X.-H. Niu, Q. Yao, D. Pavel, Z.-A. Xu, X.-G. Wan, and D.-L. Feng, *Observation of Fermi Arcs in Non-Centrosymmetric Weyl Semi-Metal Candidate NbP*, Chinese Physics Letters **32**, 107101 (2015).

[172] Y. Sun, S.-C. Wu, M. N. Ali, C. Felser, and B. Yan, *Prediction of Weyl semimetal in orthorhombic* $MoTe_2$, Phys. Rev. B **92**, 161107 (2015).

[173] Y. Qi, P. G. Naumov, M. N. Ali, C. R. Rajamathi, W. Schnelle, O. Barkalov, M. Hanfland, S.-C. Wu, C. Shekhar, Y. Sun, V. Süß, M. Schmidt, U. Schwarz, E. Pippel, P. Werner, R. Hillebrand, T. Förster, E. Kampert, S. Parkin, R. J. Cava, C. Felser, B. Yan, and S. A. Medvedev, *Superconductivity in Weyl semimetal candidate MoTe2*, Nature Communications **7**, 11038 (2016).

[174] T.-R. Chang, S.-Y. Xu, G. Chang, C.-C. Lee, S.-M. Huang, B. Wang, G. Bian, H. Zheng, D. S. Sanchez, I. Belopolski, N. Alidoust, M. Neupane, A. Bansil, H.-T. Jeng, H. Lin, and M. Zahid Hasan, *Prediction of an arc-tunable Weyl Fermion metallic state in MoxW1-xTe2*, Nature Communications **7**, 10639 (2016).

[175] S.-Y. Xu, C. Liu, S. K. Kushwaha, R. Sankar, J. W. Krizan, I. Belopolski, M. Neupane, G. Bian, N. Alidoust, T.-R. Chang, H.-T. Jeng, C.-Y. Huang, W.-F. Tsai, H. Lin, P. P. Shibayev, F.-C. Chou, R. J. Cava, and M. Z. Hasan, *Observation of Fermi arc surface states in a topological metal*, Science **347**,

294 (2015).

[176] B. Q. Lv, N. Xu, H. M. Weng, J. Z. Ma, P. Richard, X. C. Huang, L. X. Zhao, G. F. Chen, C. E. Matt, F. Bisti, V. N. Strocov, J. Mesot, Z. Fang, X. Dai, T. Qian, M. Shi, and H. Ding, *Observation of Weyl nodes in TaAs*, Nature Physics **11**, 724 (2015).

[177] K. Deng, G. Wan, P. Deng, K. Zhang, S. Ding, E. Wang, M. Yan, H. Huang, H. Zhang, Z. Xu, J. Denlinger, A. Fedorov, H. Yang, W. Duan, H. Yao, Y. Wu, S. Fan, H. Zhang, X. Chen, and S. Zhou, *Experimental observation of topological Fermi arcs in type-II Weyl semimetal MoTe2*, Nature Physics **12**, 1105 (2016).

[178] L. Huang, T. M. McCormick, M. Ochi, Z. Zhao, M.-T. Suzuki, R. Arita, Y. Wu, D. Mou, H. Cao, J. Yan, N. Trivedi, and A. Kaminski, *Spectroscopic evidence for a type II Weyl semimetallic state in MoTe2*, Nature Materials **15**, 1155 (2016).

[179] J. Jiang, Z. K. Liu, Y. Sun, H. F. Yang, C. R. Rajamathi, Y. P. Qi, L. X. Yang, C. Chen, H. Peng, C.-C. Hwang, S. Z. Sun, S.-K. Mo, I. Vobornik, J. Fujii, S. S. P. Parkin, C. Felser, B. H. Yan, and Y. L. Chen, *Signature of type-II Weyl semimetal phase in MoTe2*, Nature Communications **8**, 13973 (2017).

[180] S. Kourtis, J. Li, Z. Wang, A. Yazdani, and B. A. Bernevig, *Universal signatures of Fermi arcs in quasiparticle interference on the surface of Weyl semimetals*, Phys. Rev. B **93**, 041109 (2016).

[181] G. Chang, S.-Y. Xu, H. Zheng, C.-C. Lee, S.-M. Huang, I. Belopolski, D. S. Sanchez, G. Bian, N. Alidoust, T.-R. Chang, C.-H. Hsu, H.-T. Jeng, A. Bansil, H. Lin, and M. Z. Hasan, *Signatures of Fermi Arcs in the Quasiparticle Interferences of the Weyl Semimetals TaAs and NbP*, Phys. Rev. Lett. **116**, 066601 (2016).

[182] H. Inoue, A. Gyenis, Z. Wang, J. Li, S. W. Oh, S. Jiang, N. Ni, B. A. Bernevig, and A. Yazdani, *Quasiparticle interference of the Fermi arcs and surface-bulk connectivity of a Weyl semimetal*, Science **351**, 1184 (2016).

[183] R. Batabyal, N. Morali, N. Avraham, Y. Sun, M. Schmidt, C. Felser, A. Stern, B. Yan, and H. Beidenkopf, *Visualizing weakly bound surface Fermi arcs and their correspondence to bulk Weyl fermions*, Science Advances **2** (2016), 10.1126/sciadv.1600709.

[184] H. Zheng, S.-Y. Xu, G. Bian, C. Guo, G. Chang, D. S. Sanchez, I. Belopolski, C.-C. Lee, S.-M. Huang, X. Zhang, R. Sankar, N. Alidoust, T.-R. Chang, F. Wu, T. Neupert, F. Chou, H.-T. Jeng, N. Yao, A. Bansil, S. Jia, H. Lin, and M. Z. Hasan, *Atomic-Scale Visualization of Quantum Interference on a Weyl Semimetal Surface by Scanning Tunneling Microscopy*, ACS Nano **10**, 1378 (2016).

[185] P. Deng, Z. Xu, K. Deng, K. Zhang, Y. Wu, H. Zhang, S. Zhou, and X. Chen, *Revealing Fermi arcs and Weyl nodes in* $MoTe_2$ *by quasiparticle interference mapping*, Phys. Rev. B **95**, 245110 (2017).

[186] Y. Wu, D. Mou, N. H. Jo, K. Sun, L. Huang, S. L. Bud'ko, P. C. Canfield, and A. Kaminski, *Observation of Fermi arcs in the type-II Weyl semimetal candidate* WTe_2, Phys. Rev. B **94**, 121113 (2016).

[187] Y. Wu, N. H. Jo, M. Ochi, L. Huang, D. Mou, S. L. Bud'ko, P. C. Canfield, N. Trivedi, R. Arita, and A. Kaminski, *Temperature-Induced Lifshitz Transition in* WTe_2, Phys. Rev. Lett. **115**, 166602 (2015).

[188] F. Y. Bruno, A. Tamai, Q. S. Wu, I. Cucchi, C. Barreteau, A. de la Torre, S. McKeown Walker, S. Riccò, Z. Wang, T. K. Kim, M. Hoesch, M. Shi, N. C. Plumb, E. Giannini, A. A. Soluyanov, and F. Baumberger, *Observation of large topologically trivial Fermi arcs in the candidate type-II Weyl semimetal* WTe_2, Phys. Rev. B **94**, 121112 (2016).

[189] C. Wang, Y. Zhang, J. Huang, S. Nie, G. Liu, A. Liang, Y. Zhang, B. Shen, J. Liu, C. Hu, Y. Ding, D. Liu, Y. Hu, S. He, L. Zhao, L. Yu, J. Hu, J. Wei, Z. Mao, Y. Shi, X. Jia, F. Zhang, S. Zhang, F. Yang, Z. Wang, Q. Peng, H. Weng, X. Dai, Z. Fang, Z. Xu, C. Chen, and X. J. Zhou, *Observation of Fermi arc and its connection with bulk states in the candidate type-II Weyl semimetal* WTe_2, Phys. Rev. B **94**, 241119 (2016).

[190] A. Mar, S. Jobic, and J. A. Ibers, *Metal-metal vs tellurium-tellurium bonding in WTe2 and its ternary variants TaIrTe4 and NbIrTe4*, J. Am. Chem. Soc. **114**, 8963 (1992).

[191] Q. Li, J. Yan, B. Yang, Y. Zang, J. Zhang, K. He, M. Wu, Y. Zhao, D. Mandrus, J. Wang, Q. Xue, L. Chi, D. J. Singh, and M. Pan, *Interference evidence for Rashba-type spin splitting on a semimetallic* WTe_2 *surface*, Phys. Rev. B **94**, 115419 (2016).

[192] P. K. Das, D. Di Sante, I. Vobornik, J. Fujii, T. Okuda, E. Bruyer, A. Gyenis, B. E. Feldman, J. Tao, R. Ciancio, G. Rossi, M. N. Ali, S. Picozzi, A. Yadzani, G. Panaccione, and R. J. Cava, *Layer-dependent quantum cooperation of electron and hole states in the anomalous semimetal WTe2*, Nature Communications **7**, 10847 (2016).

[193] P. C. Canfield and Z. Fisk, *Growth of single crystals from metallic fluxes*, Philosophical Magazine B **65**, 1117 (1992).

[194] J. Jiang, F. Tang, X. C. Pan, H. M. Liu, X. H. Niu, Y. X. Wang, D. F. Xu, H. F. Yang, B. P. Xie, F. Q. Song, P. Dudin, T. K. Kim, M. Hoesch, P. K. Das, I. Vobornik, X. G. Wan, and D. L. Feng, *Signature of Strong Spin-Orbital Coupling in the Large Nonsaturating Magnetoresistance Material* WTe_2, Phys. Rev. Lett. **115**, 166601 (2015).

[195] A. K. Mitchell and L. Fritz, *Signatures of Weyl semimetals in quasiparticle interference*, Phys. Rev. B **93**, 035137 (2016).

[196] K. v. Klitzing, G. Dorda, and M. Pepper, *New Method for High-Accuracy Determination of the Fine-Structure Constant Based on Quantized Hall Resistance*, Phys. Rev. Lett. **45**, 494 (1980).

[197] F. Tang, H. C. Po, A. Vishwanath, and X. Wan, *Comprehensive search for topological materials using symmetry indicators*, Nature **566**, 486 (2019).

[198] M. G. Vergniory, L. Elcoro, C. Felser, N. Regnault, B. A. Bernevig, and Z. Wang, *A complete catalogue of high-quality topological materials*, Nature **566**, 480 (2019).

[199] T. Zhang, Y. Jiang, Z. Song, H. Huang, Y. He, Z. Fang, H. Weng, and C. Fang, *Catalogue of topological electronic materials*, Nature **566**, 475 (2019).

[200] X.-L. Qi and S.-C. Zhang, *Topological insulators and superconductors*, Rev. Mod. Phys. **83**, 1057 (2011).

[201] C.-K. Chiu, J. C. Y. Teo, A. P. Schnyder, and S. Ryu, *Classification of topological quantum matter with symmetries*, Rev. Mod. Phys. **88**, 035005 (2016).

[202] C. Nayak, S. H. Simon, A. Stern, M. Freedman, and S. Das Sarma, *Non-Abelian anyons and topological quantum computation*, Rev. Mod. Phys. **80**, 1083 (2008).

[203] L. Jiao, S. Howard, S. Ran, Z. Wang, J. O. Rodriguez, M. Sigrist, Z. Wang, N. P. Butch, and V. Madhavan, *Chiral superconductivity in heavy-fermion metal UTe2*, Nature **579**, 523 (2020).

[204] S.-Y. Xu, N. Alidoust, I. Belopolski, A. Richardella, C. Liu, M. Neupane, G. Bian, S.-H. Huang, R. Sankar, C. Fang, B. Dellabetta, W. Dai, Q. Li, M. J. Gilbert, F. Chou, N. Samarth, and M. Z. Hasan, *Momentum-space imaging of Cooper pairing in a half-Dirac-gas topological superconductor*, Nature Physics **10**, 943 (2014).

[205] H.-H. Sun, K.-W. Zhang, L.-H. Hu, C. Li, G.-Y. Wang, H.-Y. Ma, Z.-A. Xu, C.-L. Gao, D.-D. Guan, Y.-Y. Li, C. Liu, D. Qian, Y. Zhou, L. Fu, S.-C. Li, F.-C. Zhang, and J.-F. Jia, *Majorana Zero Mode Detected with Spin Selective Andreev Reflection in the Vortex of a Topological Superconductor*, Phys. Rev. Lett. **116**, 257003 (2016).

[206] H. Zhang, C.-X. Liu, X.-L. Qi, X. Dai, Z. Fang, and S.-C. Zhang, *Topological insulators in Bi2Se3, Bi2Te3 and Sb2Te3 with a single Dirac cone on the surface*, Nature Physics **5**, 438 (2009).

[207] S. Sasaki, M. Kriener, K. Segawa, K. Yada, Y. Tanaka, M. Sato, and Y. Ando, *Topological Superconductivity in* $Cu_xBi_2Se_3$, Phys. Rev. Lett. **107**, 217001 (2011).

[208] Y. S. Hor, A. J. Williams, J. G. Checkelsky, P. Roushan, J. Seo, Q. Xu, H. W. Zandbergen, A. Yazdani, N. P. Ong, and R. J. Cava, *Superconductivity in* $Cu_xBi_2Se_3$ *and its Implications for Pairing in the Undoped Topological Insulator*, Phys. Rev. Lett. **104**, 057001 (2010).

[209] M. Kriener, K. Segawa, Z. Ren, S. Sasaki, and Y. Ando, *Bulk Superconducting Phase with a Full Energy Gap in the Doped Topological Insulator* $Cu_xBi_2Se_3$, Phys. Rev. Lett. **106**, 127004 (2011).

[210] N. Levy, T. Zhang, J. Ha, F. Sharifi, A. A. Talin, Y. Kuk, and J. A. Stroscio, *Experimental Evidence for s-Wave Pairing Symmetry in Superconducting* $Cu_xBi_2Se_3$ *Single Crystals Using a Scanning Tunneling Microscope*, Phys. Rev. Lett. **110**, 117001 (2013).

[211] G. Du, J. Shao, X. Yang, Z. Du, D. Fang, J. Wang, K. Ran, J. Wen, C. Zhang, H. Yang, Y. Zhang, and H.-H. Wen, *Drive the Dirac electrons into Cooper pairs in SrxBi2Se3*, Nature Communications **8**, 14466 (2017).

[212] S. Wilfert, P. Sessi, Z. Wang, H. Schmidt, M. C. Martínez-Velarte, S. H. Lee, Y. S. Hor, A. F. Otte, Y. Ando, W. Wu, and M. Bode, *Scanning tunneling spectroscopy investigations of superconducting-doped topological insulators: Experimental pitfalls and results*, Phys. Rev. B **98**, 085133 (2018).

[213] K. Kirshenbaum, P. S. Syers, A. P. Hope, N. P. Butch, J. R. Jeffries, S. T. Weir, J. J. Hamlin, M. B. Maple, Y. K. Vohra, and J. Paglione, *Pressure-Induced Unconventional Superconducting Phase in the Topological Insulator* Bi_2Se_3, Phys. Rev. Lett. **111**, 087001 (2013).

[214] J. L. Zhang, S. J. Zhang, H. M. Weng, W. Zhang, L. X. Yang, Q. Q. Liu, S. M. Feng, X. C. Wang, R. C. Yu, L. Z. Cao, L. Wang, W. G. Yang, H. Z. Liu, W. Y. Zhao, S. C. Zhang, X. Dai, Z. Fang, and C. Q. Jin, *Pressure-induced superconductivity in topological parent compound Bi2Te3*, Proceedings of the National Academy of Sciences **108**, 24 (2011).

[215] J. Zhu, J. L. Zhang, P. P. Kong, S. J. Zhang, X. H. Yu, J. L. Zhu, Q. Q. Liu, X. Li, R. C. Yu, R. Ahuja, W. G. Yang, G. Y. Shen, H. K. Mao, H. M. Weng, X. Dai, Z. Fang, Y. S. Zhao, and C. Q. Jin, *Superconductivity in Topological Insulator Sb2Te3 Induced by Pressure*, Scientific Reports **3**, 2016 (2013).

[216] L. Aggarwal, A. Gaurav, G. S. Thakur, Z. Haque, A. K. Ganguli, and G. Sheet, *Unconventional superconductivity at mesoscopic point contacts on the 3D Dirac semimetal Cd3As2*, Nature Materials **15**, 32 (2016).

[217] H. Wang, H. Wang, H. Liu, H. Lu, W. Yang, S. Jia, X.-J. Liu, X. C. Xie, J. Wei, and J. Wang, *Observation of superconductivity induced by a point contact on 3D Dirac semimetal Cd3As2 crystals*, Nature Materials **15**, 38 (2016).

[218] L. He, Y. Jia, S. Zhang, X. Hong, C. Jin, and S. Li, *Pressure-induced superconductivity in the three-dimensional topological Dirac semimetal Cd3As2*, npj Quantum Materials **1**, 16014 (2016).

[219] M. N. Ali, Q. D. Gibson, T. Klimczuk, and R. J. Cava, *Noncentrosymmetric superconductor with a bulk three-dimensional Dirac cone gapped by strong spin-orbit coupling*, Phys. Rev. B **89**, 020505 (2014).

[220] G. Bian, T.-R. Chang, R. Sankar, S.-Y. Xu, H. Zheng, T. Neupert, C.-K. Chiu, S.-M. Huang, G. Chang, I. Belopolski, D. S. Sanchez, M. Neupane, N. Alidoust, C. Liu, B. Wang, C.-C. Lee, H.-T. Jeng, C. Zhang, Z. Yuan, S. Jia, A. Bansil, F. Chou, H. Lin, and M. Z. Hasan, *Topological nodal-line fermions in spin-orbit metal PbTaSe2*, Nature Communications **7**, 10556 (2016).

[221] T.-R. Chang, P.-J. Chen, G. Bian, S.-M. Huang, H. Zheng, T. Neupert, R. Sankar, S.-Y. Xu, I. Belopolski, G. Chang, B. Wang, F. Chou, A. Bansil, H.-T. Jeng, H. Lin, and M. Z. Hasan, *Topological Dirac surface states and superconducting pairing correlations in* $PbTaSe_2$, Phys. Rev. B **93**, 245130 (2016).

[222] M. X. Wang, Y. Xu, L. P. He, J. Zhang, X. C. Hong, P. L. Cai, Z. B. Wang, J. K. Dong, and S. Y. Li, *Nodeless superconducting gaps in noncentrosymmetric superconductor* $PbTaSe_2$ *with topological bulk nodal lines*, Phys. Rev. B **93**, 020503 (2016).

[223] C.-L. Zhang, Z. Yuan, G. Bian, S.-Y. Xu, X. Zhang, M. Z. Hasan, and S. Jia, *Superconducting properties in single crystals of the topological nodal semimetal* $PbTaSe_2$, Phys. Rev. B **93**, 054520 (2016).

[224] G. M. Pang, M. Smidman, L. X. Zhao, Y. F. Wang, Z. F. Weng, L. Q. Che, Y. Chen, X. Lu, G. F. Chen, and H. Q. Yuan, *Nodeless superconductivity in noncentrosymmetric* $PbTaSe_2$ *single crystals*, Phys. Rev. B **93**, 060506 (2016).

[225] Y. Wu, G. Drachuck, L.-L. Wang, D. D. Johnson, P. Swatek, B. Schrunk, D. Mou, L. Huang, S. L. Bud'ko, P. C. Canfield, and A. Kaminski, *Electronic structure of the topological superconductor candidate* Au_2Pb, Phys. Rev. B **98**, 161107 (2018).

[226] L. M. Schoop, L. S. Xie, R. Chen, Q. D. Gibson, S. H. Lapidus, I. Kimchi, M. Hirschberger, N. Haldolaarachchige, M. N. Ali, C. A. Belvin, T. Liang, J. B. Neaton, N. P. Ong, A. Vishwanath, and R. J. Cava, *Dirac metal to topological metal transition at a structural phase change in* Au_2Pb *and prediction of* $\mathbb{Z}_2$ *topology for the superconductor*, Phys. Rev. B **91**, 214517 (2015).

[227] K. W. Chen, D. Graf, T. Besara, A. Gallagher, N. Kikugawa, L. Balicas, T. Siegrist, A. Shekhter, and R. E. Baumbach, *Temperature-pressure phase diagram of cubic Laves phase* Au_2Pb, Phys. Rev. B **93**, 045118 (2016).

[228] J. Wu, Z. Feng, J. Wang, Q. Chen, C. Ding, T. Chen, Z. Guo, J. Wen, Y. Shi, D. Xing, and J. Sun, *Ground states of* Au_2Pb *and pressure-enhanced superconductivity*, Phys. Rev. B **100**, 060103 (2019).

[229] R. Kemmler, R. Hübner, A. Löhle, D. Neubauer, I. Voloshenko, L. M. Schoop, M. Dressel, and A. V. Pronin, *Free-carrier dynamics in Au2Pb probed by optical conductivity measurements*, Journal of Physics: Condensed Matter **30**, 485403 (2018).

[230] D. Hamilton, C. Raub, B. Matthias, E. Corenzwit, and G. Hull, *Some new superconducting compounds*, Journal of Physics and Chemistry of Solids **26**, 665 (1965).

[231] Y. Xing, H. Wang, C.-K. Li, X. Zhang, J. Liu, Y. Zhang, J. Luo, Z. Wang, Y. Wang, L. Ling, M. Tian, S. Jia, J. Feng, X.-J. Liu, J. Wei, and J. Wang, *Superconductivity in topologically nontrivial material Au2Pb*, npj Quantum Materials **1**, 16005 (2016).

[232] Y. J. Yu, Y. Xu, Y. Xing, J. Zhang, T. P. Ying, X. C. Hong, M. X. Wang, X. Zhang, S. Jia, J. Wang, and S. Y. Li, *Fully gapped superconducting state in Au 2 Pb: A natural candidate for topological superconductor*, EPL (Europhysics Letters) **116**, 67002 (2016).

[233] P. C. Canfield, *New materials physics*, Reports on Progress in Physics **83**, 016501 (2019).

[234] S. Cheon, K. H. Lee, S. B. Chung, and B.-J. Yang, *Emergence of topological superconductivity in doped topological Dirac semimetals under symmetry-lowering lattice distortions*, Scientific Reports **11**, 18539 (2021).

[235] T. O. Wehling, A. M. Black-Schaffer, and A. V. Balatsky, *Dirac materials*, Advances in Physics **63**, 1 (2014).

[236] M. Sakano, K. Okawa, M. Kanou, H. Sanjo, T. Okuda, T. Sasagawa, and K. Ishizaka, *Topologically protected surface states in a centrosymmetric superconductor β-PdBi2*, Nature Communications **6**, 8595 (2015).

[237] Z. Sun, M. Enayat, A. Maldonado, C. Lithgow, E. Yelland, D. C. Peets, A. Yaresko, A. P. Schnyder, and P. Wahl, *Dirac surface states and nature of superconductivity in Noncentrosymmetric BiPd*, Nature Communications **6**, 6633 (2015).

[238] X. Zhang, Q. Liu, J.-W. Luo, A. J. Freeman, and A. Zunger, *Hidden spin polarization in inversion-symmetric bulk crystals*, Nature Physics **10**, 387 (2014).

[239] E. Herrera, I. Guillamón, J. A. Galvis, A. Correa, A. Fente, R. F. Luccas, F. J. Mompean, M. García-Hernández, S. Vieira, J. P. Brison, and H. Suderow, *Magnetic field dependence of the density of states in the multiband superconductor β* – Bi_2Pd, Phys. Rev. B **92**, 054507 (2015).

[240] K. Iwaya, Y. Kohsaka, K. Okawa, T. Machida, M. S. Bahramy, T. Hanaguri, and T. Sasagawa, *Full-gap superconductivity in spin-polarised surface states of topological semimetal β-PdBi2*, Nature Communications **8**, 976 (2017).

[241] Y.-F. Lv, W.-L. Wang, Y.-M. Zhang, H. Ding, W. Li, L. Wang, K. He, C.-L. Song, X.-C. Ma, and Q.-K. Xue, *Experimental signature of topological superconductivity and Majorana zero modes on β-Bi2Pd thin films*, Science Bulletin **62**, 852 (2017).

[242] Y. Li, X. Xu, M.-H. Lee, M.-W. Chu, and C. L. Chien, *Observation of half-quantum flux in the unconventional superconductor β-Bi2Pd*, Science **366**, 238 (2019).

[243] R. Prozorov, A. F. Fidler, J. R. Hoberg, and P. C. Canfield, *Suprafroth in type-I superconductors*, Nature Physics **4**, 327 (2008).

[244] S. Mühlbauer, C. Pfleiderer, P. Böni, M. Laver, E. M. Forgan, D. Fort, U. Keiderling, and G. Behr, *Morphology of the Superconducting Vortex Lattice in Ultrapure Niobium*, Phys. Rev. Lett. **102**, 136408 (2009).

[245] E. H. Brandt and M. P. Das, *Attractive Vortex Interaction and the Intermediate-Mixed State of Superconductors*, Journal of Superconductivity and Novel Magnetism **24**, 57 (2011).

[246] E. H. Brandt and U. Essmann, *The Flux-Line Lattice in Type-II Superconductors*, physica status solidi (b) **144**, 13 (1987).

[247] S. Mühlbauer, D. Honecker, E. A. Périgo, F. Bergner, S. Disch, A. Heinemann, S. Erokhin, D. Berkov, C. Leighton, M. R. Eskildsen, and A. Michels, *Magnetic small-angle neutron scattering*, Rev. Mod. Phys. **91**, 015004 (2019).

[248] E. H. Brandt, *Levitation in Physics*, Science **243**, 349 (1989).

[249] E. H. Brandt, *Rigid levitation and suspension of high-temperature superconductors by magnets*, American Journal of Physics **58**, 43 (1990).

[250] M. R. Osorio, D. E. Lahera, and H. Suderow, *Magnetic levitation on a type-I superconductor as a practical demonstration experiment for students*, European Journal of Physics **33**, 1383 (2012).

[251] D. R. Aston, L. W. Dubeck, and F. Rothwarf, *"Intermediate Mixed" State of Type-II Superconductors*, Phys. Rev. B **3**, 2231 (1971).

[252] Y. Kamihara, H. Hiramatsu, M. Hirano, R. Kawamura, H. Yanagi, T. Kamiya, and H. Hosono, *Iron-Based Layered Superconductor: LaOFeP*, J. Am. Chem. Soc. **128**, 10012 (2006).

[253] T. Watanabe, H. Yanagi, T. Kamiya, Y. Kamihara, H. Hiramatsu, M. Hirano, and H. Hosono, *Nickel-Based Oxyphosphide Superconductor with a Layered Crystal Structure, LaNiOP*, Inorganic Chemistry **46**, 7719 (2007), pMID: 17705374.

[254] J. Paglione and R. L. Greene, *High-temperature superconductivity in iron-based materials*, Nature Physics **6**, 645 (2010).

[255] A. Chubukov and P. J. Hirschfeld, *Iron-based superconductors, seven years later*, Physics Today **68**, 46 (2015).

[256] I. Bozovic and C. Ahn, *A new frontier for superconductivity*, Nature Physics **10**, 892 (2014).

[257] E. Bascones, B. Valenzuela, and M. J. Calderón, *Orbital differentiation and the role of orbital ordering in the magnetic state of Fe superconductors*, Phys. Rev. B **86**, 174508 (2012).

[258] R. M. Fernandes, A. V. Chubukov, and J. Schmalian, *What drives nematic order in iron-based superconductors?*, Nature Physics **10**, 97 (2014).

[259] F.-C. Hsu, J.-Y. Luo, K.-W. Yeh, T.-K. Chen, T.-W. Huang, P. M. Wu, Y.-C. Lee, Y.-L. Huang, Y.-Y. Chu, D.-C. Yan, and M.-K. Wu, *Superconductivity in the PbO-type structure α-FeSe*, Proceedings of the National Academy of Sciences **105**, 14262 (2008).

[260] S. Kasahara, T. Watashige, T. Hanaguri, Y. Kohsaka, T. Yamashita, Y. Shimoyama, Y. Mizukami, R. Endo, H. Ikeda, K. Aoyama, T. Terashima,

S. Uji, T. Wolf, H. von Löhneysen, T. Shibauchi, and Y. Matsuda, *Field-induced superconducting phase of FeSe in the BCS-BEC cross-over*, Proceedings of the National Academy of Sciences **111**, 16309 (2014).

[261] S. Margadonna, Y. Takabayashi, M. T. McDonald, K. Kasperkiewicz, Y. Mizuguchi, Y. Takano, A. N. Fitch, E. Suard, and K. Prassides, *Crystal structure of the new $FeSe_{1-x}$ superconductor*, Chem. Commun. , 5607 (2008).

[262] T. M. McQueen, A. J. Williams, P. W. Stephens, J. Tao, Y. Zhu, V. Ksenofontov, F. Casper, C. Felser, and R. J. Cava, *Tetragonal-to-Orthorhombic Structural Phase Transition at 90 K in the Superconductor* $Fe_{1.01}Se$, Phys. Rev. Lett. **103**, 057002 (2009).

[263] S.-H. Baek, D. V. Efremov, J. M. Ok, J. S. Kim, J. van den Brink, and B. Büchner, *Orbital-driven nematicity in FeSe*, Nature Materials **14**, 210 (2015).

[264] M. Bendele, A. Amato, K. Conder, M. Elender, H. Keller, H.-H. Klauss, H. Luetkens, E. Pomjakushina, A. Raselli, and R. Khasanov, *Pressure Induced Static Magnetic Order in Superconducting* $FeSe_{1-x}$, Phys. Rev. Lett. **104**, 087003 (2010).

[265] M. Bendele, A. Ichsanow, Y. Pashkevich, L. Keller, T. Strässle, A. Gusev, E. Pomjakushina, K. Conder, R. Khasanov, and H. Keller, *Coexistence of superconductivity and magnetism in $FeSe_{1-x}$ under pressure*, Phys. Rev. B **85**, 064517 (2012).

[266] Y. Mizuguchi, F. Tomioka, S. Tsuda, T. Yamaguchi, and Y. Takano, *Superconductivity at 27K in tetragonal FeSe under high pressure*, Appl. Phys. Lett. **93**, 152505 (2008).

[267] S. Margadonna, Y. Takabayashi, Y. Ohishi, Y. Mizuguchi, Y. Takano, T. Kagayama, T. Nakagawa, M. Takata, and K. Prassides, *Pressure evolution of the low-temperature crystal structure and bonding of the superconductor FeSe* ($T_c = 37$ *K*), Phys. Rev. B **80**, 064506 (2009).

[268] S. Masaki, H. Kotegawa, Y. Hara, H. Tou, K. Murata, Y. Mizuguchi, and Y. Takano, *Precise Pressure Dependence of the Superconducting Transition Temperature of FeSe: Resistivity and 77Se-NMR Study*, J. Phys. Soc. Jpn. **78**, 063704 (2009).

[269] H. Okabe, N. Takeshita, K. Horigane, T. Muranaka, and J. Akimitsu, *Pressure-induced high-T_c superconducting phase in FeSe: Correlation between anion height and T_c*, Phys. Rev. B **81**, 205119 (2010).

[270] Q. Wang, Y. Shen, B. Pan, Y. Hao, M. Ma, F. Zhou, P. Steffens, K. Schmalzl, T. R. Forrest, M. Abdel-Hafiez, X. Chen, D. A. Chareev, A. N. Vasiliev, P. Bourges, Y. Sidis, H. Cao, and J. Zhao, *Strong interplay between stripe spin fluctuations, nematicity and superconductivity in FeSe*, Nature Materials **15**, 159 (2016).

[271] P. O. Sprau, A. Kostin, A. Kreisel, A. E. Böhmer, V. Taufour, P. C. Canfield, S. Mukherjee, P. J. Hirschfeld, B. M. Andersen, and J. C. S. Davis, *Discovery*

of orbital-selective Cooper pairing in FeSe, Science **357**, 75 (2017).

[272] P. J. Hirschfeld, D. Altenfeld, I. Eremin, and I. I. Mazin, *Robust determination of the superconducting gap sign structure via quasiparticle interference*, Phys. Rev. B **92**, 184513 (2015).

[273] J. H. J. Martiny, A. Kreisel, P. J. Hirschfeld, and B. M. Andersen, *Robustness of a quasiparticle interference test for sign-changing gaps in multiband superconductors*, Phys. Rev. B **95**, 184507 (2017).

[274] S. Gerber, S.-L. Yang, D. Zhu, H. Soifer, J. A. Sobota, S. Rebec, J. J. Lee, T. Jia, B. Moritz, C. Jia, A. Gauthier, Y. Li, D. Leuenberger, Y. Zhang, L. Chaix, W. Li, H. Jang, J.-S. Lee, M. Yi, G. L. Dakovski, S. Song, J. M. Glownia, S. Nelson, K. W. Kim, Y.-D. Chuang, Z. Hussain, R. G. Moore, T. P. Devereaux, W.-S. Lee, P. S. Kirchmann, and Z.-X. Shen, *Femtosecond electron-phonon lock-in by photoemission and x-ray free-electron laser*, Science **357**, 71 (2017).

[275] J. Maletz, V. B. Zabolotnyy, D. V. Evtushinsky, S. Thirupathaiah, A. U. B. Wolter, L. Harnagea, A. N. Yaresko, A. N. Vasiliev, D. A. Chareev, A. E. Böhmer, F. Hardy, T. Wolf, C. Meingast, E. D. L. Rienks, B. Büchner, and S. V. Borisenko, *Unusual band renormalization in the simplest iron-based superconductor $FeSe_{1-x}$*, Phys. Rev. B **89**, 220506 (2014).

[276] S. Mukherjee, A. Kreisel, P. J. Hirschfeld, and B. M. Andersen, *Model of Electronic Structure and Superconductivity in Orbitally Ordered FeSe*, Phys. Rev. Lett. **115**, 026402 (2015).

[277] A. Kreisel, S. Mukherjee, P. J. Hirschfeld, and B. M. Andersen, *Spin excitations in a model of FeSe with orbital ordering*, Phys. Rev. B **92**, 224515 (2015).

[278] Y. Suzuki, T. Shimojima, T. Sonobe, A. Nakamura, M. Sakano, H. Tsuji, J. Omachi, K. Yoshioka, M. Kuwata-Gonokami, T. Watashige, R. Kobayashi, S. Kasahara, T. Shibauchi, Y. Matsuda, Y. Yamakawa, H. Kontani, and K. Ishizaka, *Momentum-dependent sign inversion of orbital order in superconducting FeSe*, Phys. Rev. B **92**, 205117 (2015).

[279] M. D. Watson, T. K. Kim, L. C. Rhodes, M. Eschrig, M. Hoesch, A. A. Haghighirad, and A. I. Coldea, *Evidence for unidirectional nematic bond ordering in FeSe*, Phys. Rev. B **94**, 201107 (2016).

[280] T. Terashima, N. Kikugawa, A. Kiswandhi, E.-S. Choi, J. S. Brooks, S. Kasahara, T. Watashige, H. Ikeda, T. Shibauchi, Y. Matsuda, T. Wolf, A. E. Böhmer, F. Hardy, C. Meingast, H. v. Löhneysen, M.-T. Suzuki, R. Arita, and S. Uji, *Anomalous Fermi surface in FeSe seen by Shubnikov–de Haas oscillation measurements*, Phys. Rev. B **90**, 144517 (2014).

[281] M. D. Watson, T. K. Kim, A. A. Haghighirad, N. R. Davies, A. McCollam, A. Narayanan, S. F. Blake, Y. L. Chen, S. Ghannadzadeh, A. J. Schofield, M. Hoesch, C. Meingast, T. Wolf, and A. I. Coldea, *Emergence of the nematic electronic state in FeSe*, Phys. Rev. B **91**, 155106 (2015).

[282] C. Li, X. Wu, L. Wang, D. Liu, Y. Cai, Y. Wang, Q. Gao, C. Song, J. Huang, C. Dong, J. Liu, P. Ai, H. Luo, C. Yin, G. Liu, Y. Huang, Q. Wang, X. Jia, F. Zhang, S. Zhang, F. Yang, Z. Wang, Q. Peng, Z. Xu, Y. Shi, J. Hu, T. Xiang, L. Zhao, and X. J. Zhou, *Spectroscopic Evidence for an Additional Symmetry Breaking in the Nematic State of FeSe Superconductor*, Phys. Rev. X **10**, 031033 (2020).

[283] A. Kreisel, B. M. Andersen, P. O. Sprau, A. Kostin, J. C. S. Davis, and P. J. Hirschfeld, *Orbital selective pairing and gap structures of iron-based superconductors*, Phys. Rev. B **95**, 174504 (2017).

[284] R. Fernández-Martín, M. J. Calderón, L. Fanfarillo, and B. Valenzuela, *The Role of Orbital Nesting in the Superconductivity of Iron-Based Superconductors*, Condensed Matter **6** (2021), 10.3390/condmat6030034.

[285] C.-L. Song, Y.-L. Wang, P. Cheng, Y.-P. Jiang, W. Li, T. Zhang, Z. Li, K. He, L. Wang, J.-F. Jia, H.-H. Hung, C. Wu, X. Ma, X. Chen, and Q.-K. Xue, *Direct Observation of Nodes and Twofold Symmetry in FeSe Superconductor*, Science **332**, 1410 (2011).

[286] T. Watashige, S. Arsenijević, T. Yamashita, D. Terazawa, T. Onishi, L. Opherden, S. Kasahara, Y. Tokiwa, Y. Kasahara, T. Shibauchi, H. von Löhneysen, J. Wosnitza, and Y. Matsuda, *Quasiparticle Excitations in the Superconducting State of FeSe Probed by Thermal Hall Conductivity in the Vicinity of the BCS-BEC Crossover*, Journal of the Physical Society of Japan **86** (2016), 10.7566/JPSJ.86.014707.

[287] P. Fulde and R. A. Ferrell, *Superconductivity in a Strong Spin-Exchange Field*, Phys. Rev. **135**, A550 (1964).

[288] A. I. Larkin and Y. N. Ovchinnikov, *Nonuniform state of superconductors*, Zh. Eksperim. i Teor. Fiz. **47** (1964).

[289] S. Kasahara, Y. Sato, S. Licciardello, M. Čulo, S. Arsenijević, T. Ottenbros, T. Tominaga, J. Böker, I. Eremin, T. Shibauchi, J. Wosnitza, N. E. Hussey, and Y. Matsuda, *Evidence for an Fulde-Ferrell-Larkin-Ovchinnikov State with Segmented Vortices in the BCS-BEC-Crossover Superconductor FeSe*, Phys. Rev. Lett. **124**, 107001 (2020).

[290] T. Hanaguri, T. Machida, Y. Sato, K. Kasahara, T. Shibauchi, and Y. Matsuda, in *APS March Meeting 2020, Volume 65, Number 1* (2020).

[291] S. Kasahara, T. Yamashita, A. Shi, R. Kobayashi, Y. Shimoyama, T. Watashige, K. Ishida, T. Terashima, T. Wolf, F. Hardy, C. Meingast, H. v. Löhneysen, A. Levchenko, T. Shibauchi, and Y. Matsuda, *Giant superconducting fluctuations in the compensated semimetal FeSe at the BCS-BEC crossover*, Nature Communications **7**, 12843 (2016).

[292] A. V. Putilov, C. Di Giorgio, V. L. Vadimov, D. J. Trainer, E. M. Lechner, J. L. Curtis, M. Abdel-Hafiez, O. S. Volkova, A. N. Vasiliev, D. A. Chareev, G. Karapetrov, A. E. Koshelev, A. Y. Aladyshkin, A. S. Mel'nikov, and M. Iavarone, *Vortex-core properties and vortex-lattice transformation in FeSe*,

Phys. Rev. B **99**, 144514 (2019).

[293] D.-C. Lu, Y.-Y. Lv, J. Li, B.-Y. Zhu, Q.-H. Wang, H.-B. Wang, and P.-H. Wu, *Elliptical vortex and oblique vortex lattice in the FeSe superconductor based on the nematicity and mixed superconducting orders*, npj Quantum Materials **3**, 12 (2018).

[294] A. V. Putilov, C. Di Giorgio, V. L. Vadimov, D. J. Trainer, E. M. Lechner, J. L. Curtis, M. Abdel-Hafiez, O. S. Volkova, A. N. Vasiliev, D. A. Chareev, G. Karapetrov, A. E. Koshelev, A. Y. Aladyshkin, A. S. Mel'nikov, and M. Iavarone, *Vortex-core properties and vortex-lattice transformation in FeSe*, Phys. Rev. B **99**, 144514 (2019).